

Satellite Remote Sensing of Volcanic Plumes



Isabelle A. Taylor

The Queen's College

University of Oxford

A thesis submitted for the degree of

Doctor of Philosophy

Trinity 2019

Abstract

Volcanic plumes are one of many hazards associated with eruptions. Monitoring helps to mitigate against their effects, understand their environmental and climatic impacts, and interpret volcanic activity. While ground-based measurements are valuable, field campaigns and ground-based instrument networks are expensive and not always viable. Satellite remote sensing is a cost-effective alternative and can be used to track the propagation of plumes as they travel away from the source. This thesis explores some of the ways in which the Infrared Atmospheric Sounding Interferometer (IASI) can be used for this purpose.

A method known as CO₂ slicing, commonly used to obtain the altitude of meteorological clouds, was adapted for IASI to find the altitude of volcanic ash clouds. The technique was first tested on modelled data, before being successfully applied to scenes containing ash from the Eyjafjallajökull and Grimsvötn eruptions.

The second part of this thesis explores how IASI retrievals can be used to monitor volcanic emissions of sulphur dioxide (SO₂). A linear retrieval was first applied globally to identify sources of SO₂, including emissions from explosive eruptions, non-eruptive degassing and anthropogenic sources. Emissions were commonly identified in Ecuador and Kamchatka and these were explored further with an iterative retrieval which quantified the SO₂ amount in each region. The trends observed with IASI were similar to those seen with the Ozone Monitoring Instrument (OMI), and at Tungurahua, good agreement was seen with ground-based flux measurements.

The final chapter builds on this research by systematically comparing the upwind and downwind mean column amounts obtained with a linear retrieval at 166 volcanoes. This highlights the strengths and weaknesses of the retrieval and reveals emission trends at some volcanoes; sometimes agreeing well with trends from OMI and in thermal emissions. This simple procedure demonstrates the utility of using IASI for observing changes in volcanic emissions.

Extended Abstract

Volcanic plumes are one of the many hazards associated with volcanic eruptions. Monitoring them helps to mitigate against their effects, understand the impacts they have on the environment and climate, and interpret volcanic activity. While ground based measurements are valuable, field campaigns and ground based instrument networks are expensive and are sometimes not viable. Satellite remote sensing is a cost-effective alternative to some of these limitations and can be used to track the propagation of plumes in the atmosphere as they travel across the globe.

This thesis explores some of the ways in which the Infrared Atmospheric Sounding Interferometer (IASI) can be used to study volcanic plumes. IASI is an infrared sensor on-board three of EUMETSAT's meteorological satellites, all of which achieve global coverage twice a day. Within the instrument's spectral range there is sensitivity to both sulphur dioxide and volcanic ash, and as a hyperspectral sensor with a high spectral resolution, it is possible to better resolve the spectral features associated with these. This gives the instrument greater sensitivity than some broadband sensors.

To mitigate against the hazard presented by volcanic ash it is essential to know its position. This includes knowing the altitude. The first part of this thesis adapts a method known as CO₂ slicing, which has been widely applied to find the altitude of meteorological cloud, to obtain the height of volcanic ash with IASI. This method utilises an absorption feature within the thermal infrared where there is sensitivity to the height of different cloud layers. Simulated ash spectra are first exploited to select a subset of IASI channels, and then to test the validity of this technique for ash. After demonstrating that this technique has promise, it was then applied to ash scenes from the Eyjafjallajökull and Grimsvötn eruptions. It compared well against a satellite borne LiDAR used for validation and showed improved results compared to an optimal estimation scheme also developed for IASI, which is able to retrieve the ash optical depth and effective radius, as well as the height. As a relatively fast tool, it is suggested that the CO₂ slicing technique could be used to get a first estimate of the ash height which could then be used within the optimal

estimation scheme to yield improved results on operational timescales.

IASI has been widely used to study SO₂ emissions from large eruptions but its utility for investigating the emissions from smaller sources has not been fully explored. The second part of this thesis works with two retrievals developed for this instrument. The first was a ‘fast’ linear retrieval which was applied globally to identify sources of SO₂. The results were dominated by emissions from large scale eruptions but elevated signals can also be identified from smaller eruptions, strong non-eruptive volcanic sources, and industrial centres suggesting the technique has promise for detecting lower altitude emissions and smaller SO₂ mass loadings. The speed of this technique facilitates its use for near real time monitoring and for identifying interesting signals for further study with the full iterative retrieval, which can quantify the amount of gas released. SO₂ emissions were persistently detected at volcanoes in Ecuador and Kamchatka and so these were selected for further study with the iterative retrieval. Across both regions, SO₂ emissions identified with IASI corresponded well with reports of volcanic activity from other sources. At Tungurahua, it was possible to compare the IASI observations against those from the ultraviolet Ozone Monitoring Instrument (OMI) and ground based SO₂ flux measurements. The results were promising with each dataset showing similar trends, and suggested that the IASI datasets could be used alongside other tools to contribute to volcano monitoring.

This was built upon in the final part of this thesis. Here, the SO₂ linear retrieval was applied to IASI spectra between August 2007 and October 2017. The retrieval output was then rotated so that the plumes always aligned to the north, so isolating the SO₂ signal. Averaging over different time periods (monthly, annual and multi annual) enhanced the signal. A simple comparison of the upwind and downwind averaged column amounts was used to determine whether there was an elevated signal in that month, and show changes in the quantity of SO₂ over a ten year period. Applying this systematically across the globe highlighted the strengths and weaknesses of using the IASI linear retrieval. It was demonstrated that detections were uncommon at low altitude volcanoes in the tropics (in line with observations made by previous IASI studies) but that it performed well for higher altitude volcanoes, particularly those in Central and South America. For volcanoes in these regions, a simple difference in the upwind and downwind column amounts produced patterns that matched well with fluxes obtained for the OMI instrument, the frequency of thermal anomalies and descriptions of volcanic activity in literature. In addition, the study highlights the strength of using infrared instruments which are able to measure SO₂ emissions in low levels of UV,

for example in high latitude winters. This study produced a comprehensive dataset of the SO₂ emissions seen with IASI that could be used in the future, alongside other datasets, for studying different volcanoes.

Overall, the research presented in this thesis demonstrates some of the ways in which the IASI instrument can be used to understand volcanic plumes, and complement other datasets.

Funding

This research was funded by the National Environmental Research Centre (NERC; NE/L002612/1) through the Environmental Research Doctoral Training Partnership. Some of the preliminary research for chapter 2 was supported by a Met Office Academic Partnership. The Centre for Observation and Modelling of Earthquakes, Volcanoes and Tectonics (COMET) supported the project with computing resources on the JASMIN supercomputer at the Centre for Environmental Data Analysis (CEDA).



Acknowledgements

There are so many people, far more than it is possible to mention here, who over the course of my life have helped me to reach this point, and who made completing a PhD such an enjoyable experience.

At Oxford, I have been lucky to have been supported by three supervisors, Tamsin Mather, Don Grainger and Elisa Carboni, all of whom have been incredibly generous with their time and the advice they have given - on more than just the contents of my thesis. Without them this endeavour would have felt impossible. I am particularly indebted to Elisa who I have greatly enjoyed working with- I can only hope that one day I can also inspire others with sheer enthusiasm for science.

I am grateful for the considerable feedback and advice I've received from collaborators, including Nicolas Theys, Silvana Hidalgo, Brendan McCormick-Kilbride and Susanna Ebmeier .

I've been fortunate to benefit from the support from the members of the Earth Observation Data Group (EODG) - some of whom have now left. Before starting in Oxford I was unaware of how many great ideas are sparked in the pub.

Beyond the university, I have been supported by so many friends and family members, and also a few four legged companions. In particular, my thanks goes to my mum, who has always encouraged and helped me.

My final thanks go to my partner of ten years and best friend, Lee Bandettini. You have always been there - to hold my hand when everything felt overwhelming and to celebrate, no matter how big the achievement. Your love and support has meant everything to me.

Contents

Extended Abstract	iii
List of Figures	x
List of Tables	xiii
List of Abbreviations	xv
Summary of Contributions	xvii
1 Introduction	1
1.1 Satellite remote sensing of volcanic activity	1
1.1.1 Monitoring surface changes	3
1.1.2 Thermal Emissions	5
1.2 Satellite Remote Sensing of Volcanic Plumes	6
1.2.1 Volcanic gases	6
1.2.2 Volcanic ash	10
1.3 Thesis outline	14
2 An adaptation of the CO₂ slicing technique for the Infrared Atmospheric Sounding Interferometer to obtain the height of tropospheric volcanic ash clouds	17
2.1 Introduction	18
2.2 CO ₂ Slicing	23
2.3 The Infrared Atmospheric Sounding Interferometer	30
2.4 Application to simulated data	31
2.4.1 Channel selection	31
2.4.2 Simulation results	38
2.5 Application to scenes containing volcanic ash	43
2.5.1 Methods used for comparison	45
2.5.2 Comparison of results	47
2.6 Conclusions	57

3	Exploring the Utility of IASI for Monitoring Volcanic SO₂ Emissions	59
3.1	Introduction	60
3.2	Linear Retrieval	66
3.2.1	The Algorithm	66
3.2.2	Linear Retrieval Results	67
3.3	Iterative Retrieval	75
3.3.1	The Algorithm	75
3.3.2	Ecuador and South Colombia	77
3.3.3	Kamchatka	92
3.4	Conclusions	96
4	A systematic global analysis of a decade of IASI SO₂ measurements	101
4.1	Introduction	102
4.2	Methods	106
4.2.1	IASI	106
4.2.2	IASI SO ₂ linear retrieval	107
4.2.3	The rotation algorithm	107
4.2.4	Datasets used for comparison	116
4.3	Global Perspective of SO ₂ emissions seen with IASI	122
4.3.1	Comparison of different rotation approaches	122
4.3.2	Assessment of global emission detections	138
4.4	Case Studies	150
4.4.1	Popocatépetl, Mexico	151
4.4.2	Sabancaya and Ubinas, Peru	155
4.4.3	Nevado del Ruiz and Nevado del Huila, Colombia	159
4.4.4	Pacaya and Fuego, Guatemala	162
4.5	Decadal changes in volcanic emissions	164
4.6	Conclusions	169
5	Conclusions	173
5.1	Overview of results and future work	173
5.2	Future Perspectives	179
	References	183
A	CO₂ Slicing - Appendix	219
B	Monitoring SO₂ Emissions with IASI - Appendix	225
C	SO₂ rotation study - additional information	235

C.1	Computing the emission index	235
C.2	Plume rotation rankings	237
C.3	Volcano Annual Summaries	240

List of Figures

1.1	A summary of the different satellite remote sensing techniques used to monitor volcanic activity	2
1.2	Examples of SO ₂ and ash spectra	7
2.1	Demonstration of sensitivity to different heights in the atmosphere .	25
2.2	CO ₂ slicing demonstration	27
2.3	CO ₂ slicing results for simulated ash spectra for each pressure level	33
2.4	CO ₂ slicing results for simulated ash spectra for grouped pressure levels	37
2.5	Emissivity ratio for channels within the CO ₂ absorption band . . .	38
2.6	Final CO ₂ slicing heights for simulated ash spectra	41
2.7	Maps of the CO ₂ slicing output for the Eyjafjallajökull and Grímsvötn eruptions.	47
2.8	Summary of CO ₂ slicing results from the Eyjafjallajökull and Grímsvötn eruptions	50
2.9	Time series of retrieved heights during the Eyjafjallajökull eruption	51
2.10	A comparison with CALIOP for 6 th May 2010 during the Eyjafjallajökull eruption	53
2.11	A comparison with CALIOP for 9 th May 2010 during the Eyjafjallajökull eruption	54
2.12	A comparison with CALIOP for 22 nd May 2011 during the Grímsvötn eruption.	54
2.13	A comparison with CALIOP for 23 rd May 2011 during the Grímsvötn eruption.	55
3.1	Global averages of linear retrieval effective SO ₂ column amount 2007 - 2014	68
3.2	Map showing the location of different volcanoes	70
3.3	Linear retrieval output for Central and South America, and Kamchatka for 2008 and 2010 respectively	73
3.4	Bias correction example in Ecuador and Kamchatka	83

3.5	Maps of monthly average SO ₂ column amounts from the IASI and OMI retrievals over Ecuador and Kamchatka	85
3.6	IASI, OMI and ground-based measurements at Tungurahua	90
3.7	IASI and OMI measurements in Kamchatka	95
4.1	Flowchart summarising the method used to rotate the SO ₂ linear retrieval output	108
4.2	Examples of the rotation technique used within this study	109
4.3	Examples of the unrotated and rotated annual averages at Popocatépetl in 2015	113
4.4	Schematic for getting plume height	115
4.5	An example of retrieving plume height at Etna	117
4.6	Maps showing the location of volcanoes processed and the number of detections using each rotation approach	122
4.7	Summary of results for Alaska and Kamchatka	141
4.8	Number of detections with the plume rotated approach grouped by latitude	143
4.9	Comparison of the number of detections with the plume rotated technique with the OMI flux, number of OMI thermal alerts and volcano heights	145
4.10	Summary of results over Central and South America	147
4.11	Histogram of correlation coefficients comparing the plume rotated emission index, OMI flux and number of thermal alerts from MODVOLC150	153
4.12	Annual summary for Popocatépetl, Mexico	156
4.13	Annual summary for Ubinas, Peru	158
4.14	Annual summary for Sabancaya, Peru	160
4.15	Annual summary for Nevado del Huila, Colombia	161
4.16	Annual summary for Nevado del Ruiz, Colombia	163
4.17	Annual summary for Fuego and Pacaya, Guatemala	166
4.18	Emission trends computed from the plume rotation emission index	168
4.19	Comparison of the trends computed from the IASI plume rotated emission index and the OMI flux	221
A.1	Simulation results for RTTOV default atmosphere	221
A.2	Simulation results for mid-latitude day atmosphere	222
A.3	Simulation results for a mid-latitude night atmosphere	222
A.4	Simulation results for a tropical atmosphere	223
A.5	Simulation results for a polar summer atmosphere	223
A.6	Simulation results for a polar winter atmosphere	224
A.7	Final CO ₂ slicing simulation results	

B.1	Monthly average of the iterative retrieval output over Ecuador (2007)	227
B.2	Monthly average of the iterative retrieval output over Ecuador (2008)	227
B.3	Monthly average of the iterative retrieval output over Ecuador (2009)	228
B.4	Monthly average of the iterative retrieval output over Ecuador (2010)	228
B.5	Monthly average of the iterative retrieval output over Ecuador (2011)	229
B.6	Monthly average of the iterative retrieval output over Ecuador (2012)	229
B.7	Monthly average of the iterative retrieval output over Ecuador (2013)	230
B.8	Monthly average of the iterative retrieval output over Kamchatka (2007)	230
B.9	Monthly average of the iterative retrieval output over Kamchatka (2008)	231
B.10	Monthly average of the iterative retrieval output over Kamchatka (2009)	231
B.11	Monthly average of the iterative retrieval output over Kamchatka (2010)	232
B.12	Monthly average of the iterative retrieval output over Kamchatka (2011)	232
B.13	Monthly average of the iterative retrieval output over Kamchatka (2012)	233
B.14	Monthly average of the iterative retrieval output over Kamchatka (2013)	233
C.1	Experiments with the regions used to calculate the upwind and downwind signals.	236
C.2	Annual summary for Aira, Japan	241
C.3	Annual summary for Ambae, Vanuatu	241
C.4	Annual summary for Asosan, Japan	242
C.5	Annual summary for Barren Island, Indian Ocean	242
C.6	Annual summary for Bezymianny, Kamchatka	243
C.7	Annual summary for Chikurachki, Kuril Islands	243
C.8	Annual summary for Dukono, Indonesia	244
C.9	Annual summary for Ebeko, Kuril Islands	244
C.10	Annual summary for Erta Ale, Ethiopia	245
C.11	Annual summary for Etna, Italy	245
C.12	Annual summary for Galeras, Colombia	246
C.13	Annual summary for Goreley, Kamchatka	246
C.14	Annual summary for Karymsky, Kamchatka	247
C.15	Annual summary for Kilauea, Hawaii	247
C.16	Annual summary for Kizimen, Kamchatka	248
C.17	Annual summary for Klyuchevskoy, Kamchatka	248

C.18 Annual summary for Koryaksky, Kamchatka	249
C.19 Annual summary for Lascar, Chile	249
C.20 Annual summary for Lokon-Empung, Indonesia	250
C.21 Annual summary for Manam, Papua New Guinea	250
C.22 Annual summary for Miyakejima, Japan	251
C.23 Annual summary for Montagu Island, South Sandwich Islands	251
C.24 Annual summary for Nyamuragira, Democratic Republic of the Congo	252
C.25 Annual summary for Nyiragongo, Democratic Republic of the Congo	252
C.26 Annual summary for Paluweh, Indonesia	253
C.27 Annual summary for Raung, Indonesia	253
C.28 Annual summary for San Miguel, El Salvador	254
C.29 Annual summary for Sheveluch, Kamchatka	254
C.30 Annual summary for Sinabung, Indonesia	255
C.31 Annual summary for Soufriere Hills, West Indies	255
C.32 Annual summary for Tolbackik, Kamchatka	256
C.33 Annual summary for Tungurahua, Ecuador	256
C.34 Annual summary for Turrialba, Costa Rica	257
C.35 Annual summary for White Island, New Zealand	257
C.36 Annual summary for Yasur, Vanuatu	258
C.37 Annual summary for Zhupanovsky, Kamchatka	258

List of Tables

1.1 A summary of some of the satellite remote sensing techniques for studying volcanic ash	12
2.1 A summary of some of the existing methods for determining the height of volcanic ash cloud	20
2.2 A summary of some of the previous applications of the CO ₂ slicing technique.	23
2.3 The channel ranges selected for the final application of the CO ₂ slicing technique.	36
2.4 Summary of the percentage of accepted retrievals and the RMSE describing the difference between the true (simulated) and retrieved values	42

2.5	Statistics describing the comparison of the CO ₂ slicing and optimal estimation scheme against the heights obtained with CALIOP . . .	56
3.1	Summary of eruptions previously examined with IASI	64
3.2	Published ground-based estimates of SO ₂ emissions at volcanoes in Ecuador, South Colombia and Kamchatka	78
3.3	Summary of activity at Tungurahua between 2007 and 2013	89
4.1	Description of the different rotation methods	112
4.2	Table summarising plume rotation results	127
4.3	Correlation coefficients comparing IASI, OMI and MODVOLC . . .	146
C.1	Ranks for the three rotation techniques based on the number of detections	237

List of Abbreviations

AIRS	Atmospheric Infrared Sounder
ASTER	Advanced Space-borne Thermal Emission and Reflection Radiometer
CALIOP	Cloud-Aerosol Lidar with Orthogonal Polarization
CIMSS	Cooperative Institute for Meteorological Satellite Studies
CO₂	Carbon dioxide
COSPEC	Correlation Spectrometer
DOAS	Differential Optical Absorption Spectroscopy
DU	Dobson Units
ECMWF	European Centre for Medium-Range Weather Forecasts
EUMETSAT	European Organisation for the Exploitation of Meteorological Satellites
FTIR	Fourier-transform infrared spectroscopy
GOME	Global Ozone Monitoring Experiment
GOSAT	Greenhouse Gases Observing Satellite
GVP	Global Volcanism Program
IASI	Infrared Atmospheric Sounding Interferometer
InSAR	Interferometric synthetic aperture radar
IREMIS	Infrared Emissivity Database
ITPR	Infrared Temperature Profile Radiometer
LiDAR	Light Detection and Ranging
MODIS	Moderate Resolution Imaging Spectroradiometer
OMI	Ozone Monitoring Instrument
OMPS	Ozone Mapping and Profiler Suite

SEVIRI	Spinning Enhanced Visible and Infrared Imager
S-HIRS	Scanning High-Resolution Interferometer Sounder
SO₂	Sulphur dioxide
TOMS	Total Ozone Mapping Spectrometer
VAS	Visible Infrared Spin-Scan Visible Radiometer Atmospheric Sounder
VEI	Volcanic Explosivity Index

Summary of Contributions

Chapter 2

This chapter describes a new method developed to retrieve the height of volcanic ash in the troposphere. The chapter was published as Taylor, I.A., Carboni, E., Ventress, L.J., Mather, T.A. and Grainger, R.G. (2019) An adaptation of the CO₂ slicing technique for the Infrared Atmospheric Sounding Interferometer to obtain the height of tropospheric volcanic ash clouds, *Atmospheric Measurements Techniques*, 12, 3853-3883, <https://doi.org/10.5194/amt-12-3853-2019>.

IAT developed the CO₂ slicing algorithm for ash and IASI, performed the analysis and inter-comparison and wrote the manuscript with guidance from EC, TAM, RGG and LV. LV ran the optimal estimation scheme which was used for comparison.

Chapter 3

This chapter demonstrates the capability of using IASI for monitoring smaller emissions of SO₂ using the IASI instrument. It was published as Taylor, I.A., Preston, J., Carboni, E., Mather, T.A., Grainger, R.G., Theys, N., Hidalgo, S., McCormick-Kilbride, B. (2018) Exploring the Utility of IASI for Monitoring Volcanic SO₂ Emissions, *Journal of Geophysical Research: Atmospheres*, 123, 5588–5606, <https://doi.org/10.1002/2017JD027109>.

Preliminary research for this chapter was undertaken by James Preston for his Master’s project submitted in 2015. A copy can be found at: http://eodg.atm.ox.ac.uk/eodg/mphys_reports/2015_Preston.pdf. EC ran both the linear and iterative retrievals. JP then did some analysis to demonstrate some of the capabilities of IASI. IAT then expanded this analysis to complete the timeseries and extended the analysis to Kamchatka, as well as producing the published figures, animation and supplementary material. NT provided the monthly averaged OMI data used for comparison. SH provided the DOAS data used for comparison. IAT wrote the paper, using small amounts of JP’s text. Tables 1-3 were originally

produced by JP with tables 1 and 3 being expanded by IAT. All author's contributed to revising and improving the manuscript.

The linear retrieval data was achieved online as: Taylor, I.A.; Carboni, E.; Grainger, R.G. (2018): IASI global monthly averages of effective sulphur dioxide (SO₂) column amounts, 2007 - 2014, version 1.0. Centre for Environmental Data Analysis, 14th October 2019. doi:10.5285/8eb35b1ab1b2476986d174a2f0231307. <http://dx.doi.org/10.5285/8eb35b1ab1b2476986d174a2f0231307>.

Chapter 4

This chapter builds on the work in chapter 4, exploring how the IASI linear retrieval can be used to investigate emissions of SO₂ from volcanoes across the globe. The chapter has been written in preparation for submission in a volcanology journal. The analysis was undertaken by IAT with the guidance from EC, TAM and RGG. IAT wrote the manuscript which was then reviewed by EC, TAM and RGG. The authors plan to make the summary plots generated available online with the aim of encouraging further use of the IASI products outlined in this thesis. The OMI data used for comparison is from the MEaSUREs project and was downloaded from <https://so2.gsfc.nasa.gov/measures.html>. The MODVOLC thermal anomaly data was downloaded from <http://modis.higp.hawaii.edu/>.

1

Introduction

1.1 Satellite remote sensing of volcanic activity

Significant technological developments over the past few decades have created new methods for studying volcanic activity. Satellite remote sensing is now widely used to interpret activity at individual volcanoes and increasingly utilised to get a global picture of volcanic behaviour (e.g. Biggs et al., 2014; Carn et al., 2017; Furtney et al., 2018; Ebmeier et al., 2018). These developments address some of the limitations of ground based monitoring techniques. Ground based instrument networks offer a higher temporal resolution and direct measurements which would be impossible with satellite instruments and which are critical for answering short term questions and assessing activity levels. However, ground based measurements are only available

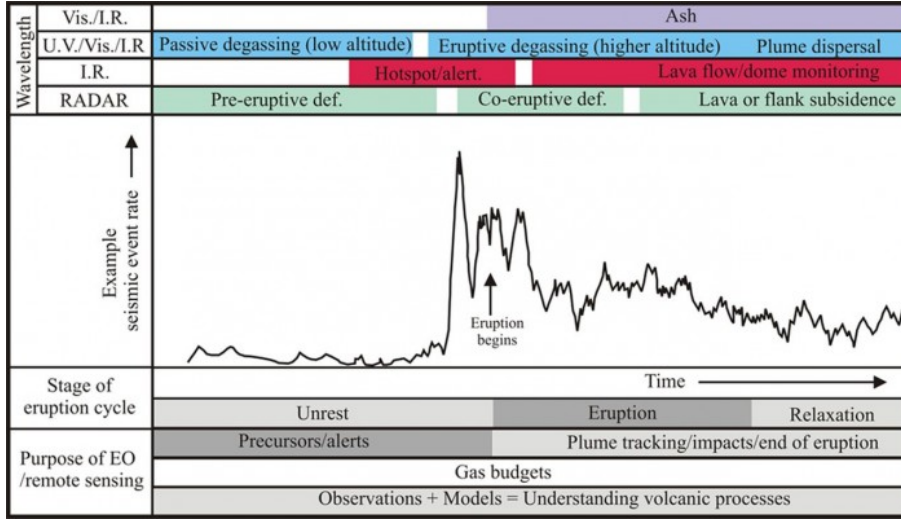


Figure 1.1: A summary of the different satellite remote sensing approaches which can be used to investigate volcanic activity divided into different parts of the electromagnetic spectrum. It also indicates which part of the eruptive cycle these methods are most likely to be used for. The seismic signal shown is based on the seismic events seen at Mt. St. Helens (March-May 1980). From: Pyle et al. 2013, page 2.

at a minority of volcanoes (Sparks et al., 2012). This can be because there are limited resources or due to the remoteness and inaccessibility of some volcanoes (Francis and Rothery, 2000; Webley et al., 2008; Thomas and Watson, 2010). Field campaigns can provide valuable results but are usually sporadic and do not offer the high temporal resolution required to fully understand the volcanic system, or necessary for volcanic hazard monitoring and mitigation. Making ground-based measurements can also be hazardous and cannot achieve the same spatial coverage that is possible with satellite data (Pyle et al., 2013).

Satellite remote sensing offers insight into a number of different aspects of volcanic activity. The three primary areas of study are changes in surface properties and topography, thermal emissions and volcanic plumes (Francis et al., 1996; Francis and Rothery, 2000). A short introduction to the study of topographic changes and

thermal emissions is given below, while the use of satellite remote sensing to study volcanic plumes is outlined further in section 1.2. These satellite measurements can be used to interpret quiescent activity and precursory signals, monitor eruption dynamics and then observe the relaxation of the volcano into its background state (Pyle et al., 2013). This is shown in figure 1.1 which shows how satellite instruments which utilise different parts of the electromagnetic spectrum, can be used to study different aspects of the eruptive cycle and the role that this can then play in monitoring volcanic hazards and understanding eruption dynamics and impacts.

In the past, the majority of satellite data has been used for in depth studies of single volcanoes and eruptive events; however, the increasing volume of data is encouraging synoptic studies of global volcanism (e.g. Biggs et al., 2014; Carn et al., 2017; Furtney et al., 2018; Ebmeier et al., 2018), and integrative studies using different types of remote sensing (e.g. Flower and Carn, 2015; Laiolo et al., 2018; Furtney et al., 2018; Reath et al., 2019). Combined with ground based measurements this is offering a deeper insight into volcanic activity and its interactions with other parts of the Earth system than ever before.

1.1.1 Monitoring surface changes

Volcanic activity can lead to considerable changes to the landscape. For example, lava and pyroclastic flows, lahars, ash deposits and landslides can all visibly alter the surface. There are also more subtle changes which can occur as magma moves beneath the surface (Biggs and Pritchard, 2017). For example, in a simplified case, as magma rises through the conduit it can cause the volcano to inflate, and following the removal of magma from the system, deflation can be observed (Dzurisin and Lu,

2007; Chaussard et al., 2013). Deformation might also occur in association with dyke emplacement (e.g. Biggs et al., 2013; Sigmundsson et al., 2014). More traditional means of measuring deformation include tilt meters and GPS; however, these are unable to measure the entire edifice. Volcano wide changes can be observed using satellite borne radar. These instruments emit a pulse of energy which is scattered by the Earth’s surface, and returned to the instrument, which records the amplitude and phase. The amplitude can be used to infer surface properties such as roughness, steepness and soil moisture. As such, this has been used for the tracking of lava flows and mapping of volcanic deposits (e.g. Wadge et al., 2012; Dumont et al., 2018). A comparison of the phase of two radar images taken at different points in time but with the same viewing geometry, using a method called Interferometric Synthetic Aperture Radar (InSAR) can indicate how much the surface has moved (Pinel et al., 2014). This powerful tool has been used to show centimetre scale changes across entire volcanic landscapes. Using this technique, the number of known deforming volcanoes has increased from 44 in 1997 to 220 volcanoes by 2017 (Biggs and Pritchard, 2017). In some cases it can indicate precursory activity although care must be exercised as some volcanoes which deform do not necessarily erupt and equally some eruptions occur without any precursory deformation being identified using InSAR (Dzurisin, 2003; Biggs et al., 2014). For full details on the use of radar for volcano monitoring see Pinel et al. (2014) and references therein.

At some volcanoes increased deformation has been accompanied by increases in the SO_2 flux before an eruption (Watson et al., 2000). However, the degree to which this is observed is affected by the nature of the volcanic system. In an open volcanic system, gas can easily rise through the conduit, resulting in only

localised deformation around the vent; whereas, in a closed system, gas can less easily escape resulting in greater overpressure and broader deformation features (Newhall, 2007; Chaussard et al., 2013; Reath et al., 2019). These are endmember states with many volcanoes exhibiting characteristics of both. It is also possible for a volcano to shift between states. For example, large explosive eruptions can have significant effects on the landscape. These might open up the conduit of a previously closed volcanic system allowing gas to be more easily released in the future, or conversely, could cause a collapse that blocks the vent and creates a more closed system (Reath et al., 2019).

1.1.2 Thermal Emissions

The high temperatures of some of the material ejected from volcanoes allows detection using satellite instruments (Dehn et al., 2000; Harris, 2013; Dehn and Harris, 2015). Lava flows and lakes, which can have temperatures of between 200 and 1100°C, are radiating significant quantities of heat. This results in an increase in the radiance measured within the short wave infrared and can subsequently be exploited to detect elevated thermal activity (Wright et al., 2002, 2004; Wright, 2015). This is not only applied to volcanic sources but can be used to identify forest fires and some anthropogenic sources (Kaufman et al., 1998; Justice et al., 2002; Giglio et al., 2003). Thermal emissions from volcanoes have been investigated with a number of different instruments including the Moderate Resolution Imaging Spectroradiometer (MODIS; e.g., Wright et al. 2002, 2004; Wright 2015; Coppola et al. 2016a), Landsat (Oppenheimer et al., 1993; Oppenheimer and Francis, 1997; Kaneko and Wooster, 1999) and the Advanced Spaceborne Thermal Emission and Reflection Radiometer

(ASTER; Jay et al. 2013; Reath et al. 2016). From these thermal measurements, simple procedures can be applied to detect elevated thermal emissions (e.g., Wright et al., 2004; Wright, 2015), and following this further information such as the heat flux can be computed (e.g. Wright and Flynn, 2004). Further interpretation is then needed to infer the type of activity (Dehn and Harris, 2015). A number of volcanic features can cause an elevated thermal signature including lava flows and lakes, lava domes, pyroclastic flows and gas/ash emissions (Dehn and Harris, 2015).

1.2 Satellite Remote Sensing of Volcanic Plumes

Volcanic plumes are a far reaching hazard associated with eruptions and have received significant attention since the 2010 eruption of Eyjafjallajökull which caused serious financial losses through the closure of airspace (IATA Economic Briefing, 2010). Satellite remote sensing, alongside modelling, has become an essential part of monitoring the dispersion of these dynamic plumes. This is helped by the large number of instruments which have the capability for monitoring these plumes, together providing wide spatial coverage and high temporal resolutions. Summaries of some the satellites and tools used for this purpose can be found in Thomas and Watson (2010) and Carn et al. (2016).

1.2.1 Volcanic gases

Gases within the magmatic system are one of the fundamental drivers of volcanic activity (Sparks, 2003*b*) and consequently, making measurements of the gases emitted can be very informative (Symonds et al., 1994; Scaillet et al., 1998; Edmonds, 2008;

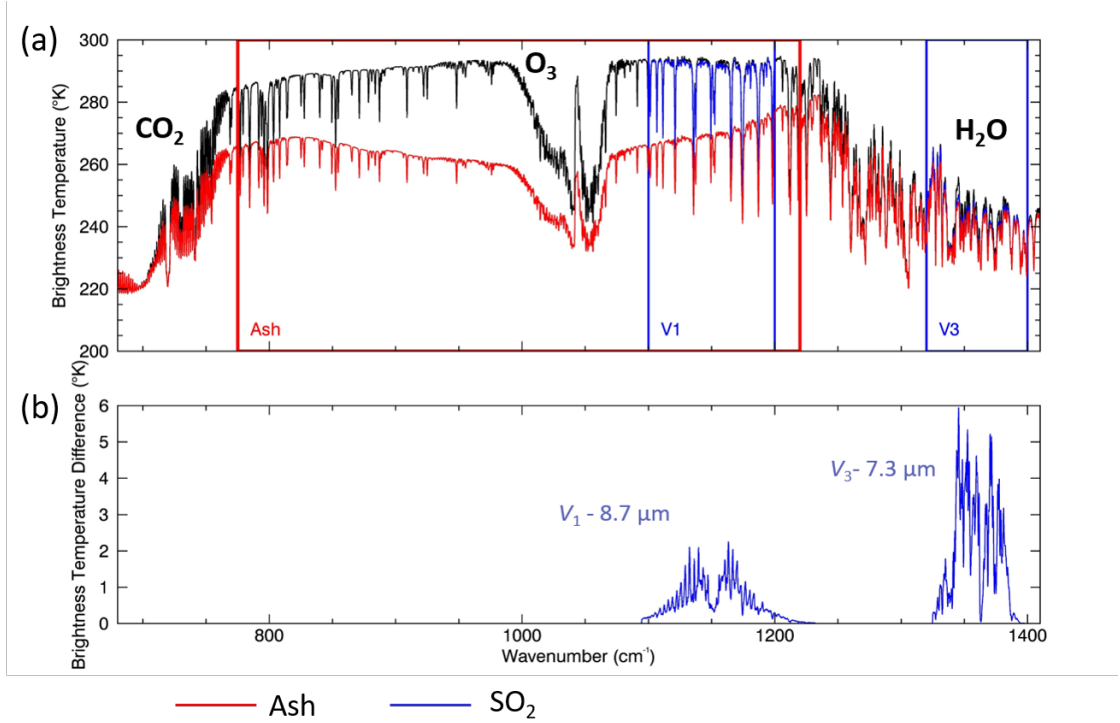


Figure 1.2: (a) A clean atmospheric spectrum simulated with the fast radiative transfer model RTTOV is shown in black. This is for the $680\text{--}1410\text{ cm}^{-1}$ spectral range. Within this it is possible to identify three significant absorption features caused by carbon dioxide, ozone and water vapour. Over plotted in red is a simulated ash spectrum (AOD= 10.0, ER= $5\text{ }\mu\text{m}$, pressure= 400 mb). In blue is a simulated SO₂ spectrum (column amount= 10 DU, pressure= 400 mb) shown for the two SO₂ absorption features within this region. This is difficult to distinguish from the clear atmospheric spectrum and so (b) shows the difference between the clean atmospheric and SO₂ spectra. This highlights the two absorption features.

Oppenheimer et al., 2014). Changes in the flux and ratios of the different gases emitted can help interpret volcanic activity and potentially warn of imminent eruptions (Malinconico, 1979, 1987; Sparks, 2003a; Edmonds, 2008). For example, an increase in the amount of SO₂ measured might suggest that magma has risen to a shallower part of the magmatic system (Edmonds et al., 2003). In contrast, a decrease in this or other gases might imply an end to activity, or might indicate that there is something preventing gas escaping, which could increase the likelihood

of an explosive eruption (Stix et al., 1997; Prata et al., 2015). In addition to this, measuring volcanic emissions is important for trying to minimise the effects of these gases on human and animal health (Hansell and Oppenheimer, 2004) and to reduce the hazard posed to aviation: both direct impacts from SO_2 (Bernard and Rose, 1990) and as a proxy for ash (e.g. Carn et al., 2007). It can also help understand the impacts of gas emissions on the environment and climate (Delmelle, 2003; Mather, 2015). For example, emissions into the troposphere can affect cloud properties (Gassó, 2008; Ebmeier et al., 2014; McCoy and Hartmann, 2015), potentially having a small cooling effect; while emissions into the stratosphere are known to have a number of major impacts including tropospheric cooling, stratospheric warming and ozone depletion (Robock, 2000a; Grainger and Highwood, 2003).

Volcanoes emit a number of different gas species including H_2O , CO_2 , SO_2 , H_2S , CO and SiF_4 , as well as a number of aerosols (McGonigle, 2005; Thomas and Watson, 2010). There are several different methods for making ground based measurements of volcanic gases. These include the direct collection of gases and the use of ground based remote sensing devices such as the COSPEC, DOAS, FLYSPEC and FTIR (Moffat and Millán, 1971; Malinconico, 1979; Stoiber et al., 1983; Casadevall et al., 1983; Galle et al., 2003; McGonigle et al., 2002; Horton et al., 2006; Elias et al., 2006). With an exception of the FTIR, which can obtain information on a number of different gas species, the ground based remote sensing techniques make measurements of SO_2 . This is because there is a relatively low abundance of SO_2 in the background atmosphere away from pollution sources and because of sensitivities to this gas within both the infrared and UV parts of the electromagnetic spectrum

(Oppenheimer, 2010; Oppenheimer et al., 2011). While ground based measurements are useful they are limited for the reasons mentioned in section 1.1.

Satellite measurements of SO₂ emission from volcanoes began in 1982 with the eruption of El Chichón in Mexico (Krueger, 1983; Krueger et al., 2008). This plume was analysed with the Total Ozone Monitoring Spectrometer (TOMS). This and other UV instruments, utilise an absorption feature within the UV between 300 and 320 nm (Oppenheimer, 2010). There is also sensitivity to SO₂ within the infrared with three absorption features caused by the vibrations and distortions of S-O bonds (Oppenheimer, 2010). These absorption features within the infrared are centred at 8.7, 7.3 and 4.0 μm (named ν_1 , ν_3 and $\nu_1 + \nu_3$ respectively). The smallest of these is the $\nu_1 + \nu_3$ band. This is not commonly used: applied only where significant levels of SO₂ mean that the other absorption features become saturated (Karagulian et al., 2010). The other two features can be seen in figure 1.2. Of these the stronger feature is the ν_3 band which has been widely used in different retrieval schemes (e.g. Prata et al., 2003; Carn et al., 2005; Prata and Bernardo, 2007; Clarisse et al., 2012). However, as is seen in figure 1.2, it is collocated with a water vapour feature limiting its use in parts of the atmosphere with high levels of water vapour, notably the boundary layer. The smaller, less sensitive, ν_1 band is unaffected by water vapour but can be affected by ash and sulphate aerosol (Thomas and Watson, 2010).

There are advantages and disadvantages of using either UV or infrared instruments (Prata et al., 2015). The UV is less affected by water vapour. This is in contrast to the infrared, which can be affected by water vapour and also by the temperature contrast between the surface and the plume (Clarisse et al., 2012). This means that the UV is more often used for making measurements of SO₂ within the

boundary layer, from volcanic degassing, or anthropogenic emissions (Carn et al., 2007; Fioletov et al., 2013, 2015, 2016; Flower et al., 2016; Krotkov et al., 2016). That does not mean that the infrared cannot also be used for these purposes. This is something which is explored within this thesis, which demonstrates some of the complementary benefits of the infrared; namely night time and high latitude winter measurements which often gives these instruments a higher temporal resolution compared to UV sensors. Some of the infrared retrievals can also make simultaneous measurements of column amount and height (Carboni et al., 2012, 2016), and these instruments also have sensitivity to volcanic ash, discussed further in the next section. Overall, there is a considerable advantage to using infrared and UV instruments together and alongside ground based measurements.

1.2.2 Volcanic ash

Volcanic ash refers to particles of all compositions, with a diameter of less than 2 mm, which are ejected from a volcano during an eruption (Cashman and Rust, 2016). Ash is formed after magma rising through the conduit, driven by volatiles within the melt, fragments (Cashman and Rust, 2016). During and after an eruption it can be transported great distances from the source (Watson et al., 2016). This can create a significant hazard to aircraft (Casadevall, 1994; Dunn and Wade, 1994; Miller and Casadevall, 2000; Pieri et al., 2002; Guffanti and Tupper, 2015; Chen and Zhao, 2015): potentially threatening human life and having significant economic implications through flights being rerouted or cancelled (IATA Economic Briefing, 2010; Alexander, 2013). In addition to this it can have serious effects on human and animal health (Horwell and Baxter, 2006; Horwell, 2007) and cause considerable

damage to agriculture and infrastructure (Durant et al., 2010; Wilson et al., 2012, 2015). Monitoring the emission and dispersion of these clouds is therefore essential.

The majority of measurements of volcanic ash are made with infrared instruments. An example of an ash spectrum, simulated with the fast radiative transfer model RTTOV, can be seen in figure 1.2a. Here the characteristic broad v shaped absorption feature between 8 and 13 μm can be seen. The strongest absorption occurs at roughly 10 μm (although this varies between different ash compositions; Mackie et al. 2014b). Numerous different techniques have exploited this feature for the detection of volcanic ash and other methods developed to quantify properties such as the ash optical depth, effective radius and height. A summary of some of these techniques can be seen in table 1.1.

Schemes for the detection of volcanic ash and retrieval of further properties have also been developed for UV instruments, for example, the UV Aerosol Index (Seftor et al., 1997). However, these are less widely used than the infrared. They are limited by a number of factors such as not being specific to volcanic ash (affected by other aerosols such as smoke), no night time measurements, ocean colour and sunglint (Carn and Krotkov, 2016).

Table 1.1: A summary of some of the techniques developed to detect volcanic ash and retrieve properties such as the effective radius, ash optical depth and height. Further information on the different techniques can be found in Clarisse and Prata (2016).

Method	Description	Examples
<i>Detection Techniques - used to identify the geographic location of volcanic ash</i>		
Split Window	Utilises the positive transmission between 10 and 12 μm in ash spectra which is in contrast to ash free and cloudy spectra. If the difference between the brightness temperature measured in these channels is less than a set threshold the pixel is flagged as containing ash. This simple technique has been widely applied using multiple instruments. There have also been a number of adaptations including the incorporation of additional channels	Prata 1989 <i>a,b</i> ; Yu et al. 2002; Ellrod et al. 2003
RGB	Commonly used to track desert dust this technique creates false colour composite images using different infrared channels. Allows for qualitative interpretation of ash movement.	Millington et al. 2012
Robust AVHRR Technique	This is similar to the split window technique but applies a temporally and spatially specific local threshold.	Pergola et al. 2004; Filizzola et al. 2007
Ratios	Similar to the split window approach but takes a ratio between two channels	Holaske and Rose 1991
Principle Component Analysis	A minimal vector space formed from pixels with no ash is used to represent background variability. Deviations from this can indicate the presence of ash.	Hillger and Clark 2002; Taylor et al. 2015
continued ...		

Method	Description	Examples
Linear Retrieval	A covariance matrix is formed from a large number of ash free spectra. The measured spectra are then weighted according to the variability usually seen in each channel. This is used to get a measure of the amount of signal relative to the background.	Walker et al. 2011; Clarisse et al. 2013; Sears et al. 2013
Spectral Distance	The measured spectra is compared against a variety of simulated ash spectra. If the distance between the two is less than a set threshold the pixel is flagged as containing ash.	Gangale et al. 2010; Clarisse et al. 2010a
Probabilistic Approach	Employs a Bayesian technique to obtain the relative probability of ash, cloud and clear sky.	Mackie and Watson 2014a
<i>Retrieval Schemes - used to quantify ash properties (e.g. optical depth, effective radius, height)</i>		
Look up tables	Measured spectra are compared against previously computed look up tables which represent the spectral variability of ash with certain parameters (e.g. optical depth and effective radius).	Wen and Rose 1994; Prata and Grant 2001a
Optimal Estimation	Spectra are forward modelled given certain atmospheric parameters. These are compared against those measured by the instrument and this is used to determine properties such as the optical depth, effective radius and height	Carboni et al. 2012; Francis et al. 2012; Ventress et al. 2016; Zhu et al. 2017

1.3 Thesis outline

The overall aim of this thesis was to investigate some of the ways in which the Infrared Atmospheric Sounding Interferometer (IASI) can be used to study volcanic plumes. This has included studies of both volcanic ash and sulphur dioxide (SO_2). The thesis is structured as follows:

Chapter 2: A method known as CO_2 slicing, which is widely used to obtain the height of meteorological clouds, has been adapted for, and applied to, volcanic ash using the IASI instrument. The technique was tested on simulated ash data before being applied to scenes containing ash from the Eyjafjallajökull and Grimsvötn eruptions. Comparisons have been made against an optimal estimation retrieval scheme developed for IASI and backscatter profiles from a satellite-borne LiDAR.

Chapter 3: The use of IASI for monitoring emissions from volcanic eruptions is explored. A ‘fast’ linear retrieval is first applied globally to identify emissions. A full quantitative iterative retrieval is then applied over Ecuador and Kamchatka to quantify the amount of SO_2 and observe trends in activity.

Chapter 4: Building on chapter 3, a more in depth study of the linear retrieval is performed. A rotation approach which isolates and enhances the SO_2 signal was applied to 166 volcanoes across the globe. A simple comparison of the upwind and downwind signal was performed to show changes in volcanic activity. These were used to compute long term emission trends. This provides a synoptic view

of the SO₂ emissions seen with IASI.

Chapter 5: This chapter summarises the main results of this thesis. It considers how satellite measurements can be used to complement existing tools for volcano monitoring and outlines further areas of study. It also considers future advancements in satellite instruments.

2

An adaptation of the CO₂ slicing technique for the Infrared Atmospheric Sounding Interferometer to obtain the height of tropospheric volcanic ash clouds

Abstract: Ash clouds are a geographically far-reaching hazard associated with volcanic eruptions. To minimise the risk that these pose to aircraft and to limit disruption to the aviation industry, it is important to closely monitor the emission and atmospheric dispersion of these plumes. The altitude of the plume is an important consideration and is an essential input into many models of ash cloud propagation. CO₂ slicing is an established technique for obtaining the top height of aqueous clouds and previous studies have demonstrated that there is potential for this method to be used for volcanic ash. In this study, the CO₂ slicing technique has been adapted for volcanic ash and applied to spectra obtained from the Infrared Atmospheric Sounding Interferometer (IASI). Simulated ash spectra are first used to select the most appropriate channels and then demonstrate that the technique has

merit for determining the altitude of the ash. These results indicate a strong match between the true heights and CO₂ slicing output with a root mean square error (RMSE) of less than 800 m. Following this, the technique was applied to spectra obtained with IASI during the Eyjafjallajökull and Grímsvötn eruptions in 2010 and 2011 respectively, both of which emitted ash clouds into the troposphere, and which have been extensively studied with satellite imagery. The CO₂ slicing results were compared against those from an optimal estimation scheme, also developed for IASI, and a satellite-borne LiDAR is used for validation. The CO₂ slicing heights returned an RMSE value of 2.2 km when compared against the LiDAR. This is lower than the RMSE for the optimal estimation scheme (2.8 km). The CO₂ slicing technique is a relatively fast tool and the results suggest that this method could be used to get a first approximation of the ash cloud height, potentially for use for hazard mitigation, or as an input for other retrieval techniques or models of ash cloud propagation.

2.1 Introduction

Encounters of aircraft with volcanic ash have demonstrated that such occurrences can cause significant damage to the plane (Casadevall, 1994; Dunn and Wade, 1994; Pieri et al., 2002; Guffanti and Tupper, 2015). In extreme cases, these have resulted in engine failure (Miller and Casadevall, 2000; Chen and Zhao, 2015) and subsequently life-threatening circumstances. Ash clouds are closely monitored by the Volcanic Ash Advisory Centres (VAACs) who use a variety of data sources including information from volcano observatories and satellite data (Prata and Tupper, 2009; Thomas and Watson, 2010; Lechner et al., 2017). This allows informed decisions on the closure of airspace during an eruption, which can result in severe disruption and

have significant financial implications. For example, the eruption of Eyjafjallajökull in 2010 resulted in the closure of a large portion of northern European airspace and subsequently the cancellation of 100,000 flights and a revenue loss of \$1.7 billion (IATA Economic Briefing, 2010). Alongside these potential impacts to the aviation industry, volcanic ash is also a hazard to health (Horwell and Baxter, 2006; Horwell, 2007) and can cause considerable damage to infrastructure (Durant et al., 2010; Wilson et al., 2012, 2015).

Satellite remote sensing, particularly using infrared instruments, has been widely used for monitoring the hazards presented by volcanic ash. This has included detection schemes which flag pixels that contain volcanic ash (e.g. Prata, 1989*a,b*; Ellrod et al., 2003; Pergola et al., 2004; Filizzola et al., 2007; Clarisse et al., 2010*a*; Mackie and Watson, 2014*a*; Taylor et al., 2015). Other methods have been developed to quantify parameters such as the mass, ash optical depth (AOD), effective radius and altitude of the ash cloud, usually relying on look-up tables or optimal estimation techniques (e.g. Wen and Rose, 1994; Yu et al., 2002; Watson et al., 2004; Corradini et al., 2008; Gangale et al., 2010; Francis et al., 2012; Grainger et al., 2013; Pavolonis et al., 2013).

Table 2.1: A summary of some of the existing methods for determining the height of volcanic ash clouds. Summaries can be found in Oppenheimer (1998); Prata and Grant (2001 *a,b*) and Zakšek et al. (2013)

Method	Description	Examples in literature
<i>Ground based methods</i>		
Infrared camera	Infrared cameras measure the heat radiated off the ash cloud. This means the plume can be distinguished from its surroundings. The top of the plume can be identified and the height calculated by counting the number of pixels between the plume top and a reference point.	Patrick (2007); Sahetapy-Engel and Harris (2009); Webb et al. (2014); Bombrun et al. (2018)
Radar	A pulse of radio energy is emitted from a transmitter. This is reflected back off clouds (aqueous or ash). This echo can be used to determine the cloud height.	Lacasse et al. (2004); Arason et al. (2011); Petersen et al. (2012)
<i>Multiple platforms</i>		
LiDAR	LiDAR is an active sensor which can be used on the ground as well as on aircraft or satellite platforms. The backscatter returned to the instrument can be used to infer the height of multiple cloud layers (including different types of cloud and ash). This is commonly used for validation of other methods.	Ansmann et al. (2010); Marengo et al. (2011); Winker et al. (2012); Vernier et al. (2013); Balis et al. (2016)
<i>Satellite techniques</i>		
Stereo view	This method requires two instruments viewing the cloud at the same time or a single instrument with two viewing angles (i.e. nadir and forward viewing). The resulting parallax can be used to determine the cloud height.	Prata and Turner (1997); Zakšek et al. (2013)
		continued ...

Method	Description	Examples in literature
Cloud shadow	<p>The shadow cast by clouds can be identified in visible satellite imagery. Combined with knowledge of the satellite viewing angle and the position of the sun, this can be used to find the height of the cloud layer. Alternatively multiple images including the cloud's shadow can be used.</p>	Holasek et al. (1996); Prata and Grant (2001b)
Cloud top temperature	<p>The cloud top temperature measured by an infrared instrument (usually at 11 μm) is compared against a temperature profile (e.g. radiosonde or weather model) to obtain the height.</p>	Holasek et al. (1996)
Backward trajectory modelling	<p>Method uses the vertical wind directions and backwards trajectory modelling to get the vertical distribution of ash. This can then be used to obtain the flux.</p>	Eckhardt et al. (2008) ¹ , Stohl et al. (2009) ² , Kristiansen et al. (2010) ¹ , Stohl et al. (2011) ² , Parrini et al. (2017, 2018) ¹
Radiance fitting	<p>Spectra are forward modelled given certain atmospheric parameters. These spectra are compared against those measured by the instrument and this is used to determine the altitude</p>	Ventress et al. (2016); Zhu et al. (2017)

¹Example using SO₂ not ash²Example using hydrofluorocarbons and hydrochlorofluorocarbon

Knowing the position of the ash cloud in three dimensions is critical for hazard mitigation. Plume height is a crucial part of this and it is also a variable in models of ash cloud propagation (Mastin et al., 2009; Stohl et al., 2011; Bonadonna et al., 2012) such as HYSPLIT (Draxier and Hess, 1998; Stein et al., 2015) or NAME (Jones, 2004; Witham et al., 2012). A number of different methods have been used to obtain the height of volcanic ash clouds. These have included the use of ground-based and airborne instruments, as well as satellite techniques (Glaze et al., 1999), some of which are summarised in table 2.1.

This problem is not unique to volcanic ash. Similar retrieval techniques exist to obtain the cloud height of aqueous clouds (i.e. water/ice clouds not associated with volcanic activity). One such method, known as the CO₂ slicing technique, described in more detail in section 2.2, has been widely used to obtain the cloud top height and has been adapted for numerous instruments, as illustrated in table 2.2. The method has been shown to have some potential when applied to volcanic ash using the Moderate Resolution Imaging Spectroradiometer (MODIS) (Richards, 2006; Tupper et al., 2007). In this study, the technique has been adapted for the Infrared Atmospheric Sounding Interferometer (IASI; see section 2.3) and applied to volcanic ash. It was first applied to simulated ash spectra (section 2.4) to select the most appropriate channels and to demonstrate that the method has promise when applied to volcanic ash. Following this it was applied to scenes containing volcanic ash from the Eyjafjallajökull and Grímsvötn eruptions (section 2.5) where it was compared against an existing method for obtaining the height of volcanic ash and data from a satellite-borne LiDAR. The results indicate that this method could be applied

Table 2.2: A summary of some of the previous applications of the CO₂ slicing technique.

Instrument	Platform type	Examples
AIRS	Satellite	Pangaud et al. (2009)
GOSAT	Satellite	Someya et al. (2016)
IASI	Satellite	Arriaga (2007)
ITPR	Satellite	Smith and Platt (1978)
MODIS	Satellite	Menzel et al. (1992); Richards (2006)*; Tupper et al. (2007)*; Menzel et al. (2008)
MODIS MAS	Airborne	Frey et al. (1999)
S-HIRS	Airborne	Holz et al. (2006)
VAS	Satellite	Menzel et al. (1983); Wylie and Menzel (1989)
AIRS- Atmospheric Infrared Sounder		
GOSAT- The Greenhouse Gases Observing Satellite		
IASI- The Infrared Atmospheric Sounding Interferometer		
ITPR- Infrared Temperature Profile Radiometer		
MODIS- Moderate Resolution Imaging Spectroradiometer		
MODIS MAS- Moderate Resolution Imaging Spectroradiometer Airborne simulator		
S-HIRS- Scanning High-Resolution Interferometer Sounder		
VAS- Visible Infrared Spin-Scan Visible Radiometer Atmospheric Sounder		
*Studies applied to ash		

to get a first approximation of the ash cloud height which could then be used for hazard mitigation and as a parameter in other retrieval methods or ash models.

2.2 CO₂ Slicing

The CO₂ slicing technique is an established method, developed for obtaining the cloud top height/pressure of aqueous cloud (Chahine, 1974; Smith and Platt, 1978; Menzel et al., 1983). Over the past four decades this tool has been adapted for different instruments, summarised in table 2.2, including both airborne and satellite

platforms. The technique uses a CO₂ absorption feature within the thermal infrared part of the electromagnetic spectrum between 665 and 750 cm⁻¹ (13.3 to 15 μm). Within this region, as wavenumber increases there is a general increase in the radiance observed. This is demonstrated in Fig. 2.1a, which shows the spectrum of a simulated clear atmosphere. This has been simulated with the fast radiative transfer model RTTOV (version 9; Saunders et al., 1998) and replicates what would be observed with IASI given specified atmospheric conditions. In this case a default atmospheric profile is used, without the addition of cloud, volcanic ash, or any trace gases or aerosols above background levels.

In the Earth's troposphere where temperature is decreasing with height, the radiances measured by the instrument are proportional to the transparency of the atmosphere for each channel (Holz et al., 2006). Subsequently, within the CO₂ absorption band, as wavenumber and the radiance measured both increase, the channels are becoming increasingly transparent (with some fluctuations). As such, the spectrum of a high-altitude cloud will begin to deviate from the clear spectrum at a lower wavenumber than a lower-altitude cloud. This is illustrated in Fig. 2.1a which shows the spectra of three ash clouds of varying heights. Effectively, until the point where the clear and ash/cloudy spectra diverge, the instrument is recording clear radiances. In theory it is possible to step through the channels, '*slicing*' through different layers of the atmosphere, until the cloud layer is visible. This concept has been used to identify channels whose cloud-free radiances can be assimilated into numerical weather prediction models rather than filtering out these pixels entirely (e.g. McNally and Watts, 2003).

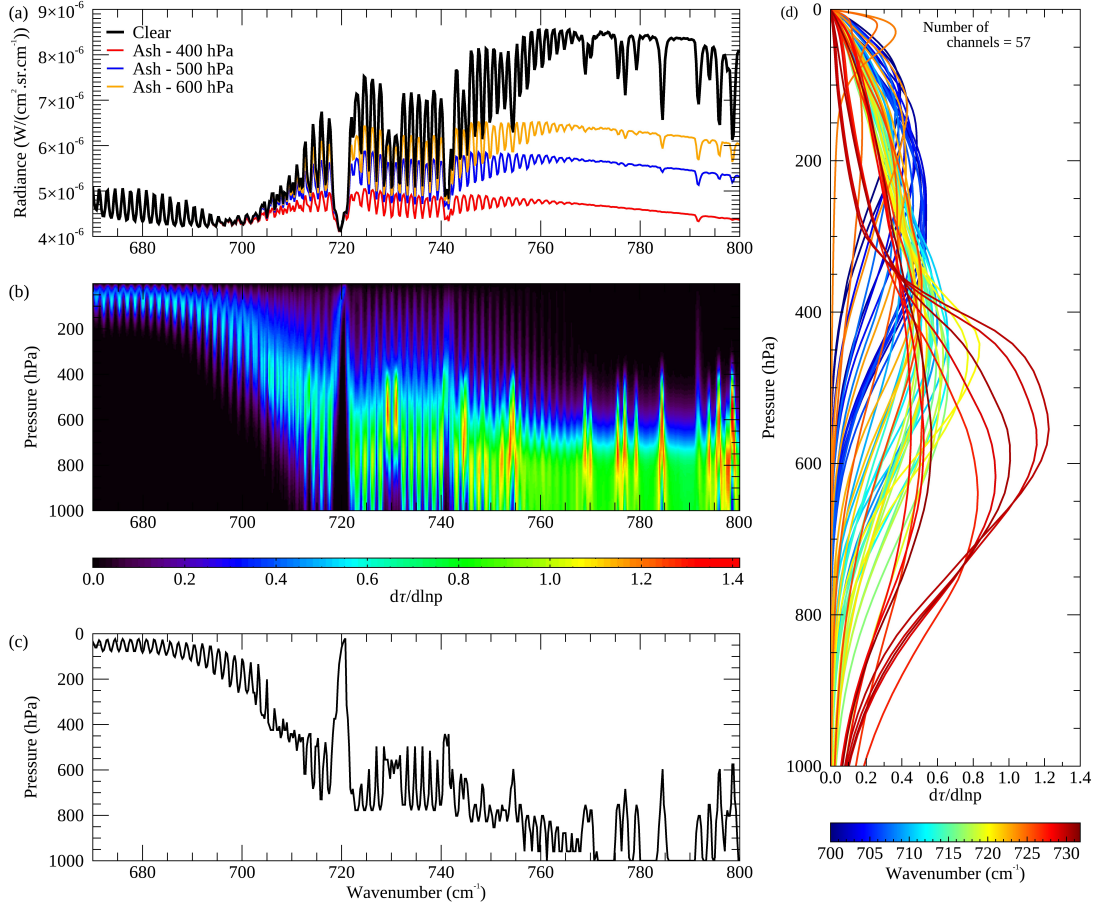


Figure 2.1: (a) Simulated spectra for a clear atmosphere (i.e. one without cloud or ash) and three ash clouds at different pressure levels: 400, 500 and 600 hPa. (b) The change in atmospheric transmittance with log pressure ($d\tau/d\ln p$). This is indicative of which part of the atmosphere each channel is sensitive to. This sensitivity is shown to shift from higher up in the atmosphere to the lower parts of the atmosphere as wavenumber increases. (c) The peak sensitivity for each channel. (d) The weighting function ($d\tau/d\ln p$) for the 57 channels used in this CO₂ slicing study.

The changing sensitivity of each of the channels to the atmospheric profile is better demonstrated in Fig. 2.1b and c. This shows the derivative of atmospheric transmittance with log pressure ($d\tau/d\ln p$) and the peak of this value respectively. This is a measure of each channel's sensitivity to each level of the atmosphere and demonstrates that this shifts from the upper atmosphere at lower wavenumbers

towards the surface at higher wavenumbers.

As the channels are sensitive to different parts of the atmosphere, it is possible to use this to estimate the height of the cloud (aqueous or in principle ash). To do this using the CO₂ slicing method, the ratio (f , Eq. 2.1) of the difference in cloudy and clear radiances (L_{obs} and L_{clr} respectively) for two channels (ν_1 and ν_2) within or close to the CO₂ absorption band is compared against a cloud pressure function (C , Eq. 2.2):

$$f(\nu_1, \nu_2) = \frac{L_{\text{obs}}(\nu_1) - L_{\text{clr}}(\nu_1)}{L_{\text{obs}}(\nu_2) - L_{\text{clr}}(\nu_2)} \quad (2.1)$$

$$C(\nu_1, \nu_2, p) = \frac{N\varepsilon_1 \int_{p_s}^{p_c} \tau(\nu_1, p) \frac{dB[\nu_1, T(p)]}{dp} dp}{N\varepsilon_2 \int_{p_s}^{p_c} \tau(\nu_2, p) \frac{dB[\nu_2, T(p)]}{dp} dp} \quad (2.2)$$

where τ is the atmospheric transmittance at channel ν of the layer between the pressure level p and the instrument (top of the atmosphere); B is the Planck radiance which is channel and temperature (and therefore pressure) dependent; p_c and p_s are the cloud and surface pressure respectively; and $N\varepsilon$ is the effective emissivity (sometimes referred to as the effective cloud amount), a product of the cloud fraction (N) and cloud emissivity (ε). Equation 2.1 is compared against Eq. 2.2 and where the two functions intersect is taken as the cloud top pressure. A demonstration of this is shown in Fig. 2.2a. Following this the effective emissivity can be computed using a channel which falls within an atmospheric window (w ; usually one close to the CO₂ absorption band):

$$N\varepsilon = \frac{L_{\text{obs}}(w) - L_{\text{clr}}(w)}{B[w, T(p_c)] - L_{\text{clr}}(w)} \quad (2.3)$$

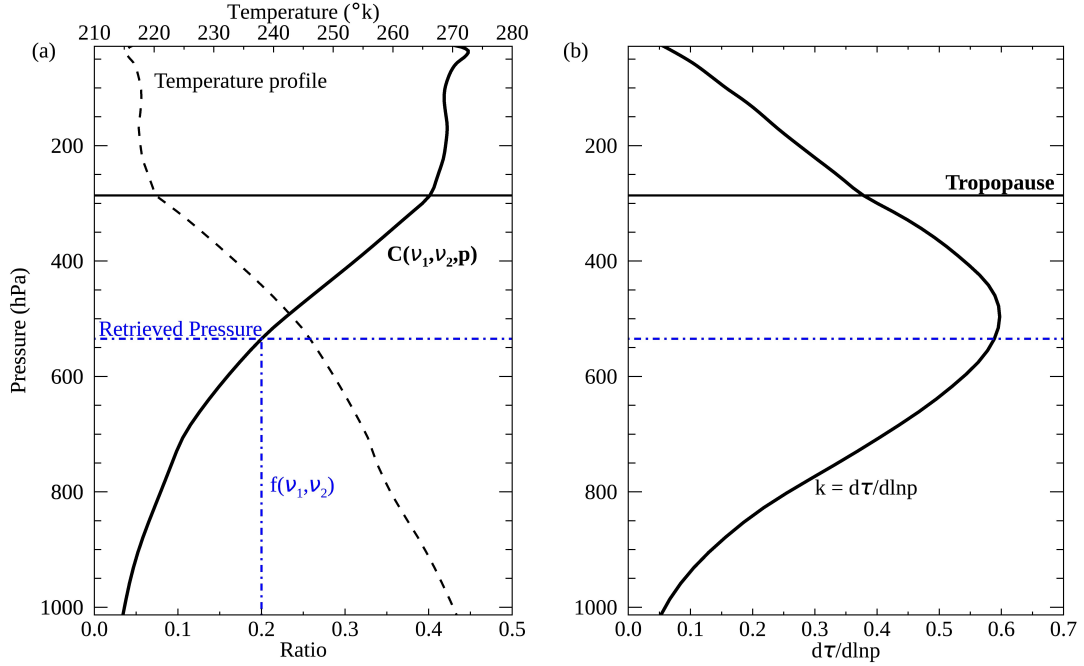


Figure 2.2: (a) An example of the cloud pressure function calculated using Eq. 2.2. This is strongly linked to the atmospheric temperature profile (dashed black line). The value obtained with Eq. 2.1 is compared against the cloud pressure function, and where these intersect is taken as the cloud pressure solution for that channel. In this example ν_1 and ν_2 are at 715 cm^{-1} and 725 cm^{-1} respectively. (b) The corresponding weighting functions ($d\tau/d\ln p$) which illustrate the changing sensitivity to the atmosphere. This is used to obtain a weighted average from multiple channel solutions.

In most applications of the CO₂ slicing technique, multiple channel pairs are used, resulting in different height solutions. In many studies, channel pairs are not considered if $L_{\text{obs}}(\nu) - L_{\text{clr}}(\nu)$ for either the CO₂ (ν_1) or reference (ν_2) channels used falls within the noise of the instrument at that channel (e.g. Menzel et al., 1992). The solution may also be rejected if the effective emissivity computed using Eq. 2.3 is not between 0 and 1.05 (e.g. Arriaga, 2007). If multiple solutions remain, then a number of different techniques can be employed to obtain a final value. This includes a top-down approach where the solution of the most opaque channel is accepted if it is within an expected height range, and if not the next most opaque

channel is considered. This is repeated until an appropriate height value is obtained (Menzel et al., 2008). Alternatively, the height and cloud fraction which best satisfies the radiative transfer equation for all the channels used is accepted as the final cloud pressure/height (e.g. Menzel et al., 1983, 1992). If all of the channel pairs are considered inappropriate, for example, if $L_{\text{obs}}(\nu) - L_{\text{clr}}(\nu)$ is within the noise of the instrument for all the channels used, then many methods assume that cloud is opaque and compare the brightness temperature measured by the instrument at 11 μm to an atmospheric temperature profile to obtain an alternative cloud height (e.g. Menzel et al., 1983, 1992; Zhang and Menzel, 2002; Menzel et al., 2008).

The issue of multiple solutions is further complicated for hyperspectral instruments as these can have hundreds of channels within the CO₂ absorption band. Some methods apply a weighting function based on each channel's sensitivity to the atmosphere (e.g. Smith and Frey, 1990). However, to avoid a high computational cost, often there needs to be some prior consideration of the most appropriate channels. This has included exploring large datasets with known cloud top heights to select the most appropriate channels (e.g. Arriaga, 2007). Other approaches include the creation of synthetic channels by averaging the radiances of channels sensitive to the same portion of the atmosphere (Someya et al., 2016) or CO₂ sorting which looks for the point where the clear and cloudy spectra deviate which is the first point where the instrument can see the cloud layer (Holz et al., 2006).

The CO₂ slicing method makes a number of assumptions: (1) the cloud is infinitesimally thin; (2) in cases where there are multiple layers of cloud, the lower-level clouds are ignored; (3) the two channels used in Eq. 2.1 are sufficiently close that the difference in emissivity between them is negligible - this is particularly

important to consider when the channel pairs are selected. Multiple cloud layers have previously been identified as a source of error in the CO₂ slicing retrieval, with the extent of this being affected by the channels used and the height of the underlying layers (Menzel et al., 1992). For example, an opaque cloud close to the surface is unlikely to affect the height retrieval of a cirrus cloud when using channels which are not sensitive to radiation from the lower troposphere. In contrast, an opaque cloud in the middle of the troposphere might lead to the underestimation of the cloud top height of a higher cirrus layer (Menzel et al., 1992). The effect of surface emissivity is expected to be minimal as channels within the CO₂ absorption band have weighting functions that peak above the surface, as shown in Fig. 2.1d.

An additional consideration has to be made when applying the CO₂ slicing method to volcanic ash. The height that a volcanic ash cloud reaches is largely dependent on the force of the eruption and the atmospheric conditions (Sparks et al., 1997), and so this can vary widely. Large explosive eruptions can generate columns which enter the stratosphere, which can then potentially affect climate (Robock, 2000a). The cloud pressure function generated using Eq. 2.2 is temperature dependent. Within the troposphere, the temperature decreases with height; however, in the stratosphere the temperature begins to climb again. This leads to a reversal in the cloud pressure function, which in some cases can result in multiple solutions: one in the troposphere and one in the stratosphere. Consequently, some prior information is required to determine whether the plume is within the troposphere and therefore if the CO₂ slicing technique is appropriate. This might include observations made on the ground or by pilots. The CO₂ slicing technique has previously only been used to determine the height of aqueous clouds in the troposphere, and so in this study,

only the tropospheric solution is accepted. Its use would therefore be inappropriate for ash clouds from large explosive eruptions into the stratosphere. The technique has been extended to obtain the height of volcanic ash in the stratosphere in Richards (2006) and Tupper et al. (2007), and given that the ash clouds from explosive volcanic eruptions can enter the stratosphere, this is an important future development for the adaptation of the retrieval presented here for IASI.

2.3 The Infrared Atmospheric Sounding Interferometer

The Infrared Atmospheric Sounding Interferometer (IASI) is an instrument on board three meteorological satellites, Metop A, B and C, launched in 2006, 2012 and 2018 respectively. Each instrument orbits the Earth twice a day. The instrument scans have a swath width of 2200 km and consist of groups of four circular pixels which have a diameter of 12 km at nadir (Clerbaux et al., 2009). The instruments measure across the infrared between 645 and 2760 cm^{-1} (3.62 to 15.5 μm) with a high spectral resolution of 0.5 cm^{-1} (Blumstein et al., 2004).

The instrument has previously been used to analyse volcanic plumes of SO_2 (e.g. Clarisse et al., 2008; Walker et al., 2012; Carboni et al., 2012; Clarisse et al., 2012, 2014; Carboni et al., 2016; Taylor et al., 2018) and ash (e.g. Clarisse et al., 2010a; Maes et al., 2016; Ventress et al., 2016) from a number of different eruptions. Previous methods for determining the height of the plume with spectra measured by IASI use the optimal estimation method (Maes et al., 2016; Ventress et al., 2016). The CO_2 slicing method has previously been applied to IASI spectra to obtain the cloud top height of aqueous cloud (Arriaga, 2007). The values obtained for the cloud

pressure and emissivity are often assimilated in numerical weather prediction models (Guidard et al., 2011; Lavanant et al., 2011). The different adaptations of the CO₂ slicing technique for IASI use different numbers and combinations of channels and can therefore give different results (Lavanant et al., 2011). In this study, channels are selected based on the technique’s performance when applied to simulated ash spectra.

2.4 Application to simulated data

2.4.1 Channel selection

IASI has over 300 channels which fall within the CO₂ absorption band, and so to ensure computational efficiency an appropriate subset of these channels must be selected. To do this the CO₂ slicing technique was first applied to 384 simulated ash spectra. These are ‘ideal’ test cases, which do not include other aerosols or aqueous cloud. These spectra include six different atmospheres: high latitude, mid-latitude day and night, tropical daytime, and polar summer and winter (including atmospheric profiles created for the Michelson Interferometer for Passive Atmospheric Sounding, MIPAS; Remedios et al. 2007). The spectra were modelled using the refractive indices of samples of volcanic ash from the Eyjafjallajökull eruption in 2010 (Peters, 2010): the main eruption considered in this study. In the future different refractive indices could be used, such as those in Prata et al. (2019). A range of ash properties were explored: cloud heights between 200 and 900 hPa (going slightly above the tropopause), ash effective radius between 5 and 10 μm , and ash optical depths between 5 and 15 (referenced at 550 nm). Typically, the effective radius is less than 8 μm for very fine ash (such as in a distal plume) and between 8 and 64 μm for fine ash (Marzano et al., 2018). The range of ash optical

depths is highly variable. Ventress et al. (2016) and Balis et al. (2016) recorded ash optical depths of less than 1.2 from dispersed plumes from Eyjafjallajökull in 2010; however much higher values can be expected closer to the volcano or following large explosive eruptions. The effective radius and AOD explored here for the channel selection are in the upper range and above what might be expected: values which may only be true close to the volcanic vent. The spectrum of an optically thin plume is more difficult to differentiate from a clear spectrum, commonly leading to the signal $(I_{obs}(v) - I_{clr}(v))$ being within the instrument noise and subsequently resulting in no retrieval. A decision was made to select the channels used using idealised optically thick cases, which may only be true close to the vent, for which the plume should be evident in the majority of the CO₂ channels. The selected channels are tested on a wider range of AODs and effective radius, including smaller values that are more representative of a disperse plume in section 2.4.2.

The CO₂ slicing method was first applied using every channel combination between 660 and 800 cm⁻¹, where the reference channel (ν_2) wavenumber is greater than the CO₂ channel (ν_1) wavenumber. In this way, the reference channel is generally more sensitive to a lower part of the atmosphere than the CO₂ channel. As with existing studies only tropospheric solutions were accepted, and in cases where the curve of the cloud pressure function resulted in multiple solutions, the solution with the greater weight (in this case the weighting function is defined as $k = d\tau[\nu_1, p]/d\ln p$) was accepted. The output from each channel pair was only accepted if it met three quality control criteria: (1) $L_{obs}(\nu_1) - L_{clr}(\nu_1)$ must be greater than the noise of the instrument at channel ν_1 (CO₂ channel; within the CO₂ absorption band the noise of the IASI instruments is between 2.55×10^{-8} and

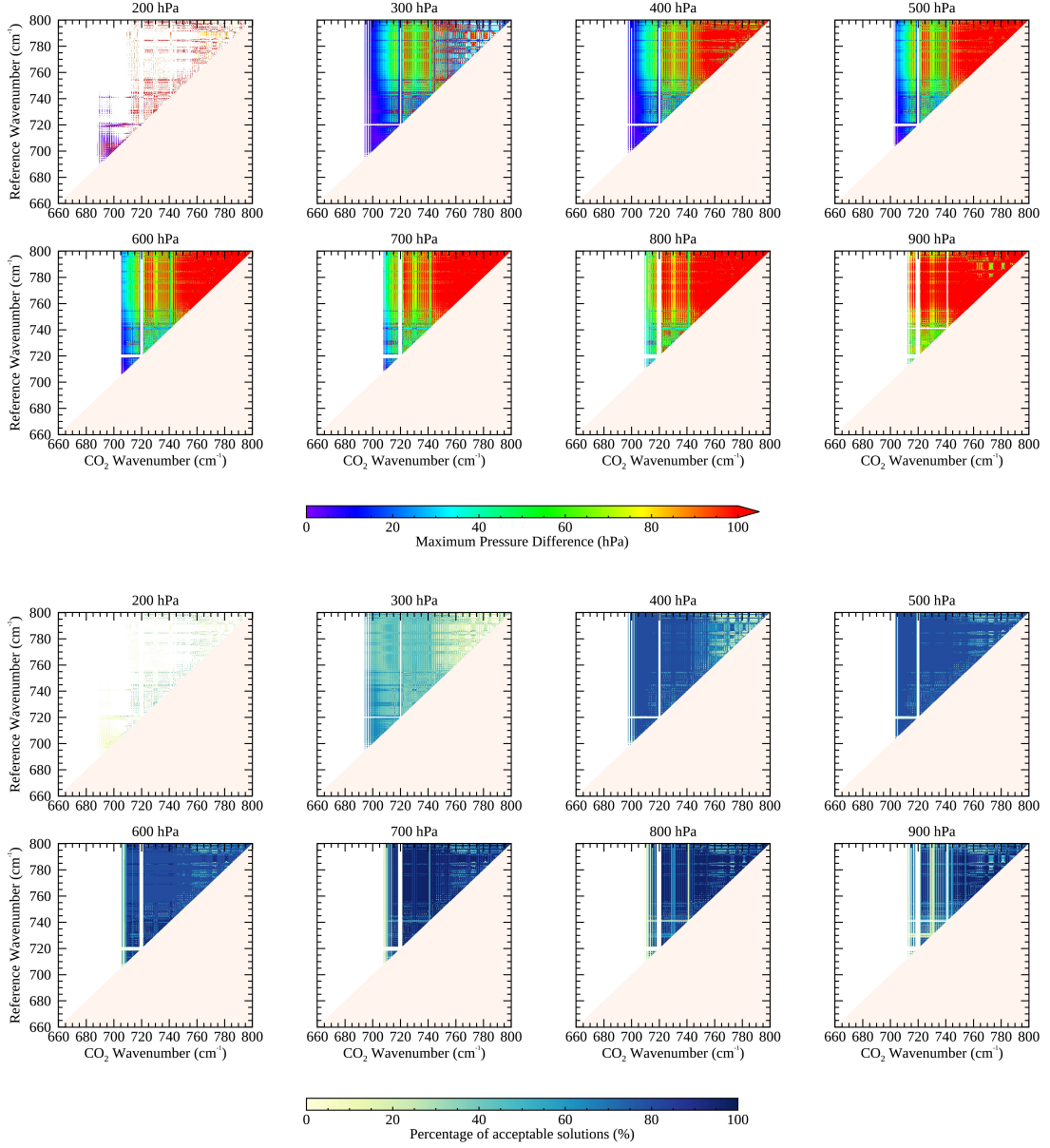


Figure 2.3: CO₂ slicing results for simulated ash spectra. The technique has been applied for each channel pair between 660 and 800 cm⁻¹. A total of 384 spectra were used which includes six different atmospheres. It also includes ash optical depths between 5 and 15, effective radius ranging between 5 and 10 μm , and pressures between 200 and 900 hPa. The first two rows of the plot show the maximum difference between the known (simulated) pressure and the pressure retrieved with the CO₂ slicing algorithm. This is divided into each pressure level. The last two rows show the percentage of successful retrievals. This is again divided into the eight different pressure levels. In these plots the colour white indicates where no successful retrieval has been made and off-white indicates channel combinations not explored in this study.

$3.77 \times 10^{-8} \text{ W}/(\text{cm}^2 \cdot \text{sr} \cdot \text{cm}^{-1})$); (2) similarly, $L_{\text{obs}}(\nu_2) - L_{\text{clr}}(\nu_2)$ must be greater than the noise of the instrument at ν_2 (reference channel); (3) the solution to Eq. 2.3 must fall between 0 and 1.05 (following Arriaga 2007).

The results are shown in Fig. 2.3. The top two rows show the maximum pressure difference between the true (simulated) and CO₂ slicing retrieved values divided into each pressure level. In total there are 48 spectra for each pressure level with these incorporating the different atmospheric profiles and ash properties. The lower two rows of Fig. 2.3 show the percentage of accepted retrievals. This refers to where there was an intersection between the two functions shown in Eq. 2.1 and 2.2, and where the value retrieved meets all three quality control conditions. This is also grouped into the eight pressure levels. The equivalent plots for the six individual atmospheres can be seen in Fig. A.1-A.6 in the appendix. Potentially, the method used in this study to select the most appropriate channels could be performed for the different atmospheres to select channels which might be more suited to specific climatologies.

Figure 2.3 demonstrates that the best-performing channel pairs vary depending on the height of the plume. For plumes at lower pressures, the maximum pressure difference between the simulated and retrieved pressures is smaller at lower CO₂ wavenumbers. For example, for the plumes simulated at 300 hPa, the maximum pressure difference was lowest (less than 20 hPa) for CO₂ channels between 700 and 710 cm⁻¹. As the pressure of the ash layer is increased, values are no longer obtained at smaller wavenumbers. For example, for a plume at 500 hPa, solutions are no longer obtained for CO₂ channels which are less than 700 cm⁻¹: the maximum pressure difference between the true and retrieved values is now smaller for slightly higher wavenumbers. For a plume at 800 hPa the maximum pressure difference is lowest

(less than 60 hPa) for CO₂ channels between 715 and 720 cm⁻¹. This observation reflects what is shown in fig. 2.1b and c: that the channel's peak sensitivity shifts from higher in the atmosphere at lower wavenumbers to close to the surface at higher wavenumbers affecting the best-performing channel combinations. Notably, at 200 hPa there are far fewer channels which pass the quality control conditions, and where a retrieval is possible, there is a large difference between the true and retrieved pressure. It is also possible to identify an increased error closer to the surface. Previous studies have acknowledged that the CO₂ slicing tool is less successful at pressures greater than 700 hPa (Menzel et al., 2008) because approaching the surface there are fewer channels with a distinction between the clear and cloudy spectra, often leading to $L_{\text{obs}}(v) - L_{\text{clr}}(v)$ being within the range of the instrument's noise and therefore the channels being excluded. Another observation that can be made from Fig. 2.3 is that channels below 700 cm⁻¹ often have a low percentage of accepted retrievals. These channels are shown in Fig. 2.1b and c to be sensitive to the heights above the tropopause. This may also be the reason for few accepted retrievals at 720 cm⁻¹. Additionally, for channels greater than 750 cm⁻¹, which are no longer in the CO₂ absorption band, the difference between the true and retrieved pressure is usually greater than 100 hPa.

Figure 2.4 shows a similar plot between 700 and 750 cm⁻¹. In this case, the spectra were also grouped into three categories: high cloud (300-400 hPa), mid-level cloud (500-600 hPa) and low-level cloud (700-800 hPa). Note that the simulated spectra at 200 and 900 hPa have been excluded. Also, the maximum pressure difference is only shown where it is less than 75 hPa and where the percentage of successful retrievals is greater than 50%. This plot has been used to manually select

Table 2.3: The channel ranges selected for the final application of the CO₂ slicing technique. In total 57 channels are used. Following Arriaga (2007), 900.50 cm⁻¹ is used as the window channel used to calculate the effective emissivity.

CO ₂ Channel Range (cm ⁻¹) (inclusive)	Reference Channel (cm ⁻¹)	Peak Sensitivity Range (hPa)	Number of Channels
700 - 703.5	715	110.25 - 314.00	15
706 - 710.5	715	328.75 - 478.00	19
713 - 713.5	725	442.00 - 496.75	3
718.25 - 719.5	728	133.75 - 441.75	6
720.5 - 721.5	728	21.00 - 496.50	5
729.75 - 731.75	735	535.25 - 639.25	9

the most appropriate set of channels. The best selection of channel pairs will be representative of the entire atmosphere (channels which peak at different heights should be selected, Fig. 2.1c), while minimising the difference between the simulated and retrieved pressures and maximising the acceptance rate (Fig. 2.4). Another consideration is the assumption that the change in emissivity between the channel pairs is negligible. The emissivity ratio for a sample of ash from the Eyjafjallajökull eruption (the main eruption considered in this study) for all channel combinations in the 680 and 800 cm⁻¹ range is shown in Fig. 2.5. For this assumption to hold true, the emissivity ratio should be as close to 1 as possible. This is usually the case for channels which are close together. Given these criteria, appropriate channel ranges have been selected. These channel ranges and the reference channels are shown in table 2.3. The weighting functions for the selected channels are shown in Fig. 2.1d.

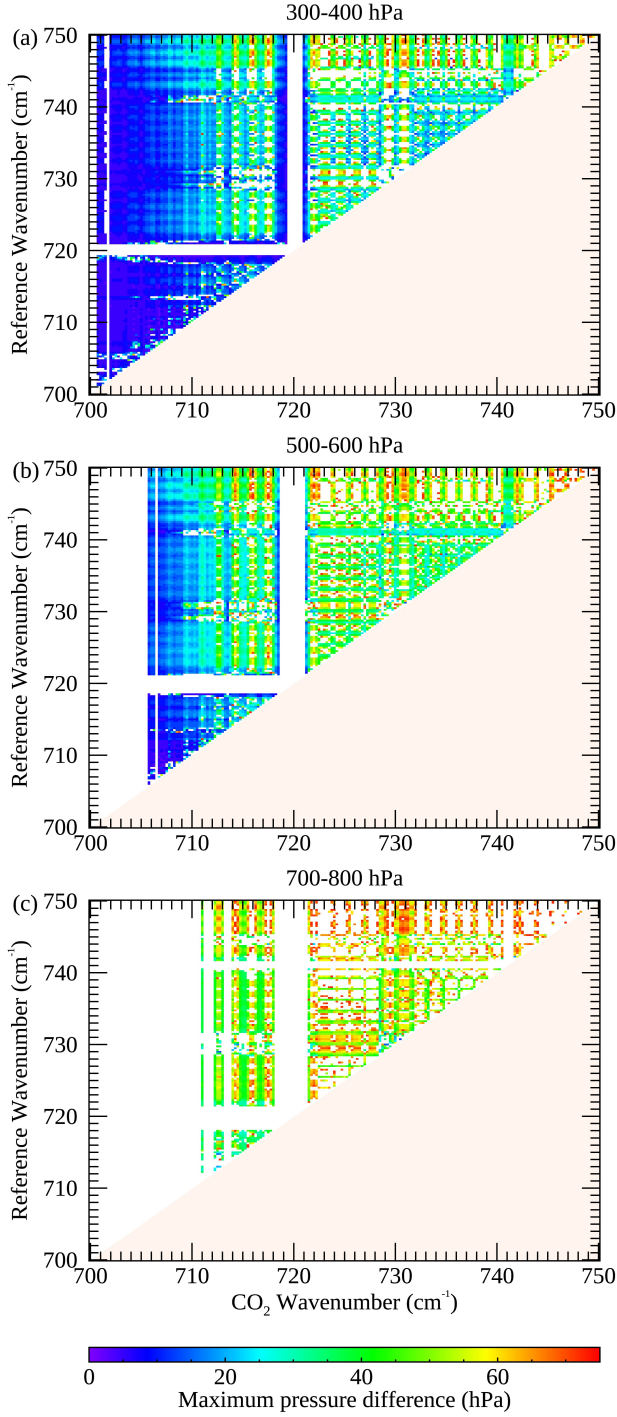
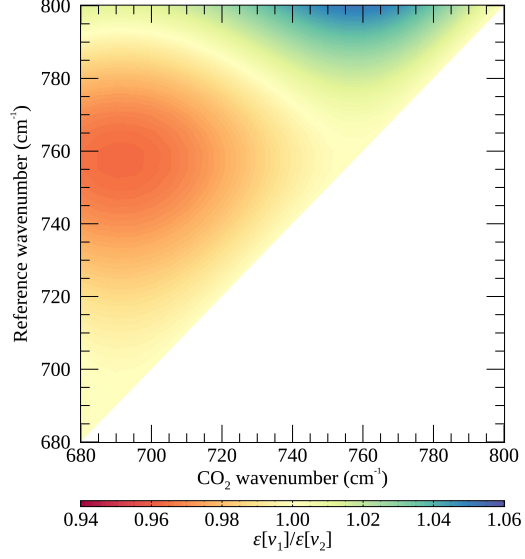


Figure 2.4: CO₂ slicing results for RTTOV simulated ash spectra. The plots show the maximum difference between the true (simulated) pressure and the pressure obtained with the CO₂ slicing algorithm. The results are split into three pressure levels: (a) high cloud (300-400 hPa), (b) mid-level cloud (500-600 hPa) and (c) low-level cloud (700-800 hPa). Note that, in this plot, results for 200 and 900 hPa are excluded. Results are only included where the maximum difference is less than 75 hPa and the percentage of successful retrievals is greater than 50%. This was used to inform the choice of channels for the final CO₂ slicing algorithm.

Figure 2.5: Emissivity ratio for channels between 680 and 800 cm^{-1} . The ash sample was from the Eyjafjallajökull eruption in 2010. The assumption that the emissivity does not vary significantly for the pair of channels used for the CO_2 slicing is important. For this to hold true, ideally the emissivity ratio should be close to 1.



2.4.2 Simulation results

Following the selection of channels, the final pressure values (P) were computed by taking a weighted average of the results:

$$P = \frac{\sum p_c(\nu) k^2(\nu)}{\sum k^2(\nu)} \quad (2.4)$$

where p_c is the pressure retrieved for channels ν and k refers to the weighting function based on the derivative of atmospheric transmittance computed for each pressure level with RTTOV with respect to the log of atmospheric pressure ($d\tau[\nu, p]/d\ln p$). On this occasion, the retrieval was applied to 1344 simulated ash spectra including those with lower ash optical depths (ranging from 0.5 to 15) and smaller effective radius (ranging from 1 to 10 μm). This includes spectra representative of thinner ash clouds which were not considered during the channel selection.

The results are displayed in Fig. 2.6a-f which plots the true (simulated) pressures against the final weighted pressures obtained with the CO_2 slicing technique. The different atmospheres are displayed separately and the percentage of accepted

retrievals are indicated below each plot. Table 2.4 reports the root mean square error (RMSE) for each atmosphere. These results suggest that the technique does have merit for obtaining the height of ash clouds but that it performs better in some atmospheres (e.g. mid latitudes) than others (e.g. polar winter).

Figures 2.6g-i give some indication of where and why the retrieval was unsuccessful. Figure 2.6g-h show there are slightly more failed cases for ash spectra with the lowest optical depth (0.5) and effective radius ($1\ \mu\text{m}$). These low values are representative of thinner ash clouds whose spectra are more similar to clear atmospheric spectra. Subsequently, these cases are likely to fail the signal to noise quality control tests (Menzel et al., 1992, 2008). For example, an ash cloud at 500 hPa only has 7 channels which pass the $L_{\text{obs}}(\nu_1) - L_{\text{clr}}(\nu_1)$ quality control condition when the ash optical depth is 0.1. However, the number of channels passing this criterion increases to 38 at an ash optical depth of 2.3. This observation is supported by Fig. 2.6j-k, which show the number of cases where the difference between the simulated and retrieved pressure is less than 0.5 km, which is slightly lower for a smaller effective radius and ash optical depth.

The majority of failed cases are shown to be at the pressure extremes (Fig. 2.6i). Similarly, Fig. 2.6l indicates that there are fewer cases where the pressure difference between the simulated and retrieved pressures is less than 0.5 km at these pressures. Close to the surface this can again be attributed to less distinction between the clear and ashy spectra (Menzel et al., 2008). For example, for the RTTOV default atmosphere, an ash plume at 900 hPa fails the signal to noise condition for all the channels used regardless of the optical depth and effective radius of the simulation. The lowest simulation pressure (200 hPa) is close to or above the tropopause for all

six atmospheres, and for this example the CO₂ slicing method was allowed to retrieve up to the height of the reversal of the temperature profile (which is slightly above the tropopause). At these heights, the temperature gradient (dT/dp) is relatively stable, causing a similar effect in the cloud pressure function (best illustrated in Fig. 2.2) and subsequently a greater number of unsuccessful retrievals: the CO₂ slicing technique has previously been shown to perform poorly in isothermal regions of the atmosphere (Richards et al., 2006). This may also be the reason for the poor performance of the CO₂ slicing technique when applied to the polar summer atmosphere for which the technique only retrieved values for 29% of cases.

Figure 2.6: Final CO₂ slicing pressure results for RTTOV simulated ash spectra (a total of 224 spectra per atmosphere). Panels (a)-(f) show the true (simulated) pressure plotted against the CO₂ slicing retrieved value for the six different atmospheres. (a) RTTOV default atmosphere (high latitude), (b) mid-latitude day, (c) mid-latitude night, (d) tropical day, (e) polar summer, and (f) polar winter. In this case, the simulated spectra include the following ash properties: ash optical depth ranging between 0.5 and 15, ash effective radius ranging between 1 and 10 μm , and pressure values between 200 and 900 hPa. Below each plot is a value indicating the percentage of successful retrievals (where a height value can be obtained and all quality control conditions have been met). (g) The frequency of ash optical depths for which the CO₂ slicing technique was unable to return a height value. (h) Same as (g) for the effective radius. (i) Same as (g) for the ash cloud pressure. (j) The frequency of ash optical depths for which the difference between the simulation and CO₂ slicing height is less than 0.5 km. (k) The same as (j) for effective radius. (l) The same as (j) for ash cloud pressure. Related statistics can be seen in table 2.4. The equivalent plot, where the quality control was not applied, has been included in the appendix (figure A.7).

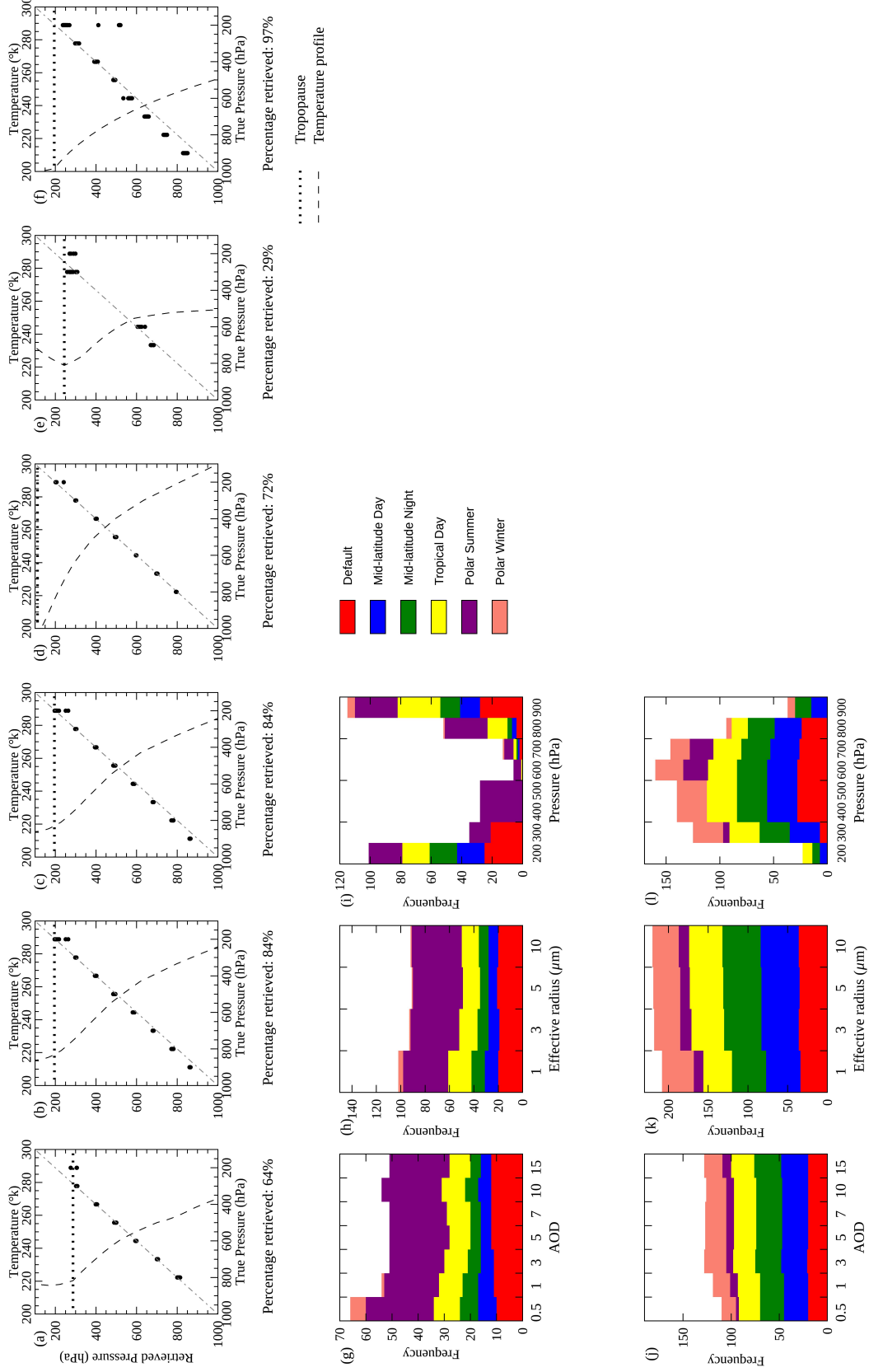


Figure 2.6: Caption on previous page

The RMSE and the percentage of accepted retrievals for the CO₂ slicing technique, without the quality control criteria applied, are shown in table 2.4. Figure A.7 shows the equivalent plot to Fig. 2.6 without the quality control. The addition of the quality control compromises the number of successful retrievals for an overall reduction in the RMSE. Overall, the reduction is around 200 m but in individual cases by up to 1.4 km (e.g. tropical atmosphere). Figure A.7 indicates that the addition of the quality control is particularly advantageous for lower-level ash layers which without the quality control are often overestimated. Overall, the results show that this adaptation of the CO₂ slicing technique has promise for obtaining the height of volcanic ash clouds within the troposphere, although its use is limited in cases of low-level or thin clouds or where there is a steep temperature gradient.

Table 2.4: Summary of the percentage of accepted retrievals and the RMSE describing the difference between the true (simulated) and retrieved values

Atmosphere	No quality control		With quality Control	
	RMSE (m)	Success Percentage	RMSE (m)	Success Percentage
RTTOV Standard	706	91	424	64
Mid-Latitude Day	635	100	282	84
Mid-Latitude Night	635	100	282	84
Tropical Day	1483	100	141	72
Polar Summer	1271	95	777	29
Polar Winter	565	100	1553	97
All	988	97.7	777	71.9

2.5 Application to scenes containing volcanic ash

The CO₂ slicing method has been applied to scenes containing ash from the Eyjafjallajökull (63.63°N, 19.63°W; 1651 m) and Grímsvötn (64.42°N, 17.33°W; 1725 m) eruptions in 2010 and 2011 respectively. The plumes from both eruptions were closely monitored using a variety of instrumentation which included ground-based remote sensing, airborne measurements and the use of satellite products (e.g. Gudmundsson et al., 2010; Weber et al., 2012). The ash and gas clouds from these eruptions have since been extensively studied (e.g. Kerminen et al., 2011; Tesche et al., 2012; Flemming and Inness, 2013; Cooke et al., 2014; Ventress et al., 2016). They are commonly used to demonstrate the utility of new remote sensing developments (e.g. Mackie and Watson, 2014a; Taylor et al., 2015; Ventress et al., 2016; Western et al., 2017) and similarly are often used in modelling research (Matthias et al., 2012; Webster et al., 2012; Moxnes et al., 2014a; Wilkins et al., 2016). This makes them the ideal first candidates for the CO₂ slicing technique. Another reason for choosing these eruptions is that, in both cases, the ash clouds were confined to the troposphere, making them an appropriate target for the CO₂ slicing technique.

In this application of the retrieval, it has only been applied to pixels which are flagged as containing volcanic ash by a linear ash retrieval developed for IASI (Ventress et al. 2016; Sears et al. 2013: following the method developed for SO₂ by Walker et al. 2012). This method compares each IASI spectra against a covariance matrix formed from pixels which contain no volcanic ash, thereby representing the spectral variability associated with interfering gas species or clouds, and also the instrument noise. A least-squares fit is performed for three ash altitudes (400, 600

and 800 hPa) to retrieve a value for ash optical depth. A pixel is then flagged if it exceeds a threshold at any height. As SO_2 can, with caution, be used as a proxy for volcanic ash (Carn et al., 2009; Thomas and Prata, 2011) the retrieval has also been run for pixels flagged for SO_2 using the same approach (Walker et al., 2011, 2012; Carboni et al., 2012, 2016). For the CO_2 slicing, values for L_{clr} were obtained using the radiative transfer model RTTOV using the European Centre for Medium-Range Weather Forecasts (ECMWF) atmospheric profile as an input and using the default ocean emissivity within RTTOV. The effect of surface emissivity is thought to be minimal as for the channels used the weighting functions peak above the surface, Fig. 2.1d. The temperature and humidity profiles needed to calculate the Planck radiance and τ were acquired from the ECMWF. The closest ECMWF profile to each individual IASI pixel was used. RTTOV was used to compute the transmittance values. Another point to note is that, in section 2.4, the maximum height that could be retrieved was defined as the height at which the temperature profile inverts and has a positive gradient. This is slightly above the tropopause, which is defined by the World Meteorological Organisation (WMO) as the point at which the lapse rate is less than $2^\circ\text{C}/\text{km}$, and remains lower than this for at least 2 km. This was done to demonstrate how the CO_2 slicing method performs above the troposphere where the atmospheric temperature does not vary significantly: the atmospheric lapse rate here approaches zero. Figure 2.6 demonstrates that the CO_2 slicing method performs poorly in these cases, and so in the application to real data the CO_2 slicing method is only able to retrieve values up to the tropopause as defined by the WMO.

2.5.1 Methods used for comparison

2.5.1.1 Optimal Estimation Scheme

The CO₂ slicing plume altitude results have been compared against the plume altitude obtained using the optimal estimation (OE) retrieval scheme developed by Ventress et al. (2016). The retrieval scheme combines a clear-sky forward model with a (geometrically) infinitely thin ash layer to simulate atmospheric spectra, using ECMWF data as input atmospheric parameters. The simulated spectra are compared to the satellite measurements and, using the cost function (a measure of retrieval fit), the spectrum that most closely matches the spectrum obtained with IASI is used to determine the ash plume properties. This method retrieves the effective radius and ash optical depth, which can be used to calculate the mass of ash within the plume. For more information on this technique, refer to Ventress et al. (2016).

2.5.1.2 CALIOP

While a comparison against another IASI retrieval is useful, such comparisons have limitations. All retrieval techniques make assumptions and have different limitations and so it is not expected that the results would be the same, or even similar, in all cases. An additional comparison is made with the Cloud-Aerosol LiDAR with Orthogonal Polarization (CALIOP) instrument, on board the the Cloud-Aerosol LiDAR and Infrared Pathfinder Satellite Observation (CALIPSO) satellite. This active sensor was launched in 2006 and forms part of NASA's afternoon constellation (A-Train) of satellites. The instrument has a 30 m vertical resolution and 335 m spatial resolution, and orbits roughly every 16 days (Winker et al., 2009; Hunt et al.,

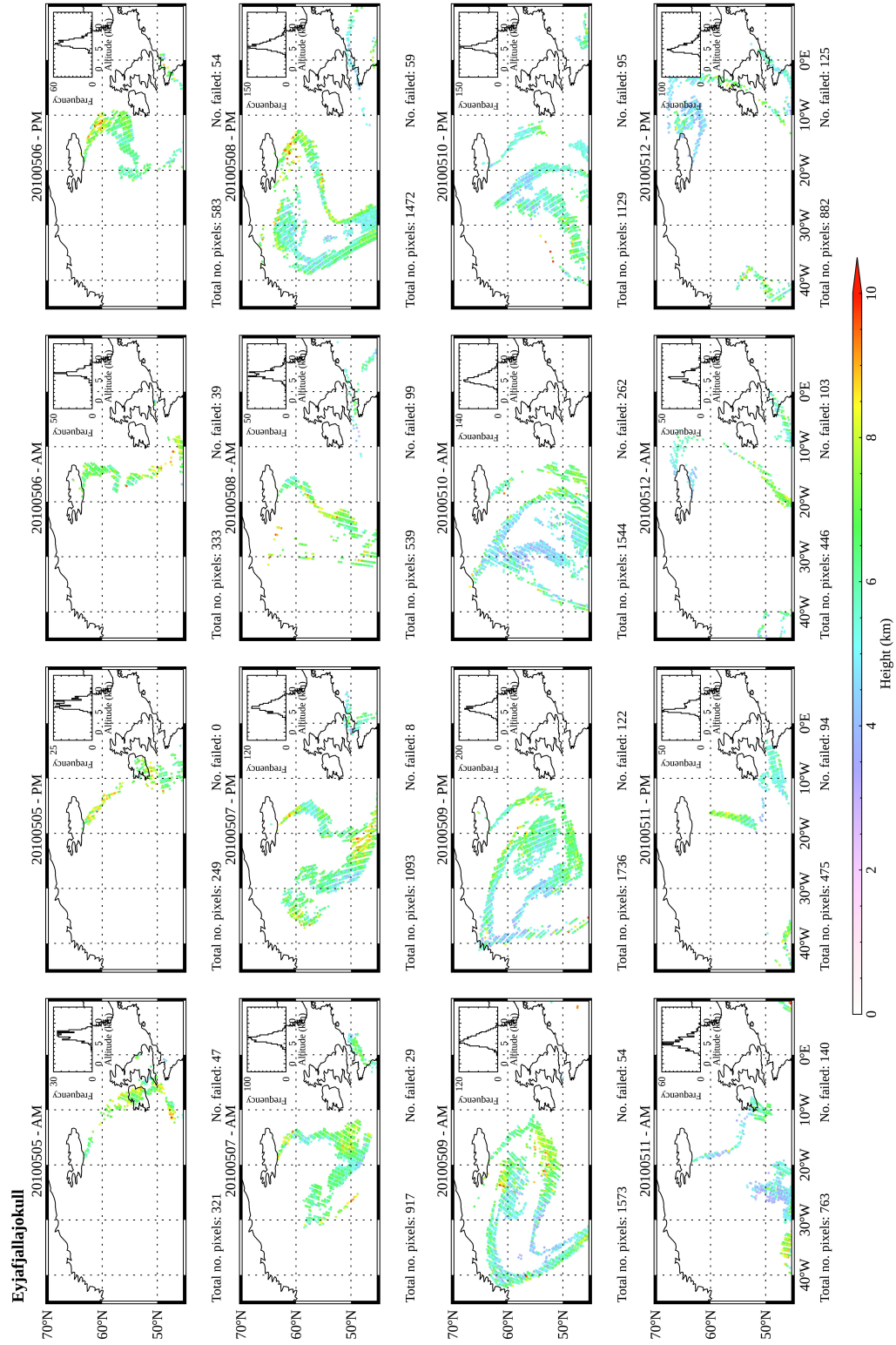
2009). The backscatter profile obtained with LiDAR instruments can be used to obtain the vertical structure of the atmosphere, providing information on the height and thickness of different scattering layers, including both ash and cloud. CALIOP and other LiDAR instruments are commonly used as a tool for the validation of cloud heights, including previous studies with the CO₂ slicing technique (e.g. Smith and Platt, 1978; Frey et al., 1999; Holz et al., 2006, 2008), and a number of ash retrievals (e.g. Stohl et al., 2011; Ventress et al., 2016).

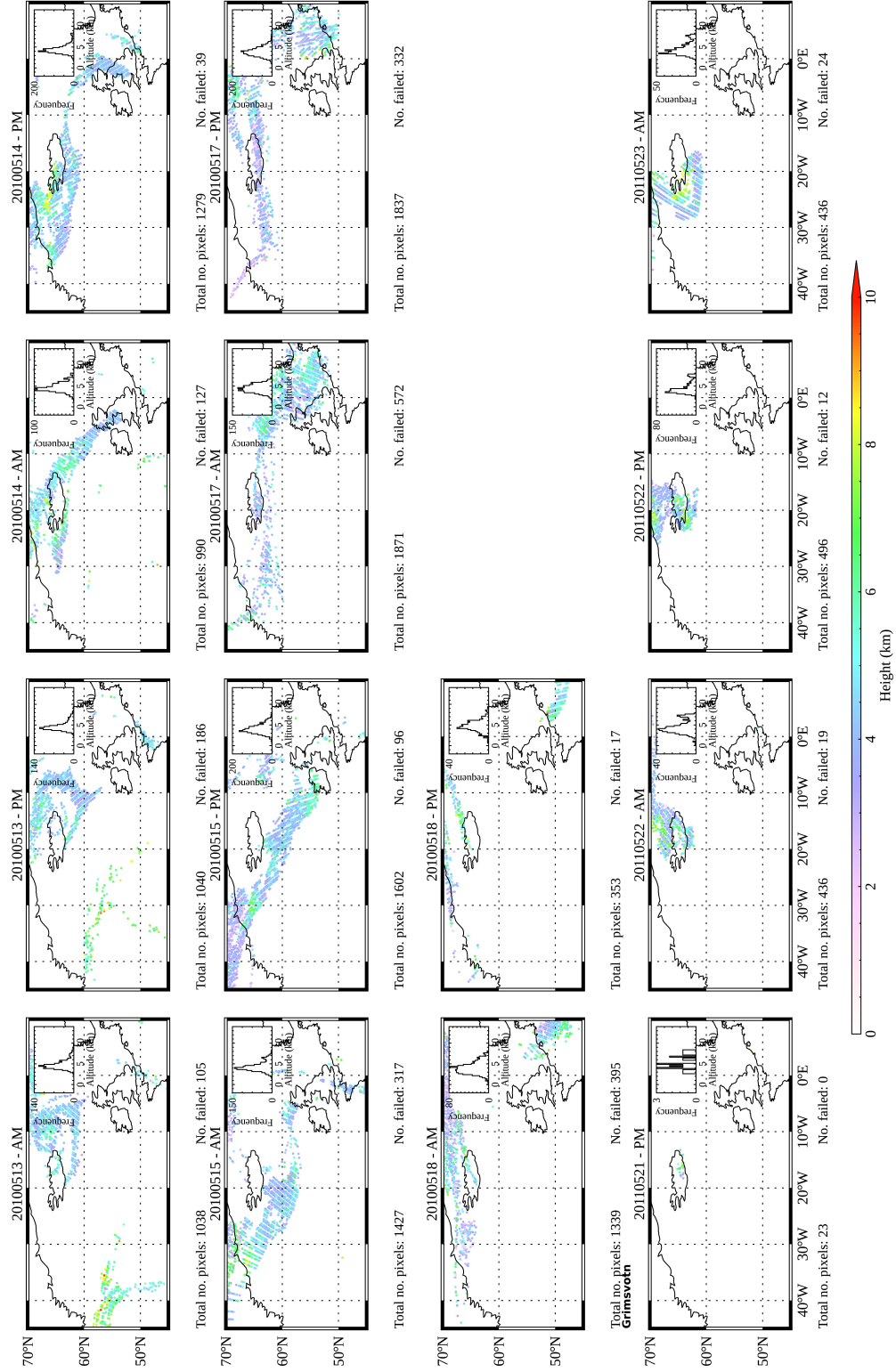
To conduct a comparison between the heights obtained using the CO₂ slicing and OE techniques with CALIOP the data from the two instruments were first collocated. CALIOP overpasses which intersected with the ash plumes were identified using false colour images from the Spinning Enhanced Visible and Infrared Imager (SEVIRI) (Thomas and Siddans, 2015). The backscatter profiles were then averaged vertically to a 250 m resolution. The CALIOP data were smoothed to IASI's spatial resolution of 12 km and collocation was identified where measurements made by the two instruments fell within 50 km and 2 hours of each other. If multiple CALIOP pixels were matched to an IASI pixel then the CALIOP pixel which was closest in distance was selected for comparison. A cloud top height is obtained from the backscatter profiles allowing a comparison with the CO₂ slicing and OE methods. This was done by (1) calculating the mean backscatter above 15 km and subtracting this from the total backscatter, (2) calculating a cumulative backscatter for each pixel, and (3) determining where the atmospheric extinction exceeded a specified threshold. Where the threshold was exceeded was taken as the cloud top height. This threshold has been manually set for each scene, chosen to obtain the best match to the cloud top height shown in the CALIOP backscatter images.

2.5.2 Comparison of results

The CO₂ slicing technique was applied to IASI ash flagged pixels from 13 and 3 days from the Eyjafjallajökull and Grímsvötn eruptions respectively. Maps of these results, with the orbits divided into morning and afternoon, are shown in Fig. 2.7. For each map there is a histogram showing the distribution of the retrieved heights. Encouragingly, initial examination of the maps shows that the retrieved values are spatially consistent with only a few outliers. These outliers are usually individual pixels whose altitudes are higher than those surrounding them. Below each map are numbers indicating the total number of pixels in each plot and the number of pixels for which the CO₂ slicing technique was unable to obtain a height, either because there is no intersection between the two functions shown in Eq. 2.1 and 2.2 or because of the failure of one or more of the quality control measures outlined in section 2.4. Overall, the CO₂ slicing technique was able to obtain a height value for 88% of pixels from the two eruptions.

Figure 2.7: [On the following page] Maps of the CO₂ slicing output (with quality control applied) for the Eyjafjallajökull and Grímsvötn eruptions. Each plot consists of multiple orbits, divided into morning and afternoon. On each plot is a histogram showing the distribution of heights for each scene. Beneath each plot are numbers showing the total number of pixels in each image and the number of pixels for which the CO₂ slicing method was unable to return a value





The CO₂ slicing results have been compared against those obtained with an optimal estimation (OE) scheme. Distributions of the heights obtained for all pixels from the two eruptions are shown in Fig. 2.8a and b. In both cases, the peak of the distribution for the CO₂ slicing heights is higher than for the OE scheme. Figure 2.9 shows how the average height obtained with the two retrievals has changed over the 13 days studied from the Eyjafjallajökull eruption. This plot shows that on 5th May the CO₂ slicing method retrieved an average altitude of roughly 7 km and

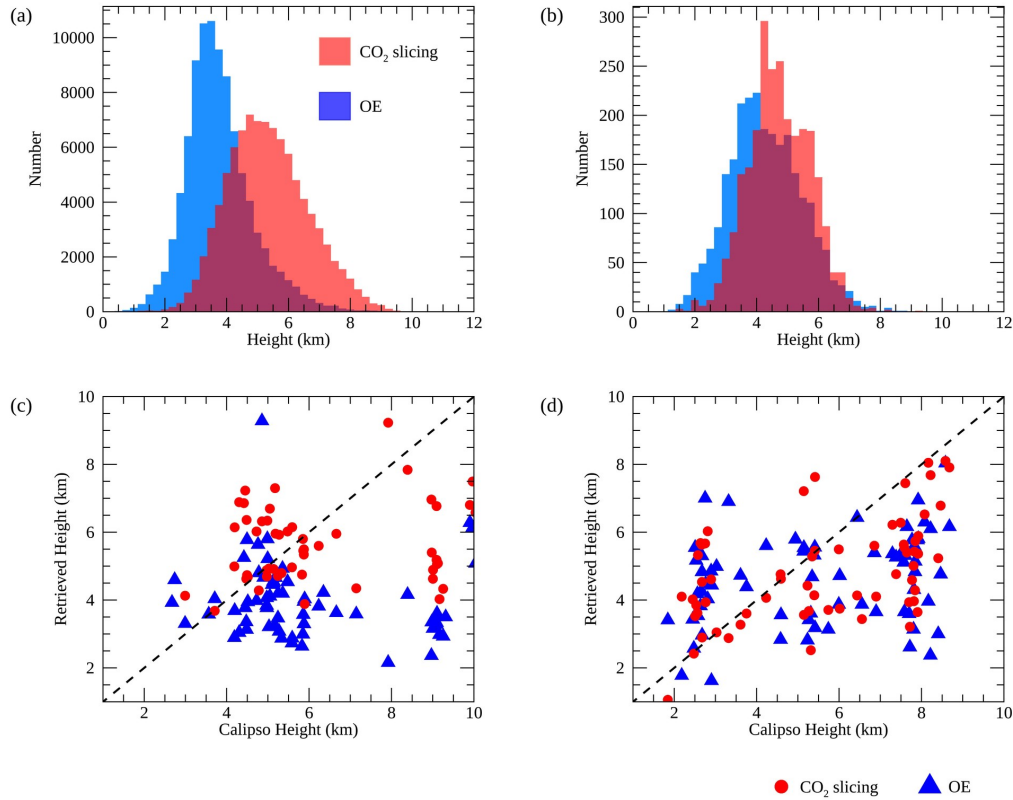


Figure 2.8: (a) Distribution of the CO₂ slicing and optimal estimation (OE) retrieved ash heights for all pixels from the Eyjafjallajökull eruption. (b) Same as (a) for the Grímsvötn eruption. (c) Comparison of the CALIOP heights with those obtained with the CO₂ slicing and optimal estimation techniques for a subset of pixels (where measurements fell within 50 km and 2 hours of each other) from the Eyjafjallajökull eruption. (d) Same as (c) for the Grímsvötn eruption. Related statistics can be seen in table 2.5.

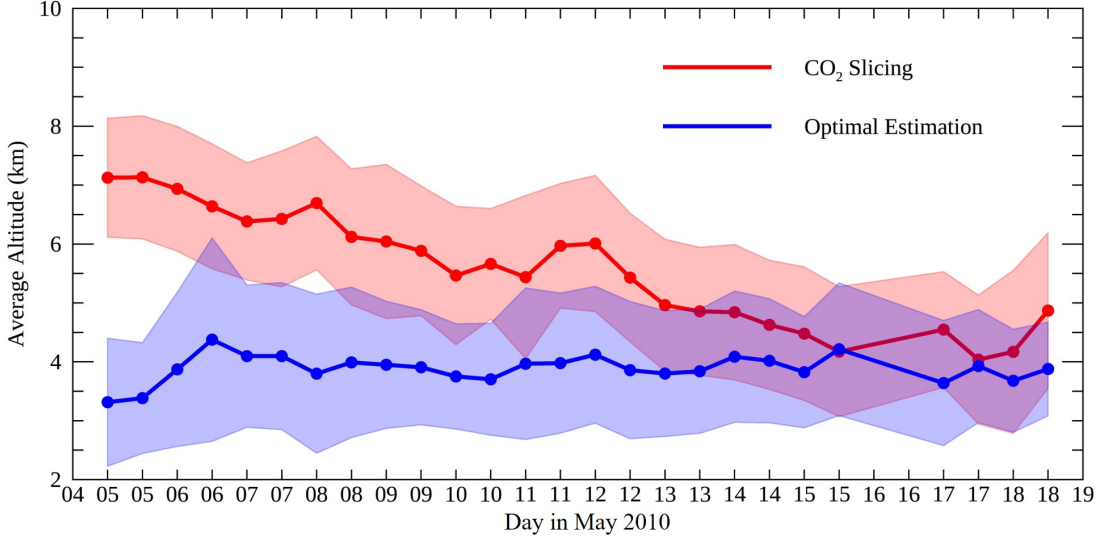


Figure 2.9: Time series showing how the average retrieved height for the CO₂ slicing and optimal estimation techniques varies during the Eyjafjallajökull eruption. The shaded polygon represents one standard deviation from the mean.

that this then fell throughout the remainder of the study period. This corresponds to observations made about the volcano’s activity. Activity at the volcano became more explosive on 5th May 2010 with increased emission of ash and SO₂, with plumes rising to greater than 8 km. This was followed by a fall in the plume height to 6-7 km, interspersed with higher plumes during more explosive activity (Petersen, 2010). The average CO₂ slicing heights shown in Fig. 2.9 are probably lower because these are values for the entire plumes including further away from the source. However, it does capture the changing elevation of the plume throughout the eruption. By contrast, the OE average heights are less variable: between 3 and 4.25 km throughout the period studied. Some example maps of the OE heights are shown in Fig. 2.10 to 2.13b, alongside the ash mass (panel c) calculated from the OE retrievals of AOD and effective radius, assuming an ash density. The maps of ash mass show that in general the ash mass falls with transportation away from

the vent: the plumes become more disperse. The different design, assumptions and limitations of the two techniques mean that it is not expected that the two retrievals will return the same or even similar values. The optimal estimation scheme uses only 105 channels between 680.75 and 1204.5 cm^{-1} ($\sim 8.3 - 14.6 \mu\text{m}$) to improve computational efficiency. This includes 14 channels within the CO_2 absorption band, only one of which is in common with the CO_2 slicing. However, unlike the CO_2 slicing method presented here, the channels used by the optimal estimation scheme have not been optimised for retrieving the height of the ash layer. Ventress et al. (2016) noted that the optimal estimation retrieval could be further refined by altering the channels used. For example, channels with more height information could be selected. Similarly, Ventress et al. (2016) suggested that channels could be selected to minimise the effect of the underlying cloud layers following observations that the OE method can underestimate the cloud top height in cases of multiple cloud layers (Ventress et al., 2016). In the current application of the optimal estimation scheme, where there is not sufficient information about the height of the ash layer within the channels used, the retrieval height output will tend to the a priori height which in this case is around 3.5 km. This is potentially the reason for the persistently lower average height shown in Fig. 2.9 which suggests a strong dependence on the a priori. In future applications of the OE scheme, the CO_2 slicing results could be used as the a priori if the one CO_2 channel that the two retrievals have in common was removed from the optimal estimation scheme. Other differences in the results may arise from the nature of the two techniques. The OE scheme returns values for the ash optical depth, effective radius and height by fitting simulated spectra to those obtained with IASI. Ventress et al. (2016)

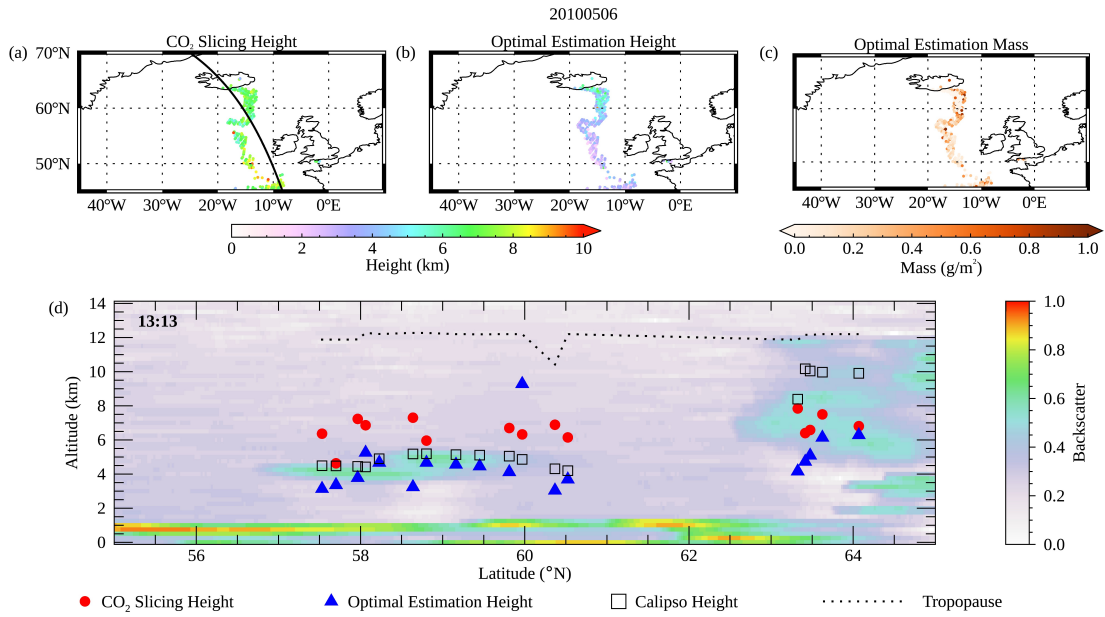


Figure 2.10: (a) CO₂ slicing results for 6th May 2010 during the Eyjafjallajökull eruption. Overplotted on this is the CALIPSO track. (b) The optimal estimation scheme heights. (c) The ash mass obtained with the optimal estimation scheme. (d) The CALIOP backscatter plot, with the CO₂ slicing results and the optimal estimation scheme heights plotted on top. Indicated on the top left-hand side of the plot is the time of the CALIOP overpass. The dashed line indicates the height of the tropopause.

identified that in some cases the retrieval underestimated the altitude of the plume and obtained a high ash optical depth in order to fit the measured spectra when in reality the ash layer might have a lower optical depth and higher altitude.

A comparison has been made against backscatter profiles and cloud altitudes obtained with CALIOP to assess how successfully the two retrievals perform. These backscatter profiles are shown in Fig. 2.10-2.13d. The heights obtained from the OE and CO₂ slicing methods for pixels which fall within 2 hours and 50 km are overplotted, along with the heights obtained with CALIOP and the tropopause height. In these plots it is possible to observe that both methods are capable of capturing the height of the ash layer, but there are clear cases where one technique

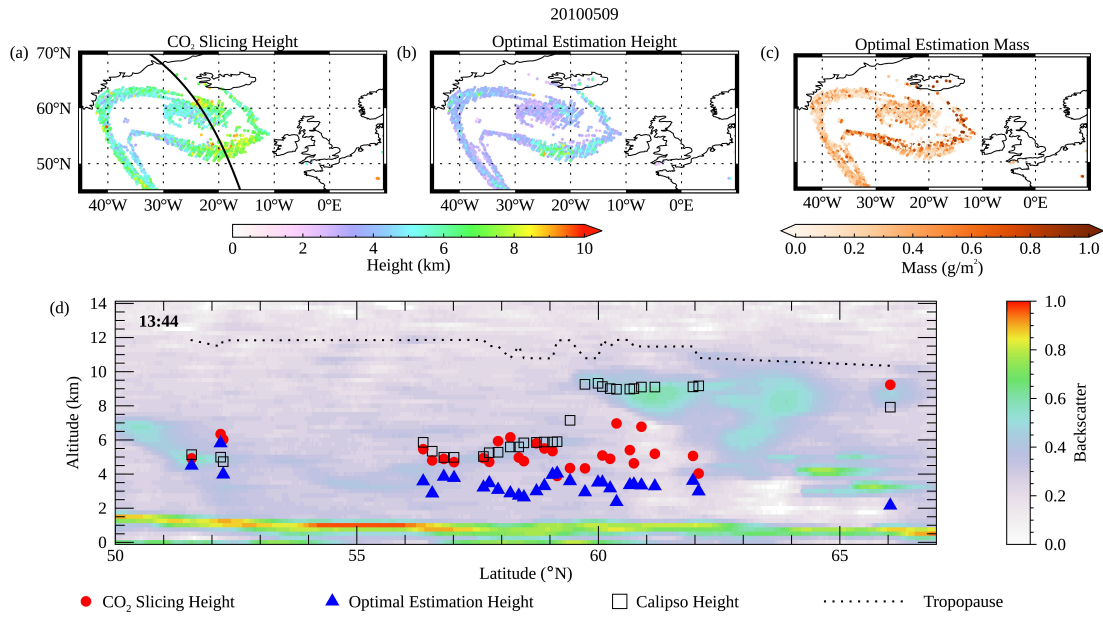


Figure 2.11: Same as figure 2.10 for 9th May 2010 during the Eyjafjallajökull eruption.

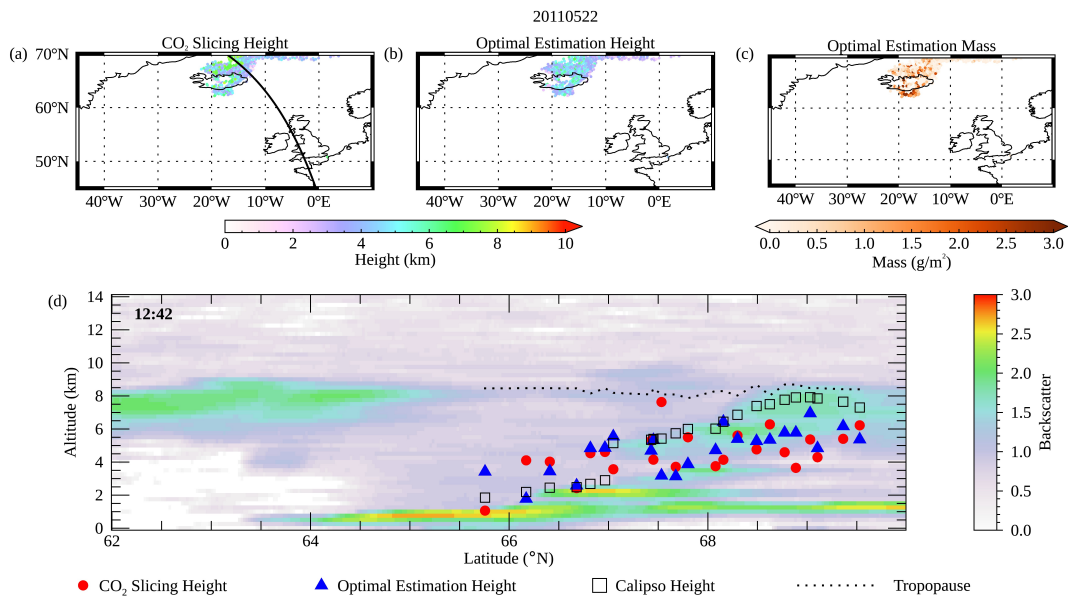


Figure 2.12: Same as figure 2.10 for 22nd May 2011 during the Grimsvötn eruption.

outperforms the other. In Fig. 2.10 which shows the backscatter plot for 6th May 2010, the CO₂ slicing method places the ash cloud between 5 and 7 km between 57.5 and 60.5°N. This is shown to be higher than the CALIOP heights (4-5 km)

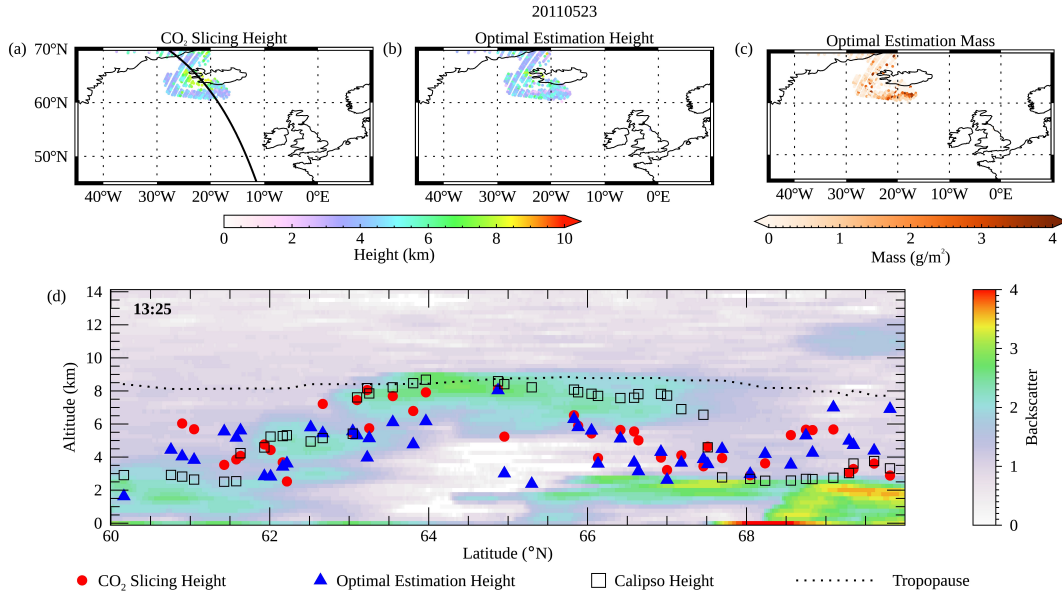


Figure 2.13: Same as figure 2.10 for 23rd May 2011 during the Grímsvötn eruption.

to which the OE results are a closer match. In the same image, between 63 and 64°N the CO₂ slicing results are again higher than the OE results but this time are closer to, but lower than, the heights obtained from CALIOP. The lower heights of both the CO₂ slicing and OE scheme relative to CALIOP might be related to the thick underlying cloud layer. Figure 2.11d shows another example from 9th May 2010. Here between 51 and 53°N the heights obtained with both methods match those obtained with CALIOP. However, further north, between 56 and 60°N, the CO₂ slicing results agree more closely compared to those from the OE scheme. At 66°N, the CO₂ technique obtains a value close to the cloud top height, whereas the OE scheme obtains a value which is more representative of a lower layer of cloud. Figures 2.12 and 2.13 shows examples from the Grímsvötn eruption and in both cases both height retrievals are shown to resemble the shape of the ash cloud layer shown by CALIOP. There are cases where both retrievals underestimate the cloud top height which may be due to multiple layers of cloud.

Table 2.5: Statistics describing the comparison of the CO₂ slicing and optimal estimation scheme against the heights obtained with CALIOP.

CC = correlation coefficient.

	CO ₂ slicing			Optimal Estimation		
Volcano	Number of pixels	CC	RSME (km)	Number of pixels	CC	RSME (km)
Eyjafjallajökull	53	0.2	2.2	67	-0.1	3.2
Grímsvötn	65	0.5	2.1	69	0.3	2.4
All	118	0.4	2.2	136	0.1	2.8

Pearson's correlation values and the root square mean error (RMSE) were computed to compare the two retrieval methods against the heights obtained with CALIOP. These are shown in table 2.5 and scatter plots comparing the retrieved values are shown in Fig. 2.8c and d. The Pearson correlation values are greater for the CO₂ slicing than for the OE scheme, while the RMSE values are lower: 2.2 and 2.1 km for the Eyjafjallajökull and Grímsvötn eruptions respectively for the CO₂ slicing technique, compared to 3.2 and 2.4 km obtained for the OE method. This implies an improved height retrieval from the CO₂ slicing method.

Although comparisons against LiDAR backscatter profiles are a common way of validating retrievals of ash and aqueous cloud height, these comparisons can be limited. CALIOP and IASI measure different things. The first measures backscattering while the latter measures thermal emission. Measurements are made with significantly different horizontal spatial resolutions (335 m compared to 12 km for CALIOP and IASI respectively) and in different locations (a maximum difference of 50 km). Clouds can also vary significantly in very short spaces of time. Although only pixels with a difference of 2 hours have been considered in

this comparison, this is still sufficient time for changes in the cloud's position both vertically and horizontally. These may account for some of the differences seen between the CALIOP profiles and the results obtained with the CO₂ slicing and the OE scheme. The cloud heights obtained from the CALIOP profile are not always a perfect representation of the cloud top height which may also contribute to the differences observed. Although these limitations exist, comparisons against LiDAR instruments are still one of the best methods for validating cloud heights and in this case demonstrate that the CO₂ slicing technique has potential as a tool for obtaining the cloud top height of volcanic ash.

2.6 Conclusions

The CO₂ slicing technique is an established method, used for decades, for retrieving the cloud top height of aqueous cloud. Although it has previously been acknowledged that it can be applied to volcanic ash, it is not commonly used for this purpose, and it has only been applied to MODIS. In this study, the technique was adapted for IASI using simulated ash data to select the most appropriate channels and then demonstrate the technique's capability. When applied to the simulated data, the technique was shown to perform well in five out of six atmospheres. However, an increased failure rate was seen above and close to the tropopause and close to the surface. This was also true of ash with lower optical depths and effective radius. Similar observations have been made by previous CO₂ slicing studies. In this application, three quality control criteria have been applied which successfully remove the majority of cases where there are large differences between the true

and retrieved pressures. When applied to ash scenes from the Eyjafjallajökull and Grímsvötn eruptions, the CO₂ slicing results compared well against the CALIOP backscatter profiles. It was also demonstrated that the CO₂ slicing method obtained heights which more closely matched CALIOP than the optimal estimation scheme used for comparison.

This is the first application of the CO₂ slicing technique to obtain the height of volcanic ash from IASI spectra, and the results are very encouraging. One advantage of this algorithm is that it can be run fairly quickly (taking several seconds per pixel) and so it could be applied to get a first approximation of the height, which could then be used to help assist hazard mitigation. It can also then be used as an input parameter into models of ash cloud propagation or as an a priori in other retrieval schemes. There is also potential for the further development of this technique in the future. Previous applications to cloud have created synthetic channels (multiple channels averaged together) which could be used to further improve the algorithm and its sensitivity to lower-level clouds (Someya et al., 2016). It would also be possible to explore other options for selecting channels or obtaining the final cloud height. The channel selection in this study was based on simulated data in six different atmospheres; another avenue to explore would be the selection of atmospheric specific channel pairs. Further work would also help appreciate the strengths and limitations of this technique and therefore where its use is most appropriate.

3

Exploring the Utility of IASI for Monitoring Volcanic SO₂ Emissions

Abstract: Satellite remote sensing is a valuable method for detecting and quantifying sulphur dioxide (SO₂) emissions at volcanoes. The use of ultra-violet satellite instruments for monitoring purposes has been assessed in numerous studies, but there are advantages to using infrared measurements, including that they can operate at night and during high-latitude winters. This study focuses on the Infrared Atmospheric Sounding Interferometer (IASI). Retrievals developed for this instrument have been shown to be successful when applied to large eruptions, but little has been done to explore their potential for detecting and quantifying emissions from smaller and lower altitude emissions or for the assessment of ongoing activity. Here, a ‘fast’ linear retrieval has been applied across the globe to detect volcanic sources of SO₂. The results are dominated by emissions from explosive eruptions, but signals are also evident from weak eruptions, passive degassing, and anthropogenic activity. Ecuador and Kamchatka were selected for further study

with a more processing intensive iterative retrieval which can quantify the SO_2 amount. At Tungurahua in Ecuador, good agreement was seen between IASI, the Ozone Monitoring Instrument (OMI) and ground-based flux data, demonstrating that the retrieval is capable of capturing relative changes in activity. Similarly, good agreement was found between IASI and OMI in Kamchatka. In this high-latitude region, OMI is unable to operate for three or four months in each year. It is therefore suggested that IASI could be used alongside other instruments for evaluating changes in volcanic activity.

3.1 Introduction

Geochemical observations provide insight into the magmatic, volcanic and hydrothermal processes at volcanoes and consequently, play a fundamental role in understanding and monitoring their behaviour (Symonds et al., 1994; Scaillet et al., 1998; Edmonds, 2008; Oppenheimer et al., 2014). Sulphur dioxide (SO_2) typically comprises only 5% of the total gas emission but as the atmospheric background abundance of the gas is low, and because SO_2 has a distinct spectral signature in both the ultraviolet and infrared regions of the electromagnetic spectrum, the gas has been widely studied (Oppenheimer, 2010; Oppenheimer et al., 2011). Ground-based UV instruments, such as the COSPEC (Moffat and Millán, 1971; Malinconico, 1979; Stoiber et al., 1983; Casadevall et al., 1983), and then the smaller mini-DOAS (Galle et al., 2003; McGonigle et al., 2002) and Flyspec (Horton et al., 2006; Elias et al., 2006) instruments, have enabled numerous field campaigns and facilitated the installation of automated SO_2 monitoring networks at several volcanoes (e.g. Edmonds et al., 2003; Galle et al., 2003; McGonigle et al., 2004; Galle et al.,

2010). However, such field campaigns and instrument networks are expensive and logistically challenging, and so many volcanoes in developing countries and in remote regions have little or no ground-based SO₂ monitoring, and where ground-based measurements are available these are often limited to daytime monitoring and cannot track plumes across large geographic areas.

Satellite technology offers a cost effective solution to some of the limitations of ground-based monitoring, and advances over the past few decades mean that it is now possible to monitor many aspects of volcanic behaviour from space, including the detection and retrieval of SO₂ emissions from volcanoes across the globe. Volcanic SO₂ was first observed with the Total Ozone Mapping Spectrometer (TOMS) following the eruption of El Chichón in 1982 (Krueger, 1983; Krueger et al., 2008). Since then numerous satellite based sensors have been used to detect and track SO₂ emissions including the Moderate Resolution Imaging Spectroradiometer (MODIS) (e.g. Watson et al., 2004; Novak et al., 2008; Corradini et al., 2009, 2010); the Advanced Spaceborne Thermal Emission and Reflection Radiometer (ASTER) (e.g. Urai, 2004; Pugnaghi et al., 2006; Campion et al., 2010); the Atmospheric Infrared Sounder (AIRS) (e.g. Carn et al., 2005; Prata and Bernardo, 2007; Carn and Prata, 2010); the Ozone Monitoring Instrument (OMI) (e.g. Carn et al., 2008, 2013; McCormick et al., 2013; Theys et al., 2013, 2015; Carn et al., 2016, 2017); the Spinning Enhanced Visible and Infrared Imager (SEVIRI) (e.g. Prata and Kerkmann, 2007; Prata et al., 2007; Corradini et al., 2009); the Infrared Atmospheric Sounding Interferometer (IASI) (e.g. Clarisse et al., 2008; Walker et al., 2011, 2012; Carboni et al., 2012; Clarisse et al., 2012; Carboni et al., 2016); the Global Ozone Monitoring Experiment (GOME-1 and GOME-2) (e.g. Eisinger and Burrows, 1998; Rix et al.,

2009); and Ozone Mapping and Profiler Suite (OMPS) (e.g. Carn et al., 2015). The higher spatial and spectral resolutions of newer instruments mean it is now possible to detect weaker sources of SO₂, such as smaller eruptive events, non-eruptive volcanic degassing and anthropogenic emissions (e.g. Fioletov et al., 2015, 2016; Carn, 2016; Koukouli et al., 2016). Subsequently measurements of volcanic SO₂ made by satellite instruments have been used in conjunction with ground-based observations to interpret volcanic activity (e.g. Rix et al., 2009; Surono et al., 2012; McCormick et al., 2013).

Within the infrared there are three SO₂ absorption features, ν_1 , ν_3 and $\nu_1 + \nu_3$ (centred at 8.7, 7.3 and 4.0 μm respectively), which can be used to obtain information on the gas (Thomas and Watson, 2010). Of these the $\nu_1 + \nu_3$ band is the weakest feature and so it is only used when large quantities of SO₂ cause saturation of the other channels (Karagulian et al., 2010). It is also affected by reflected solar radiation and so this must be accounted for in retrieval techniques (Karagulian et al., 2010). The ν_3 band has been widely used to retrieve SO₂ properties (e.g. Prata et al., 2003; Carn et al., 2005; Prata and Bernardo, 2007). It is the strongest feature; but it is collocated with strong water vapour absorption, which reduces its sensitivity to emissions in the lower part of the troposphere if there are high levels of water vapour. In contrast, the ν_1 feature is situated within an atmospheric window making it the most appropriate method for monitoring emissions into the lower troposphere (Realmuto et al., 1994, 1997; Realmuto, 2000), although it can in turn be affected by volcanic ash and sulphate aerosol (Thomas and Watson, 2010).

The Infrared Atmospheric Sounding Interferometer (IASI) is on-board two of EUMETSAT's meteorological satellites, MetOp A and B, launched in 2006 and

2012 respectively. These advanced Fourier transform spectrometers are coupled with an infrared imager (Blumstein et al., 2004). The two satellites occupy the same orbit with fifty minutes between them, and both achieve near global coverage every 12 hours. Each scan has a swath width of 2200 km comprised of circular pixels with a diameter of 12 km at nadir (Clerbaux et al., 2009). One of IASI's main strengths is that it measures across the 645 to 2760 cm^{-1} (3.62 to 15.5 μm) spectral range with a high spectral resolution of 0.5 cm^{-1} (Blumstein et al., 2004; EUMETSAT, 2017), meaning it is possible to better resolve spectral features. This range incorporates the three previously mentioned SO₂ absorption features, and a number of techniques have been developed to exploit these (e.g. Clarisse et al., 2008; Carboni et al., 2012; Walker et al., 2012; Clarisse et al., 2012). These retrievals have been successfully applied to a number of different eruptions, summarised in table 3.1, however, most of these studies are applications to large explosive eruptions which emit substantial quantities of SO₂ into the atmosphere: the majority of the eruptions listed in table 3.1 have a Volcanic Explosivity Index (VEI) of 3 or above. In contrast, very little has been done to explore the potential of this instrument for monitoring weaker emissions, such as those from smaller explosive eruptions and non-eruptive passive degassing. In this study, a linear retrieval (Walker et al., 2011, 2012) has been used to detect volcanic emissions across the globe, following which an iterative retrieval (Carboni et al., 2012, 2016) has been applied to quantify mass loading of SO₂ in Ecuador and Kamchatka, the aim of this being to demonstrate, for the first time, that there is some utility for using these retrievals to capture long-term changes in volcanic activity.

3.2 Linear Retrieval

3.2.1 The Algorithm

The ‘fast’ linear retrieval developed by Walker et al. (2011, 2012) works by separating the signal of the target species (SO_2) from that of the spectral background. To do this, a covariance matrix is formed from an ensemble of SO_2 free pixels which represent variability in the spectra due to the parameters which are not being retrieved. The spectra of pixels containing SO_2 deviate from this background so allowing them to be quickly distinguished. The speed of this technique (which takes a few seconds to process an entire orbit) facilitates its use for scanning large datasets in near real time; for example, for hazard assessments or for the identification of sites for further study. But by using the full spectra in either the ν_1 or ν_3 absorption bands (in this study the ν_3 was used), it has been shown to be more sensitive to the presence of SO_2 than techniques developed for IASI which only use a small selection of channels (Walker et al., 2011, 2012). The detection limit of this technique ranges from 0.3 DU at altitudes of 14 to 18 km, to 17.0 DU close to the surface (0-2 km), or 1.3 DU at between 4 to 6 km, more similar to the height of volcanic plumes from smaller or non eruptive activity (Walker et al., 2012).

The output of the linear retrieval is an ‘effective’ SO_2 column amount under the assumption of a standard atmospheric profile and that the SO_2 profile that has a uniform distribution between 0 and 20 km. It is used here as a tool to flag volcanic emissions, following which the Carboni et al. (2012) iterative retrieval can be used to fully quantify the amount of gas. As with previous studies using this technique (Walker et al., 2011, 2012), the covariance matrix used is formed from pixels over

the North Atlantic and Europe in May 2009: this was originally created for the Eyjafjallajökull eruption in Iceland but has been shown to perform well globally. This can produce systematic errors in areas with notably different climatologies. Future research may wish to consider the creation of new covariance matrices, both local and global, and different seasons, to investigate the impact this has on the results

3.2.2 Linear Retrieval Results

To enhance the SO₂ signal, and particularly to emphasise smaller emissions, the linear retrieval output has been gridded to a 0.125° latitude by 0.125° longitude grid, and averaged for each year studied. This includes both the morning and evening overpasses and does not filter for cloud. The results are shown in figure 3.1. Alongside this, monthly average results are displayed in the animation in appendix B (SM1) and are referred to by their frame number. These plots provide a snapshot of activity within the represented time frame; a function of numerous factors such as the quantity of SO₂ emitted, the rate of SO₂ decay and transportation, and the atmospheric state at the time of the instrument overpass.

3.2.2.1 Volcanic Emissions Across the Globe

The linear retrieval yearly averages, shown in figure 3.1, are largely dominated by emissions from major eruptions during each year, most notably Kasatochi, Sarychev Peak and Nabro in 2008, 2009 and 2011 respectively. Most of the SO₂ emissions previously explored with IASI (listed in table 3.1) can be identified within the yearly averages and all can be identified in the monthly averages shown in SM1.

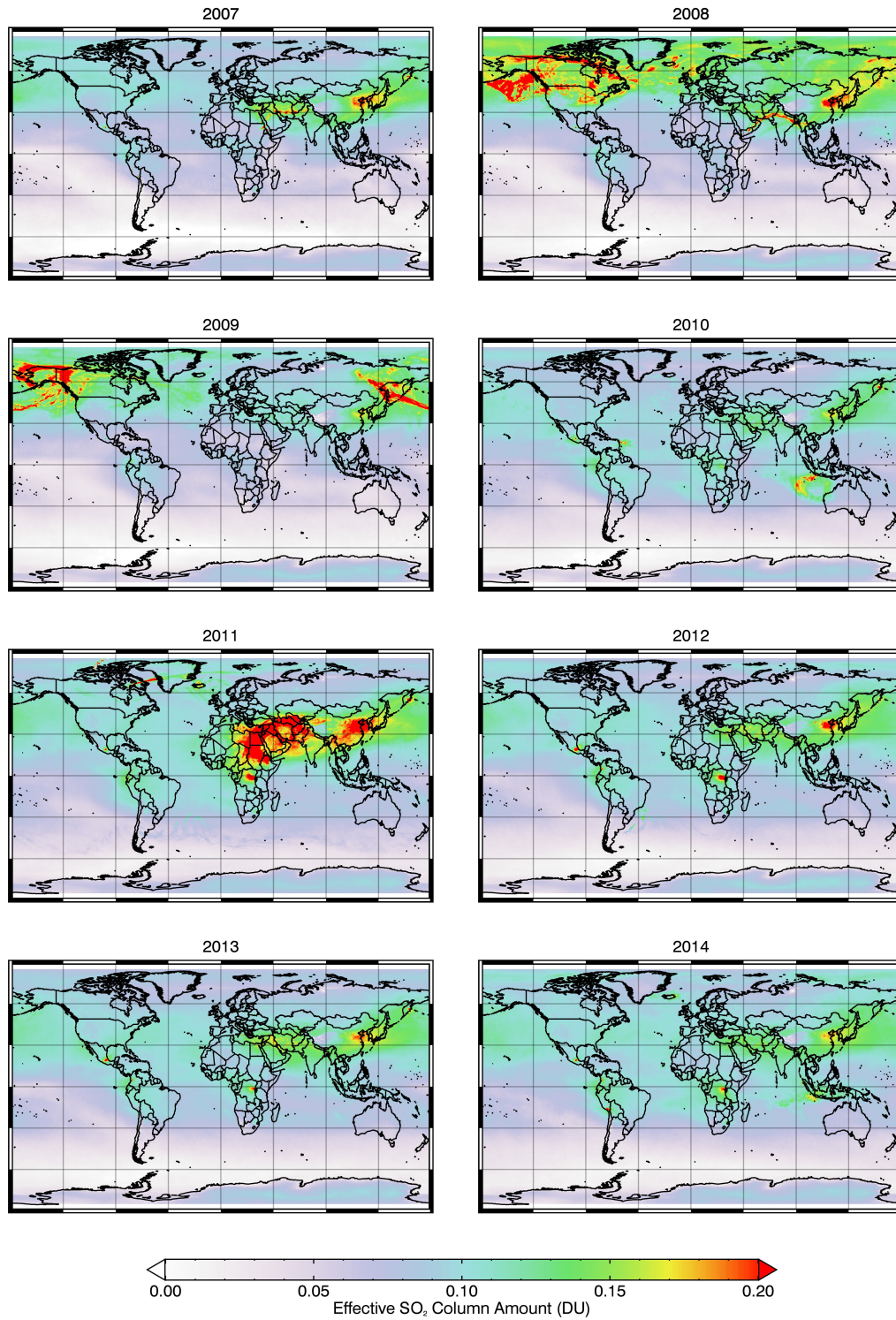


Figure 3.1

Figure 3.1: Global averages of the linear retrieval ‘effective’ SO₂ column amounts for the years 2007 to 2014. Emissions from large eruptions can be identified in each year, along with emissions from persistently degassing volcanoes and emissions from anthropogenic sources. Slightly elevated values over Antarctica are attributed to the extreme in climate here with respect to the covariance matrix applied. Low levels of SO₂ are also apparent over the ocean. In some cases, this might be related to volcanic or anthropogenic emissions. For example, higher values over the Pacific Ocean east of China may be due to drifting pollution. In some cases, however, this maybe is an artefact of the retrieval. Figure 3.2 shows the location of the volcanoes discussed in this chapter.

Smaller signals can also be identified in the global yearly and monthly averages. For example, elevated signals can be regularly identified at Popocatépetl which is one of Mexico’s most active volcanoes (Grutter et al., 2008; Delgado Granados and Cardenas Gonzalez, 2013). Other examples of plumes from effusive activity are Fernandina in the Galapagos in April 2009 (frame 3.4) and at Pico do Fogo in Cape Verde in November 2014 (frame 8.11). Emissions from low level activity or passive degassing, can also be commonly identified across the Central and South American volcanic arcs, in Kamchatka and in Indonesia, the Philippines, Papua New Guinea and Vanuatu. These, and other, lower level emissions can be seen more clearly in regional plots, and Central and South America and Kamchatka are explored in the following section.

3.2.2.2 Regional Volcanic Emissions

Central and South America, and Kamchatka (Eastern Russia), are two volcanic arcs where emissions are frequently identified with the linear retrieval. Expanded views over these regions are presented in figure 3.3. These offer more detail on the activity occurring within these regions. In this figure, (a) and (c) are yearly

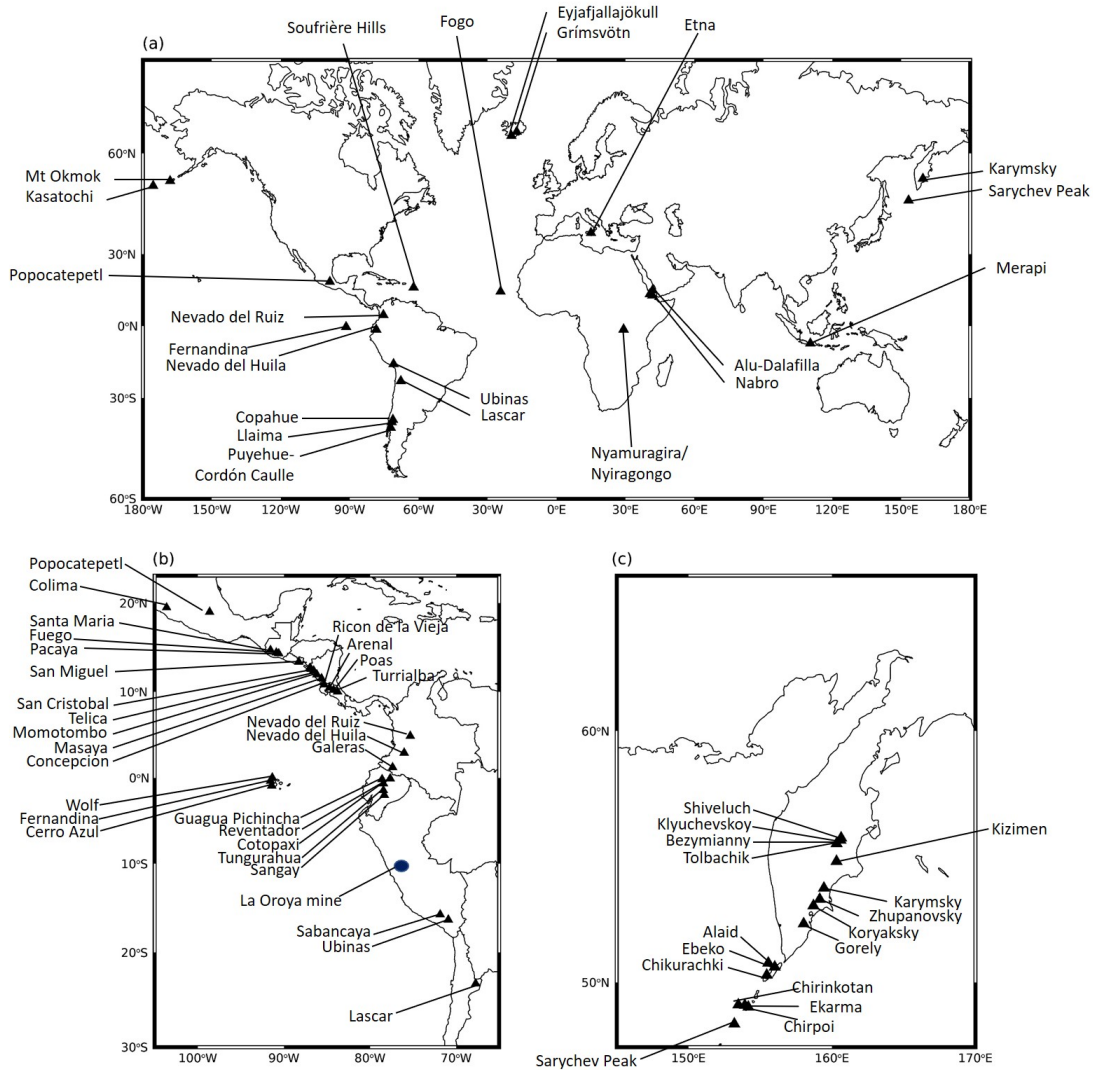


Figure 3.2: Maps showing the position of volcanoes discussed in this chapter. (a) Global map showing the location of some of the volcanoes mentioned. (b) Volcanoes in Central and South America which have been active since 2007. (c) Volcanoes in Kamchatka which have been active since 2007.

averages computed for the regions, and (b) and (d) show monthly averages for each region, displayed with a colour bar that ranges from one standard deviation below the mean to three standard deviations above it, computed separately for each region and month.

Figure 3.3a and b shows the expanded view over Central and South America for 2008. In both the yearly and monthly averages, low SO_2 column amounts

can commonly be seen off the west coast of Colombia, Ecuador and Peru and sometimes over the landmass as well. Some of this might be from low levels of SO₂ but in many cases this is likely to be due to parameters not fully represented within the covariance matrix. However, despite this elevated levels of volcanic SO₂ can be easily identified. As noted in the previous section, Popocatépetl is the strongest and most persistent source in the region and can be clearly identified in each of the monthly averages shown in figure 3.3b. From April 2008, emissions can be easily seen at Nevado del Huila in Colombia, which was active throughout 2008 (GVP, 2012*a*). Signals are also commonly seen at Tungurahua in Ecuador (e.g. January-May, December 2008). Alongside this, elevated levels of SO₂ can be identified in Northern Ecuador in November 2008 which is likely to be from eruptions at Reventador (GVP, 2009*b*). Reventador entered a period of explosive activity in July 2008 which continued to October 2009. During this episode there was an increase in the number of explosions which occasionally generated ash clouds that rose to 6 km, which was accompanied by dome building and lava flows (Naranjo et al., 2016). Further emissions can be seen in Peru and Chile. In the south of Peru this is coincident with the volcano Ubinas which was actively erupting or degassing throughout the year (Rivera et al., 2010). In 2008, there is also commonly a signal over Lascar in Chile, and while there were no GVP reports of volcanic activity at the volcano in this year, the volcano is known to be a persistent passive source of SO₂ (Menard et al., 2014). The use of this retrieval could therefore be valuable for assessing increased levels of volcanic activity. In both Peru and Chile, the source of elevated emissions can be somewhat ambiguous due to numerous copper smelting sites in the region. In Central Peru, where there are no known

Figure 3.3: Regional linear retrieval output. (a) 2008 yearly average effective SO₂ column amounts over Central and South America. (b) Monthly average effective SO₂ column amounts over Central and South America in 2008. These are displayed with a colour bar that ranges between one standard deviation below the mean to three standard deviations above it. These values have been computed for the region and each month separately. This helps emphasise SO₂ sources in the region. (c) 2010 yearly average effective SO₂ column amounts at Kamchatka. Note that there are relatively high background values across the region. This is potentially linked to pollution from China which is blown north-east with prevailing winds. (d) as (b) for Kamchatka in 2010.

active volcanoes, a strong and persistent plume of SO₂ can be identified in each month in 2008. This is consistent with the location of the La Oroya multi-metal smelter which was studied with OMI in Carn et al. (2007), who demonstrated that it emitted roughly 0.07 ± 0.03 Tg of SO₂ annually in 2004 and 2005.

The Kamchatka region in Eastern Russia is displayed in figure 3.3c and d for 2010. The volcanoes in this region are remote and have little ground-based monitoring, consequently satellite remote sensing has been widely employed here to monitor the risk to aviation (Dean and Dehn, 2015). In this region, high background levels in the yearly average may be associated with pollution transported north-east from China. Volcanic SO₂ emissions are seen across the arc, but the high number of active volcanoes in close proximity makes it difficult to accurately discern the origin without information from other sources. In the monthly averages, it is possible to see emissions in the northern part of the Kamchatka region, originating from Klyuchevskoy, which was actively erupting throughout 2010 (GVP, 2010*a*, 2013*b*). Shiveluch was also active during this period (GVP, 2010*c,d*) and may be a contributor to the plumes seen. Elevated signals can also be observed towards the south of the Kamchatka peninsula (for example, in March and December) and

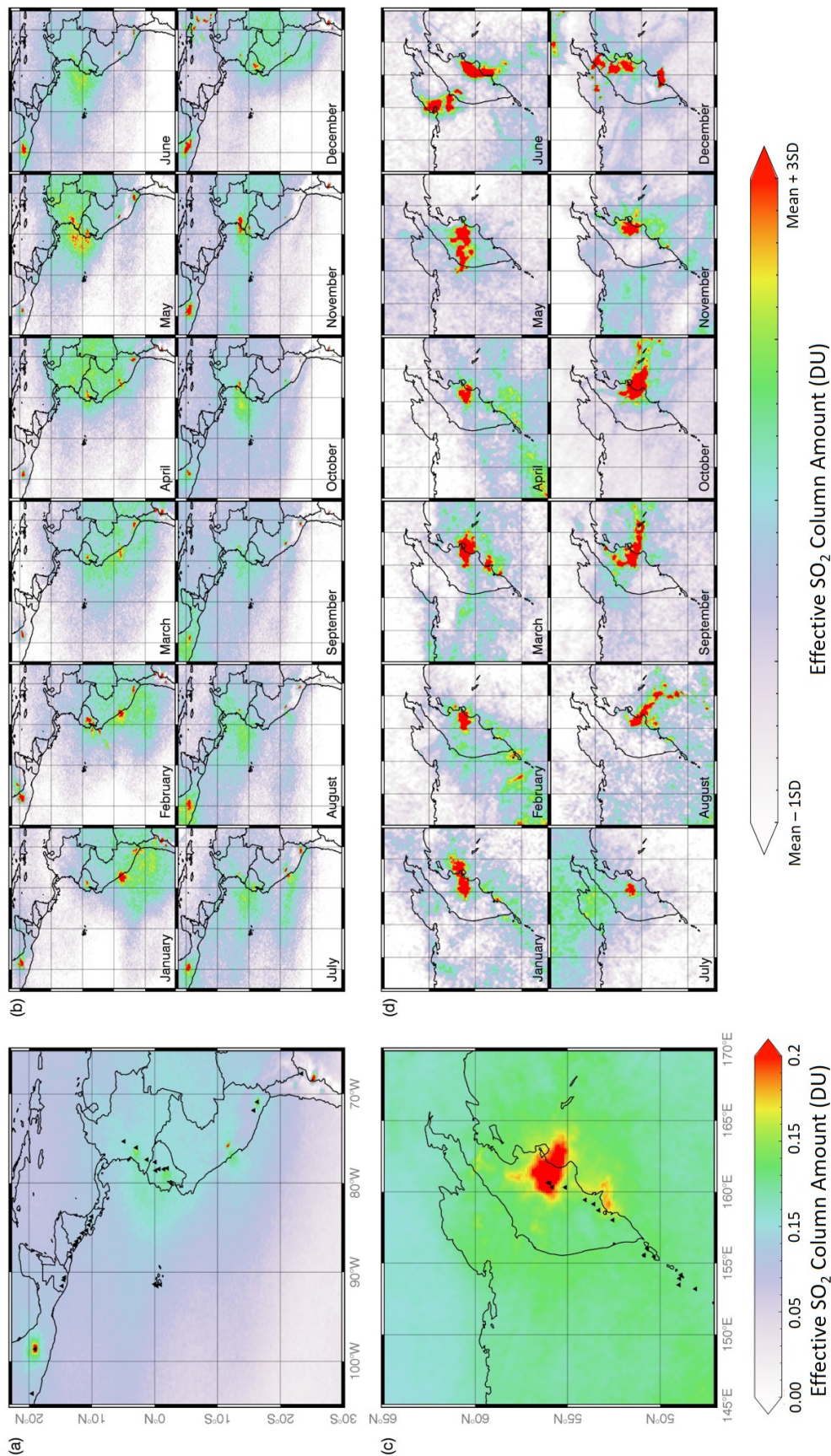


Figure 3.3:

can be attributed to activity at Karymsky volcano, which experienced vulcanian and strombolian eruptions throughout 2010 (Neal et al., 2014).

3.2.2.3 Anthropogenic Emissions

As already noted it is possible to detect SO₂ emissions from anthropogenic sources with IASI. Numerous studies have been conducted looking at these emissions with OMI (e.g. Carn et al., 2007; Fioletov et al., 2013, 2016; Krotkov et al., 2016), but to date, there have been relatively few studies undertaken with IASI (Bauduin et al., 2014, 2016). In figure 3.1 and SM1, a number of different anthropogenic sources can be identified. The easiest to identify is pollution from China which has a prominent signal across the north eastern coast of the country. Despite air quality policies, China remains the largest emitter of SO₂; responsible for roughly 30% of global emissions in 2010 with the majority of this resulting from coal burning (Klimont et al., 2013). Two elevated peaks can also be observed in Iran (clearest in 2012 and 2013, or in the monthly averages- frames 2.3, 4.11 and 5.4) which are in the proximity of the Isfahan heavy oil fired power plant and Sarcheshmeh copper complex also identified in Fioletov et al. (2013, 2016). Another spike of SO₂ is present close to Johannesburg in South Africa (e.g. frames 1.9, 4.9, 5.9 and 8.7), the result of a cluster of power plants burning fossil fuels (Fioletov et al., 2016). Given the relatively sparse availability of literature on using IASI to detect anthropogenic emissions, these areas could be selected for further study in the future.

3.3 Iterative Retrieval

Emissions were commonly identified with the linear retrieval in Ecuador and Kamchatka and these regions were selected for further study with the iterative retrieval to quantify SO₂ emissions from volcanic activity at the two arcs. Additional reasons for the selection of these two regions are given below.

3.3.1 The Algorithm

The spectra measured by IASI are a function of a number of atmospheric constituents such as meteorological cloud, H₂O, CO₂, CO, O₃, N₂O, CH₄ and SO₂, each with different concentrations and vertical atmospheric distributions, alongside additional variations caused by temperature, atmospheric pressure and instrument viewing geometries. The problem of retrieving SO₂ can be simplified by representing the spectral variability generated by other parameters within a covariance matrix, allowing SO₂ to be independently retrieved (Carboni et al., 2012). In this study, the global covariance matrix from Carboni et al. (2016) has been used. The Carboni et al. (2012) iterative retrieval uses European Centre for Medium-Range Weather Forecasts (ECMWF) data (including temperature and water vapour vertical profiles) within the fast radiative transfer model RTTOV with the addition of SO₂ coefficients, to forward model a clear (i.e. free of meteorological cloud) IASI atmospheric spectra. A range of SO₂ plumes are simulated for the established clear sky atmosphere, for the entire ν_1 and ν_3 bands. The modelled spectra which best matches the observed spectra, determined with a cost function, is taken as the SO₂ column amount and altitude solution, together with the surface temperature (Carboni et al., 2012). In

this case, where the iterative retrieval is being applied to pixels containing low concentrations of SO_2 from small explosive eruptions or degassing, there is not enough information within the IASI spectra to obtain both the SO_2 altitude and column amount, and therefore the plume altitude has been set at 500 mb (~ 5600 m), based on the height of volcanoes in the regions studied, table 3.2, as is done for many other satellite instruments (e.g. Carn et al., 2013). Note that the true plume height will vary between different volcanoes, different styles of activity and during eruptions as the cloud disperses and if the true altitude of the plume is lower than the assumed value, then the SO_2 column amount will be underestimated, and vice versa.

One of the advantages of this technique is that it generates a comprehensive error matrix which represents the discrepancy between the modelled and observed spectra in scenes free of SO_2 , thereby incorporating forward model and forward model parameter errors, and providing quality control and comprehensive error estimates of the retrieved state. The detection limit of the iterative retrieval is strongly dependent on the altitude of the SO_2 plume and the temperature contrast between the surface and the atmospheric temperature at the plume layer. It can therefore range from around 10.5 DU at the surface to 0.1 DU at the tropopause. Typically, at 3 km the detection limit is around 1 DU. Given this, greater errors are usually associated with small, low altitude plumes. Error analysis conducted by Carboni et al. (2012) has also demonstrated that thick meteorological cloud or ash above the plume can affect the signal obtained by the instrument and therefore cause the SO_2 column amount to be underestimated. For example, an ash layer with an optical depth of 2 would cause the SO_2 amount to be underestimated by around 50% and an ash layer with an optical depth of 5 would mask the SO_2

entirely. Meteorological cloud has a similar effect. In both cases, this would be distinguishable in the cost function which would increase. The iterative retrieval is slower than the linear retrieval taking a few tens of seconds per pixel to produce an output making it important to restrict the area to which it is applied. This means that this retrieval is more suited for analysing plumes of SO₂ and areas of interest identified with the linear retrieval.

3.3.2 Ecuador and South Colombia

3.3.2.1 Background

There are a number of active volcanoes in both Ecuador and Colombia and these are monitored by the Instituto Geofísico of Escuela Politécnica Nacional (IGEPN) and the Servicio Geológico Colombiano (SGC) respectively. At Tungurahua, in Ecuador, this includes measurements of gas emissions made by a DOAS network (Hidalgo et al., 2015). A summary of ground-based SO₂ flux measurements for volcanoes in the region is reported in table 3.2. The availability of this ground-based dataset and previous satellite studies of volcanic emissions of SO₂ in the region (Carn et al., 2008; McCormick et al., 2014) make this an appropriate region to begin assessing the strengths and limitations of the Carboni et al. (2012) iterative retrieval. In this study, the iterative retrieval has been applied between June 2007 and December 2013, over a region which includes five active volcanoes: Reventador, Guagua Pichincha, Tungurahua and Sangay in Ecuador, and Galeras in Southern Colombia.

Table 3.2: Published ground-based estimates of SO₂ emissions at active volcanoes in Ecuador, South Colombia and Kamchatka

Volcano	Coordinates	Altitude (m)	Average SO ₂ Flux (tday ⁻¹)	Method Used	Years	References
<i>Ecuador/Colombia</i>						
Galeras	1.22°N 77.37°W	4276	~200	COSPEC	1992 - 1993	Fischer et al. (1994)
			~500	DOAS	2012 - 2013	GVP (2013a)
Reventador	0.08°S 77.66°W	3562	1000	DOAS	2009	GVP (2009c)
Guagua Pichincha	0.17°S 78.60°W	4784	170 (max)	COSPEC	1998	GVP (1999)
Tungurahua	1.47°S 78.44°W	5023	1458	COSPEC/ DOAS	1999 - 2008	Arellano et al. (2008)
			~948	DOAS	2008 - 2013	Hidalgo et al. (2015)
Sangay ^a	2.01°S 78.34°W	5300	-	-	-	
<i>Kamchatka</i>						
Shiveluch	56.65°N 161.36 °E	3307	> 500	Visual Estimate ^b	-	Taran (2009)
Klyuchevskoy	56.06°N 160.64 °E	4750	>300	Visual Estimate ^b	-	Taran (2009)
Bezymianny	55.97°N 160.6°E	2882	400	FLYSPEC	2007	Clark et al. (2007)

continued ...

Volcano	Coordinates	Altitude (m)	Average SO ₂ Flux (tday ⁻¹)	Method Used	Years	References
Mutnovsky	52.45°N 158.2°E	2322	480	DOAS	2012 - 2013	Melnikov et al. (2014)

^a No reports on SO₂ flux available at Sangay

^b Based on the frequency and size of the eruptive plume compared to volcanoes elsewhere in the world where SO₂ flux is recorded

^c Estimated by measuring temperatures of escaping gas and using thermodynamic mass balances

3.3.2.2 Negative Bias Characteristics and Correction

Following the application of the iterative retrieval over Ecuador, persistent negative values of up to -0.4 DU were observed (for example, figure 3.4c). This has not been noted in previous applications of this algorithm and while some, near zero, background fluctuations might be expected due to instrument noise, an offset of this magnitude implies other factors are influencing the result. As seen in figure 3.4, the bulk of the negative values are situated to the North of Ecuador, consistent with mountainous terrain to the north of the country.

One of the possible explanations for this is the covariance matrix used within the retrieval. As in Carboni et al. (2012, 2016) a covariance matrix consisting of more than 5 million SO₂ free pixels from across the globe, and from four seasons in 2009, was used. This global matrix could under-represent the variability in the environment, climate and surface conditions in this region; for example, surface emissivity in the region varies significantly from tropical rainforest to rocky mountainous terrain. In an attempt to improve this, local emissivity values from the Cooperative Institute for Meteorological Satellite Studies (CIMSS) Infrared Emissivity Database (IREMIS) have been incorporated into the RTTOV model, leading to a reduction of the bias by 20-30%. However a significant offset remains.

Ideally, new localised covariance matrices would have been formed; however, this process is not straightforward. A large number of pixels are required to represent background variability in the covariance matrix however, these must be free of SO₂. In both regions studied there are continuously degassing volcanoes and frequent eruptions, making it difficult to select appropriate pixels. This is further complicated

in Kamchatka (discussed in more detail in section 3.3.3.2) where SO_2 has been carried into the region from other eruptions (e.g. Kasatochi and Sarychev Peak, SM1- frames 2.8, 3.6) and from pollution in China.

Previous studies have corrected for negative values by adjusting the output using an area free from SO_2 (Carn et al., 2008; McCormick et al., 2014). In this case, the spatial variability of the negative values, coupled with the close proximity of volcanoes emitting varying degrees of SO_2 (making it difficult to determine which boxes are truly SO_2 free) makes this method inappropriate. Instead, the following steps were implemented to remove the majority of the bias: (1) data was gridded into 0.125° by 0.125° grid boxes and averaged for each month (incorporating both morning and evening overpasses). (2) For each grid box the average and standard deviation of the SO_2 column amount were computed for the periods before and after May 2010, during which there was a calibration change to the instrument which

Figure 3.4: Bias correction over Ecuador and Kamchatka. (a) Distribution of the uncorrected (blue) and corrected (red) monthly average SO_2 column amounts for a single grid box in the Ecuador region. Solid line shows the mean and the dashed line shows one standard deviation from the mean. The lowest value, for each grid box, which fell within one standard deviation of the mean was used to correct the average column amount. (b) The correction applied over the Ecuador region for the June 2007 to May 2010 time period. (c) Uncorrected monthly average SO_2 column values over Ecuador in January 2010. (d) Corrected values for January 2010. (e) Distribution of SO_2 column amounts in the northern Kamchatka region for September 2010. The uncorrected values are shown in blue. The dashed black line is the average of the uncorrected grid boxes after pixels which contain SO_2 have been removed. This is used to correct the bias. The distribution of corrected values is shown in red. (f) Uncorrected monthly average SO_2 column amount for September 2010. (g) Uncorrected monthly average SO_2 column amount for September 2010 excluding pixels that contained SO_2 . (h) Corrected values for September 2010.

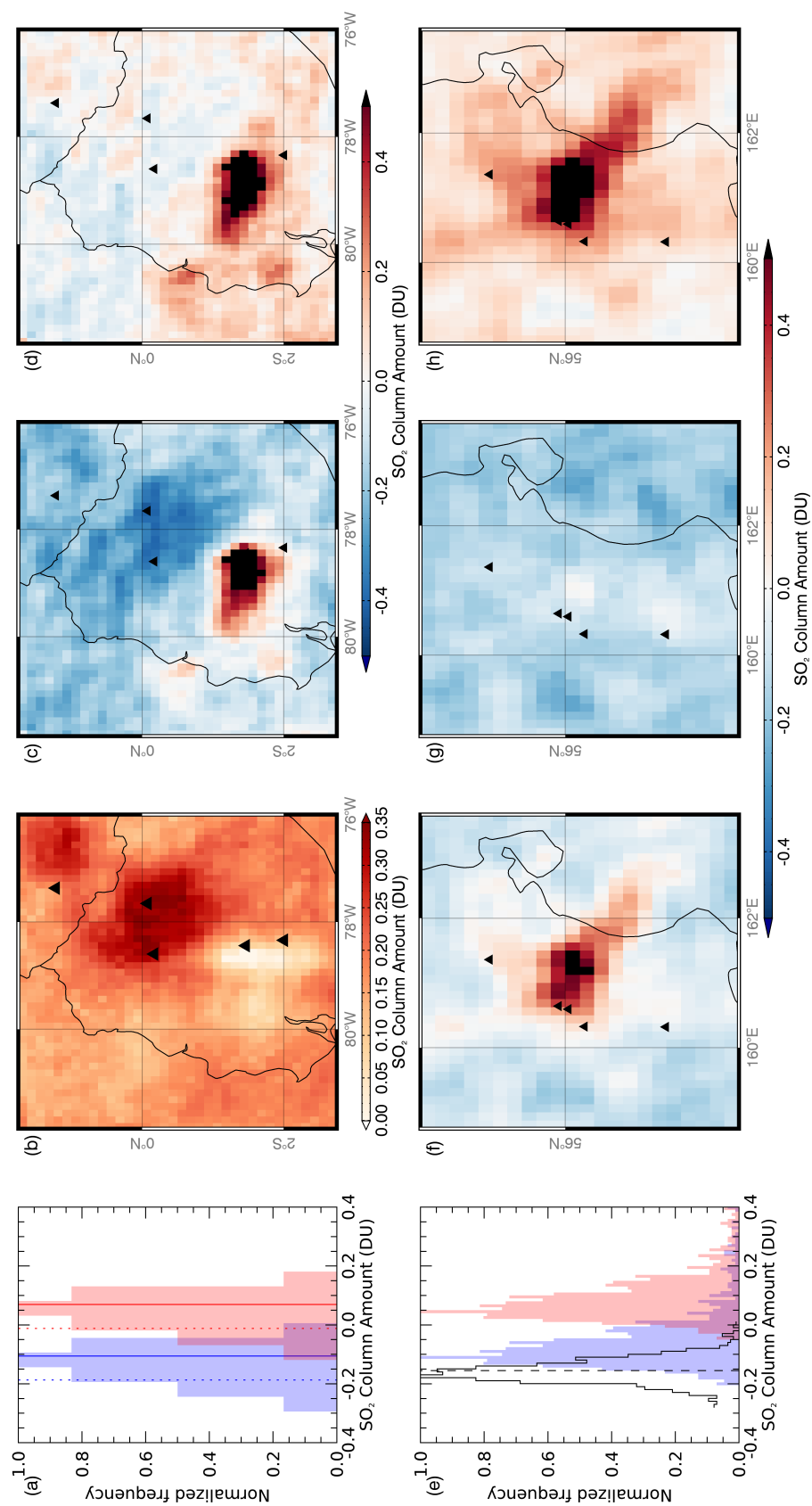


Figure 3.4:

caused a jump in the magnitude of the bias. (3) The lowest value, for each grid box, which fell within one standard deviation of the mean was used to correct the total column amount. Figure 3.4b shows how this correction value, for the pre-May 2010 period, changes across the region. This removes the majority of the bias as can be seen in figures 3.4c and d which show the average SO₂ column amount in January 2010 before and after the correction has been applied. However, it is possible that the correction may be underestimated in some cases. For example, as seen in figure 3.4b, the correction applied varies significantly across the region and west of Tungurahua and Sangay, the correction is close to zero. It is possible that these areas are simply bias free, however, it is also possible that this is a consequence of higher levels of SO₂ in the region meaning that no negative values were produced, and so the bias correction may be underestimated. Nonetheless, this technique removes the majority of the bias from the region allowing interpretation of changing quantities of SO₂.

3.3.2.3 Arc-scale Observations

The iterative retrieval was run over Ecuador and the south of Colombia from June 2007 to December 2013. Maps of the monthly average SO₂ column amounts are presented in figures B.1-B.7 in appendix B. These show that throughout the time period explored, Tungurahua dominates emissions across the arc. Emissions however, are also observed from Reventador and Galeras.

A small selection of the iterative retrieval monthly averages are presented in figure 3.5 alongside the monthly average output from a DOAS retrieval developed for OMI by Theys et al. (2015). Note that this procedure assumes an altitude of 7 km, more similar to the height of plumes from explosive activity in the region.

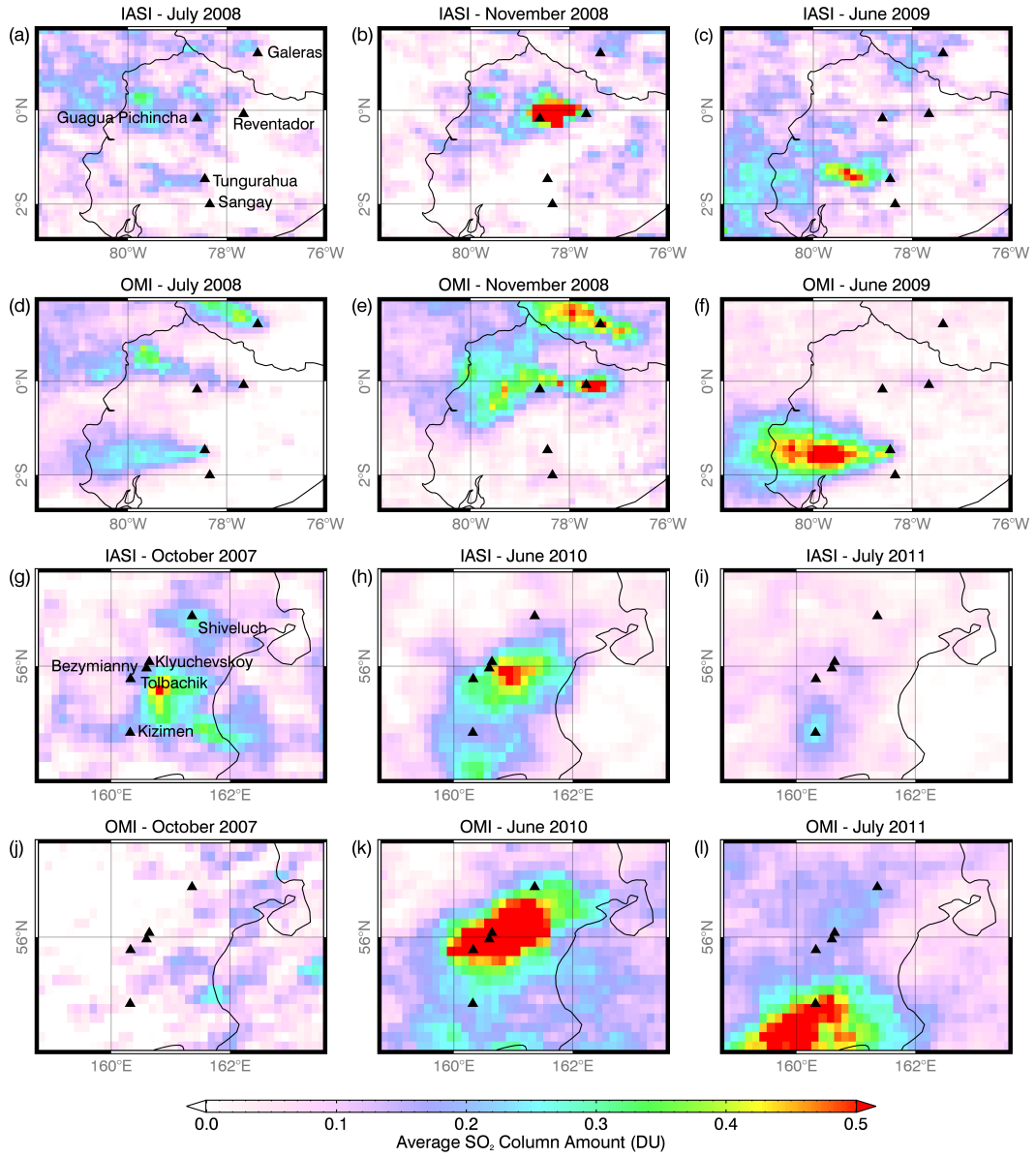


Figure 3.5: Maps of monthly average SO₂ column amounts from the IASI and OMI retrievals over Ecuador and Kamchatka

This could result in a difference of 15% compared to the retrieval if it had been run using the same plume height assumed in the IASI retrieval (roughly 5.6 km).

Figure 3.5 shows that plumes identified with the OMI DOAS procedure are larger and more defined than those seen with IASI. For example, three substantial plumes can be seen in figure 3.5d, but in the IASI monthly averages the plumes

are not so clearly defined. Similarly, in November 2008, plumes can be seen at Reventador and Galeras in figure 3.5e but only at Reventador with IASI. Also, a much larger plume is seen at Tungurahua in figure 3.5f than in figure 3.5c. There are a number of possible explanations for these results. Firstly, the altitude assumed in the iterative retrieval is based on typical emission heights at Tungurahua, the second highest and the most active volcano in the region. By comparison Galeras and Reventador are over 700 m lower and so it follows that the plume altitude would also be lower. Therefore, potentially this may lead to the underestimation of the SO₂ column amounts. Ultra-violet measurements by comparison, are less sensitive to the assumed altitude. As IASI is an infrared instrument it is also limited in the lower part of the troposphere by the temperature contrast between the Earth's surface and the air above it so lowering the sensitivity of the instrument (Deeter et al., 2007; Bauduin et al., 2014). The iterative retrieval also has a higher detection limit than the OMI retrieval in the lower parts of the troposphere, at roughly 1 DU at 3 km. In contrast, the detection limit for the OMI retrieval is much lower at around 0.5-0.6 DU in the boundary layer and 0.25-0.3 DU at the assumed retrieval height. Additional variations may also arise from differences in SO₂ and in atmospheric conditions in the different overpasses. While in general clearer stronger plumes can be seen with OMI, in June 2009, a faint plume can be seen at Galeras with the IASI technique, but this is non existent in the OMI output. This corresponds to a period of elevated activity including increased gas and ash emissions (GVP, 2009a).

As mentioned in the previous paragraph, infrared retrievals are limited in the lower part of the troposphere due to the requirements that there is a temperature contrast between the surface and the layer above it, and when using the ν_3 band

due to water vapour. This increases the detection limit closer to the surface. The influence of the height of the volcano and subsequently, the height of the plume on the frequency of detection with the Walker et al. (2011, 2012) linear retrieval is explored further in chapter 4. However, it is important to note here, that the height of volcanoes in Ecuador aids the retrieval and that it may not be as well suited for examining smaller emissions from lower altitude volcanoes in other regions.

3.3.2.4 Activity at Tungurahua

As shown in figures B.1-B.7, Tungurahua is the most active volcano in the studied region, and regular monitoring at the volcano means that activity here is well constrained. Monitoring efforts include gas measurements made by a ground-based DOAS network set up in 2007. A synthesis of these results was produced by Hidalgo et al. (2015) and using these measurements, activity at the volcano between 2007 and 2013 was divided into four periods, summarised in table 3.3. Average total masses of SO₂ at Tungurahua were calculated from the monthly average SO₂ column amounts, shown in figures B.1-B.7 in appendix B, using the area shown in the map in figure 3.6a. The results, figure 3.6a, demonstrate that there is generally good agreement here between the OMI and IASI results, and that these match periods of activity at the volcano (shaded in grey). One notable difference in the timeseries for the two instruments is in April 2011. During this month there was explosive activity with plumes exceeding the assumed height of 5.6 km which may have led to overestimation of the IASI average total SO₂ mass. Average total SO₂ masses obtained with the IASI iterative retrieval and OMI DOAS procedure have a high correlation coefficient of 0.91 for June 2007 to May 2010. Following

this there was a change to IASI's calibration, resulting in a generally higher total average SO_2 mass relative to OMI, which rarely returns to zero during periods of quiescence. Despite this, the correlation coefficient remains relatively high at 0.87 for the remainder of the study period, implying that both instruments are faithfully recording prevailing activity. It is important to note that the average total amount of SO_2 reported in figure 3.6a at Tungurahua is computed for a small region shown in the map in figure 3.6a, which is where SO_2 is typically seen with the IASI iterative retrieval, and the same area is used for the OMI data for comparison. However, as seen in figure 3.5, the plumes as seen with OMI are much larger and so these values are not a true representation of the absolute magnitude of SO_2 . Using an area more reflective of the plumes seen with OMI sees a drop in the correlation coefficient to 0.48 and 0.76 before and after May 2010 respectively. A change in the gradient of the regression line describing the relationship between the two is also noted, with a fall from 1.08 to 0.8 in the first period, and an increase from 0.61 to 0.75 in the second. Nevertheless, it is clear that both instruments are capable of detecting relative changes in volcanic activity and that these match the periods of activity as noted in Hidalgo et al. (2015).

The average total mass values have also been compared against the ground-based SO_2 flux measurements made by the DOAS network, shown in figure 3.6a. It is important to emphasise that these flux measurements are distinct from those made by the satellite instruments. The former is a flux (tonnes per day) obtained by continuous measurements over a small footprint throughout daylight hours and averaged for each month, while the second is a measure of the total SO_2 in tons across a wider region obtained through daily (OMI) or twice daily (IASI)

Table 3.3: Summary of activity at Tungurahua between 2007 and 2013. Modified from Hidalgo et al. (2015). The SO₂ flux is given for each time period and phase and also shows the variability in the data- standard deviation from the averages

Period	Phase	Start	End	Average Height Above Crater (km)	Number of Explosions	Average Daily SO ₂ Flux (tonnes)	Activity Description
1	I	24/02/2007	04/08/2008	2.7	1763	674 ± 667	Near continuous activity with paroxysm in February 2008, followed by a drop in activity
2	II III IV V VI VII	16/12/2008 28/03/2009 30/12/2009 26/05/2010 22/11/2010 20/04/2011	01/03/2009 03/08/2010 03/01/2011 26/05/2011	2.6 2.3 2.5 2.9 2.7 3.5	377 212 521 1351 111 64	1675 ± 1229 934 ± 694 1807 ± 1394 1466 ± 1358 1169 ± 1176 1661 ± 1505	Six short episodes of strombolian activity
3	-	27/11/2011	09/04/2012	3.3	194	826 ± 1289	Near continuous activity with sharp spike at the onset
4	VIII IX X XI	14/12/2012 01/03/2013 27/04/2013 14/07/2013	10/01/2013 17/03/2013 16/05/2013 05/08/2013	2.8 2.2 2.0 3.8	453 118 151 64	1241 ± 1051 1186 ± 787 1872 ± 1637 1430 ± 929	Four phases of strombolian activity

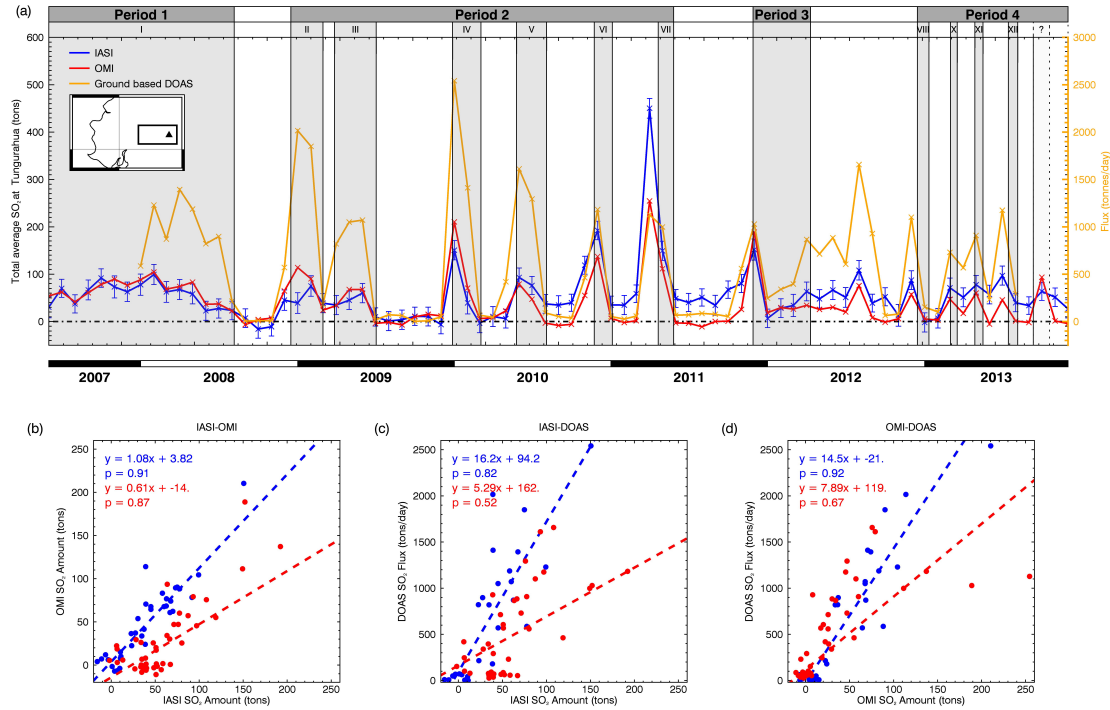


Figure 3.6: (a) Timeseries of total monthly average of SO₂ around Tungurahua from IASI and OMI for June 2007 to December 2013, and the monthly average SO₂ flux recorded with a ground-based DOAS network and published in Hidalgo et al. (2015). Average total masses of SO₂ at Tungurahua were calculated from the monthly SO₂ column amounts using the box area shown in the map. Shaded in grey are episodes of activity noted in the Hidalgo et al. (2015) paper, described in table 3.3. The error bars on the IASI average total SO₂ masses incorporate the instrumental error, and errors associated with the forward model, meteorological data and non-perfect representation of gas absorption and errors due to the presence of a cloud. In this plot it is possible to identify an increase in the IASI baseline SO₂ amount in May 2010. This is following a change to the IASI instrument. A notable difference between the IASI and OMI values can be seen in April 2011: here the IASI average total SO₂ is significantly higher. This is likely to be due to an incorrect assumption of the plume height. (b) Comparison of IASI and OMI total monthly averages of SO₂ amounts at Tungurahua. Shown in red are the equation of the line describing the relationship and correlation coefficients for the period before May 2010 and in blue the same for the period after May 2010. (c) Same as (b) for IASI and ground-based flux measurements averaged for each month. (d) Same as (b) for OMI and ground-based DOAS measurements

measurements averaged for each month. The flux measure is also a function of wind speed. While these measurements are not directly equivalent, they should in principle be correlated, and as shown in figure 3.6a this is generally the case. High correlation coefficients of 0.92 and 0.67 were computed for the OMI-DOAS instrument combination for the periods January 2008 to May 2010, and May 2010 to August 2013. Fairly high values, 0.82 and 0.52, were also recorded for the IASI-DOAS combination. If a steady state of emissions and an SO₂ lifetime of one day were assumed at Tungurahua it would be expected that the average total SO₂ mass would be equivalent to the monthly average flux (McCormick et al., 2014). However, this is not the case with an order of magnitude difference between the average total SO₂ mass obtained with the satellite retrievals and the average flux. In this case, however, the area used to calculate the total monthly average SO₂ mass at Tungurahua does not always represent the full extent of the plume and this may be one reason why the total SO₂ mass is lower than the emission rate. Given this, a closer match between the monthly average total SO₂ mass obtained with OMI and IASI and the average flux from the ground-based DOAS, is obtained if a wider area around Tungurahua is considered. This is more reflective of the larger plumes seen with OMI. Additional variations may arise from high plume transport speeds which carry the gas away from the vent and the area being used to calculate the SO₂ mass, and SO₂ depletion and dissipation away from the source leading to it being no longer detectable by the satellite instruments. It is also possible, that in Ecuador's tropical climate, the lifetime of SO₂ in the region is less than one day as is discussed in McCormick et al. (2014). Nonetheless, looking beyond the absolute values, these results suggest that the IASI (and OMI) retrievals are able to convincingly detect

relative changes in volcanic activity. The published flux data cease in August 2013, but following this there is an additional rise and fall in October 2013, implying an additional episode of strombolian activity in period 4. This is supported by GVP reports which note an increase in activity with elevated levels of seismicity, increased strombolian explosions and ash emissions beginning on the 6th October 2013 (GVP, 2013c) and continuing throughout the month with a maximum SO₂ flux of 725 tons per day in the last week of October (GVP, 2013d). Activity remained high in November, primarily characterised by ash clouds, some rising a few kilometers above the vent (GVP, 2013e), before activity subsided mid way through the month.

3.3.3 Kamchatka

3.3.3.1 Background

There are numerous, remote volcanoes on the Kamchatka peninsula and nearby Kuril Islands, and these pose a significant hazard to the high volume of aircraft which pass over or near to the region (Dean and Dehn, 2015). Their remote nature means that monitoring efforts are highly dependent on satellite remote sensing. Despite significant degassing across the arc, Kamchatka has previously been poorly represented in global volcanic SO₂ budgets (Andres and Kasgnoc, 1998; Halmer et al., 2002) and field campaigns such as Arellano et al. (2012) and Melnikov et al. (2014) (results summarised in table 3.2) only represent a snapshot of ongoing activity. Using UV satellite sensors, the latest global volcanic SO₂ budget better represents volcanic SO₂ emissions from Kamchatka (Carn et al., 2017). However, these instruments are limited by the loss of sunlight hours in winter (McCormick et al., 2013), meaning there is a potential advantage to using infrared sensors like

IASI. Here the IASI iterative retrieval is run over the northern Kamchatka region for a seven year period during which activity was reported at five volcanoes: Shiveluch, Klyuchevskoy, Bezymianny, Tolbachik and Kizimen.

3.3.3.2 Bias Characteristics and Correction

As with Ecuador, negative SO₂ column amounts can be observed over the northern Kamchatka region. Here, there is no strong geographic trend but there is significant seasonal variation, with the bias being more extensive during the summer and autumn (May-September). This seasonality suggests surface components such as surface temperature, moisture changes or snow, or atmospheric parameters which all vary throughout the year, are not sufficiently represented within the method's covariance matrix. Due to this seasonal variation, the correction method used over Ecuador, is inappropriate. The correction is also complicated by near-continuous volcanic activity in the Kamchatka region, and both volcanic (e.g. from the Kasatochi and Sarychev Peak eruptions) and anthropogenic (pollution from China) emissions carried into the region.

Instead each month has been individually corrected with the following steps. (1) The data are again gridded to a 0.125° by 0.125° grid box and the orbits averaged for each month, but this time removing pixels which are flagged as containing SO₂ by the linear retrieval, figure 3.4g. (2) For each individual month, an average SO₂ free column amount is calculated for the northern Kamchatka region and this is used to correct for the bias in that month: shifting the SO₂ free distribution for the month to be centred at 0. An example from September 2010 is shown in the histogram in figure 3.4e: the blue histogram shows before the correction value has

been applied and the red shows the distribution following the correction. A before and after of the average SO₂ column amounts is shown in figure 3.4f and h.

3.3.3.3 Arc-scale Observations

As with Ecuador, the iterative retrieval output over Kamchatka was gridded to a 0.125° latitude by 0.125° longitude grid and averaged for each month (again incorporating both the morning and evening overpasses). These results are shown in figures B.8-B.14 in appendix B. During the period examined emissions could be identified at each of the five volcanoes in the region, however, in some cases the signal was faint and so it is only with existing knowledge of volcanic activity in the region that these could be identified. In other cases, it was also difficult to discern which volcano the plumes originated from, without information from alternative sources, such as the GVP reports and other literature, due to the close proximity of volcanoes in the region.

The results for three months, October 2007, June 2010 and July 2011, are presented in figure 3.5g-l alongside the results from the OMI retrieval. In each of these, volcanic plumes can be identified. However, as before, the plumes observed with OMI are significantly larger than those seen with IASI. This difference is reflected in figure 3.7 which shows the average total mass calculated for the northern Kamchatka region for both instruments. Note that, the mass has been calculated for the entire region, rather than for individual volcanoes due to the frequency with which plumes span multiple volcanic centres. The discrepancy between the results for the two instruments could be related to the different detection limits of the two instruments. The IASI iterative retrieval may also underestimate if the gas

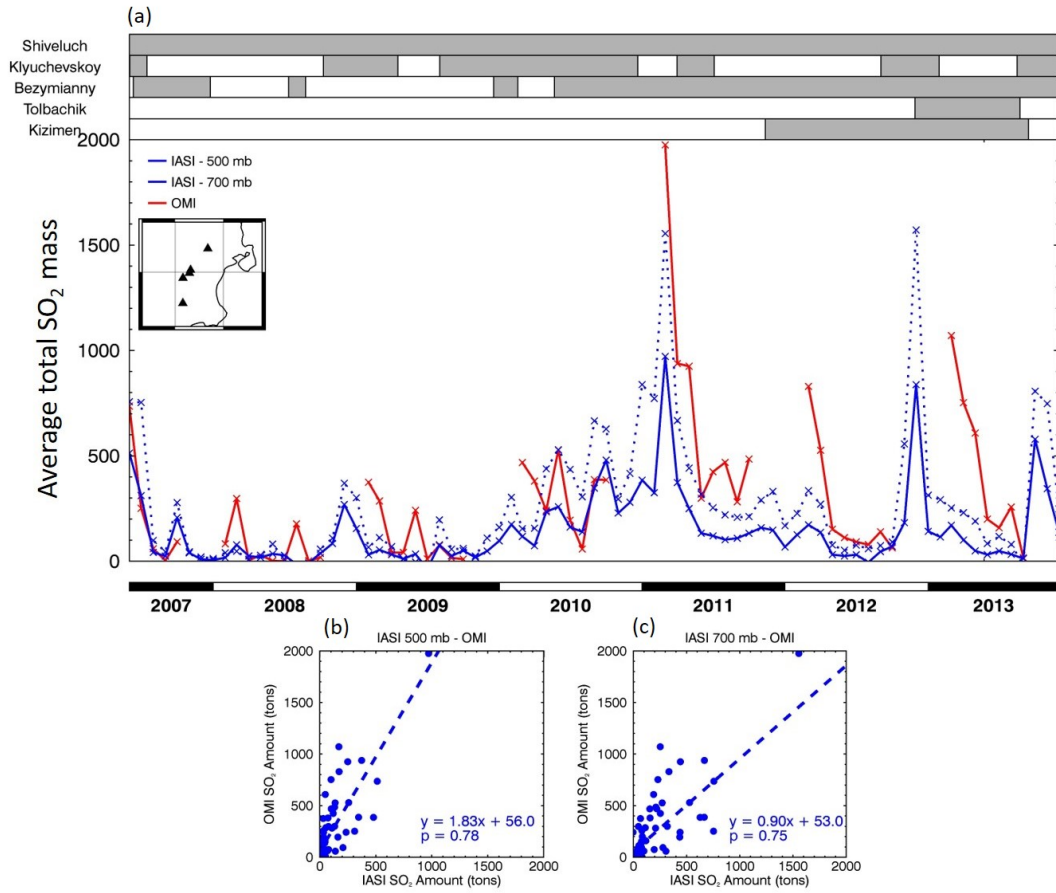


Figure 3.7: (a) Timeseries of average total SO₂ in the northern Kamchatka region calculated for IASI (assuming plume heights of 500 and 700 mb) and OMI. Eruptive periods as defined by the GVP are displayed at the top. (b) Scatter plot comparing the average total SO₂ mass obtained with the IASI and OMI retrievals, with the IASI retrieval assuming a plume height of 500 mb. (c) Same as (b) with the IASI retrieval assuming a plume altitude of 700 mb

is beneath a thick ash or meteorological cloud, or if the true height of the plume is less than the altitude assumed in the retrieval. For example, in this part of Kamchatka, the volcano heights vary between less than 3000 m to closer to 5000 m, see table 3.2. Therefore, the altitude assumption of 500 mb (~ 5600) may be incorrect. To demonstrate the impact of this, the retrieval was also run using a fixed altitude of 700 mb (roughly 2.5 km), which led to increased SO₂ average total mass values as seen in figure 3.7. It is also possible for the OMI DOAS retrieval

to overestimate the SO_2 mass, if for example, there was a highly reflective surface, such as snow, ice or cloud, beneath the SO_2 plume.

Despite the discrepancy between the IASI and OMI results, reasonably high correlation coefficients of 0.78 and 0.75 were obtained for IASI-OMI combination with the 500 and 700 mb plume height assumption for the IASI retrieval respectively, and while the average SO_2 mass magnitudes may not be the same, looking at figure 3.7 it is apparent that both instruments are observing the same peaks in activity. Results are also available from the iterative retrieval during the winter months when there is no sunlight. During November and December 2012 for example, emissions can be seen from Tolbachik following a dual fissure eruption (GVP, 2012*d*). During these months, OMI, and other UV sensors, are unable to obtain data due to the lack of sunlight. It is therefore recommended that IASI should be used to complement existing UV retrievals, particularly during winter months, to better understand ongoing activity.

3.4 Conclusions

Previous applications of retrievals developed for IASI have been to larger eruptions, while few studies exist looking at smaller emissions of SO_2 into the troposphere, such as those from smaller explosive eruptions, non-eruptive volcanic degassing, and emissions from anthropogenic sources. This study has demonstrated that there is some potential for using the infrared sensor IASI for both identifying emissions and for assessing long-term changes in SO_2 in different regions.

The linear retrieval applied here, is a fast method for scanning large datasets for elevated levels of SO₂. The results shown in this paper were largely dominated by emissions from large eruptions such as Kasatochi, Sarychev Peak and Nabro. However, emissions could also be identified from smaller sources, including both ongoing eruptive activity and smaller explosive eruptions. Signals were also identified from anthropogenic activity, such as from coal burning and copper smelting. These results demonstrate that there is potential for using this retrieval for detecting volcanic emissions, which could be done for rapid identification of SO₂ plumes in near real time or to highlight regions for further study. The results presented here are by no means a full catalogue of emissions which are detectable with IASI and future work is encouraged to fully appreciate the strengths and limitations of this method across the globe, to determine how successfully this can be applied to monitor volcanic emissions. The technique could also be further enhanced by forming local covariance matrices which better represent the background variability of a specific region, or through the use of techniques such as plume rotation (as employed by Carn et al. 2017 and explored further in chapter 4) to enhance the result and improve source detection.

Following the identification of SO₂ emissions with the linear retrieval, a slower, but fully quantitative iterative retrieval can be applied to compute the SO₂ column amounts in a selected region. Here, this has been applied over Ecuador and Kamchatka, both regions containing numerous active volcanoes. The quantification of emissions was initially complicated by prominent negative column amounts across both regions which had not been identified in previous applications of the iterative retrieval (applications to larger eruptions), probably linked to poor representation

of background variability in these regions within the covariance matrix used. Two different methods for correcting this bias are presented. The first, is a pixel specific correction suitable in regions where the bias is spatially and temporally consistent, while the second is based on the monthly mean column amount for the region after pixels containing SO_2 have been removed, suitable when there is significant seasonal variability in the results. Following the removal of this bias, it is shown that the iterative retrieval results are able to capture relative changes in volcanic activity. Although the magnitude of the average total SO_2 masses differs between IASI and OMI (possibly related to the different detection limits, the plume altitude assumption and the temperature contrast between the Earth's surface and the lower part of the atmosphere) the trends observed by these and ground-based DOAS measurements at Tungurahua agree well, and matched episodes of activity noted in existing literature. This is also generally true for IASI and OMI in Kamchatka. Here, the IASI instrument is capable of obtaining data in winter and so could be used to complement OMI by filling this winter gap in their record. Further long-term studies of emissions at different volcanoes and at different time intervals would improve understanding of the advantages and disadvantages of this tool.

Retrievals developed for IASI are not commonly applied to volcanic emissions into the troposphere or to assess long-term changes in volcanic activity. The results presented here have demonstrated that the linear retrieval can identify multiple source types across the globe, and that quantification of SO_2 amounts in individual regions with the iterative retrieval can show relative changes in volcanic activity. Numerous other signals, volcanic and anthropogenic, were identified in the linear retrieval results and this could inspire similar long-term studies with the iterative

retrieval. This study opens a number of promising avenues for further work and such work would be valuable for both understanding volcanic activity and for appreciating the strengths and limitations of the IASI retrievals.

4

A systematic global analysis of a decade of IASI SO₂ measurements

Abstract: Measurements of volcanic plumes of sulphur dioxide (SO₂) can give valuable insights into volcanic behaviour and are important for understanding the impacts of volcanism on the atmosphere. There are considerable advantages to studying them with satellite instruments. A number of SO₂ retrieval schemes have been developed for the Infrared Atmospheric Sounding Interferometer (IASI) and previous studies have demonstrated their value for studying volcanic plumes. However, the instrument has been underutilised for the study of SO₂ plumes from smaller sources and for the assessment of ongoing emissions. Building on work done by Taylor et al. (2018) this study takes a systematic approach to explore volcanic SO₂ emissions globally with this instrument. It applied a linear SO₂ retrieval over 166 volcanoes from 2007 to 2017. The output was rotated so that the plumes always aligned to the north, thereby isolating the SO₂ signal. The signal was then enhanced by averaging over monthly, annual and multi annual periods. A simple comparison of

the upwind and downwind column amounts indicated when and where the retrieval was able to identify emissions, and a rough magnitude. This approach highlighted where the use of this retrieval was most appropriate. Fewer emissions were seen at lower altitude volcanoes for example. Whereas, emissions were commonly identified at higher altitude volcanoes in Central and South America: here a simple comparison of upwind and downwind values showed changes in activity which matched well with SO₂ flux measurements from the Ozone Monitoring Instrument, thermal alerts and observations made in literature. The advantage of using IASI (or other infrared sensors) during high latitude winters, when UV levels are low, was also highlighted: of the 166 volcanoes studied, 34 are at latitudes where UV retrievals are limited in the winter months. Overall, this study illustrates some of the advantages of using this instrument and retrieval. It has also generated an extensive dataset which could be used to complement other studies of volcanic activity.

4.1 Introduction

Advances in satellite technology over the past few decades mean that it is possible to get a global perspective of volcanic activity (e.g. Biggs et al., 2014; McCormick Kilbride et al., 2016; Carn et al., 2017; Furtney et al., 2018; Ebmeier et al., 2018). This is enabling the study of volcanoes which have little or no continuous ground based monitoring, whether this be due to limited funding to purchase equipment or inaccessibility because of remoteness or political instability (Sparks et al., 2012). This global picture of volcanic activity is particularly important for the study of volcanic plumes. These present a health hazard to local communities (e.g. Hansell and Oppenheimer, 2004) and affect the environment around the volcano

(e.g. Delmelle, 2003). Making measurements of gas emissions helps to understand these impacts and can help interpret some of the processes taking place within the magmatic system (Malinconico, 1979, 1987; Symonds et al., 1994; Scaillet et al., 1998; Sparks, 2003*a*; Edmonds, 2008; Oppenheimer et al., 2014). Volcanic plumes can also stretch considerable distances from their source, subsequently presenting a hazard to aircraft (Bernard and Rose, 1990; Carn et al., 2007) and having wider impacts on the environment and climate (Robock, 2000*b*; Grainger and Highwood, 2003; Mather, 2015). Satellite data offers an opportunity to track these plumes as they are carried across the globe, better estimate the total contribution of volcanic emissions to the atmosphere and establish long-term trends and background activity at different volcanoes worldwide.

Sulphur dioxide (SO₂) is the most common gas species targeted with remote sensing instruments on the ground (e.g. COSPEC, DOAS and Flyspec instruments; Moffat and Millán 1971; Galle et al. 2003; McGonigle et al. 2002; Horton et al. 2006) and with satellite borne instruments (Thomas and Watson, 2010; Carn et al., 2016). This is despite it not being the dominant gas species emitted from volcanoes: generally water vapour (H₂O) and carbon dioxide (CO₂) are emitted in greater quantities (Edmonds, 2008; Oppenheimer et al., 2011). This is because of the low background abundance of SO₂ away from volcanic and anthropogenic sources, and sensitivities to this gas species within the UV and infrared regions of the electromagnetic spectrum (Oppenheimer, 2010; Oppenheimer et al., 2011).

Satellite data has been used to study SO₂ emissions from volcanoes for over 30 years (Carn et al., 2016), with an early example being the eruption of El Chichón in Mexico in 1982 with the Total Ozone Monitoring Instrument (TOMS; Krueger 1983;

Krueger et al. 2008). Since then technology has advanced significantly, and increased spatial and spectral resolutions mean that it is now possible to make measurements of smaller quantities of SO_2 ; for example, from small explosive eruptions, non-eruptive volcanic degassing and anthropogenic sources (e.g. Fioletov et al., 2015, 2016; Koukouli et al., 2016; Carn et al., 2017). These developments mean that it is now possible to use satellite data, alongside ground based instruments, to monitor volcanic activity (e.g. Rix et al., 2009; Surono et al., 2012). Comparisons have been made with other satellite measurements which give indications of volcanic unrest and activity such as deformation using InSAR (e.g. McCormick Kilbride et al., 2016) and thermal anomalies (e.g. MODVOLC and MIROVA, e.g. Flower and Carn 2015). This allows inferences such as whether a volcano can be classified as being in an open or closed system state or if transitions between these two end member states can be observed (Reath et al., 2019).

Measurements of SO_2 have been more commonly made with UV instruments such as the Ozone Monitoring Instrument (OMI) (e.g. Carn et al., 2008, 2013; McCormick et al., 2013; Theys et al., 2013, 2015; Carn et al., 2016, 2017) and more recently, exciting results have been seen with the newer TROPOMI instrument launched in 2017 (e.g. Theys et al., 2019; Quei er et al., 2019). However, there are advantages to using infrared instruments. For example, they can make measurements at night and during high latitude winters when UV levels are low. This means they can fill some of the gaps in the UV record and are a powerful complementary tool. There is also greater sensitivity to the height of the SO_2 within the infrared meaning that this information can be extracted from the satellite data (e.g. Carboni et al., 2012, 2016): an important factor for assessing the hazard presented by these plumes and

their impacts on the environment and climate. These instruments exploit three absorption features within the thermal infrared (Thomas and Watson, 2010). The first of these is the $\nu_1 + \nu_3$ absorption located at 4 μm . This is a weak absorption feature which is not commonly used except where very high levels of SO₂ cause saturation of the other two absorption bands (Karagulian et al., 2010). The ν_3 band, at 7.3 μm , is the strongest of the absorption features and subsequently has been used in many infrared retrievals of SO₂ properties (e.g. Prata et al., 2003; Carn et al., 2005; Prata and Bernardo, 2007; Clarisse et al., 2012). It is colocated with a water vapour absorption feature which reduces its sensitivity in parts of the atmosphere with high levels of water vapour. The final SO₂ absorption feature, the ν_1 band, centred at 8.7 μm , is smaller than the ν_3 but is less affected by water vapour (Realmuto et al., 1994, 1997; Realmuto, 2000) and is sensitive down to the surface, potentially allowing it to be used for lower level emissions such as those from anthropogenic sources. It can be affected by volcanic ash, sulphate aerosol, and the surface temperature and emissivity (Thomas and Watson, 2010; Clarisse et al., 2012). All three bands require there be a temperature contrast between the surface and the temperature at the height of the plume (Clarisse et al., 2012).

The Infrared Atmospheric Sounding Interferometer (IASI) described in further detail in section 4.2.1 has been used to study the plumes from large eruptions (e.g. Clarisse et al., 2008; Haywood et al., 2010; Karagulian et al., 2010; Clarisse et al., 2012; Surono et al., 2012; Clarisse et al., 2014; Cooke et al., 2014; Moxnes et al., 2014*b*; Carboni et al., 2016) and more recently, the instrument has been shown to have the capability for observing emissions from smaller volcanic (Moussallam et al., 2017; Taylor et al., 2018) and anthropogenic (Bauduin et al., 2014; Boynard

et al., 2014; Bauduin et al., 2016) sources. There has been no global systematic study of continuous volcanic emissions with this instrument. With over ten years of IASI data now available, this paper builds on a study by Taylor et al. (2018) to demonstrate the strengths of this instrument for making measurements of SO₂. Over ten years of IASI SO₂ data at volcanoes across the globe are evaluated using an algorithm described in section 4.2.3. This is used to assess where the instrument's use is most appropriate (section 4.3) and to identify changes in volcanic activity over different timescales (sections 4.4 and 4.5).

4.2 Methods

4.2.1 IASI

The IASI instrument is a Fourier transform spectrometer coupled with an infrared imager and is on-board three of EUMETSAT's meteorological satellites, Metop-A, -B and -C, launched in 2006, 2012 and 2018 respectively. Each instrument achieves near global coverage twice a day. The instruments have a swath width of 2,200 km and the instantaneous fields of view consist of four circular pixels each of which is 12 km in diameter (Clerboux et al., 2009). The instruments measure in the infrared between 645 to 2760 cm⁻¹ (3.62 to 15.5 μm) with a spectral resolution of 0.5 cm⁻¹ (Blumstein et al., 2004). This spectral range covers the three SO₂ absorption features mentioned in section 4.1 and so a number of retrievals have been developed for this gas species (e.g. Clarisse et al., 2010b; Walker et al., 2011, 2012; Clarisse et al., 2012; Carboni et al., 2012).

4.2.2 IASI SO₂ linear retrieval

The retrieval used in this study is the ‘fast’ linear retrieval developed by Walker et al. (2011, 2012). This method works by separating the signal of the target species (SO₂) from the spectral background by representing the variability of the spectral background within a covariance matrix which is formed from pixels containing no volcanic plumes of SO₂. Pixels which contain SO₂ deviate from this spectral background allowing them to be distinguished. The technique uses the full spectra within either the ν_1 or ν_3 absorption bands which gives it greater sensitivity to SO₂ than techniques developed for IASI which use just a few channels (Walker et al., 2011, 2012). One of the advantages of this technique is that it is fast, meaning that it can be used to identify plumes of SO₂ in near real time or to identify regions of interest for further study with the quantitative iterative retrieval (Carboni et al., 2012; Taylor et al., 2018). In this application of the linear SO₂ retrieval, the ν_3 band is used and the covariance matrix is formed from pixels over the North Atlantic and Europe in May 2009. The technique uses a standard atmospheric profile and assumes that the SO₂ gas is evenly distributed between 0 and 20 km in height.

4.2.3 The rotation algorithm

To systematically evaluate the performance of the IASI linear retrieval for the detection and monitoring of SO₂ emissions from volcanoes across the globe, the upwind and downwind SO₂ signal averaged over different time periods was compared at each volcano. To do this, the linear retrieval for each IASI orbit has been rotated using wind direction data from the European Centre for Medium-Range Weather

Figure 4.1: Flowchart summarising the method used to rotate the SO₂ linear retrieval output. Further detail on how this is done is outlined in section 4.2.3. Example plots can be seen in figure 4.2.

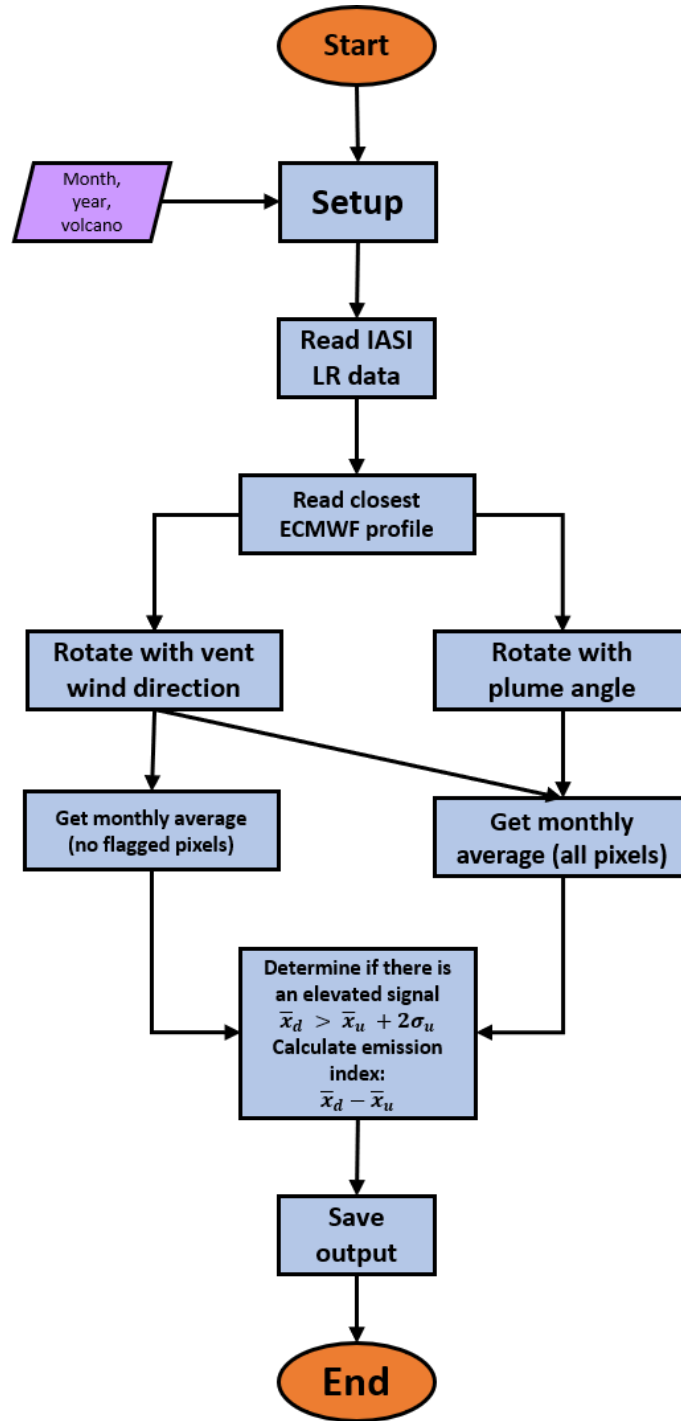
LR = linear retrieval;

The plume angle is the angle between north and the mean latitude and longitude of flagged pixels within 200 km of the source.

\bar{x}_d = mean effective SO₂ column amount (Dobson Units, DU) within the downwind direction

\bar{x}_u = mean effective SO₂ column amount (DU) in the upwind direction

σ_u = standard deviation of the effective SO₂ column amount (DU) in the upwind direction.



Forecasts (ECMWF). Other studies have taken a similar approach to enhance the signal (e.g. Ebmeier et al., 2014; Fioletov et al., 2016; Carn et al., 2017)

Figure 4.1 summarises the algorithm applied to the SO₂ linear retrieval output to systematically assess whether or not an elevated signal is present. To start the

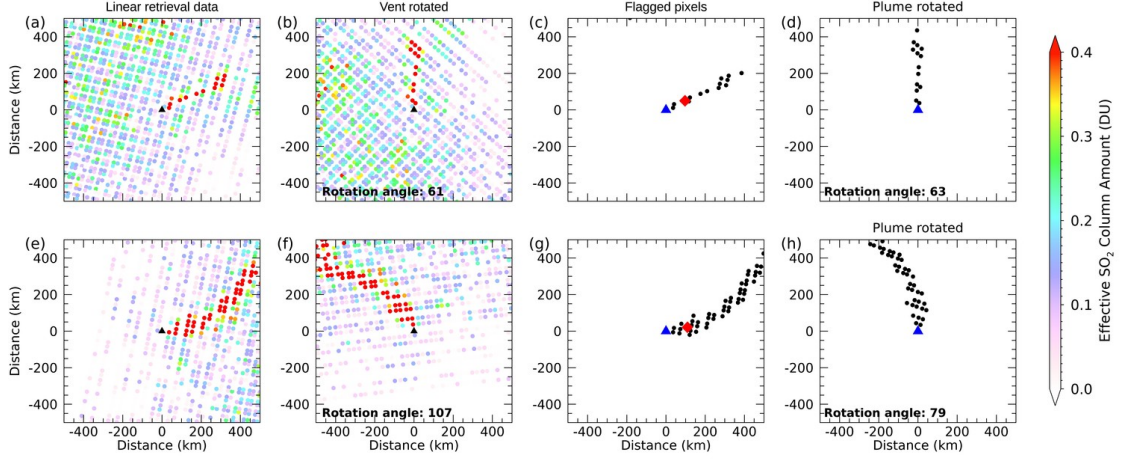


Figure 4.2: Examples of the rotations performed by the rotation algorithm outlined in figure 4.1. (a) IASI linear retrieval output over Popocatépetl for 10th May 2013 1614 UTC. (b) IASI output rotated using the wind direction at the volcano's vent. (c) SO₂ flagged pixels. Marked in red is the average point of flagged pixels within 200 km of the volcano. The angle between north and this point is used to rotate the IASI data giving the results shown in (d). Here the results look very similar to those shown in (b) implying that the assumption that the plume is roughly at the height of the vent is correct. (e) IASI linear retrieval output for Popocatépetl on the 17th April 2013 1530 UTC. (f) IASI output rotated with the vent wind direction. Here the plume does not align to north implying that the assumption that the plume is at the height of the vent is incorrect. (g) SO₂ flagged pixels, showing the average latitude and longitude. (h) Flagged pixels rotated with the plume angle. This produces a better result than using the vent rotation.

linear retrieval output was reduced to a box around the volcano with a width and height of 12 degrees. Following this the closest ECMWF atmospheric profile (in time and space) to the volcano was identified. These profiles had a spatial resolution of 0.75° and are available in 6 hour intervals. Therefore, the maximum difference in time and space from the IASI overpass time is 3 hours and 0.375°. The ECMWF wind profiles include u and v vector components from which the wind speed and wind direction can be computed. Future applications of this approach could consider using radiosonde data. Two types of rotation are then performed (summarised

in table 4.1). (1) **Vent rotation**: the linear retrieval output is rotated with the wind direction at the altitude of the vent of volcano, as shown in figure 4.2a and b. This is most appropriate for non-eruptive degassing and plumes from smaller explosive eruptions which do not rise substantially above the volcano's vent. Where the assumption that the plume is emitted at the vent height does not hold true, the rotation angle may be inappropriate as demonstrated in figure 4.2f. (2) **Plume rotation**: A plume is identified in the linear retrieval output where five or more pixels are flagged within a 200 km radius of the volcano, figure 4.2c,g. A positive detection is defined as where the linear retrieval output exceeds a threshold of 0.49 effective DU, which was set by Walker et al. (2012) based on the standard deviation of the column amounts obtained for the background atmosphere. If a plume is identified then the angle between the north line and the centre of the flagged pixels (obtained by taking an average of the latitudes and longitudes of the flagged pixels), is used to rotate the plume around the volcano so that the plume is always aligned to the north, figure 4.2d,h. Where no plume is identified then the linear retrieval output is rotated with the wind direction at the vent. The unrotated and the rotated data were then gridded to a 0.125° latitude by 0.125° longitude grid, following which monthly, annual and multi-annual averages of these grids were calculated. Averaging the grids helps to smooth the signal and remove background noise.

In addition to the two rotations mentioned above, a third grid type is obtained. Pixels which have been flagged within the vent rotated data (again using the threshold set by Walker et al. 2012) were removed before monthly, annual and multi-annual averages are computed from the remaining data. This is referred to as the **passive emission rotation**. This is perhaps more reflective of emissions from

non-eruptive or passive degassing, and is more similar to Carn et al. (2017) which is used for comparison (see section 4.2.4.1). Doing this can be useful for assessing the relative amounts of SO₂ emitted from explosive and passive activity, establishing baseline emissions rates and assessing the impacts of emissions during quiescent periods on the environment and climate. The results are included in this study and are briefly discussed in section 4.3.1 but are not the main focus of this paper, which will primarily focus on the results from the plume rotation method. This is for a number of reasons. Firstly, the threshold used to flag elevated SO₂ column amounts is not necessarily a good distinguisher between passive and eruptive emissions (not having been designed for this purpose). This study also aims to assess the overall performance of the IASI SO₂ linear retrieval for detecting and monitoring changes in SO₂ and the removal of large emissions of SO₂ would detract from this. Excluding higher column amounts also removes a critical part of the eruptive cycle. Further study on the topic of passive and explosive emissions is encouraged in the future. Such a study would first be required to set a more appropriate threshold which is likely to differ between volcanoes, and potentially at a single volcano over time.

An example of the unrotated, vent rotated and plume rotated averaged grids, at Popocatépetl in 2015, are shown in figure 4.3. This figure shows how the elevated signal is isolated in the downwind (to the north of the volcano) and emphasises the difference between the vent rotation and plume rotation. The vent rotation approach here is successful but is more dispersed, whereas the plume rotation is narrower and elongated. This suggests that the assumption made by the vent rotation approach, that the plume is emitted at the height of the vent, is not always correct meaning that the rotation angle is not always appropriate. To some extent

the uncertainty in the angle used is reflected in the width of the plume seen in the averaged grids. A wider plume (e.g. figure 4.3b) indicates that the uncertainty is greater. However, the width is also controlled by the magnitude of the emission and the wind speed. In addition to the monthly, annual and multi annual grids, the average effective column amount of the linear retrieval output and number of flagged pixels within 200 km of the volcano, and within 200 km of the volcano in the upwind and downwind directions are saved for each orbit. These are not discussed in this paper but could be explored further in the future.

Rotating the linear retrieval output helps to isolate and enhance the SO₂ signal in the monthly and annual averages which can then be used to determine if there is an elevated SO₂ signal at the volcano. This is defined as where:

Table 4.1: Description of the different rotation methods

Method	Description	Limitations
Plume rotation	If more than five pixels within 200 km of the source are flagged, then the angle between north and the mean flagged latitudes and longitudes is used to rotate the plume. Where this is not the case the vent rotation is applied.	This does not differentiate between sources. If the flagged SO ₂ emissions are from another source (e.g. a near by volcano) then these will be incorrectly attributed to the current volcano.
Vent rotation	The linear retrieval output is rotated using the wind direction at the height of the vent.	This only works if the plume is emitted at the vent height.
Passive emission rotation	Pixels which are flagged as containing SO ₂ are removed and then the vent rotation is applied.	The threshold used may not be an appropriate differentiator between emissions from quiescent degassing and emissions from explosive activity. This method will not detect emissions from explosive eruptions.

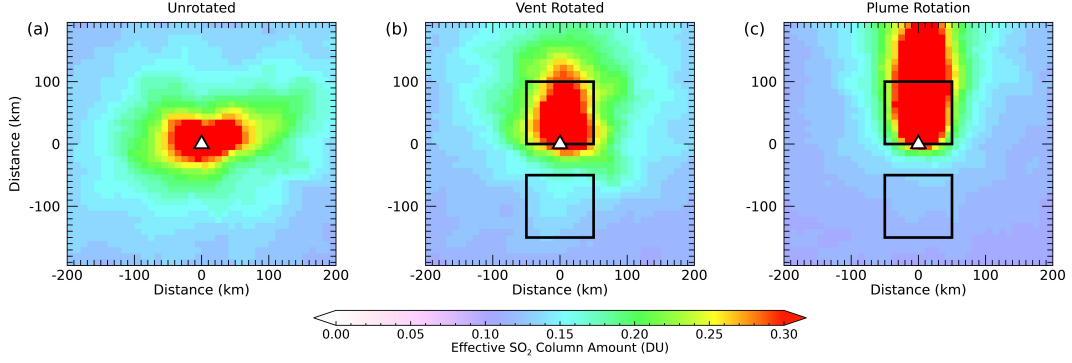


Figure 4.3: (a) Unrotated annual average at Popocatepetl for 2015; (b) Vent rotated annual average; (c) Plume rotated annual average. In (b) and (c) the two boxes used to calculate the upwind and downwind means and standard deviations are shown. These are used to determine whether there is an elevated signal and to compute the emission index.

$$\bar{x}_d > \bar{x}_u + 2\sigma_u \quad (4.1)$$

where \bar{x} is the mean SO₂ effective column amount in the upwind (u ; 50-150 km in the upwind and 100 km in width) and downwind (d ; 0-100 km in downwind and 100 km width) and σ is the standard deviation of the SO₂ effective column amount. The boxes used to compute this are shown in figure 4.3. An emission index (EI) is defined as:

$$EI = \bar{x}_d - \bar{x}_u \quad (4.2)$$

This was computed for each month, year and for the entire study period and can give some indication of the relative amounts of SO₂ and be used to infer changes in activity. This approach does not allow for direct comparisons with other volcanoes because the retrieval does not account for the different heights of the SO₂ emissions and this method looks at quite a tight region around the volcano which does

not necessarily reflect the full extent of the plume. In addition, the wind speed at the volcano affects the dispersion which could also affect inter-comparisons. Experimentation with the distance and angles used to compute the emission index and to assess whether there is elevated activity can be seen in appendix C.

One of the main limitations of this approach is potential contamination from plumes from other volcanoes: either when these are in close proximity to the volcano in question (e.g. Kamchatka) or where there are plumes from large explosive eruptions which travel significant distances (e.g. Nabro, 2011). Cases of false alerts are more common using the plume rotation method but are also possible when the vent and passive emission rotations are performed. Volcanoes where false classification are possible due to multiple volcanoes in close proximity are highlighted in the results. Despite the chance for falsely elevated signals at individual volcanoes, regions with elevated activity can be identified. At this stage, manual inspection of the averaged grids may help distinguish the source. Alternatively, investigation of the linear retrieval output for each IASI orbit could be considered to help identify the source of the plume. In addition to this, other data sources could be used to help inform the results; for example, data from OMI or thermal emissions. A few cases of false classification are highlighted in sections 4.3 and 4.4 and the implications discussed further.

An additional output of this rotation algorithm is potentially the height of the SO₂ layer. A schematic illustrating how this is done is shown in figure 4.4. Essentially, where the linear retrieval output has been rotated using the angle between north and the identified plume, this angle can be compared against a wind profile to obtain a possible height of the plume. It should be noted that for a single

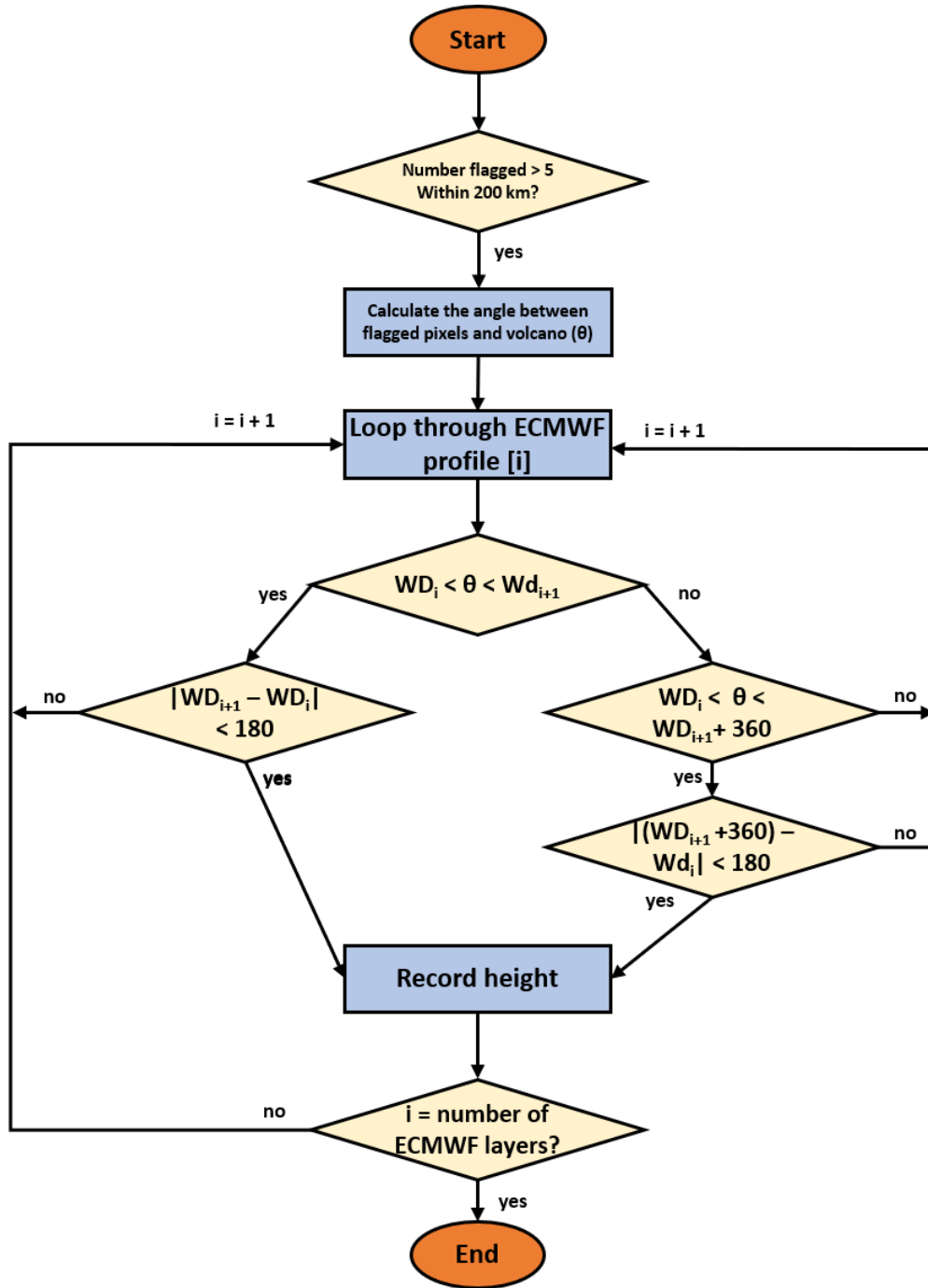


Figure 4.4: A schematic summarising how the height of the plume might be quickly inferred from the wind direction atmospheric profile. An examples from Etna can be seen in figure 4.5

θ = angle between north and the mean latitude and longitude of flagged pixels

i = incremental layer of atmospheric profile

WD = wind direction

orbit there may be multiple height solutions as there may be multiple intersections between the calculated angle and the wind direction profile. This can be seen in an example from Etna (8th September 2011, 0932 UTC) shown in figure 4.5. This method is similar in some aspects (although significantly simpler) to Pardini et al. (2017) which obtains the height and flux from volcanoes. It can be applied very quickly using whatever atmospheric profile and satellite data (this method is not restricted to the linear retrieval or IASI) is already available, making it a potentially useful tool immediately following an eruption. Its use is not restricted to SO₂ emissions; for example, it could also be applied to volcanic ash and again this could be with any simple detection tool or satellite instrument. Further validation of this approach is required and improvements could be made by using higher resolution meteorological data (both horizontally and vertically) such as the ERA5 ECMWF or radiosonde data. The dispersion of the plume could also be considered to help distinguish which solution is correct: a high wind speed would generate a narrower plume, whereas a low wind speed would cause the plume to be more dispersed.

4.2.4 Datasets used for comparison

The IASI emission index has been compared against the Carn et al. (2017) OMI emission database and thermal anomalies detected using the MODVOLC algorithm (Wright et al., 2004; Wright, 2015). Further description of these two databases is given below. There are fundamental differences between the datasets which means that while they can be used to help the interpretation of the results, it is not necessarily expected for the results to be correlated. In addition to these databases

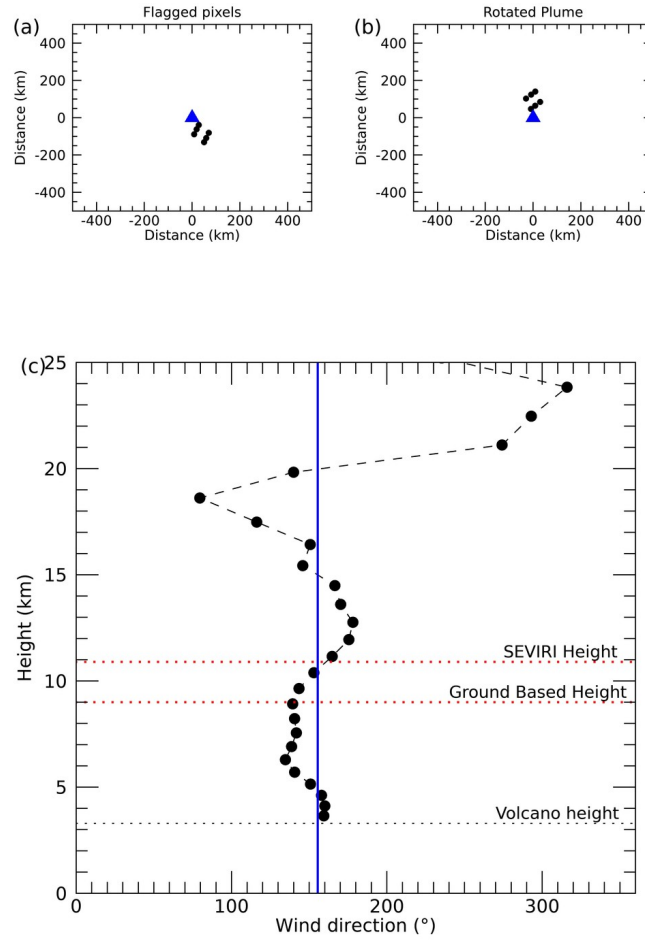


Figure 4.5: An example of how the height of the volcanic plume can be inferred from the wind direction atmospheric profile. (a) Flagged linear retrieval pixels at Etna on 8th September 2011 at 0932 UTC. (b) Rotated flagged pixels. (c) Atmospheric wind direction profile from the closest (time and spatially) ECMWF profile. The plume angle is marked in blue. This is compared against the wind profile to estimate the height. The algorithm returns a height at around 5, 11, 15 and 20 km. The dashed red lines indicate the plume heights obtained from ground based (upper limit = 9 km) and SEVIRI measurements (Scollo et al., 2014). In this case one of the outputs from the rotation heights matches closely to that obtained with SEVIRI.

reference has been made to the Smithsonian’s Global Volcanism Program’s reports (GVP, 2013f) and other literature.

4.2.4.1 OMI Emission Database

The Ozone Monitoring Instrument (OMI) has been widely used to study the emission of SO₂ from volcanoes and anthropogenic sources (e.g. Carn et al., 2007, 2008; Fioletov et al., 2013, 2015, 2016; Flower et al., 2016b; Krotkov et al., 2016; Koukouli et al., 2016). Carn et al. (2017) produced a global SO₂ emission inventory which estimated the emissions from passive degassing (i.e., no coincident eruption of magma) at 91 volcanoes worldwide between 2004 and 2015 (since extended, this can be downloaded at <https://so2.gsfc.nasa.gov/measures.html>; MEaSUREs 2019). This dataset has been compared against the emission index computed for IASI.

The OMI data was processed using a principle component algorithm developed by Li et al. (2013). This excludes pixels where the solar zenith angle is greater than 70° which avoids noise in high latitudes where there is limited sunlight during the winter. This is a significant advantage of using IASI or other infrared instruments which can make measurements at these times. The OMI retrieval also excludes pixels where the cloud fraction is greater than 20% and if they are affected by the OMI row anomaly (for further information see McCormick et al., 2013): another advantage of using IASI (or other instruments unaffected by this) to complement the OMI record. A wind rotation based on the height of source was then applied to the output from the OMI retrieval. A flux was then computed using a method developed by Beirle et al. (2011, 2014) which fits an exponentially modified Gaussian function to the annual or multi-annual averages of the rotated data. An air mass correction

factor was applied based on the height of the volcano to account for the different emission heights. As this study aimed to investigate the passive emission flux, data with column amounts greater than 5-15 DU were removed. This was based on measurements usually made by OMI in plumes from both explosive and passive activity. This method to compute the flux was previously applied to anthropogenic sources (e.g. Beirle et al., 2011; Lu et al., 2015; Fioletov et al., 2016).

The emission indices computed for IASI in this study have been compared against the emission dataset produced by Carn et al. (2017). It should be noted that while there are some similarities in the techniques applied, there are also fundamental differences which is important to remember when comparing the two datasets. Notably, the exclusion of plumes with high column amounts in the Carn et al. (2017) emission inventory will lead to different trends when compared against the plume rotated and vent rotated results generated from the IASI linear retrieval data. Even a comparison against the passive emission rotation results may produce different results as the thresholds used are not necessarily equivalent: having been defined in different ways and applied to different dataset types. For example, the linear retrieval gives an effective SO₂ column amount which indicates the relative amount of SO₂ with respect to the background rather than quantifying the mass. The emission index is also a measure of the relative amount of signal compared to the background, rather than a flux. A future study could compute fluxes from the rotated IASI data to get a quantitative estimate of the emissions seen with IASI. This however is beyond the scope of this current work as it would benefit from using the Carboni et al. (2012) iterative retrieval which also quantifies the height of the plume and uses local atmospheric profiles (rather than a standard atmospheric

profile). This retrieval is more computationally expensive and therefore would be better suited to individual case studies rather than been applied globally. It is suggested that some of the most commonly identified volcanoes in this study be selected for long term studies with the iterative retrieval. An advantage of doing this is its ability to retrieve the plume height which could possibly be a differentiator between emissions from explosive and passive activity.

4.2.4.2 MODVOLC

The IASI emission index dataset has also been compared against the outputs from the MODVOLC algorithm developed for MODIS (Wright et al., 2002, 2004; Wright, 2015). This data can be easily downloaded at <http://modis.higp.hawaii.edu/>.

A number of different algorithms have been developed for the detection and monitoring of thermal emissions from volcanoes and this has been performed using many satellites (Oppenheimer, 1998; Harris, 2013). The extreme temperatures (200-1100°C) that are associated with lava flows, domes and lakes cause a significant increase in the radiances measured within the shortwave infrared relative to the thermal infrared and so this can be exploited to detect thermal anomalies (Wright et al., 2004). This includes thermal emissions from volcanoes but can also be used to detect elevated thermal emissions from wildfires (Kaufman et al., 1998; Dehn et al., 2000; Justice et al., 2002; Giglio et al., 2003; Wright et al., 2004; Wright and Flynn, 2004).

The MODVOLC algorithm was developed by Wright et al. (2002, 2004) for the Moderate Resolution Imaging Spectroradiometer (MODIS) on-board the Terra and Aqua satellites launched in 1999 and 2002 respectively. This instrument offers

relatively low spatial resolution (1 km at nadir to 2x5 km at the edge of the swath) but can make daily measurements if the scenes are cloud free. The algorithm computes a normalised thermal index for MODIS bands 22 (3.929 - 3.989 μm) and 32 (4.020 - 4.08 μm), alternatively using band 21 (3.929 - 3.989 μm) if band 22 is saturated. A threshold is applied to distinguish pixels within which there is a thermal anomaly. This threshold has been set to ensure reliable detection while minimising the number of false detections. This means that this algorithm is more reliable for detecting larger thermal increases such as those associated with active eruptions. A different threshold is applied to daytime measurements which are also discarded if there is sunglint. Further information about MODVOLC can be found in Wright et al. (2002, 2004); Wright (2015).

For this study, thermal anomaly data has been downloaded for each of the studied volcanoes. The region size varies between volcanoes but is the default set on the MODVOLC website. The total number of thermal anomalies was then computed for each month and year. This was then compared against the emission index computed from the IASI linear retrieval output. As already mentioned the MODVOLC data is a good indicator of active eruptions (e.g. ones with lava flows and lakes etc.) and so can tentatively be used to indicate successful detections in the IASI dataset. However, it will most likely only indicate successful/unsuccessful detections from active eruptions rather than where there are increases in the SO₂ emissions associated with strong degassing. Thermal detections may be missed in cloudy conditions and so the results should be interpreted with caution.

MODVOLC was selected for comparison because it is a simple indicator of activity with a long record of thermal emissions which are easily accessed online.

Future studies, might want to consider using the output from the MIROVA algorithm which was also developed for MODIS (Coppola et al., 2016a). This has previously been used to monitor thermal emissions at a number of different volcanoes (Coppola et al., 2015, 2016b,c) and has been shown to have a greater accuracy than MODVOLC and also a greater sensitivity to smaller thermal emissions due to the use of both spectral and spatial filtering (Coppola et al., 2016a).

4.3 Global Perspective of SO₂ emissions seen with IASI

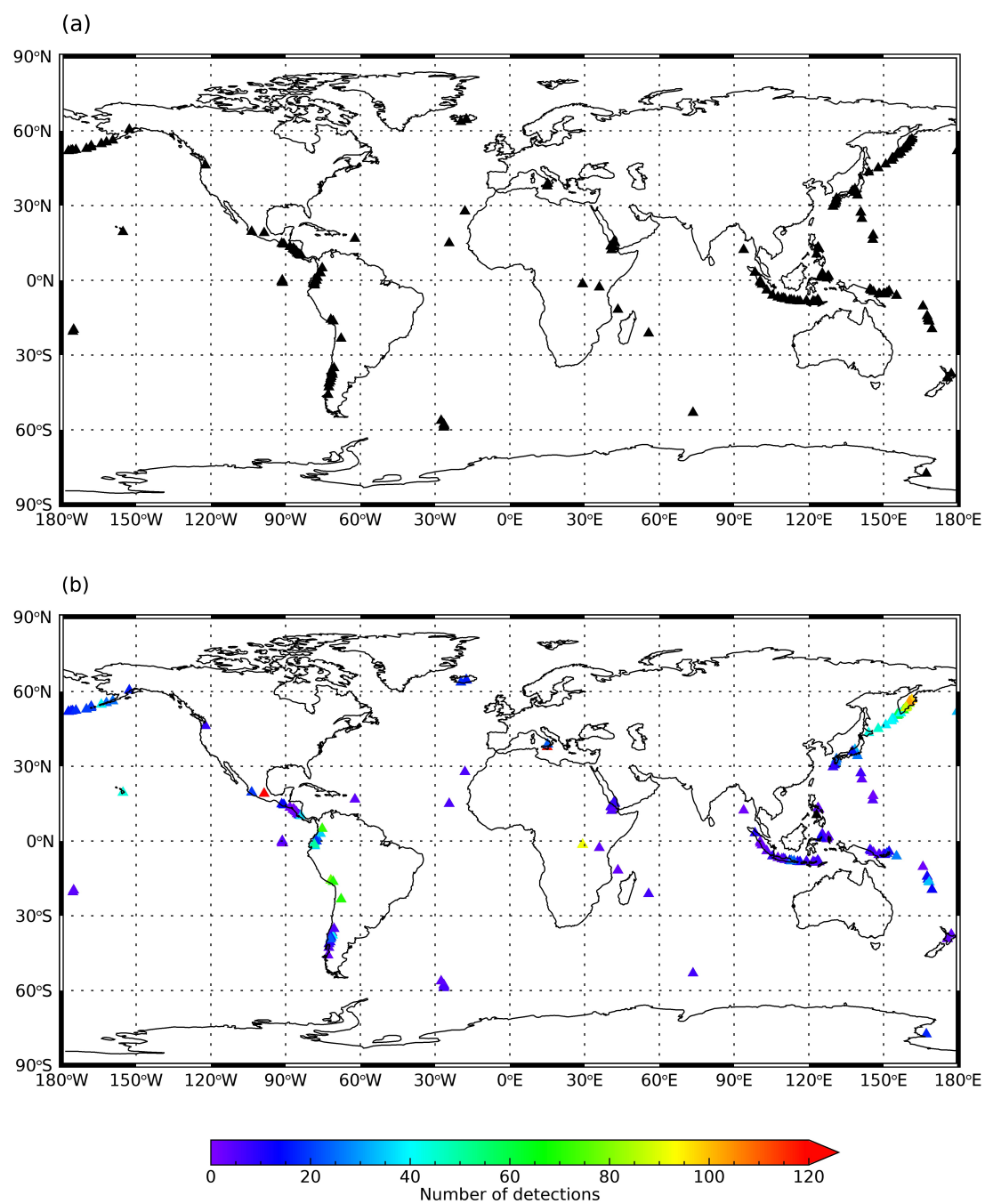
4.3.1 Comparison of different rotation approaches

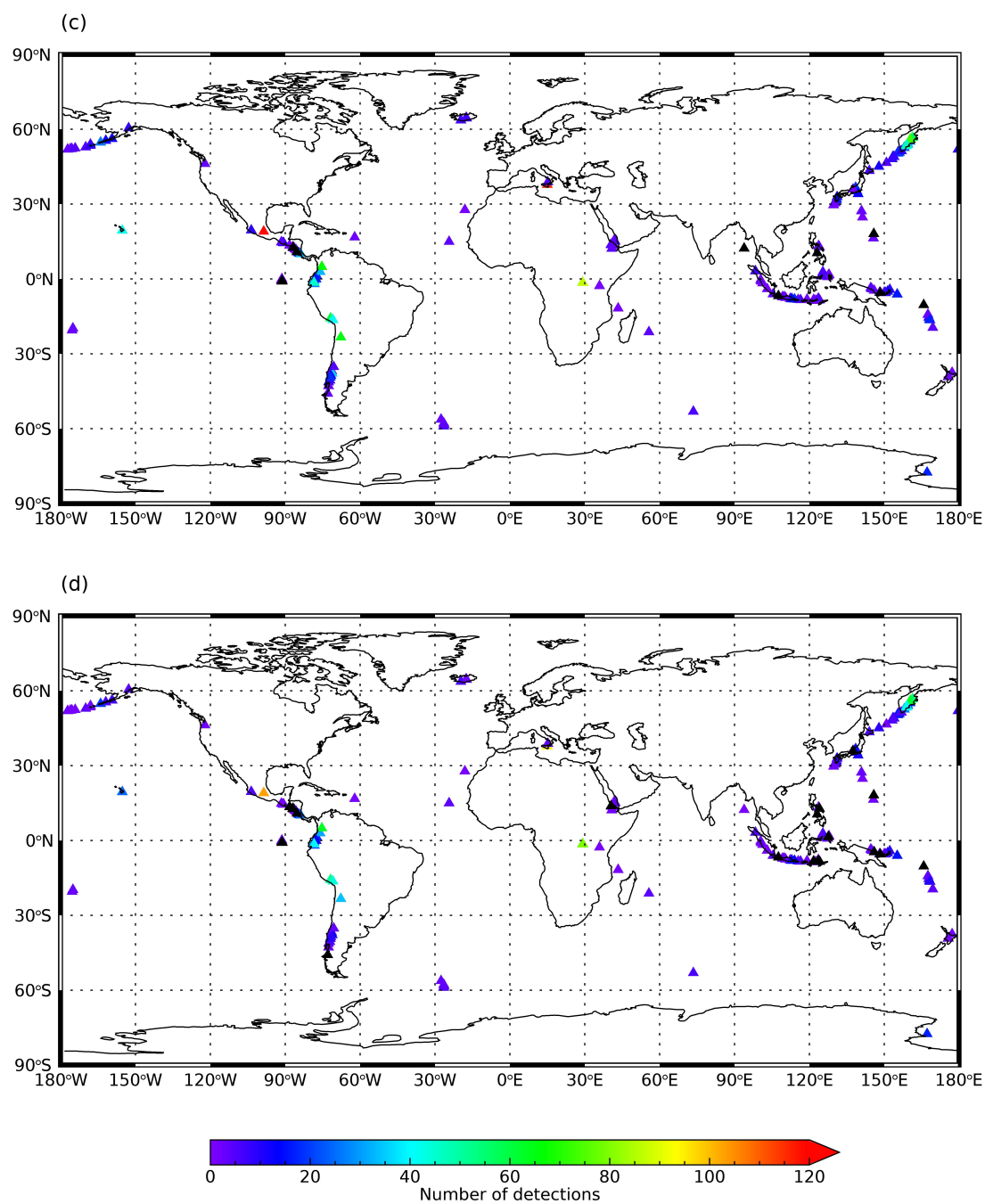
Figure 4.6a shows the location of the 166 volcanoes to which the rotation algorithm, outlined in section 4.2.3, was applied. All of these volcanoes have been listed as having activity since 2007 (the first year for which data is available from IASI) within the Volcanoes of the World database (GVP, 2013f). The rotation scheme was applied to the IASI linear SO₂ retrieval output from August 2007 to October 2017. The number of elevated SO₂ signals which are detected at each volcano during this time period, using the ‘plume’, ‘vent’ and ‘passive emission’ rotation methods, are

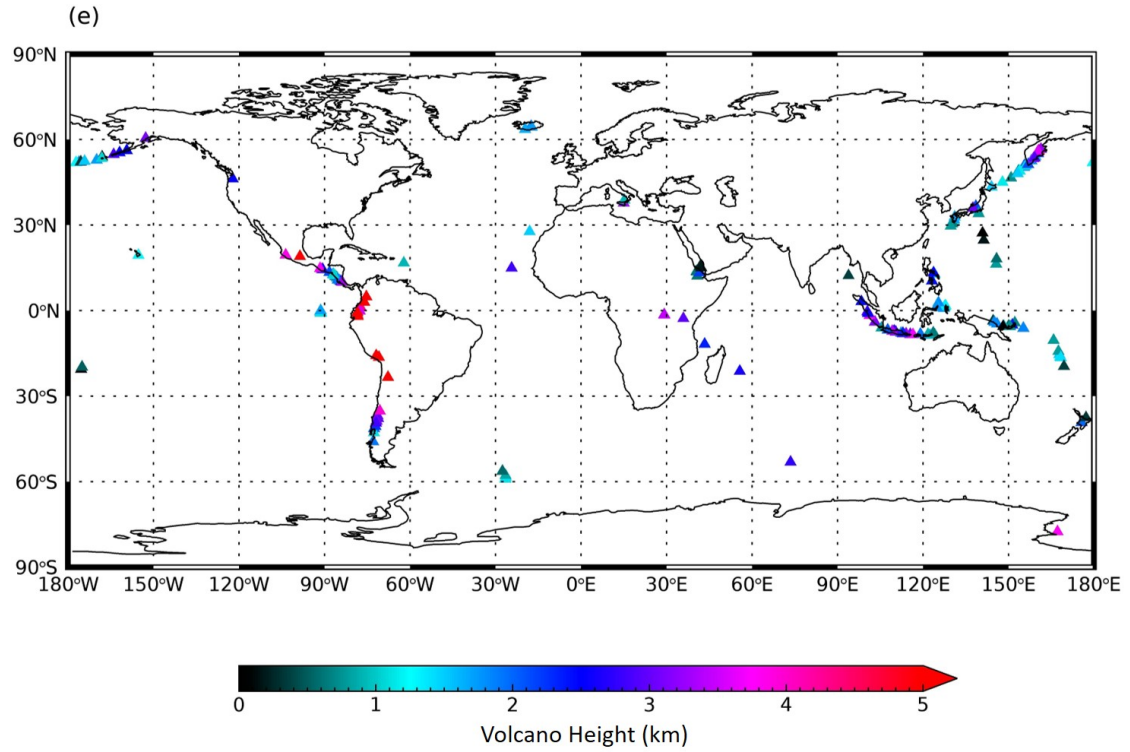
Figure 4.6: *(on the following page)* (a) Volcanoes to which the rotation algorithm, described in section 4.2.3, was applied. These were all listed as having been active since 2007 in the Volcanoes of the World database (GVP, 2013f). (b) The number of elevated signals which are identified with the plume rotation algorithm. (c) The number of detections at each volcano using the vent rotated algorithm (d) The number of elevated signals which are identified with the passive emission rotation. For each case, an elevated signal is defined as $\bar{x}_d > \bar{x}_u + 2\sigma_u$. (e) The volcano heights.

Statistics summarising the results for each volcano can be seen in table 4.2.

A summary of the different rotation techniques is given in tables 4.1.







shown in figure 4.6b, c and d respectively. Each volcano was ranked according to the number of times an elevated signal was identified. These rankings and number of elevated signals for the plume rotated approach are included in table 4.2. The rankings for all three approaches can be seen in table C.1 in appendix C.

For each of the three rotation types applied, the volcano with the greatest number of detections was Popocatepetl in Central Mexico. At this volcano, there were a total of 122 detections with the plume rotated technique meaning it was flagged for all but one month studied. Etna was the next most flagged volcano with an elevated signal in 118 out of the 123 months analysed (using the plume rotation approach). After this, the rankings of the three rotation approaches differed (seen in table C.1). Figure 4.6 shows that the greatest number of detections at each volcano are identified with the plume rotation approach and that the number of elevated signals falls when the vent or passive emission rotation methods are applied: with

the greatest difference seen with the latter. This is due to the removal of falsely elevated signals (and potentially also true signals). These can occur with the plume rotated technique if flagged pixels are identified within 200 km of the volcano but these are actually from another source. This may be due to emissions from a nearby volcano or another strong source of SO_2 , or a large plume emitted during an explosive eruption which has been transported away from the original source.

The vent rotation approach can reduce the number of falsely detected signals where the elevated emissions are from another source. When this occurs, in plots of averaged results a ring of elevated SO_2 can be seen around the source (see for example figure C.16). This increases the value for \bar{x}_u and subsequently, the chance of an elevated signal is reduced. However, taking this approach will lead to no detection where the plume from the volcano being analysed is emitted at a height above the vent where the wind direction is different. This may mean that when the plume is rotated it is not aligned to the north of the source, as was demonstrated in figure 4.2.

Unsurprisingly, the lowest number of detections is seen with the passive emission rotation approach because this removes all SO_2 flagged pixels. Overall, using the passive emission rotation method, there are 22 volcanoes where there are no detections during the ten year study period. Again, although this does reduce false classifications, it also removes true detections. A quick inspection of figure 4.6d and e shows that volcanoes with a higher altitude are detected more frequently. This is expected as the height of the plume effects the detection limit of the retrieval. At volcanoes where elevated emissions are identified less often with this approach, it is likely that the emissions from degassing increased for a short duration before falling beneath the detection limit again.

Table 4.2: Table summarising the plume rotation results for each of the volcanoes studied.

R1 = plume rotation rank based on number of detections in the period 2007-2017; R2 = rank from Carn et al. (2017) study (based on mean flux, 2005-2015). Num. = Number of detections with the plume rotation technique (defined as where $\bar{x}_d > \bar{x}_u + 2\sigma_u$; I-O = the plume rotated emission index correlated with OMI flux; I-M = the plume rotated emission index correlated with the number of thermal alerts with MODVOLC.

R1	R2	Volcano	Code	Region	Latitude (°N)	Longitude (°E)	Altitude (m)	Num. detection	I-O	I-M
1	9	Popocatepetl	Popo	Mexico	19.02	-98.62	5393	122	0.86	0.85
2	6	Etna	Etn	Italy	37.74	14.99	3295	118	0.57	0.31
3	-	Tolbachik	Tol	Kamchatka	55.83	160.32	3611	104	-	-0.16
4	91	Klyuchevskoy	kly	Kamchatka	56.05	160.64	4754	102	0.83	0.65
5	-	Bezymianny	Bez	Kamchatka	55.97	160.59	2882	101	-	0.35
6	35	Sheveluch	She	Kamchatka	56.65	161.36	3283	98	0.53	-0.11
7	-	Nyiragongo	Nyi	Democratic Republic of the Congo	-1.52	29.25	3470	92	-	0.03
8	-	Zhupanovsky	Zh	Kamchatka	53.58	159.15	2899	88	-	0.45
9	-	Koryaksky	Kor	Kamchatka	53.32	158.71	3430	87	-	-
10	-	Nyamuragira	Nya	Democratic Republic of the Congo	-1.40	29.20	3058	85	0.63	0.08
11	23	Kizimen	Kiz	Kamchatka	55.13	160.32	2334	83	0.92	0.93
11	17	Karymsky	Kary	Kamchatka	54.04	159.44	1513	83	0.47	0.53
13	79	Sabancaya	Sab	Peru	-15.78	-71.85	5960	77	0.97	0.82
14	14	Nevado del Ruiz	NR	Colombia	4.89	-75.32	5279	72	0.93	0.33
15	60	Ubinas	Ub	Peru	-16.35	-70.90	5672	70	0.56	0.38

continued ...

...continued

R1	R2	Volcano	Code	Region	Latitude (°N)	Longitude (°E)	Altitude (m)	Num. detec- tions	I-O	I-M
15	-	Lascar	Las	Chile	-23.37	-67.73	5592	70	-	0.53
17	-	Gorely	Gor	Kamchatka	52.55	158.03	1799	66	-	0.38
18	-	Chikurachki	Chi	Kuril Islands	50.32	155.46	1781	63	-0.06	-
19	-	Ebeko	Eb	Kuril Islands	50.68	156.01	1103	58	-	-
20	43	Tungurahua	Tun	Ecuador	-1.46	-78.44	5023	50	0.14	-0.06
21	-	Alaid	Ala	Kuril Islands	50.86	155.56	2285	49	-	-0.26
22	-	Etorofu- Yakeyama	EY	Kuril Islands	45.01	147.87	1158	45	-	-
23	2	Kilauea	Kil	Hawaii	19.42	-155.28	1222	44	0.88	-0.39
23	-	Chirinkotan	Ch	Kuril Islands	48.98	153.48	724	44	-	-0.21
25	-	Akan	Aka	Japan	43.38	144.01	1499	43	-	-
26	38	Asamayama	Asa	Japan	36.40	138.52	2568	41	0.32	-
27	52	Sarychev Peak	SP	Russia	48.09	153.20	1496	40	0.75	0.97
27	-	Kambalny	Kamb	Kamchatka	51.30	156.87	2116	40	-	-
27	-	Cotopaxi	Cot	Ecuador	-0.67	-78.43	5911	40	-	-0.17
27	44	Copahue	Cop	Chile- Argentina	-37.85	-71.18	2953	40	0.48	0.20
31	42	Shishaldin	Shi	Alaska	54.75	-163.97	2857	39	0.42	0.12

continued ...

...continued

R1	R2	Volcano	Code	Region	Latitude (°N)	Longitude (°E)	Altitude (m)	Num. detec- tions	I-O	I-M
31	-	Chirpoi	Chir	Kuril Islands	46.53	150.87	742	39	-	-0.18
33	-	Ekarna	Ek	Kuril Islands	48.95	153.93	1170	38	-	-
34	-	Turrialba	Tur	Costa Rica	10.02	-83.76	3340	37	0.80	0.52
35	-	Sangay	San	Ecuador	-2.00	-78.34	5286	36	-	-0.26
35	30	Nevado del Huila	NH	Colombia	2.93	-76.03	5364	36	0.85	0.82
37	1	Ambrym	Ambr	Vanuatu	-16.25	168.12	1334	35	0.01	0.19
38	-	Lopevi	Lop	Vanuatu	-16.50	168.34	1413	34	-	-0.20
39	-	Semisopochnoi	Sem	Alaska	51.93	179.58	1221	33	-	-
39	-	Kusatsu- Shiranesan	KS	Japan	36.61	138.52	2165	33	-	-
41	15	Aira	Ai	Japan	31.59	130.65	1117	30	0.83	0.38
42	-	Semeru	Se	Indonesia	-8.10	112.92	3657	28	-	0.35
43	-	Hakoneyama	Ha	Japan	35.23	139.02	1438	27	-	-
43	3	Bagana	Bag	Papua New Guinea	-6.13	155.19	1855	27	0.40	0.57
45	16	Miyakejima	Mi	Japan	34.09	139.52	775	26	0.80	-
45	29	Asosan	Aso	Japan	32.88	131.10	1592	26	-0.17	-0.04
47	54	Veniaminof	Ve	Alaska	56.17	-159.38	2507	25	0.39	-0.10
48	91	Tengger Caldera	TC	Indonesia	-7.94	112.95	2329	24	0.48	0.35
48	-	Poas	Poa	Costa Rica	10.20	-84.23	2708	24	-	-
48	-	Pavlof	Pav	Alaska	55.41	-161.89	2493	24	-	0.06

continued ...

...continued

R1	R2	Volcano	Code	Region	Latitude (°N)	Longitude (°E)	Altitude (m)	Num. detec- tions	I-O	I-M
48	-	Kirishimayama	Kir	Japan	31.93	130.86	1700	24	-	0.71
48	61	Galeras	Gal	Colombia	1.22	-77.37	4276	24	0.18	0.04
53	50	Villarrica	Vi	Chile	-39.42	-71.93	2847	23	0.22	0.86
53	68	Stromboli	Str	Italy	38.78	15.21	924	23	0.45	-0.08
53	91	Raung	Rau	Indonesia	-8.11	114.05	3260	23	0.65	0.95
56	32	Kikai	Kik	Japan	30.79	130.30	704	22	0.32	-
56	-	Fuego	Fue	Guatemala	14.47	-90.88	3763	22	0.60	0.16
58	-	Okmok	Ok	Alaska	53.43	-168.13	1073	20	-	-
58	69	Cleveland	Cl	Alaska	52.82	-169.94	1730	20	-	-0.30
60	27	Ulawun	Ul	Papua New Guinea	-5.05	151.33	2334	19	-0.45	-
60	64	Reventador	Rev	Ecuador	-0.07	-77.65	3562	19	-0.07	0.28
60	-	Colima	Col	Mexico	19.51	-103.62	3850	19	-	0.08
60	-	Bardarbunga	Bar	Iceland	64.63	-17.51	2000	19	-	-
64	66	Korovin	Ko	Alaska	52.38	-174.16	1518	18	-0.34	-
64	-	Eyjafjallajökull	Eyj	Iceland	63.63	-19.63	1651	18	-	0.62
64	5	Ambae	Amba	Vanuatu	-15.38	167.83	1496	18	0.39	0.99
67	89	Erebus	Ere	Antarctica	-77.53	167.17	3794	17	-0.05	-0.38
68	41	Redoubt	Red	Alaska	60.48	-152.74	3108	16	0.98	0.98
68	-	Llaima	ll	Chile	-38.69	-71.72	3125	16	-	-0.06
68	-	Kasatochi	Kasa	Alaska	52.17	-175.50	314	16	-	-
68	-	Kanaga	Kana	Alaska	51.92	-177.16	1307	16	-	-
68	-	Grimsvotn	Gri	Iceland	64.41	-17.31	1719	16	-	-

continued ...

...continued

R1	R2	Volcano	Code	Region	Latitude (°N)	Longitude (°E)	Altitude (m)	Num. detec- tions	I-O	I-M
68	-	Great Sitkin	GS	Alaska	52.07	-176.13	1740	16	-	-
68	-	Bogoslof	Bog	Alaska	53.93	-168.03	150	16	-	0.08
75	-	Ontakesan	On	Japan	35.89	137.48	3067	15	-	-
76	-	Pacaya	Pa	Guatemala	14.38	-90.60	2569	14	-	0.00
77	11	Yasur	Ya	Vanuatu	-19.53	169.44	361	13	0.31	0.27
77	58	Santa Maria	SMa	Guatemala	14.75	-91.55	3745	13	0.00	-0.36
79	-	Soputan	So	Indonesia	1.11	124.73	1785	12	-	0.14
79	-	Kelut	Kel	Indonesia	-7.93	112.30	1731	12	-	-0.26
79	39	Gaua	Gau	Vanuatu	-14.27	167.50	797	12	-0.06	0.51
82	82	Rinjani	Ri	Indonesia	-8.42	116.47	3726	11	0.39	0.13
82	7	Rabaul	Rab	Papua New Guinea	-4.27	152.20	688	11	0.78	0.77
82	-	Kuchinoerabujima	Kuc	Japan	30.44	130.21	657	11	-	-
82	-	Arenal	Are	Costa Rica	10.46	-84.70	1670	11	0.80	-0.32
86	-	Witori	Wi	Papua New Guinea	-5.57	150.51	724	10	-	-0.11
86	45	Sinabung	Sin	Indonesia	3.17	98.39	2460	10	0.94	0.78
86	65	Lokon-Empung	LE	Indonesia	1.35	124.79	1580	10	-0.25	-0.36
86	-	Agung	Agu	Indonesia	-8.34	115.50	2997	10	-	-0.29
90	-	Puyehue-Cordon Caulle	PCC	Chile	-40.59	-72.11	2236	9	-	-
90	-	Dieng Volcanic Complex	DVC	Indonesia	-7.20	109.87	2565	9	-	-0.11

continued ...

...continued

R1	R2	Volcano	Code	Region	Latitude (°N)	Longitude (°E)	Altitude (m)	Num. detec- tions	I-O	I-M
92	-	Zubair Group	Zu	Yemen	15.05	42.18	191	8	-	0.25
92	76	Jebel at Tair	JT	Yemen	15.55	41.83	244	8	0.68	0.78
92	19	Suwanosejima	Su	Japan	29.63	129.71	796	8	-0.31	0.16
92	-	St. Helens	MSH	United States	46.20	-122.18	2549	8	-	-
92	91	Merapi	Me	Indonesia	-7.54	110.44	2910	8	0.67	0.80
92	47	Krakatau	Kra	Indonesia	-6.10	105.42	813	8	-0.14	-0.21
92	-	Kadovar	Kad	Papua New Guinea	-3.60	144.58	365	8	-	-
92	-	Calbuco	Cal	Chile	-41.33	-72.61	1974	8	-	0.82
100	-	Batu Tara	BT	Indonesia	-7.79	123.58	633	7	-	-
100	84	Sangeang Api	SA	Indonesia	-8.20	119.07	1949	7	0.81	0.85
100	-	Nishinoshima	Ni	Japan	27.24	140.87	25	7	-0.19	-0.18
100	10	Manam	Man	Papua New Guinea	-4.08	145.03	1807	7	0.18	-0.14
100	-	Heard	He	Indian Ocean	-53.10	73.51	2745	7	-	0.09
100	91	Piton de la Four- naise	PF	Indian Ocean	-21.24	55.70	2632	7	-0.27	0.88
100	91	Erta Ale	EA	Ethiopia	13.60	40.67	613	7	-0.08	-0.11
100	-	Egon	Eg	Indonesia	-8.67	122.45	1661	7	-	-0.08

continued ...

...continued

R1	R2	Volcano	Code	Region	Latitude (°N)	Longitude (°E)	Altitude (m)	Num. detec- tions	I-O	I-M
100	-	Bristol Island	BrI	South Sandwich Islands	-59.01	-26.53	1100	7	-	-
109	51	Saunders	Sa	South Sandwich Islands	-57.80	-26.48	843	6	-0.26	-
109	-	Ritter Island	RI	Papua New Guinea	-5.51	148.11	75	6	-	-
109	87	Paluweh	Pal	Indonesia	-8.32	121.70	875	6	0.40	-0.12
109	70	Montagu Island	MI	South Sandwich Islands	-58.44	-26.37	1370	6	-0.37	-0.39
109	-	Manda Hararo	MH	Ethiopia	12.17	40.82	600	6	-	-0.09
109	46	Karagetang	Kar	Indonesia	2.78	125.40	1797	6	-0.10	0.28
109	-	Iliwerung	Ili	Indonesia	-8.53	123.57	1018	6	-	0.13
109	-	Hierro	Hi	Canary Is- lands	27.73	-18.03	1500	6	-	-
109	-	Fogo	Fo	Cape Verde	14.95	-24.35	2829	6	-	0.99
109	8	Dukono	Duk	Indonesia	1.69	127.89	1229	6	-0.00	-0.15
119	-	Wolf	Wo	Galapagos	0.02	-91.35	1710	5	-	0.98
119	63	Slamet	Sl	Indonesia	-7.24	109.20	3428	5	0.68	-0.03
119	40	Sirung	Sir	Indonesia	-8.50	124.13	862	5	0.17	0.15

continued ...

...continued

R1	R2	Volcano	Code	Region	Latitude (°N)	Longitude (°E)	Altitude (m)	Num. detec- tions	I-O	I-M
130	-	Ruapehu	Ru	New Zealand	-39.28	175.57	2797	4	-	-
130	-	Nabro	Nab	Eritrea	13.37	41.70	2218	4	-	0.99
130	37	Mayon	May	Philippines	13.25	123.68	2462	4	0.04	0.19
130	-	Ol Doinyo Lengai	ODL	Tanzania	-2.76	35.91	2962	4	-	-0.06
130	-	Ioto	Ioto	Japan	24.75	141.28	169	4	-	-
130	-	Dempo	Dem	Indonesia	-4.01	103.12	3142	4	-	-0.13
130	-	Concepcion	Con	Nicaragua	11.53	-85.62	1700	4	-	0.41
142	-	Tongariro	Ton	New Zealand	-39.15	175.63	1978	3	-	-
142	-	Rincon de Vieja	RV	Costa Rica	10.83	-85.32	1916	3	-	-0.25
142	-	Momotombo	Mo	Nicaragua	12.42	-86.53	1270	3	-	0.00
142	90	Marapi	Mar	Indonesia	-0.38	100.47	2885	3	-	-
142	48	Kerinci	Ker	Indonesia	-1.69	101.26	3800	3	-0.19	-0.12
142	-	Karthala	Kart	Comoros	-11.75	43.38	2361	3	-	0.24
142	-	Ibu	Ibu	Indonesia	1.48	127.63	1325	3	-	0.38
142	-	Hudson Cerro	CH	Chile	-45.90	-72.97	1905	3	-	-
142	-	Gamalama	Ga	Indonesia	0.80	127.33	1715	3	-	-0.12
142	-	Fernandina	Fer	Galapagos	-0.37	-91.55	1476	3	-	-0.01
152	53	Tinakula	Tin	Solomon Is-lands	-10.38	165.80	796	2	-0.01	-0.08

continued ...

...continued

R1	R2	Volcano	Code	Region	Latitude (°N)	Longitude (°E)	Altitude (m)	Num. detec- tions	I-O	I-M
152	-	Talang	Tal	Indonesia	-0.97	100.68	2575	2	-	-
152	77	San Miguel	SMi	El Salvador	13.43	-88.26	2130	2	-0.17	0.12
152	33	Pagan	Pag	Mariana Is- lands	18.13	145.80	570	2	0.12	0.02
152	91	Negra Sierra	SN	Galapagos	-0.83	-91.17	1124	2	-0.50	-
152	18	Masaya	Mas	Nicaragua	11.98	-86.16	635	2	0.03	0.07
152	28	Langila	Lan	Papua New Guinea	-5.52	148.42	1330	2	0.13	-0.01
152	-	Gamkonora	Gam	Indonesia	1.38	127.53	1635	2	-	-0.59
152	59	Barren Island	BaI	Indonesia	12.27	93.85	354	2	0.06	0.42
152	-	Cerro Azul	CA	Galapagos	-0.92	-91.40	1640	2	-	-0.05
162	-	Telica	Tel	Nicaragua	12.60	-86.84	1036	1	-	-0.09
162	91	San Cristobal	SC	Nicaragua	12.70	-87.00	1745	1	0.07	0.26
162	-	Karkar	Kar	Papua New Guinea	-4.64	145.96	1839	1	-	-
162	62	Bulusan	Bul	Philippines	12.76	124.05	1535	1	0.13	-
166	85	Kanlaon	Kanl	Philippines	10.41	123.13	2435	0	-0.18	-0.18

There is a fundamental limitation with the passive emission rotation approach, in both this study and the paper by Carn et al. (2017), which is setting the threshold between what is considered non-eruptive degassing and eruptive plumes. In this study, the threshold applied to the IASI linear retrieval output is the one used by Walker et al. (2012) to flag SO₂ pixels. This is set fairly high to avoid false alerts and may not be the best differentiator between plumes from more explosive activity and quiescent degassing. This is something which could be considered further in the future, but it is likely that the most appropriate threshold will differ between volcanoes, depending on their background state, and potentially also over time. Such a study could be interesting for assessing the relative amounts of SO₂ from eruptive and non-eruptive states, assessing the tropospheric burden caused by the conversion of sulphur to sulphate aerosol, and potentially for characterising the background emission at individual volcanoes; which might have implications for hazard assessments. Assessing this would benefit from the use of multiple instruments (e.g. both UV and infrared sensors) and as such it would be important to select an equivalent threshold to separate passive and eruptive SO₂ for each instrument and technique applied.

Given the removal of true detections with the vent and passive emission rotations, the remainder of this paper will focus on the results from the plume rotation technique, sometimes drawing on the vent rotation output to indicate where there are falsely elevated results. This is inline with the main aim of this study which is to investigate how the IASI instrument can be best be used for monitoring changes in emissions at volcanoes across the globe, which includes emissions from larger eruptions.

4.3.2 Assessment of global emission detections

It has already been noted that the most frequently identified volcanoes, using the plume rotation technique, are Popocatépetl and Etna. Both volcanoes are known to be significant degassers and were ranked as 9th and 6th respectively in the emission dataset produced by Carn et al. (2017). Both are ideal candidates for this rotation approach because of their height and significant levels of degassing. Both are near to other sources of SO_2 , for example the Talu Industrial Complex (Mexico) and Stromboli (Italy), but both of these are small emitters by comparison and the latter is limited by the usual height of emissions.

Overall there is a poor agreement between the ranking based on the number of detections with IASI (using the plume rotation) and the OMI emission ranking from Carn et al. (2017) which is based on the average flux obtained for each volcano (the ranks from Carn et al. 2017 are included alongside those from this study in table 4.2). For example, using the plume rotated techniques applied to the IASI linear retrieval data, after Popocatépetl and Etna, the next most frequently detected region is Kamchatka in Eastern Russia. Of the top 30 volcanoes, ranked using the number of detections with the plume rotation approach, 15 of these are in this region; whereas the first of the Kamchatka volcanoes to appear in the Carn et al. (2017) emission inventory is Karymsky at rank 17. Overall, in Carn et al. (2017) only 5 volcanoes in this region feature in the top 30: although two of these are treated as the same point source due to their close proximity. This close proximity is the primary reason for the high rank of the volcanoes in Kamchatka using the plume rotation approach applied to IASI data. Plumes emitted within this region are likely to be

falsely attributed to multiple volcanoes, as this adaptation of the rotation technique searches for flagged pixels within 200 km and uses this to perform the rotation.

The Kamchatka and Alaska region is shown in more detail in figure 4.7. The first row of this plot shows the multi annual average of the linear retrieval output over the region. In this, the plume tracks from large explosive eruptions in Alaska persist despite the averaging: demonstrating the significance of these eruptions. Elevated emissions from pollution in China and persistent degassing in Kamchatka are also visible. The chart beneath this shows when a signal was identified (using equation 4.1) and the intensity of this (equation 4.2). Immediately evident from inspecting this plot is that the signal is commonly elevated at multiple neighbouring volcanoes. As the volcanoes have been sorted by region and then by latitude, where proximate volcanoes have been flagged in a single month, this suggests that some of the alerts may be triggered by emissions from a different source. In some cases, the elevated emissions may also be caused by larger plumes from eruptions in Alaska and the Kuril Islands (e.g. Okmok and Kasatochi, Redoubt and Sarychev Peak in July-August 2008, August 2008 and June 2009 respectively) and Iceland (e.g. Holuhraun eruption in 2014-2015). This highlights the importance of investigating the data further or using multiple data sources. This could be done, for example, by looking at the IASI linear retrieval SO₂ output for individual IASI orbits or plume data from other instruments (in particular geostationary instruments with a high temporal resolution) which may help identify the plume sources. Thermal emission data from algorithms such as MIROVA or MODVOLC, or records of deformation from InSAR, could be particularly beneficial in these cases because these indicators of activity are usually limited to the flanks of the volcano. If using a rotation based approach

Figure 4.7: A more detailed look at Kamchatka, the Kuril Islands and Alaska. The top row shows the multi annual average (2007-2017) of the linear retrieval output over the region. The chart beneath shows the months in which a signal has been identified and the intensity of the emission index. The volcanoes are sorted first by region and then by latitude. Where multiple volcanoes, in close proximity, are flagged in the same month this may indicate false alerts.

to study long term emission trends at volcanoes, it is particularly important to consult other data sources in order to extract the true signal from the emission data. This problem is less likely in the OMI dataset because they applied a threshold to remove high SO_2 column amounts and so do not see large emissions of the gas. However, Carn et al. (2017) treated some volcanoes as one source (volcanoes less than 50 km apart; e.g. Bezymianny and Klyuchevskoy in Kamchatka), highlighting the difficulty of differentiating between some emission sources.

One of the advantages of using an infrared instrument like IASI is that these instruments are able to make measurements at night (meaning that there are multiple measurements each day) and during high latitude winters. Figure 4.8 shows the number of detections across the globe with the plume rotation algorithm in each month grouped by latitude. The results show that there are frequent detections in the high northern latitudes ($50-60^\circ$) where there are a large number of very active volcanoes in close proximity (e.g. Kamchatka). Marked on figure 4.8 are where the solar zenith angle at 13.30 UTC (the approximate time of OMI overpass) exceeds specified thresholds (70 and 90°) in each month. Where the solar zenith angle is greater than 90° there is no sunlight and therefore no results from UV instruments. This affects latitudes greater than 70° : which in this study only includes one volcano, Erebus. Note that, detections at Erebus are likely to be



false positives caused by an artefact in the linear retrieval. There is also a greater amount of noise in the UV data when the solar zenith angle is greater than 70° , thus increasing the detection limit (Carn et al., 2013; McCormick et al., 2013). Subsequently, the retrieval used in the Carn et al. (2017) paper removes all pixels where the solar zenith angle is greater than 70° . This then affects 34 of the 166 volcanoes considered in this study. Notably this includes those in Kamchatka, Alaska and Iceland: all regions where there is potential for significant disruption to aviation (Alexander, 2013; Dean and Dehn, 2015) and where the tropopause is lower meaning that emissions may reach the stratosphere where they can have climate impacts. The eruption of Bárðarbunga in Iceland in 2014-2015 is a good example of where there is a significant gap in the UV record and the advantage of using IASI alongside other instruments (Carboni et al., 2019). In total there are 3733 detections during the study period, 465 of which occur in high latitudes when the solar zenith angle exceeds 70° . This suggests that roughly 12% of the detections made with the plume rotated IASI linear retrieval data would have been missed by UV satellite instruments: although it should be emphasised that this does not take into account false detections or emissions missed by IASI. Given this, it is essential to use multiple instruments (including both UV and infrared sensors) together for the monitoring of volcanic plumes.

Elevated signals are also commonly identified in the tropics (roughly 23°S - 23°N). Within this latitude band are a number of very active volcanic areas including Central America, Ecuador, Colombia and Peru, Central Africa, the West Indies, Indonesia, the Philippines, Papua New Guinea and Vanuatu. Although there are commonly detections within these latitude bands, there are fewer than at high

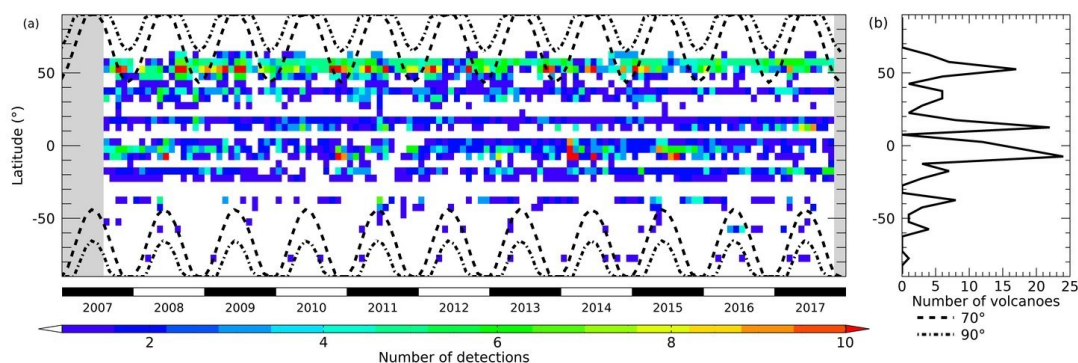


Figure 4.8: (a) The number of detected signals using the plume rotated approach for each month in the study period grouped by latitude. Marked on this are where the solar zenith angle at 13.30 (rough time of the OMI overpass) exceeds 70 and 90°. (b) The number of volcanoes in each latitude band.

northern latitudes, despite a larger number of volcanoes, something supported by figure 4.6. This region includes some of the most prolific degassers: 15 of the top 20 degassers in Carn et al. (2017) are within the tropics and yet many of these volcanoes are seldomly detected using the rotation detection scheme presented here. This reflects the different sensitivities of the two instruments used. The UV has a greater sensitivity to SO_2 emissions in the lower part of the troposphere than an infrared instrument using the ν_3 absorption band. At altitudes of 14-18 km the detection limit for the IASI linear retrieval using the ν_3 band is around 0.3 DU. However, this increases significantly (around 17.0 DU) closer to the surface (0-2 km) (Walker et al., 2012). This reflects the sensitivity of the retrieval to the difference between the surface temperature and the temperature of the atmosphere at the height of the plume. In addition, this application of the linear retrieval uses the ν_3 absorption band, which has some sensitivity to water vapour which can increase the amount of noise in the background atmosphere. Clarisse et al. (2012) notes that due to this retrievals using the ν_3 band are unlikely to perform well at

altitudes of less than 3-5 km. This to some extent explains the global distribution of detections shown in figure 4.6. A lower number of detections are seen in Indonesia, Papua New Guinea and Vanuatu, and where these occur they are often associated with large explosive eruptions such as the 2010 eruption of Merapi, which eject large quantities of SO_2 at higher altitudes. Similarly, signals are rarely detected at Kilauea in Hawaii (1222 m), which is reportedly emitting an average of 5019 t/d between 2005 and 2015 (Carn et al., 2017). An increase in the IASI emission index can be identified following the onset of increased activity and the emergence of the summit lava lake in April 2008 (see figure C.15 in appendix C). However, after 2008, there is an overall fall and stabilisation of the plume rotated emission index (equation 4.2), and fewer detections. It is likely that the magnitude of gas emitted during 2008 was sufficient to be visible with IASI but that as emissions decreased it fell beneath the detection limit.

The effect of height on the number of detections is partially demonstrated in figure 4.9d which compares these two values. The correlation coefficient describing the relationship between volcano height and the number of detections with the plume rotated algorithm is only 0.48. Figure 4.9d shows that there is a cluster of points where there are a low number of detections (fewer than 20): many of these are volcanoes which have lower levels of activity and are seldomly detected due to this. Despite this, the plot indicates that a greater number of detections are identified at volcanoes with higher altitudes. At these heights, the SO_2 emission is likely to be above the majority of the water vapour, and there will be a greater difference between the atmospheric and surface temperature. This may explain the greater number of detections identified at volcanoes in Central and South America, where

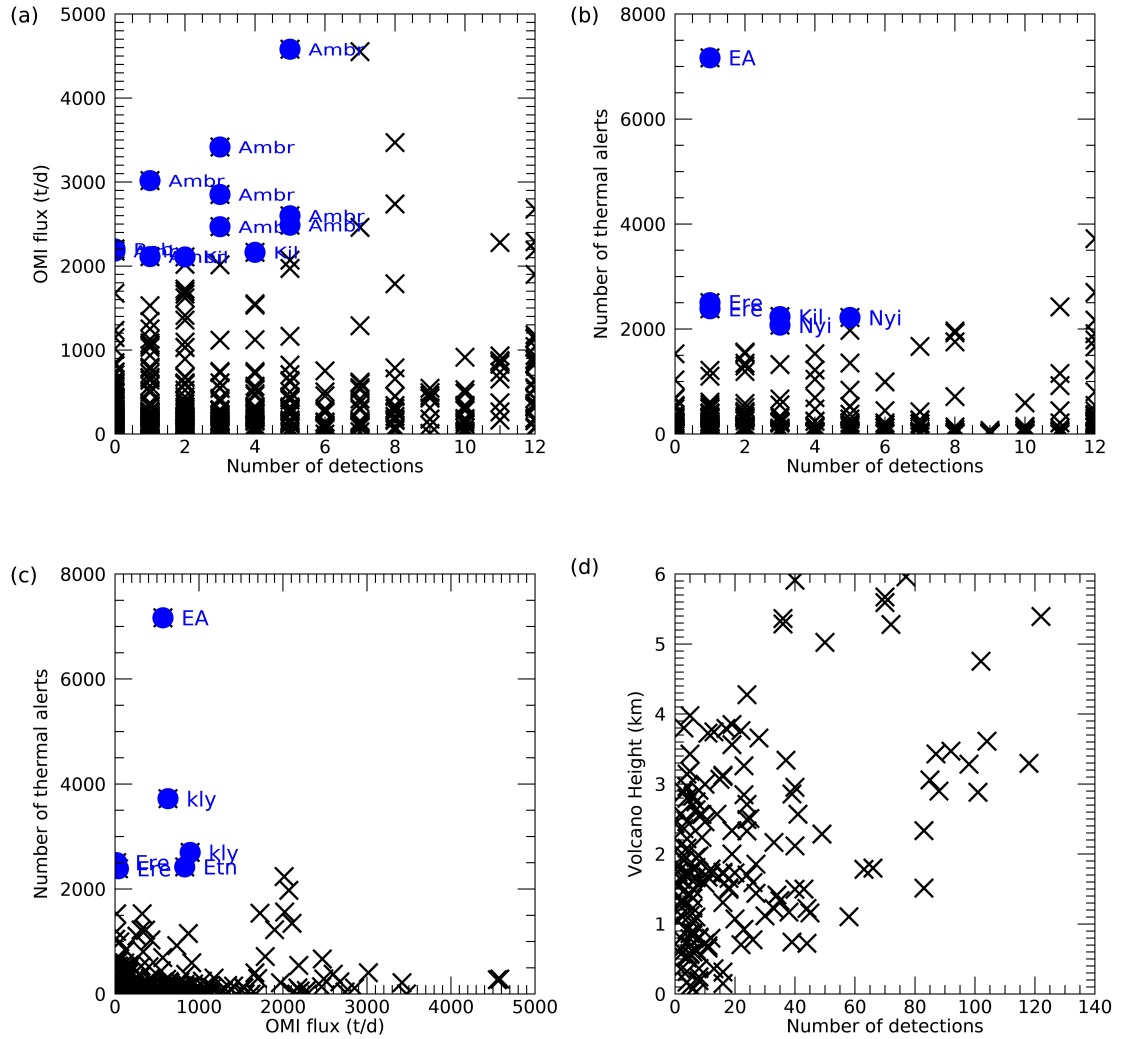


Figure 4.9: (a) Comparison of the number of detections with the IASI emission index against the flux obtained with OMI for each year. Highlighted in blue are examples where the OMI flux is high (greater than 2100 t/d) but the number of detections in the IASI plume rotated data are low (less than 6). (b) Comparison of the number of detections with the IASI emission index against the number of thermal anomalies detected with MODVOLC in each year. Highlighted are where there was a low number of detections within the plume rotated IASI linear retrieval data (less than 6) but the number of detections with the MODVOLC algorithm are high (greater than 2000). (c) The OMI flux compared against the number of thermal alerts detected with MODVOLC. In blue are examples where the number of thermal anomalies detected with MODVOLC are high (greater than 2000) but the OMI flux is fairly low (less than 2000 t/d). (d) Comparison of the IASI emission index against volcano height. The correlation coefficients describing these relationships are shown in table 4.3. The volcanoes which the labels refer to can be seen in table 4.2.

there are a number of high altitude volcanoes. For example Sabancaya and Ubinas in Peru peak above 5000 m. A summary plot for this region is shown in figure 4.10. The top row of this plot shows the multi-annual averages of the linear retrieval output over Central America, and the northern part of South America (2007-2017). This shows the strong emissions from some of the volcanoes in this region. It is possible to identify likely false detections at some neighbouring volcanoes, although far fewer than for Kamchatka and Alaska (figure 4.7). At some volcanoes, interesting trends can be seen in the emission index, some of which are explored in section 4.4.

Table 4.3 summarises the correlation coefficients describing the relationship between the metrics used in this section of this paper: the number of detections identified using the plume rotation algorithm applied to the IASI linear retrieval dataset, the OMI flux, the number of thermal alerts from MODVOLC and the height of each volcano. Figure 4.9a plots the number of times a signal was identified at each volcano in each year (using the plume rotation technique applied to the IASI linear retrieval data) against the OMI flux. This and table 4.3 confirms that there is a poor correspondence between these (a correlation of just 0.31), most likely for the reasons already mentioned in this section. Within this figure, a few cases

Table 4.3: Correlation coefficients describing the correspondence between the number of detections using the plume rotation technique applied to IASI SO_2 linear retrieval data, the OMI SO_2 flux, the number of thermal anomalies detected with MODVOLC and the height of the volcanoes studied.

	IASI	OMI flux (t/d)	MODVOLC	Volcano Height (km)
IASI	-	0.31	0.2	0.48
OMI (t/d)	-	-	0.2	-0.16
MODVOLC	-	-	-	0.16

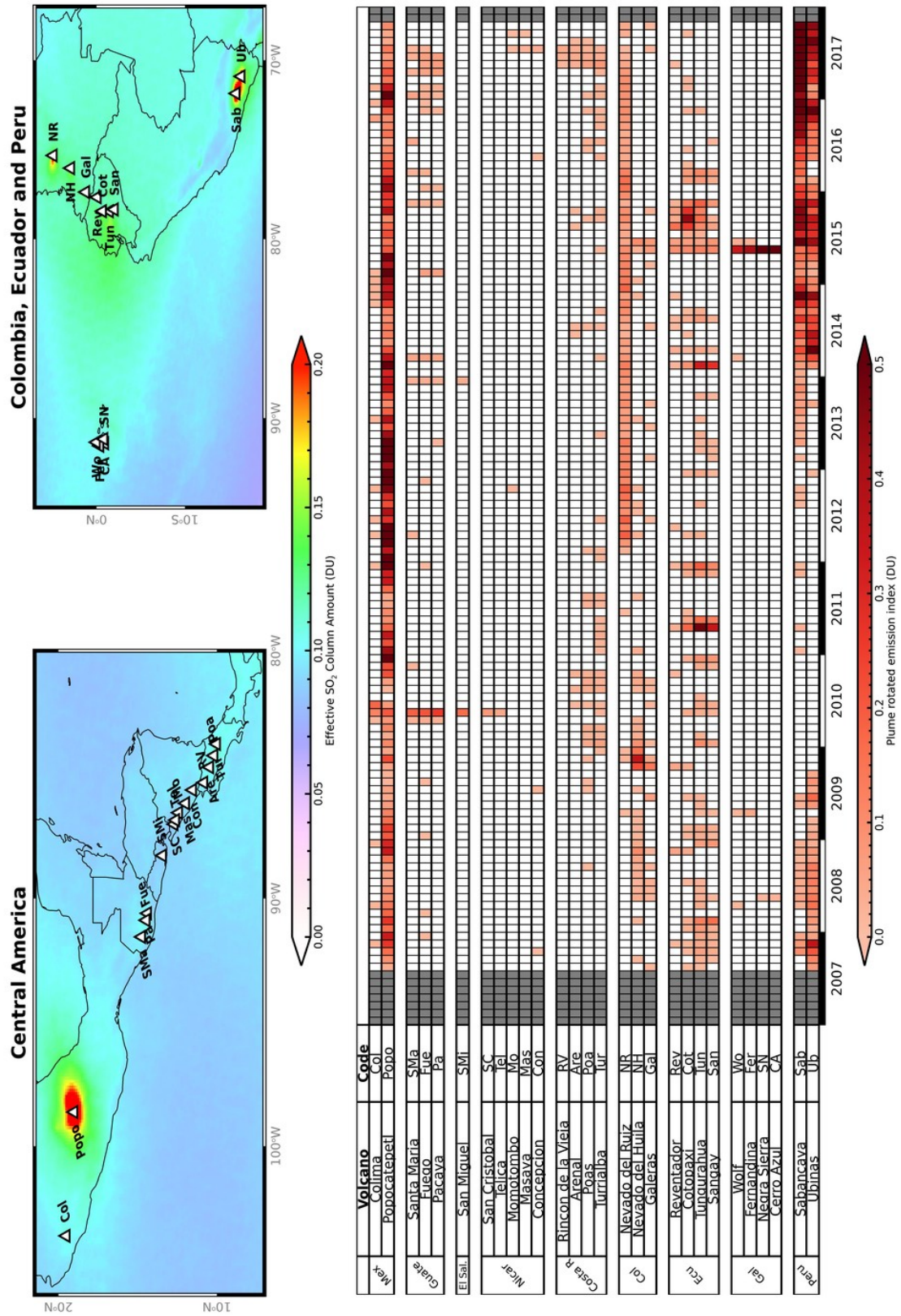


Figure 4.10: As figure 4.7 for Central and South America.

where the OMI flux is high (greater than 2100 t/d) but the number of detections with IASI is low (less than 6) are highlighted in blue. Of these 12 highlighted points, 9 are at Ambrym in Vanuatu: the strongest SO_2 source seen in Carn et al. (2017), emitting an average of 7356 t/d between 2005 and 2015. This volcano is in a tropical location and has a low altitude of 1334 m. It is therefore likely that the SO_2 emission is not normally sufficient to exceed the linear retrieval detection limit. This is also likely to be the cause of the low number of detections at Kilauea (Hawaii) in 2009 and 2013. Both Ambrym and Kilauea have basaltic magmas and lava lakes: the effects of these characteristics on the quantity of gas emissions is something that should be explored further in the future.

Figure 4.9b indicates that there is also a poor correspondence between the number of emission detections using the plume rotation technique and the number of thermal alerts from MODVOLC at each volcano. The number of thermal alerts detected with MODVOLC is also shown to correlate poorly with the OMI flux (-0.16 correlation coefficient). Figure 4.9b and c highlight some of the cases where the number of thermal alerts are notably high (greater than 2000 detections) compared to the number of detections using the plume rotation algorithm applied to the IASI linear retrieval (less than 6 detections) data and the OMI flux respectively (less than 2100 t/d). Common to both is the Erta Ale eruption in Ethiopia in 2017, during which there were extensive lava flows and a lava lake (GVP, 2017a), leading to a high number of thermal alerts (greater than 6500 alerts in 2017). Figure C.10 in appendix C shows a summary plot for this volcano. Within this an increase in the OMI flux is seen within 2017. However there is no change in the IASI emission index timeseries. Given the height of this volcano (613 m) it is likely

that the SO₂ emission was not strong enough for it to be identified in the lower part of the atmosphere. The other highlighted examples in the comparison of the number of elevated signals identified with the plume rotation technique and the number of MODVOLC thermal alerts are all from volcanoes with lava lakes (Erebus, Kilauea, Nyiragongo) which explains the greater number of thermal alerts. The 2008 eruption at Etna is highlighted in the comparison of the number of thermal alerts and the OMI flux (figure 4.9c). The May 2008 eruption was characterised by extensive lava flows and fire fountaining leading to the increased thermal alerts (GVP, 2008; Bonaccorso et al., 2011). The significant amounts of SO₂ from this eruption (an increase can be seen in this month using the IASI plume rotation in figure C.11 in the appendix) will have been removed in the Carn et al. (2017) analysis which removes all SO₂ emissions above a threshold. The other highlighted volcano in figure 4.9c is Klyuchevskoy (2010, 2016) in Kamchatka. Again, it is likely that this is because of removal of SO₂ flagged pixels reducing the magnitude of the flux, relative to the number of thermal alerts.

Overall the results in figure 4.9 suggest that there is a poor correspondence between the different metrics used. The correlation coefficients describing the correspondence between the emission index computed using the plume rotated approach for the IASI linear retrieval data and the OMI flux, and with the number of thermal alerts from MODVOLC, for each volcano are listed in table 4.2. This indicates that these vary significantly between each volcano. A histogram showing the distribution of these results can be seen in figure 4.11. This implies that these metrics are difficult to compare globally but that there are strong agreements at individual volcanoes. It is important to remember that the three datasets compared

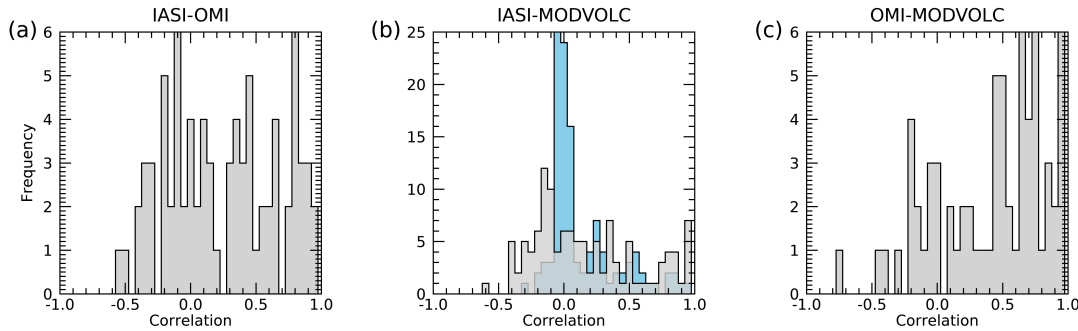


Figure 4.11: (a) Distribution of the correlation coefficients describing the relationship between the annual IASI emission index (plume rotation, equation 4.2) and the yearly OMI fluxes for each volcano. (b) Distribution of the correlation coefficients describing the relationship between the IASI emission index (plume rotation) and number of thermal anomalies detected using MODVOLC. Comparison of yearly values are shown in gray and a monthly comparison shown in blue. (c) Distribution of the correlation coefficients describing the relationship between the yearly OMI flux and the number of MODVOLC thermal anomaly detections in each year.

here are all measures of different things. Each has its own strengths and limitations and it is therefore unsurprising that the correlation coefficients describing the correspondence between them can be quite variable. Future studies would benefit from combining the results from these datasets, other satellites products and ground based measurements to get a comprehensive view of volcanic activity.

4.4 Case Studies

In the previous section it was demonstrated that there is not necessarily a good agreement between the number of detections with the IASI plume rotation algorithm and the flux values obtained with OMI across the globe, but that there were individual cases where there is a strong correspondence. This section explores the trends observed at a few volcanoes. Figures 4.12 to 4.17 summarise the results for the rotation algorithm for 7 volcanoes in Central and South America: one

of the regions where elevated emissions were commonly identified in section 4.3. Equivalent plots for 36 volcanoes (including the top 20 most frequently detected volcanoes with the plume rotation technique and any others discussed in this paper) are available in the appendix C.

4.4.1 Popocatépetl, Mexico

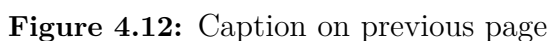
The volcano where elevated emissions were most frequently identified was Popocatépetl in central Mexico. In fact, a signal was observed in almost every month studied (122 out of 123). This is likely to be because Popocatépetl is one of the highest targets in this study at 5393 m and it is one of the most active volcanoes in the region (Grutter et al., 2008; Delgado Granados and Cardenas Gonzalez, 2013; Campion et al., 2018). Previous flux estimates have suggested emissions vary between 3000 and 5000 t/d for degassing, but rise considerably (25000 t/d) during eruptive episodes (Delgado-Granados et al., 2001; Grutter et al., 2008; Campion et al., 2018; Taquet et al., 2019).

It is perhaps the ideal target for this technique as it is far from other significantly degassing volcanoes. There are some pollution sources in the region, for example a power plant and oil refinery at the Tula industrial complex, roughly 60 km northwest of Mexico city. A small increase in the effective SO₂ column amount can be seen to the north east of the volcano in the annual and multi-annual unrotated averages in figure 4.12, which is the rough location of this industrial centre. Between 2007 and 2017 the OMI SO₂ flux database indicates that the emission from the Tula industrial complex was between 136 and 295 t/d (Fioletov et al., 2016; MEaSURES, 2019). This is fairly insignificant compared to Popocatépetl where the flux reportedly ranges from 325 to 1180 t/d (and this value excludes higher column amounts and

therefore the larger eruptions at Popocatépetl). Given this it is unlikely that this source would greatly effect the IASI emission index computed for Popocatépetl.

Figure 4.12 summarises the activity at this volcano during the studied period. Here a close match can be observed between the IASI emission indices, the flux obtained with OMI and the number of MODVOLC thermal alerts with correlation coefficients of 0.86 and 0.85 respectively. Such a close match between the emissions seen with IASI and OMI, implies that despite applying a threshold to remove large column amounts of SO_2 before computing a flux, the approach taken by Carn et al. (2017) may not always be accurately distinguishing between plumes from eruptive and passive activity. This problem was acknowledged by Carn et al. (2017) and

Figure 4.12: Annual summary plot for Popocatépetl, Mexico. The first row shows a map of the region used for the initial processing (a 12° box around the volcano). The number of volcanoes, which have been active since 2007, within specified distances are listed to the right of the map (these are also plotted on the map in the corresponding colours). This gives some indication of the potential for false classifications and contamination of the computed emission index. In this case, there are no volcanoes within 300 km making it unlikely that there is contamination from other volcanic sources. To the right of this are plots showing the multi-annual average (2007-2017) for the unrotated (UR; included as these help identify other SO_2 sources in the region), unrotated without SO_2 flagged pixels (UR - PE), passive emission rotation (PER), vent rotated (VR) and plume rotated grids (PR). Note that these have been reduced to 200 km from the volcano to better show the plumes. Beneath this are the equivalent plots for each year (years going across, and the different grids going down). The third plot shows the vent (blue) and plume (red) rotated emission index (equation 4.2) for each year along with the flux obtained with OMI (right axis) and the number of thermal anomalies identified by MODVOLC in each year (2nd axis on the right). The chart beneath this shows the emission index computed using passive emission, vent and plume rotated methods respectively. An increase in colour intensity implies an increase in SO_2 emission. The final line shows the number of MODVOLC thermal anomalies for each month studied.



Activity is shown to increase from 2009, peaking in 2012, before falling again, with a second peak in activity seen in 2015. The monthly emission index shows gradual increases and decreases in the amount of SO₂. For example, the SO₂ emission is shown to climb slightly from the end of 2011 to a peak in April and

May 2012, which corresponds to the frequency of plumes noted in the May 2012 GVP bulletin report (GVP, 2012*c*). A slow decrease in emission is seen throughout 2012 and remains low in 2014. A similar behaviour is seen in the MODVOLC alerts. The GVP bulletin report for February 2015 (GVP, 2015*a*) note that throughout 2014 there were a lower number of alerts of ash plumes issued by the Washington VAAC, although these still occurred almost every month. A second peak in activity can be identified in 2015, with a greater emission seen at the beginning of the year. A slightly seasonal trend may be visible: with both the emission index and number of thermal alerts increasing in November to February each year. It is possible that both the IASI linear retrieval and MODVOLC may be exhibiting a seasonal bias. With the IASI linear retrieval this might be related to the use of a standard atmospheric profile (which does not vary seasonally) and covariance matrix which may not perfectly represent conditions in this region. It is possible that both the IASI linear retrieval and MODVOLC thermal detections, may have a seasonal bias due to cloud cover obscuring plumes or hot spots. For the linear retrieval the use of the upwind mean within the emission index should reduce a seasonal bias to some extent but further bias correction (e.g. Taylor et al., 2018) could be considered in the future. A seasonal bias in the linear retrieval output is not something that is immediately obvious at other volcanoes and should be explored further.

It would be interesting to explore the emissions at this volcano further using the Carboni et al. (2012) iterative retrieval which can quantify the amount of SO_2 . In general, it would be expected that there would be an increase in SO_2 with an increase in the extrusion of lava; although, at times obstructions in the vent may suppress gas emissions. To truly capture the pulses in and the nature

of lava extrusion and subsequent effects of gas emissions, it would be essential to consider the IASI gas data and the thermal anomalies at a finer temporal resolution (weekly, daily, sub-daily). Potentially, it would also be better to use the more sensitive MIROVA algorithm. The success of the plume rotation technique here also makes it an ideal test case for investigating the heights of plumes using the method outlined in section 4.2.3, for which a comparison against the iterative retrieval heights would be a good first step.

4.4.2 Sabancaya and Ubinas, Peru

Ubinas and Sabancaya are volcanoes in Southern Peru which are just over 120 km apart. They are both significant emitters of volcanic gases, and IASI data has previously been used to complement ground based measurements at these two volcanoes (Moussallam et al., 2017), demonstrating an increase in activity in late 2012 and late 2013 respectively. The annual summary plots for Ubinas, figure 4.13, shows that between 2007 and 2009 the SO₂ emission from the volcano fell. This corresponds to observations of the volcano's activity outlined in Rivera et al. (2010, 2014): eruptive activity beginning in March 2006, intensifying between April 2006 and September 2007, and then activity declining until the end of 2009. Between 2009 and 2013, the annual IASI emission index for Ubinas remains fairly constant, with only a few alerts in the monthly analysis. This is followed by a significant rise in 2014, which is also apparent in the OMI annual flux. This is accompanied by an increase in the number of thermal anomalies detected with MODVOLC. This corresponds to a new eruptive phase which began in September 2013 (as can be noted by the increase in the emission index seen in this month) with activity peaking

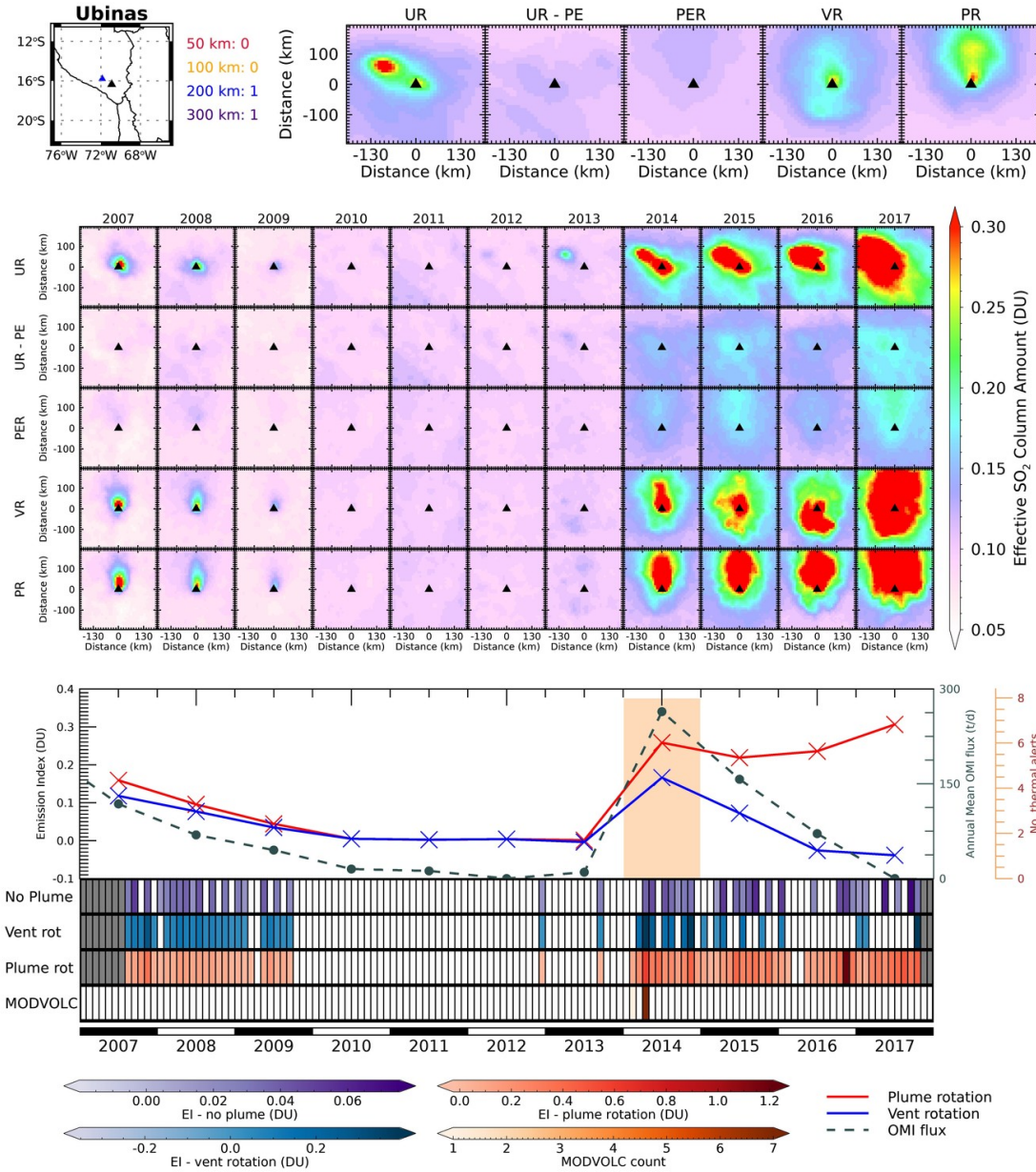


Figure 4.13: As figure 4.12 for Ubinas, Peru

in April 2014 (Coppola et al., 2015). Following 2014, a departure is seen between the trends in the OMI flux dataset and the plume rotated IASI emission index. This is following an increase in activity at the nearby Sabancaya volcano, whose activity also increased in 2014. As the plume rotation technique identifies plumes within 200 km of the volcano in question it can be affected by other emissions in

the area. When this occurs (i.e. if two volcanoes within a close distance of each other are both flagged as having an elevated signal) then it is important to consider other data sources. This is avoided in the OMI dataset by removing pixels with elevated SO₂ amounts from the analysis; however, this then removes emissions from explosive eruptions. In this case, a better representation of the trend in activity can be observed in the IASI vent rotated emission index, which following the peak in activity in 2014 shows a decrease in the SO₂ amount, closer to the trend seen with OMI and with activity noted in literature.

By contrast, the impact of Ubinas on the emission index trend of Sabancaya is smaller, although some false alerts can be seen in the monthly emission index between 2007 and 2010. The annual average plots for 2007-2009 clearly reveal a second emission source in the region encouraging wariness when interpreting the results. Despite this, the yearly emission index is shown to be fairly constant between 2007 and 2012. In December 2012, activity at Sabancaya increased after fifteen years of quiescence. Two phreatic eruptions occurred in August 2014 (Moussallam et al., 2017) resulting in a slight intensification in the monthly emission index. Moussallam et al. (2017) also notes that ash plumes were emitted in November 2012: a month which is again associated with an increase in the monthly emission index. The yearly and monthly emission index (both plume and vent rotated) shows an intensification of the SO₂ signal at the volcano between 2013 and 2017, peaking in 2017 when thermal alerts were also reported at the volcano. MIROVA, which has a greater sensitivity to thermal emissions than MODVOLC, indicated the first thermal emissions in November 2016, which is the month with the greatest monthly

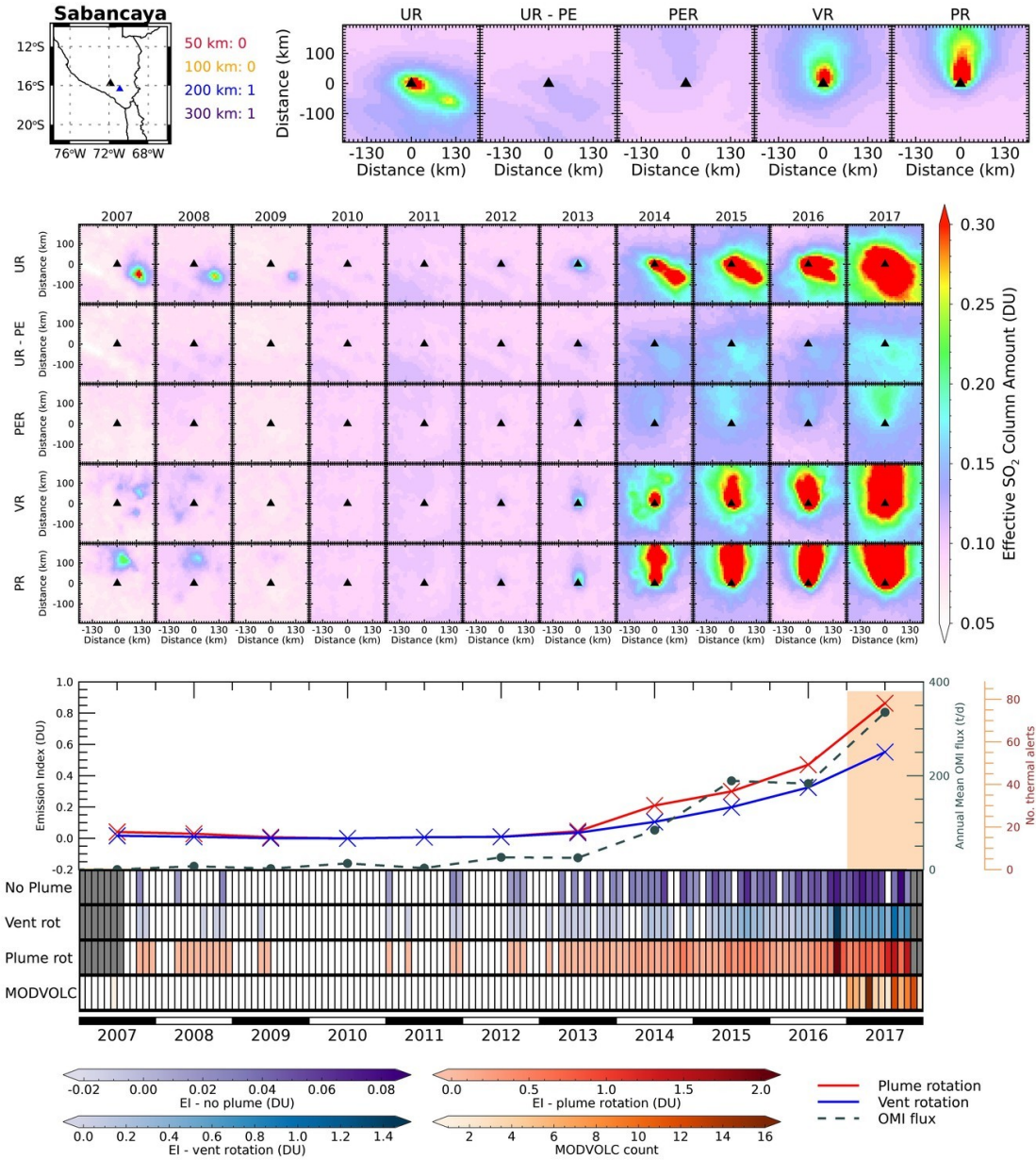


Figure 4.14: As figure 4.12 for Sabancaya, Peru

plume rotated emission index. Overall, the plume rotated emission index agrees well with the OMI flux measurements with a correlation of 0.97.

The results at these two volcanoes are very encouraging implying that the emission index is capturing the changing activity levels at both volcanoes. Like Popocatepetl, the measurements here are helped by the high elevation of the two

volcanoes, both having vents above 5.5 km.

4.4.3 Nevado del Ruiz and Nevado del Huila, Colombia

Figures 4.15 and 4.16 show the annual summaries for Nevado del Huila and Nevado del Ruiz in Colombia. Figure 4.15 shows that elevated emissions were detected at Nevado del Huila for the first half of the study period. Emissions are shown to increase between 2007 and 2009, before falling and then remaining fairly constant for the remainder of the study period. This is fairly similar to the trends seen with OMI and the thermal anomalies with correlations of 0.85 and 0.82 respectively. A small increase in the plume rotated emission index is seen in 2015, while the vent rotation emission index remains low. This is likely to have been influenced by the eruption of Wolf volcano in the Galapagos in May. Wolf produced a 15 km high SO₂ cloud, with an estimated mass of around 200 kt (GVP, 2015b). This travelled eastward across northern South America and led to false detections at a number of volcanoes in this region as can be seen in figure 4.10. This again highlights the importance of manual interpretation of the results. Where multiple volcanoes in the same region are flagged at the same time, or there are differences in the plume and vent rotated emission indices, the data should be carefully evaluated to ensure that the results are understood correctly.

Nevado del Ruiz exhibits an opposite trend to Nevado del Huila. For the first few years of this study, only a few months have flagged emissions and these are likely to be false alerts caused by plumes from other volcanoes. From December 2011, an elevated signal is detected in every month to the end of the study period. The gas emission is shown to increase significantly in 2012. The GVP bulletin report

for Nevado del Ruiz in August 2012 (GVP, 2012b) notes that there was steady increase in SO_2 emissions between 2010 and 2012, measured with ground-based DOAS instrument, with a dramatic increase in activity in February 2012 (when emissions are first detected with IASI), with SO_2 emissions peaking in May and June 2012 at 33,000 t/d, again reflected in the monthly emission index computed

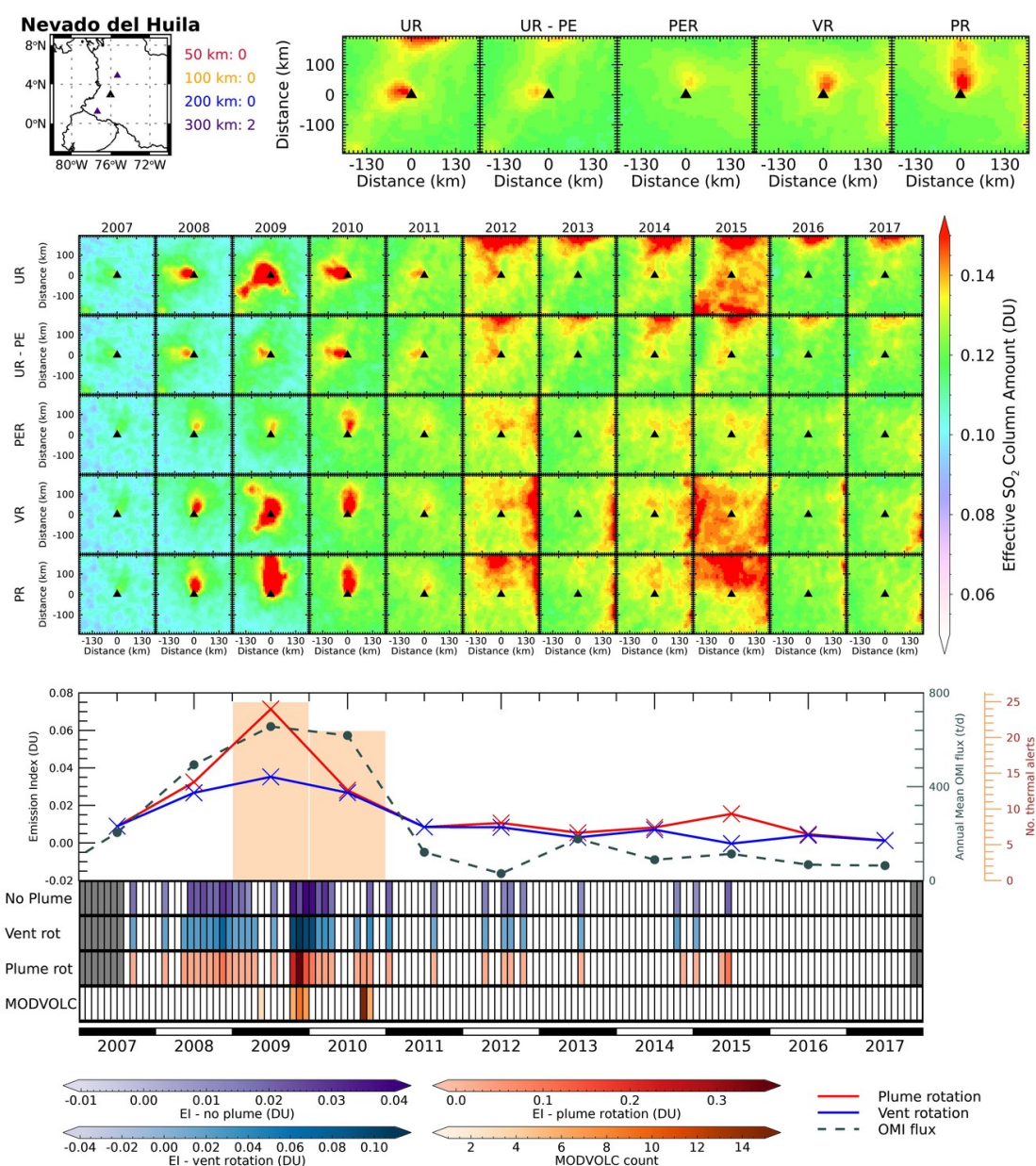


Figure 4.15: As figure 4.12 for Nevado del Huila, Colombia

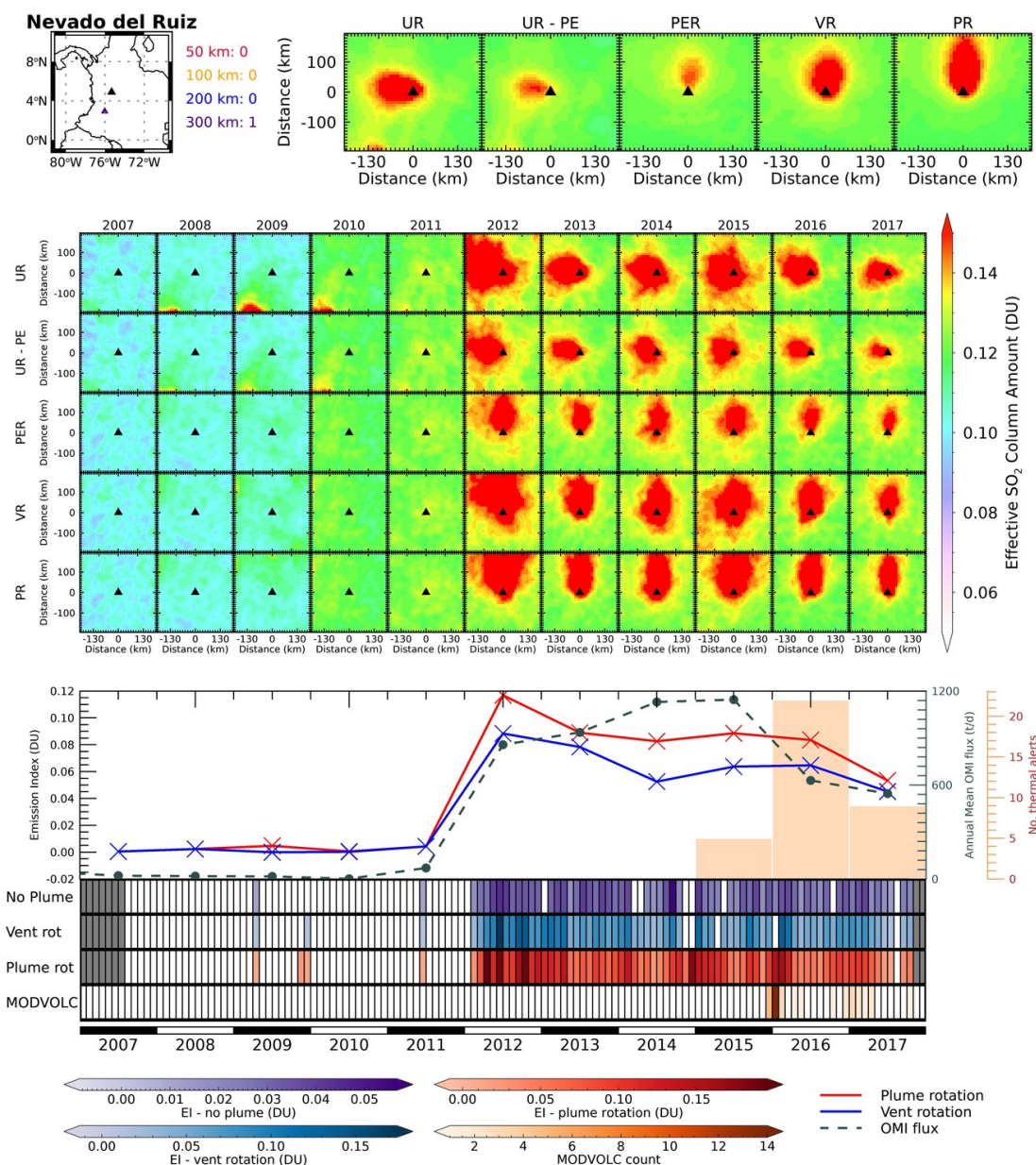


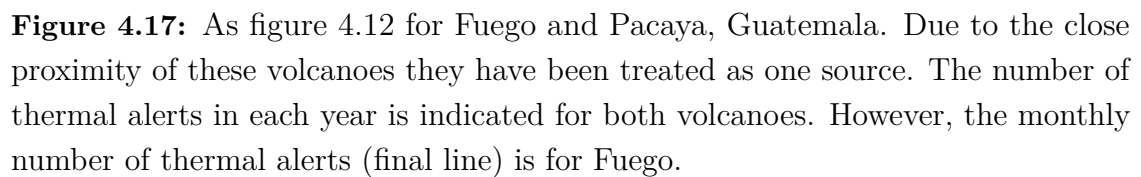
Figure 4.16: As figure 4.12 for Nevado del Ruiz, Colombia

from the IASI linear retrieval data. Following 2012, there is a slight decrease in the IASI emission index. This is in contrast to the OMI flux which sees an increase in emission. This may reflect the different nature of the two techniques: with the IASI rotation including all activity types and the OMI flux reflecting passive emissions only. Despite this the correlation coefficient with the IASI plume rotation method is

high at 0.93. A much lower correlation coefficient (0.33) is obtained when compared against the number of thermal anomalies which only begin in late 2015, four years after the gas emissions increased. This could possibly be related to the extrusion of a lava dome in the latter part of 2015 for which there is some seismic evidence as well as an increase in the number and magnitude of thermal anomalies (GVP, 2017b).

4.4.4 Pacaya and Fuego, Guatemala

Figure 4.17 shows summary plots for Fuego and Pacaya in Guatemala. These volcanoes are within 35 km of each other and so have been considered together, as they were in Carn et al. (2017). The annual averages show a peak in activity in 2010 with the strongest signal being seen in May. This corresponds to an explosive eruption at Pacaya during which there was significant ash emission and extensive lava flows (GVP, 2010b), thereby causing a considerable increase in the number of thermal alerts. Following this a steady increase in the emission index can be observed culminating in 2017. This reflects an increase in activity at Fuego volcano as noted by Naismith et al. (2019). In their study they suggest that a new eruptive regime began in 2015 after which there were a greater number of paroxysmal eruptions usually preceded by lava effusion. This changing activity is captured well in the IASI plume rotated emission index and the OMI flux data. The two agree reasonably well with a correlation of 0.6. This value is lower than for other volcanoes explored in this section, but highlights one of the main differences between the IASI and OMI datasets: the OMI flux removed high column amounts to get a number more indicative of the emission from non-eruptive degassing, which would remove the significant eruption from Pacaya. The vent rotated emission



index departs from the plume rotated index in 2017. This implies that the plume is emitted at heights greater than the volcano.

4.5 Decadal changes in volcanic emissions

In the previous section it was shown that at a few volcanoes it is possible to observe changes in volcanic activity with the emission index (equation 4.2) computed from the plume rotated data. It is a useful exercise to consider how emissions have varied over the decade studied, and if these changes are the same as those identified in the UV flux dataset. This was done by applying a linear fit to the plume rotated emission index for each volcano studied. The standard deviation of the upwind column amounts (σ_u), which represents the background variability, was used as the error within this computation. There were few volcanoes for which the linear fit is considered a good representation of the data (based on there being a probability of 0.1 or greater that the computed goodness of fit has at least a value of chi-squared). This is not surprising. Firstly, because the error used to perform the linear fit is very small (the error with respect to the signal, \bar{x}_d , is usually less than 5%), making it unlikely that the model will fit the measurements. In addition, there are spikes in the timeseries which mean that the linear fit may not be applicable. There is also the question of whether or not a linear trend is really appropriate for describing changes in gas emissions at volcanoes. At Sabancaya, for example, the increase in SO₂ with the plume rotated approach is shown to be exponential. In contrast, a step change can be seen at Nevado del Ruiz in 2012. As a result, the values computed here are simply used as an indicator of whether there has been

an overall increase or decrease in SO₂ emissions during the studied time period and should not be interpreted as a linear change in emissions.

A linear fit was applied to all volcanoes for which the linear correlation coefficient (r ; describing the strength of the linear relationship) was greater than 0.5 or less than -0.5, as in Carn et al. (2017). Of the 166 volcanoes studied, 11 exhibited a positive trend ($r > 0.5$) and 28 showed a negative trends ($r < -0.5$). A subset of these volcanoes, chosen because they were included in the Carn et al. (2017) trend analysis or because of their inclusion in section 4.4, are shown in figure 4.18a. These plots show the changing plume rotated emission index and the computed linear fit and are colour coded based on the gradient of the linear fit: which gives an impression of whether there has been a positive or negative change in SO₂ over this period.

In their analysis Carn et al. (2017) found 32 volcanoes for which a linear fit could be applied ($r > 0.5$ or $r < -0.5$). This linear fit has been recomputed, using the same routine applied to the IASI emission index, from the MEaSURES (2019) dataset available online, which contains the annual fluxes for each year considered in the current study (2007-2017). Note that this excludes volcanoes which were not listed as having being active since 2007 in the GVP (2013f) database. The linear fit gradients computed from the OMI fluxes and IASI emission index are compared in figure 4.19. This is divided into four boxes which indicate whether the two techniques are observing the same positive or negative trends. First inspection of this plot suggests that for the most part this is the case. However, of the 23 volcanoes analysed, only four had values for r which exceeded 0.5 or were less than -0.5 in both datasets. Of these, a downward trend is observed in both the OMI fluxes and IASI emission index at Nevado del Huila and Miyakejima. However, this

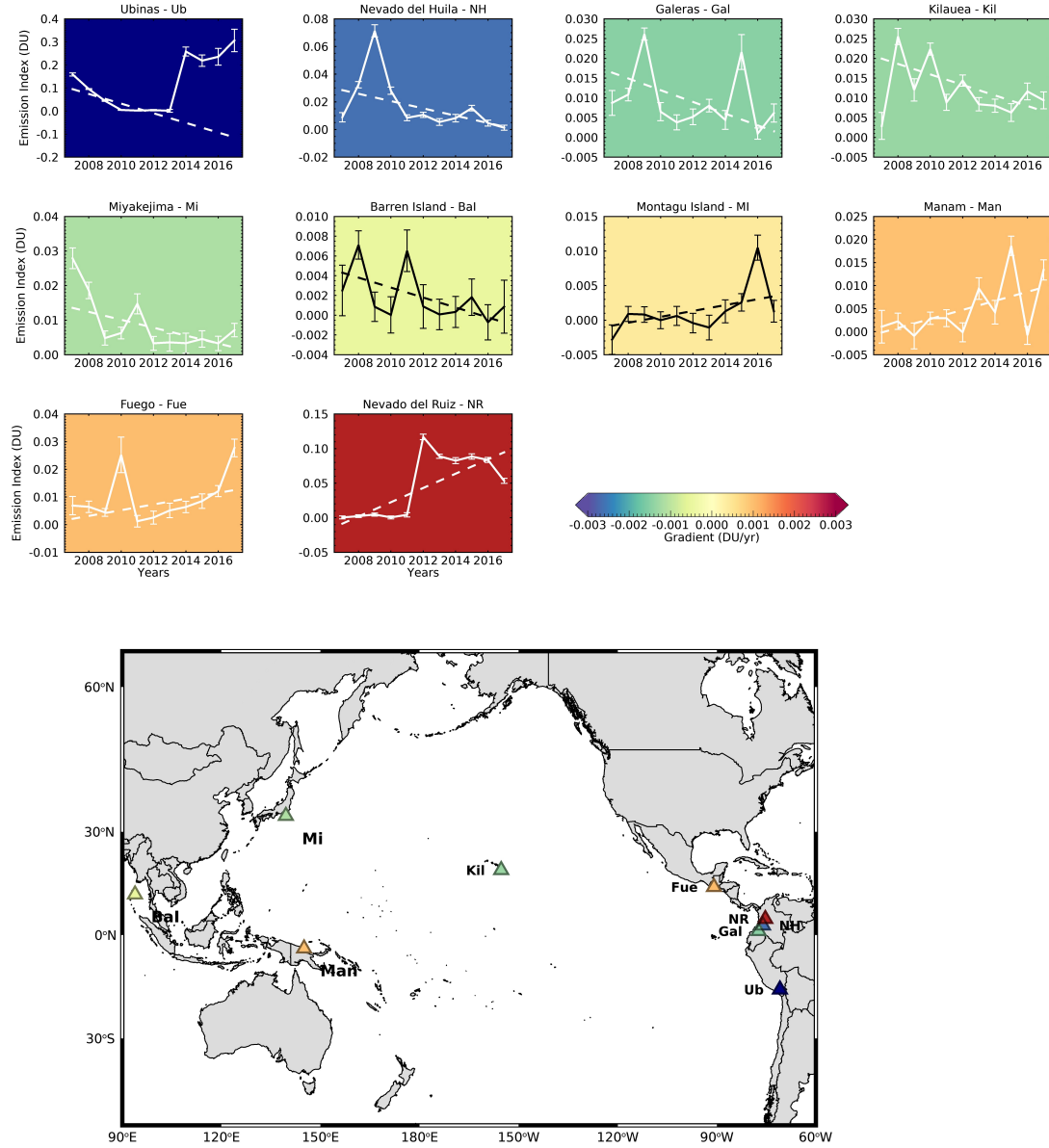


Figure 4.18: The graphs show how the plume rotated emission index varies over the 11 years studied for 10 volcanoes. These have been colour coded according to the gradient computed with the linear fit. Overplotted on this is the linear fit. The map shows the location of these volcanoes and again the symbols are colour coded by the computed gradient. The volcanoes are labelled with the codes listed in table 4.2 and can also be seen in the titles of the graphs above.

is not the case at Montagu Island (a positive trend is seen with IASI and not with OMI) or Kilauea (positive trend seen in the OMI fluxes but not in the IASI emission index). At Montagu Island this is due to a spike in the emission index in 2016: it is unclear if this is a true signal as there are no reports of activity in this month. At Kilauea, it is possible to identify a downward trend in both datasets (figure C.15), following an increase in the SO₂ flux in 2008. The linear trend computed for OMI has been greatly affected by the increased emission between 2007 and 2008: highlighting a limitation of using a linear trend when there may be jumps in the dataset used. If removed a downward trend would also be observed.

There are many volcanoes for which a strong correspondence ($r > 0.5$ or $r < -0.5$) could be seen in the OMI fluxes but not in the IASI emission index. Figure 4.19 indicates that many of these cluster around where the gradient of the linear fit describing the IASI data is around 0. This implies that the IASI emission index is showing little change. This is related to some of the limitations noted in section 4.3, primarily the height of the emitted plumes. For example, Yasur and Dukono have altitudes of less than 1300 m. Another reason why trends can be observed with the OMI fluxes and not in the IASI emission index (and vice versa) are the different natures of the two techniques: the OMI fluxes emitting large plumes while the IASI emission index incorporates these. This affects the appropriateness of fitting a linear line to the respective datasets. For example, at Sabancaya (Peru), there is an exponential increase in the IASI emission index which is more extreme than that seen in the OMI fluxes due to the inclusion of large plumes. Similarly, at Ambae (Vanuatu) a sudden step increase is seen in 2017 in the IASI emission index following a large eruption (GVP, 2018). This increase is amplified by few

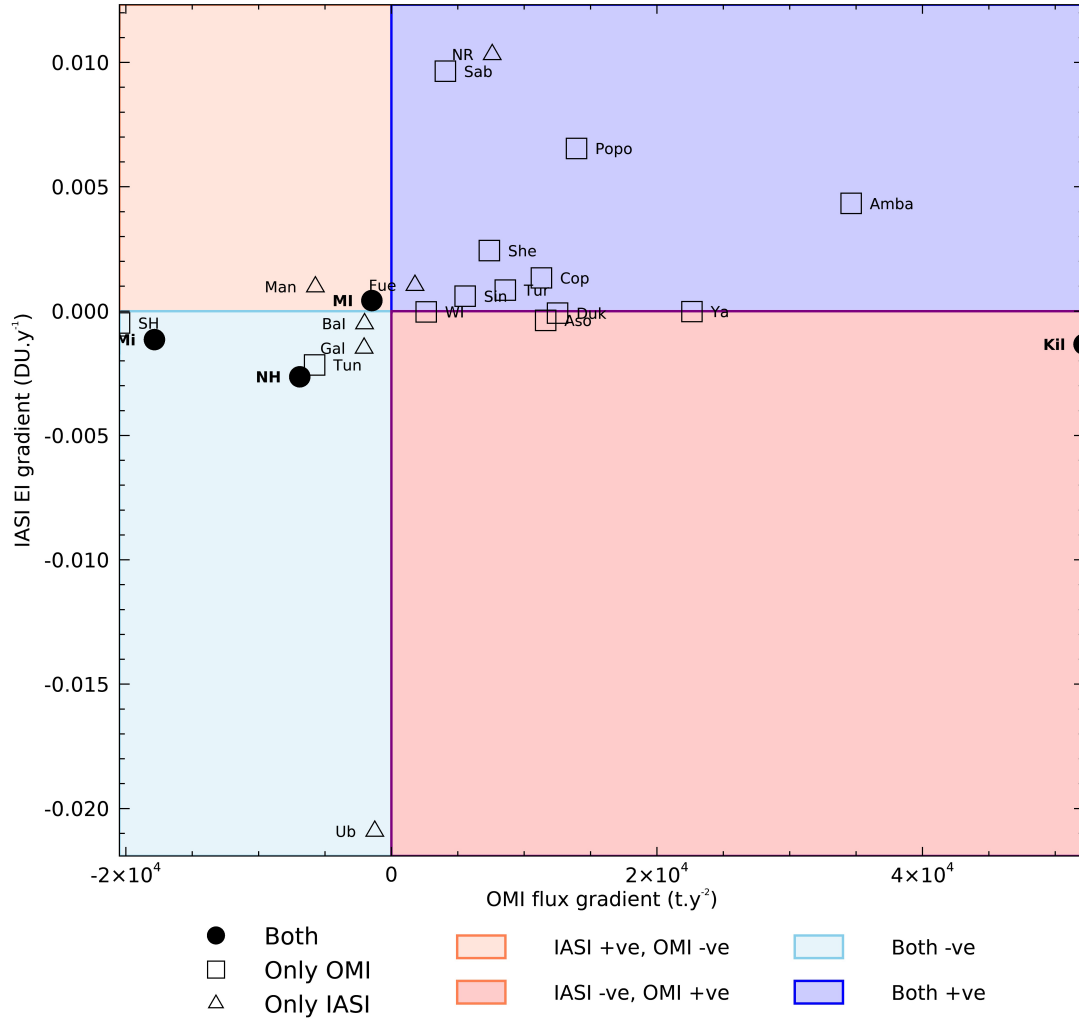


Figure 4.19: A comparison of the gradients computed with a linear fit applied to the IASI plume rotated emission index and the OMI fluxes from Carn et al. (2017). The filled circles indicate where $r \leq 0.5$ or $r \geq 0.5$ for both techniques. Squares indicate where this was only the case for the OMI fluxes and triangles indicate where this was only true for the IASI plume rotated emission index. The plot is divided into four rectangles (clockwise from the top left): negative trend seen with the IASI plume rotated emission index, positive trends seen with both, positive trend seen with OMI but not IASI and negative trend seen with both. Each point is labelled with the codes listed in table 4.2.

detections prior to the eruption in 2017 (due to the height of emissions) and the inclusion of high SO₂ column amounts in the data. For both Sabancaya and Ambae a linear fit is not an appropriate descriptor of the emission index timeseries.

Applying a linear trend is a useful tool for assessing broad changes in activity. This could be useful for comparisons against other datasets which show changes in volcanic behaviour. In some cases there may be potential to identify precursory signals. However, as mentioned before, the results from a linear trend should be considered very carefully, as it is not expected that volcanoes behave linearly. An interesting future direction would be to look at cycles and trends in the monthly emission index or even finer temporal resolutions. Comparisons of this with a similar product from UV instruments, and other satellite and ground based indicators of volcanic activity, might give greater insight into volcanic processes.

4.6 Conclusions

This study investigates how the linear retrieval developed by Walker et al. (2011, 2012) can be used to monitor emissions of SO₂ across the globe. It takes a similar approach to Ebmeier et al. (2014), Fioletov et al. (2016) and Carn et al. (2017) by rotating the linear retrieval output so that the plume is always aligned to the north. A simple comparison of the upwind and downwind signal can then be used to indicate when and where there are elevated emissions, and can show changes in the magnitude of these. Unlike the paper by Carn et al. (2017), this study investigated finer time scales, thereby offering more information on how the emissions varied over time. Also, the main rotation approach taken in this paper did not discount

emissions from large eruptions where measurements are crucial for understanding the impacts of these plumes. This also avoided the difficulty of defining a threshold between passive and eruptive degassing. It did however, come at the cost of a greater number of false detections, which was a particular limitation in regions with lots of volcanoes in close proximity.

Applying this method systematically to volcanoes across the globe demonstrated the strengths and weaknesses of the IASI linear retrieval. For example, it highlighted that the retrieval, which is using a part of the infrared which is also sensitive to water vapour, does not generally perform well at volcanoes at lower altitudes. That is, unless these volcanoes erupt explosively so emitting large quantities of SO_2 higher up in the atmosphere. This observation is inline with previous studies. Where the technique did perform well was at high altitude volcanoes, such as those in Central and South America. Here there were regular detections, and a simple difference in the mean upwind and downwind column amounts revealed changes in emissions that matched closely with the fluxes produced from OMI data, thermal alerts and observations made in literature. In addition, there is a considerable advantage to using infrared instruments such as IASI for monitoring in low UV conditions. In this paper, there are gaps in UV monitoring for 34 of the 166 volcanoes studied.

There is considerable potential for further study using this technique. Adaptations could be made to the rotation algorithm such as the inclusion of tests which can evaluate the likelihood that the rotated plume originated from the volcano in question. An obvious future direction would be to apply the rotation tool to the the Carboni et al. (2012) retrieval, after which it would be possible to compute a flux: which is more directly comparable to the results from Carn et al. (2017).

Future studies might also want to utilise the comprehensive dataset produced here alongside other data products (both SO₂ and other indicators of volcanic unrest) to further investigate activity at individual volcanoes and across arc settings.

Retrievals developed for the IASI instrument have been underutilised in studies of long-term emission trends at volcanoes. This study builds on that by Taylor et al. (2018) to demonstrate that while this tool has some limitations, it can address some of the weaknesses of other instruments. Ultimately, the use of multiple satellite tools together will ensure the most reliable understanding of volcanic activity.

5

Conclusions

5.1 Overview of results and future work

This thesis explored a number of different ways in which the IASI instrument can be used to monitor volcanic activity.

CO₂ Slicing

Chapter 2 demonstrated that the CO₂ slicing technique, which has been extensively used to obtain the height of meteorological clouds, could also be successfully applied to volcanic ash. When applied to simulated ash spectra, the technique was shown to successfully obtain the ash heights. However, it was noted that it did not perform so well for ash with low optical depths or close to the surface

because of a low signal compared to the instrument noise. It was also shown to perform badly in isothermal conditions. Having demonstrated that the technique performed well for the simulated cases, the technique was applied to scenes from the Eyjafjallajökull and Grimsvötn eruptions. The technique was shown to perform better than the Ventress et al. (2016) optimal estimation scheme when compared against the backscatter profiles from CALIOP.

Further work is encouraged to fully appreciate the strengths and limitations of the CO₂ slicing technique presented here. In particular it should be applied to volcanic ash plumes from different volcanoes. However, the results are promising and given the fast nature of the technique it could be used to obtain the ash cloud height which could then be used as an input into the optimal estimation scheme. Alternatively, the channels selected for the CO₂ slicing technique, which have been shown to be sensitive to volcanic ash clouds in the troposphere, could be incorporated within the optimal estimation scheme to improve the retrieval's height estimate. A further adaptation could be to extend the use of the technique to ash clouds in the stratosphere which has previously been done by Richards (2006) and Tupper et al. (2007).

IASI SO₂

Chapters 3 and 4 explored the use of the SO₂ retrievals developed for IASI in Oxford for monitoring emissions of SO₂ from volcanoes across the globe. In chapter 3, the linear retrieval was applied globally and revealed numerous different sources of SO₂. This includes large explosive eruptions and also smaller eruptions and persistent non-eruptive degassing, and anthropogenic sources. One of the strengths of this

technique is that it is fast and so can be applied in real time. This also meant that it could be relatively quickly applied to a ten year dataset to evaluate its performance. This was done in chapter 4. Here the linear retrieval output for each orbit was rotated to align the plume to the north. The rotated data was then averaged for each month and year. A comparison of the upwind and downwind signal for each year and month allowed an assessment of when and where emissions are detected with IASI. SO₂ from large explosive eruptions were usually identified and very often caused false alerts at other volcanoes because the rotation technique searches for flagged pixels within 200 km of the source. It was also noted that the technique performed well for volcanoes in central and south America which have fairly high altitudes, and at many of these volcanoes long-term trends could be observed. In contrast, little was seen at low altitude volcanoes unless it was from explosive activity. One notable benefit of using IASI (or other infrared sensors) is the detection of emissions during high-latitude winters, which was demonstrated in this study.

Two regions where plumes were commonly identified with the linear retrieval were Ecuador and Kamchatka. The Carboni et al. (2012) iterative retrieval was run over these regions to quantify the amount of SO₂. Initial results showed a negative bias over the regions which first had to be corrected. Once the correction was performed it was evident that the plumes seen with IASI were smaller and less well defined than those seen with OMI, primarily related to the different detection limits of the two instrument's retrievals. Despite this, a comparison of the total average SO₂ masses at Tungurahua showed good agreement with OMI and ground based flux measurements. The trend in the total average SO₂ mass computed over the Kamchatka region also showed similar trends compared to OMI even

if the magnitudes differed. Again, the ability for infrared instruments to make measurements during high latitude winters was demonstrated and it is suggested that IASI be used as a complementary tool to OMI.

These studies have opened up a number of potential avenues for further work. Chapter 4 identified a number of volcanoes where the linear retrieval performed well. These could be selected for further study with the Carboni et al. (2012) iterative retrieval which could give a greater appreciation of the strengths and limitations of this technique, and how it can be best used to monitor volcanic activity. Further improvements could be made to the rotation algorithm, for example, the inclusion of tests which can assess whether the plume originates from the current source being explored. In addition, it would be beneficial to apply the rotation technique to the Carboni et al. (2012) iterative retrieval. From this it would be possible to quantify emissions and compute a flux which can be directly compared against those obtained for OMI. The height retrieval from Carboni et al. (2012) would also allow testing of the height output from the rotation scheme.

Additional comparisons with ground based emission data could further highlight the strengths and limitations of the IASI retrievals. Comparisons against SO_2 fluxes from DOAS and/or Flyspec instruments could help establish if the same patterns are being observed. In addition, comparisons against FTIR instruments could be interesting. Ground based FTIR instruments are able to obtain estimates of the emission rates of different gas species (e.g. CO_2 , H_2O , HCl). The ratio of these gases (e.g. SO_2/CO_2) can then be used to get an estimate of the emission of other gases from the satellite measurements of SO_2 . There are obvious similarities between the ground based FTIR and IASI (which is an FTIR instrument) which means that the

optimal estimation retrievals developed for IASI could be adapted for the ground based FTIR spectra in the future to obtain further information on ash and SO₂.

Chapters 3 and 4 primarily focused on identifying the strengths and weaknesses of the IASI instruments for the long term assessment of volcanic emissions and activity. This was a useful exercise to demonstrate the instrument's capability for making measurements at different volcanoes and hopefully will encourage new users of the IASI retrievals developed in Oxford. The dataset produced here could provide a valuable contribution to a number of different studies. Most obviously, if combined with SO₂ estimates from other satellite instruments, such as OMI and TROPOMI, it could help to better constrain global emissions of SO₂ from volcanic sources: essential for understanding the environmental and climatic impacts of these plumes. Utilising measurements of gas ratios made by ground based FTIR and combining this with satellite data, would then make it possible to get global estimates of the other gas species emitted during eruptions (e.g. CO₂, H₂O). A considerable benefit of using IASI alongside the UV instruments is the potential to estimate the height of the plume (using either the rotation approach or the iterative retrieval height estimate): a factor which can greatly affect the impacts of these plumes. Further knowledge can be obtained by subdividing these emissions into different categories. Carn et al. (2017) for example divided them into eruptive and passive emissions. Based on observations made in chapter 4, future studies could subdivide these further. For example, it would be interesting to assess the relative emissions from non-eruptive activity, effusive eruptions (e.g. lava flows and lakes) and explosive eruptions, and from this evaluate the different impacts. Another suggestion would be to subdivide the emissions into magma type or arc setting.

Not only can these long term, global studies benefit our understanding of the effects of volcanic emissions on the atmosphere and surrounding environment, but they also have potential to better understand volcanic processes. The division into groups such as magma type, arc setting and eruption types could potentially help to identify commonalities and differences between volcanoes worldwide. While care should be exercised when making such intercomparisons, these could help to further develop models of the processes happening beneath the surface. This could then potentially help to understand and mitigate against the hazards presented by volcanic activity. It would be unrealistic to develop such models based off satellite measurements of gas emissions alone. Instead it would benefit from utilising satellite measurements of gas emissions, thermal anomalies and deformation, as well as ground measurements of the same, and laboratory analysis. A recent study by Reath et al. (2019) compared satellite measurements of gas emissions, thermal anomalies and deformation across Latin America. Part of this study looked at whether these volcanoes could be characterised as open (gas rises easily through the system resulting in little deformation and fairly constant gas emission) or closed (gas does not easily leave the system resulting in a build-up in pressure and subsequently more surface deformation) system. While some volcanoes could be classified as such, others exhibited characteristics of both, while some displayed neither. Synoptic studies like this begin to improve and challenge current understandings of volcanic processes and there are exciting possibilities for further work which uses data from multiple sources, which could include results from IASI. One interesting area to explore could be to look at how the openness of the conduit and ease of degassing

effects the heights of volcanic plumes which is something that retrievals developed for IASI could help to contribute to.

5.2 Future Perspectives

The work in this thesis has demonstrated that IASI has the utility for studying volcanic ash clouds and emissions of SO₂ from multiple sources. With the launch of Metop-C last year, there are currently three IASI instruments in orbit, and this instrument ensures the continuity of these measurements for at least another ten years (based off the current of lifespan of IASI-A; 12 years). Inevitably there will be other explosive eruptions during this time which will provide opportunities to further test the retrievals used in this thesis, and learn more about volcanic emissions and their impacts. For a short time, until the inevitable failure of IASI-A, there will be three IASI instruments in orbit, orbiting roughly 40 minutes apart, increasing the temporal resolution, and if used together could potentially give greater insights into plume dynamics. This thesis has demonstrated that the instrument can also be used for monitoring the plumes from smaller eruptions, particularly in central and south America. It is therefore possible that IASI could be used as a monitoring tool in this region. Equally, the use of IASI in high latitude regions such as Kamchatka, Iceland and Alaska in winter is incredibly valuable.

Future studies would benefit from using the IASI retrievals alongside those for other instruments such as the new UV sensor TROPOMI, which is currently on-board Sentinel 5p, launched in 2017. TROPOMI offers a higher spatial resolution (7 x 3.5 km) and achieves global coverage once a day. This will offer new and exciting

insights into volcanic activity that are not possible with previous satellites including both OMI and IASI. However, these older instruments will still provide crucial information. Critically they can provide a longer record of volcanic activity which can be used to understand baseline emissions and to observe patterns in activity, making them complementary to newer instruments. In addition, IASI can be used to obtain coverage during the night and during high latitude winters. Infrared instruments are also more sensitive to the height of volcanic SO₂ emissions. The heights retrieved with IASI could be useful a priori information for UV retrievals of SO₂ and could be used for validation of new UV methods for obtaining the heights.

The next generation of Metop satellites is planned for launch in 2022. On-board will be a new IASI instrument (IASI-NG, EUMETSAT 2019a). This instrument will have a higher spectral resolution of 0.25 cm⁻¹ which is expected to reduce radiometric noise and so could improve future retrievals. The retrievals (optimal estimation scheme and CO₂ slicing) used in this thesis could be adapted for this instrument. This is an exciting opportunity to continue measuring SO₂ and ash. Any work done over the next few years should consider the context of this new instrument and the new opportunities that it will present. On-board the Metop next generation satellites will also be Sentinel 5 (similar instrument to Sentinel 5p; TROPOMI). This will allow direct comparisons of plumes with these two instruments. In addition to this, it is possible that the two instruments could be used together, for example, using height information obtained with IASI-NG as an a priori in the retrievals done by Sentinel 5.

In addition to this, there is the planned launch of the Meteosat third generation instruments, planned for launch in 2021 (EUMETSAT, 2019b). These will be

geostationary platforms. On-board will be a flexible combined imager (to replace SEVIRI) with a spatial resolution of 1 km and a very high temporal resolution. It will have bands for each of the SO₂ absorption features and within the broad spectral range affected by ash. On the same platform there is a lightning sensor and an infrared sounder. The latter will have a 4 km spatial resolution and covers the 680 to 1210 cm⁻¹ (8.26–14.70 μm) spectral range. While it is disappointing that this does not cover the stronger SO₂ ν_3 absorption feature it does include the ν_1 absorption feature and has sensitivity to volcanic ash. It will also measure within the CO₂ absorption band. The CO₂ slicing technique could therefore be adapted for this instrument, and combined with an ash retrieval, it could offer higher frequency ash measurements. With ever improving satellite measurements there are lots of exciting opportunities to explore.

References

- Aiuppa, A., Giudice, G., Liuzzo, M., Tamburello, G., Allard, P., Calabrese, S., Chaplygin, I., McGonigle, A. and Taran, Y. (2012), ‘First volatile inventory for Gorely volcano, Kamchatka’, *Geophysical Research Letters* **39**(6), L06307.
URL: <http://onlinelibrary.wiley.com/doi/10.1029/2012GL051177/abstract;jsessionid=A025CDCE0F90754A78EB9CEABB3DA1B9.f04t04>
- Alexander, D. (2013), ‘Volcanic ash in the atmosphere and risks for civil aviation: a study in european crisis management’, *International Journal of Disaster Risk Science* **4**(1), 9–19.
URL: <https://doi.org/10.1007/s13753-013-0003-0>
- Andres, R. and Kasgnoc, A. (1998), ‘A time-averaged inventory of subaerial volcanic sulfur emissions’, *Journal of Geophysical Research: Atmospheres* (1984–2012) **103**(D19), 25251–25261.
URL: <http://onlinelibrary.wiley.com/doi/10.1029/98JD02091/abstract>
- Ansmann, A., Tesche, M., Groß, S., Freudenthaler, V., Seifert, P., Hiebsch, A., Schmidt, J., Wandinger, U., Mattis, I., Müller, D. and Wiegner, M. (2010), ‘The 16 April 2010 major volcanic ash plume over central Europe: EARLINET lidar and AERONET photometer observations at Leipzig and Munich, Germany’, *Geophysical Research Letters* **37**(13), L13810.
URL: <https://agupubs.onlinelibrary.wiley.com/doi/abs/10.1029/2010GL043809>
- Arason, P., Petersen, G. N. and Bjornsson, H. (2011), ‘Observations of the altitude of the volcanic plume during the eruption of Eyjafjallajökull, April-May 2010’, *Earth System Science Data* **3**(1), 9–17.
URL: <https://www.earth-syst-sci-data.net/3/9/2011/>
- Arellano, S., Galle, B. and Melnikov, D. (2012), Gas flux measurements of episodic bimodal eruptive activity at Karymsky volcano (Kamchatka, Russia), in ‘EGU General Assembly Conference Abstracts’, Vol. 14, p. 8325.
- Arellano, S., Hall, M., Samaniego, P., Le Pennec, J.-L., Ruiz, A., Molina, I. and Yepes, H. (2008), ‘Degassing patterns of Tungurahua volcano (Ecuador) during the 1999-2006 eruptive period, inferred from remote spectroscopic measurements of SO₂ emissions’, *Journal of Volcanology and Geothermal Research* **176**(1), 151–

162.

URL: <https://doi.org/10.1016/j.jvolgeores.2008.07.007>

Arriaga, A. (2007), *CO₂ Slicing Algorithm for the IASI L2 Product Processing Facility*, EUMETSAT, Darmstadt, Germany, 2007.

Balis, D., Koukouli, M.-E., Siomos, N., Dimopoulos, S., Mona, L., Pappalardo, G., Marenco, F., Clarisse, L., Ventress, L. J., Carboni, E., Grainger, R. G., Wang, P., Tilstra, G., van der A, R., Theys, N. and Zehner, C. (2016), ‘Validation of ash optical depth and layer height retrieved from passive satellite sensors using EARLINET and airborne lidar data: the case of the Eyjafjallajökull eruption’, *Atmospheric Chemistry and Physics* **16**(9), 5705–5720.

URL: <https://www.atmos-chem-phys.net/16/5705/2016/>

Bauduin, S., Clarisse, L., Clerbaux, C., Hurtmans, D. and Coheur, P.-F. (2014), ‘IASI observations of sulfur dioxide (SO₂) in the boundary layer of Norilsk’, *Journal of Geophysical Research: Atmospheres* **119**(7), 4253–4263.

URL: <http://onlinelibrary.wiley.com/doi/10.1002/2013JD021405/abstract>

Bauduin, S., Clarisse, L., Hadji-Lazaro, J., Theys, N., Clerbaux, C. and Coheur, P.-F. (2016), ‘Retrieval of near-surface sulfur dioxide (SO₂) concentrations at a global scale using IASI satellite observations’, *Atmospheric Measurement Techniques* **9**, 721–740.

URL: <http://www.atmos-meas-tech.net/9/721/2016/>

Beirle, S., Boersma, K. F., Platt, U., Lawrence, M. G. and Wagner, T. (2011), ‘Megacity Emissions and Lifetimes of Nitrogen Oxides Probed from Space’, *Science* **333**(6050), 1737–1739.

URL: <https://science.sciencemag.org/content/333/6050/1737>

Beirle, S., Hörmann, C., Penning de Vries, M., Dörner, S., Kern, C. and Wagner, T. (2014), ‘Estimating the volcanic emission rate and atmospheric lifetime of SO₂ from space: a case study for Kilauea volcano, Hawaii’, *Atmospheric Chemistry and Physics* **14**(16), 8309–8322.

URL: <https://www.atmos-chem-phys.net/14/8309/2014/>

Bernard, A. and Rose, W. I. (1990), ‘The injection of sulfuric acid aerosols in the stratosphere by the El Chichón volcano and its related hazards to the international air traffic’, *Natural Hazards* **3**(1), 59–67.

URL: <https://doi.org/10.1007/BF00144974>

Biggs, J., Chivers, M. and Hutchinson, M. C. (2013), ‘Surface deformation and stress interactions during the 2007–2010 sequence of earthquake, dyke intrusion and eruption in northern Tanzania’, *Geophysical Journal International* **195**(1), 16–26.

URL: <https://doi.org/10.1093/gji/ggt226>

Biggs, J., Ebmeier, S., Aspinall, W., Lu, Z., Pritchard, M., Sparks, R. and Mather,

- T. (2014), ‘Global link between deformation and volcanic eruption quantified by satellite imagery’, *Nature Communications* **5**(3471), 1–7.
URL: <http://www.nature.com/articles/ncomms4471>
- Biggs, J. and Pritchard, M. E. (2017), ‘Global volcano monitoring: What does it mean when volcanoes deform?’, *Elements* **13**(1), 17.
URL: <http://dx.doi.org/10.2113/gselements.13.1.17>
- Blumstein, D., Chalon, G., Carlier, T., Buil, C., Hebert, P., Maciaszek, T., Ponce, G., Phulpin, T., Tournier, B., Simeoni, D., Astruc, P., Clauss, A., Kayal, G. and Jegou, R. (2004), ‘IASI instrument: Technical overview and measured performances’, *Proc.SPIE* **5543**, 196–207.
URL: <http://dx.doi.org/10.1117/12.560907>
- Boichu, M., Menut, L., Khvorostyanov, D., Clarisse, L., Clerbaux, C., Turquety, S. and Coheur, P.-F. (2013), ‘Inverting for volcanic SO₂ flux at high temporal resolution using spaceborne plume imagery and chemistry-transport modelling: the 2010 Eyjafjallajökull eruption case study’, *Atmospheric Chemistry and Physics* **13**(17), 8569–8584.
URL: <http://www.atmos-chem-phys.net/13/8569/2013/>
- Bombrun, M., Jessop, D., Harris, A. and Barra, V. (2018), ‘An algorithm for the detection and characterisation of volcanic plumes using thermal camera imagery’, *Journal of Volcanology and Geothermal Research* **352**, 26–37.
URL: <http://www.sciencedirect.com/science/article/pii/S037702731730450X>
- Bonaccorso, A., Bonforte, A., Calvari, S., Del Negro, C., Di Grazia, G., Ganci, G., Neri, M., Vicari, A. and Boschi, E. (2011), ‘The initial phases of the 2008–2009 Mount Etna eruption: A multidisciplinary approach for hazard assessment’, *Journal of Geophysical Research: Solid Earth* **116**(B3), B03203.
URL: <https://agupubs.onlinelibrary.wiley.com/doi/abs/10.1029/2010JB007906>
- Bonadonna, C., Folch, A., Loughlin, S. and Puempel, H. (2012), ‘Future developments in modelling and monitoring of volcanic ash clouds: outcomes from the first IAVCEI-WMO workshop on Ash Dispersal Forecast and Civil Aviation’, *Bulletin of Volcanology* **74**(1), 1–10.
URL: <https://doi.org/10.1007/s00445-011-0508-6>
- Boynard, A., Clerbaux, C., Clarisse, L., Safieddine, S., Pommier, M., Van Damme, M., Bauduin, S., Oudot, C., Hadji-Lazaro, J., Hurtmans, D. and Coheur, P.-F. (2014), ‘First simultaneous space measurements of atmospheric pollutants in the boundary layer from IASI: A case study in the North China Plain’, *Geophysical Research Letters* **41**(2), 645–651.
URL: <https://agupubs.onlinelibrary.wiley.com/doi/abs/10.1002/2013GL058333>
- Campion, R., Delgado-Granados, H., Legrand, D., Taquet, N., Boulesteix, T.,

- Pedraza-Espitía, S. and Lecocq, T. (2018), ‘Breathing and Coughing: The Extraordinarily High Degassing of Popocatepetl Volcano Investigated With an SO₂ Camera’, *Frontiers in Earth Science* **6**, 163.
URL: <https://www.frontiersin.org/article/10.3389/feart.2018.00163>
- Campion, R., Salerno, G. G., Coheur, P.-F., Hurtmans, D., Clarisse, L., Kazahaya, K., Burton, M., Caltabiano, T., Clerbaux, C. and Bernard, A. (2010), ‘Measuring volcanic degassing of SO₂ in the lower troposphere with ASTER band ratios’, *Journal of Volcanology and Geothermal Research* **194**(1-3), 42–54.
- Carboni, E., Grainger, R. C., Mather, T. A., Pyle, D. M., Thomas, G., Siddans, R., Smith, A., Dudhia, A., Koukouli, M. L. and Balis, D. (2016), ‘The vertical distribution of Volcanic SO₂ plumes measured by IASI’, *Atmospheric Chemistry and Physics* **16**, 4343–4367.
URL: www.atmos-chem-phys.net/16/4343/2016/
- Carboni, E., Grainger, R., Walker, J., Dudhia, A. and Siddans, R. (2012), ‘A new scheme for sulphur dioxide retrieval from IASI measurements: application to the Eyjafjallajökull eruption of April and May 2010’, *Atmospheric Chemistry and Physics* **12**(23), 11417–11434.
URL: www.atmos-chem-phys.net/12/11417/2012/
- Carboni, E., Mather, T. A., Schmidt, A., Grainger, R. G., Pfeffer, M. A., Ialongo, I. and Theys, N. (2019), ‘Satellite-derived sulfur dioxide (SO₂) emissions from the 2014–2015 Holuhraun eruption (Iceland)’, *Atmospheric Chemistry and Physics* **19**(7), 4851–4862.
URL: <https://www.atmos-chem-phys.net/19/4851/2019/>
- Carn, S. (2016), ‘On the detection and monitoring of effusive eruptions using satellite SO₂ measurements’, *Geological Society, London, Special Publications* **426**, 277–292.
URL: <http://sp.lyellcollection.org/content/early/2016/03/16/SP426.28.abstract>
- Carn, S. A. and Prata, F. J. (2010), ‘Satellite-based constraints on explosive SO₂ release from Soufrière Hills Volcano, Montserrat’, *Geophysical Research Letters* **37**(19), L00E22.
URL: <http://onlinelibrary.wiley.com/doi/10.1029/2010GL044971/abstract;jsessionid=EF64C05F7936FFD9A4FE343EB2F4C103.f03t03>
- Carn, S. A., Yang, K., Prata, A. J. and Krotkov, N. A. (2015), ‘Extending the long-term record of volcanic SO₂ emissions with the Ozone Mapping and Profiler Suite nadir mapper’, *Geophysical Research Letters* **42**(3), 925–932.
- Carn, S., Clarisse, L. and Prata, A. (2016), ‘Multi-decadal satellite measurements of global volcanic degassing’, *Journal of Volcanology and Geothermal Research* **311**, 99–134.

- URL:** <http://linkinghub.elsevier.com/retrieve/pii/S0377027316000032>
- Carn, S., Fioletov, V., McLinden, C., Li, C. and NA, K. (2017), 'A decade of global volcanic SO₂ emissions measured from space', *Nature* **7**(44095).
- URL:** <http://www.nature.com/articles/srep44095>
- Carn, S. and Krotkov, N. (2016), Ultraviolet Satellite Measurements of Volcanic Ash, in S. Mackie, K. Cashman, H. Ricketts, A. Rust and M. Watson, eds, 'Volcanic Ash: Hazard Observation', Elsevier, pp. 217–231.
- Carn, S., Krotkov, N., Yang, K. and Krueger, A. (2013), 'Measuring global volcanic degassing with the Ozone Monitoring Instrument (OMI)', *Geological Society, London, Special Publications* **380**(1), 229–257.
- URL:** <http://sp.lyellcollection.org/content/early/2013/07/11/SP380.12>
- Carn, S., Krueger, A., Arellano, S., Krotkov, N. and Yang, K. (2008), 'Daily monitoring of Ecuadorian volcanic degassing from space', *Journal of Volcanology and Geothermal Research* **176**(1), 141–150.
- URL:** <http://dx.doi.org/10.1016/j.jvolgeores.2008.01.029>
- Carn, S., Krueger, A., Krotkov, N., Yang, K. and Evans, K. (2009), 'Tracking volcanic sulfur dioxide clouds for aviation hazard mitigation', *Natural Hazards* **51**, 325–343.
- URL:** <http://dx.doi.org/10.1007/s11069-008-9228-4>
- Carn, S., Krueger, A., Krotkov, N., Yang, K. and Levelt, P. (2007), 'Sulfur dioxide emissions from Peruvian copper smelters detected by the Ozone Monitoring Instrument', *Geophysical Research Letters* **34**(9), L09801.
- URL:** <http://onlinelibrary.wiley.com/doi/10.1029/2006GL029020/abstract>
- Carn, S., Strow, L., de Souza-Machado, S., Edmonds, Y. and Hannon, S. (2005), 'Quantifying tropospheric volcanic emissions with AIRS: The 2002 eruption of Mt. Etna (Italy)', *Geophysical Research Letters* **32**(2), L02301.
- URL:** <http://onlinelibrary.wiley.com/doi/10.1029/2004GL021034/full>
- Casadevall, T. J. (1994), 'The 1989–1990 eruption of Redoubt Volcano, Alaska: impacts on aircraft operations', *Journal of Volcanology and Geothermal Research* **62**(1), 301 – 316.
- URL:** <http://www.sciencedirect.com/science/article/pii/0377027394900388>
- Casadevall, T., Rose, W., Gerlach, T., Greenland, L., Ewert, J., Wunderman, R. and Symonds, R. (1983), 'Gas emissions and the eruption of Mt. St. Helens through 1982', *Science* **5**, 1383–1385.
- URL:** <http://science.sciencemag.org/content/221/4618/1383>
- Cashman, K. and Rust, A. (2016), Volcanic Ash: Generation and Spatial Variations, in S. Mackie, K. Cashman, H. Ricketts, A. Rust and M. Watson, eds, 'Volcanic Ash: Hazard Observation', Elsevier, pp. 5–24.

- Chahine, M. T. (1974), 'Remote Sounding of Cloudy Atmospheres. I. The Single Cloud Layer', *Journal of the Atmospheric Sciences* **31**(1), 233–243.
URL: [https://doi.org/10.1175/1520-0469\(1974\)031<0233:RSOCAI>2.0.CO;2](https://doi.org/10.1175/1520-0469(1974)031<0233:RSOCAI>2.0.CO;2)
- Chaussard, E., Amelung, F. and Aoki, Y. (2013), 'Characterization of open and closed volcanic systems in Indonesia and Mexico using InSAR time series', *Journal of Geophysical Research: Solid Earth* **118**(8), 3957–3969.
URL: <https://agupubs.onlinelibrary.wiley.com/doi/abs/10.1002/jgrb.50288>
- Chen, W. and Zhao, L. (2015), 'Review – Volcanic Ash and its Influence on Aircraft Engine Components', *Procedia Engineering* **99**, 795 – 803.
URL: <http://www.sciencedirect.com/science/article/pii/S1877705814037187>
- Clarisse, L., Coheur, P.-F., Prata, A. J., Hurtmans, D., Razavi, A., Phulpin, T., Hadji-Lazaro, J. and Clerbaux, C. (2008), 'Tracking and quantifying volcanic SO₂ with IASI, the September 2007 eruption at Jebel at Tair', *Atmospheric Chemistry and Physics* **8**(24), 7723–7734.
URL: www.atmos-chem-phys.net/8/7723/2008/
- Clarisse, L., Coheur, P.-F., Prata, F., Hadji-Lazaro, J., Hurtmans, D. and Clerbaux, C. (2013), 'A unified approach to infrared aerosol remote sensing and type specification', *Atmospheric Chemistry and Physics* **13**(4), 2195–2221.
URL: <https://www.atmos-chem-phys.net/13/2195/2013/>
- Clarisse, L., Coheur, P.-F., Theys, N., Hurtmans, D. and Clerbaux, C. (2014), 'The 2011 Nabro eruption, a SO₂ plume height analysis using IASI measurements', *Atmospheric Chemistry and Physics* **14**(6), 3095–3111.
URL: <http://www.atmos-chem-phys.net/14/3095/2014/>
- Clarisse, L., Hurtmans, D., Clerbaux, C., Hadji-Lazaro, J., Ngadi, Y. and Coheur, P.-F. (2012), 'Retrieval of sulphur dioxide from the Infrared Atmospheric Sounding Interferometer (IASI)', *Atmospheric Measurement Techniques* **5**(3), 581–594.
URL: <http://www.atmos-meas-tech.net/5/581/2012/>
- Clarisse, L., Hurtmans, D., Prata, A. J., Karagulian, F., Clerbaux, C., De Mazière, M. and Coheur, P.-F. (2010b), 'Retrieving radius, concentration, optical depth, and mass of different types of aerosols from high-resolution infrared nadir spectra', *Applied optics* **49**(19), 3713–3722.
- Clarisse, L. and Prata, F. (2016), Infrared Sounding of Volcanic Ash, *in* S. Mackie, K. Cashman, H. Ricketts, A. Rust and M. Watson, eds, 'Volcanic Ash: Hazard Observation', Elsevier, pp. 49–78.
- Clarisse, L., Prata, F., Lacour, J.-L., Hurtmans, D., Clerbaux, C. and Coheur, P.-F. (2010a), 'A correlation method for volcanic ash detection using hyperspectral infrared measurements', *Geophysical Research Letters* **37**(19), L19806.
URL: <https://agupubs.onlinelibrary.wiley.com/doi/abs/10.1029/2010GL044828>

- Clark, T., Lopez, T. and Ushakov, S. (2007), Sulfur Dioxide Emissions from Bezymianny Volcano, Kamchatka: Results from the 2007 Field Season, *in* ‘AGU Fall Meeting Abstracts’, Vol. 1, p. 606.
URL: <http://adsabs.harvard.edu/abs/2007AGUFM.V41B0606C>
- Clerbaux, C., Boynard, A., Clarisse, L., George, M., Hadji-Lazaro, J., Herbin, H., Hurtmans, D., Pommier, M., Razavi, A., Turquety, S. et al. (2009), ‘Monitoring of atmospheric composition using the thermal infrared IASI/MetOp sounder’, *Atmospheric Chemistry and Physics* **9**(16), 6041–6054.
URL: www.atmos-chem-phys.net/9/6041/2009/
- Cooke, M. C., Francis, P. N., Millington, S., Saunders, R. and Witham, C. (2014), ‘Detection of the Grímsvötn 2011 volcanic eruption plumes using infrared satellite measurements’, *Atmospheric Science Letters* **154**, 321–327.
URL: <http://onlinelibrary.wiley.com/doi/10.1002/asl2.506/abstract>
- Coppola, D., Campion, R., Laiolo, M., Cuoco, E., Balagizi, C., Ripepe, M., Cigolini, C. and Tedesco, D. (2016c), ‘Birth of a lava lake: Nyamulagira volcano 2011–2015’, *Bulletin of Volcanology* **78**(3), 20.
URL: <https://doi.org/10.1007/s00445-016-1014-7>
- Coppola, D., Laiolo, M. and Cigolini, C. (2016b), ‘Fifteen years of thermal activity at vanuatu’s volcanoes (2000–2015) revealed by mirova’, *Journal of Volcanology and Geothermal Research* **322**, 6 – 19.
URL: <http://www.sciencedirect.com/science/article/pii/S0377027315003716>
- Coppola, D., Laiolo, M., Cigolini, C., Donne, D. D. and Ripepe, M. (2016a), ‘Enhanced volcanic hot-spot detection using MODIS IR data: results from the MIROVA system’, *Geological Society, London, Special Publications* **426**(1), 181–205.
URL: <https://sp.lyellcollection.org/content/426/1/181>
- Coppola, D., Macedo, O., Ramos, D., Finizola, A., Donne, D., del Carpio, J., White, R., McCausland, W., Centeno, R., Rivera, M., Apaza, F., Ccallata, B., Chilo, W., Cigolini, C., Laiolo, M., Lazarte, I., Machaca, R., Masias, P., Ortega, M., Puma, N. and Taïpe, E. (2015), ‘Magma extrusion during the Ubinas 2013–2014 eruptive crisis based on satellite thermal imaging (MIROVA) and ground-based monitoring’, *Journal of Volcanology and Geothermal Research* **302**, 199 – 210.
URL: <http://www.sciencedirect.com/science/article/pii/S0377027315002139>
- Corradini, S., Merucci, L. and Prata, A. J. (2009), ‘Retrieval of SO₂ from thermal infrared satellite measurements: correction procedures for the effects of volcanic ash’, *Atmospheric Measurement Techniques* **2**(1), 177–191.
URL: <http://www.atmos-meas-tech.net/2/177/2009/>
- Corradini, S., Merucci, L., Prata, A. and Piscini, A. (2010), ‘Volcanic ash and SO₂

- in the 2008 Kasatochi eruption: retrievals comparison from different IR satellite sensors', *Journal of Geophysical Research: Atmospheres* **115**(D2), D00L21.
URL: <http://onlinelibrary.wiley.com/doi/10.1029/2009JD013634/abstract>
- Corradini, S., Spinetti, C., Carboni, E., Tirelli, C., Buongiorno, M. F., Pugnaghi, S. and Gangale, G. (2008), 'Mt. Etna tropospheric ash retrieval and sensitivity analysis using moderate resolution imaging spectroradiometer measurements', *Journal of Applied Remote Sensing* **2**(1), 023550.
URL: <https://doi.org/10.1117/1.3046674>
- Dean, K. and Dehn, J. (2015), *Monitoring Volcanoes in the North Pacific: Observations from Space*, Springer.
URL: <http://www.springer.com/gb/book/9783540241256>
- Deeter, M., Edwards, D., JC, G. and Drummond, J. (2007), 'Sensitivity of MOPITT observations to carbon monoxide in the lower troposphere', *Journal of Geophysical Research: Atmospheres* **112**(D24), D24306.
- Dehn, J., Dean, K. and Engle, K. (2000), 'Thermal monitoring of North Pacific volcanoes from space', *Geology* **28**(8), 755.
URL: [http://geology.gsapubs.org/cgi/doi/10.1130/0091-7613\(2000\)28<755:TMONPV>2.0.CO;2](http://geology.gsapubs.org/cgi/doi/10.1130/0091-7613(2000)28<755:TMONPV>2.0.CO;2)
- Dehn, J. and Harris, A. (2015), Thermal anomalies at volcanoes, in K. Dean and J. Dehn, eds, 'Monitoring Volcanoes in the North Pacific', Springer, pp. 49–78.
- Delgado Granados, H. and Cardenas Gonzalez, L. (2013), ~ 20 years of SO₂ measurements at Popocatépetl volcano (Mexico) using COSPEC: volcanological interpretation of the data and use for validation of instrumental developments, in 'AGU Fall Meeting Abstracts', Vol. 1, p. 2874.
URL: <http://adsabs.harvard.edu/abs/2013AGUFM.V43B2874D>
- Delgado-Granados, H., González, H. and Sánchez, N. (2001), 'Sulfur dioxide emissions from Popocatépetl volcano (Mexico): case study of a high-emission rate, passively degassing erupting volcano', *Journal of Volcanology and Geothermal Research* **108**(1), 107 – 120.
URL: <http://www.sciencedirect.com/science/article/pii/S0377027300002808>
- Delmelle, P. (2003), 'Environmental impacts of tropospheric volcanic gas plumes', *Geological Society, London, Special Publications* **213**(1), 381–399.
URL: <https://sp.lyellcollection.org/content/213/1/381>
- Draxier, R. and Hess, G. (1998), 'An overview of the HYSPLIT₄ modeling system of trajectories, dispersion, and deposition', *Australian Meteorological Magazine* **47**(4), 295–308.
- Dumont, S., Sigmundsson, F., Parks, M. M., Drouin, V. J. P., Pedersen, G. B. M., Jónsdóttir, I., Höskuldsson, , Hooper, A., Spaans, K., Bagnardi, M., Gudmundsson,

- M. T., Barsotti, S., Jónsdóttir, K., Högnadóttir, T., Magnússon, E., Hjartardóttir, R., Dürig, T., Rossi, C. and Oddsson, B. (2018), 'Integration of SAR Data Into Monitoring of the 2014–2015 Holuhraun Eruption, Iceland: Contribution of the Icelandic Volcanoes Supersite and the FutureVolc Projects', *Frontiers in Earth Science* **6**, 231.
URL: <https://www.frontiersin.org/article/10.3389/feart.2018.00231>
- Dunn, M. G. and Wade, D. P. (1994), Influence of volcanic ash clouds on gas turbine engines, in T. J. Casadevall, ed., 'Volcanic ash and aviation safety: Proceedings of the first international symposium on volcanic ash and aviation safety', U.S. Geological Survey Bulletin 2047, pp. 107–117.
- Durant, A. J., Bonadonna, C. and Horwell, C. J. (2010), 'Atmospheric and Environmental Impacts of Volcanic Particulates', *Elements* **6**(4), 235.
URL: <http://dx.doi.org/10.2113/gselements.6.4.235>
- Dzurisin, D. (2003), 'A comprehensive approach to monitoring volcano deformation as a window on the eruption cycle', *Reviews of Geophysics* **41**(1).
URL: <https://agupubs.onlinelibrary.wiley.com/doi/abs/10.1029/2001RG000107>
- Dzurisin, D. and Lu, Z. (2007), *Volcano deformation—Geodetic monitoring techniques*, Springer-Verlag, Berlin.
URL: <http://pubs.er.usgs.gov/publication/70170367>
- Ebmeier, S. K., Andrews, B. J., Araya, M. C., Arnold, D. W. D., Biggs, J., Cooper, C., Cottrell, E., Furtney, M., Hickey, J., Jay, J., Lloyd, R., Parker, A. L., Pritchard, M. E., Robertson, E., Venzke, E. and Williamson, J. L. (2018), 'Synthesis of global satellite observations of magmatic and volcanic deformation: implications for volcano monitoring & the lateral extent of magmatic domains', *Journal of Applied Volcanology* **7**(1), 2.
URL: <https://doi.org/10.1186/s13617-018-0071-3>
- Ebmeier, S. K., Sayer, A. M., Grainger, R. G., Mather, T. A. and Carboni, E. (2014), 'Systematic satellite observations of the impact of aerosols from passive volcanic degassing on local cloud properties', *Atmospheric Chemistry and Physics* **14**(19), 10601–10618.
URL: <https://www.atmos-chem-phys.net/14/10601/2014/>
- Eckhardt, S., Prata, A. J., Seibert, P., Stebel, K. and Stohl, A. (2008), 'Estimation of the vertical profile of sulfur dioxide injection into the atmosphere by a volcanic eruption using satellite column measurements and inverse transport modeling', *Atmospheric Chemistry and Physics* **8**(14), 3881–3897.
URL: <https://www.atmos-chem-phys.net/8/3881/2008/>
- Edmonds, M. (2008), 'New geochemical insights into volcanic degassing', *Philosophical Transactions of the Royal Society A: Mathematical, Physical and Engineering*

- Sciences* **366**(1885), 4559–4579.
- Edmonds, M., Herd, R. A., Galle, B. and Oppenheimer, C. M. (2003), ‘Automated, high time-resolution measurements of SO₂ flux at Soufriere Hills Volcano, Montserrat’, *Bulletin of Volcanology* **65**(8), 578–586.
URL: <http://link.springer.com/10.1007/s00445-003-0286-x>
- Eisinger, M. and Burrows, J. P. (1998), ‘Tropospheric sulfur dioxide observed by the ERS-2 GOME instrument’, *Geophysical Research Letters* **25**(22), 4177–4180.
URL: <http://onlinelibrary.wiley.com/doi/10.1029/1998GL900128/full>
- Elias, T., Sutton, A. J., Oppenheimer, C., Horton, K. A., Garbeil, H., Tsanev, V., McGonigle, A. J. S. and Williams-Jones, G. (2006), ‘Comparison of COSPEC and two miniature ultraviolet spectrometer systems for SO₂ measurements using scattered sunlight’, *Bulletin of Volcanology* **68**(4), 313–322.
URL: <http://link.springer.com/10.1007/s00445-005-0026-5>
- Ellrod, G. P., Connell, B. H. and Hillger, D. W. (2003), ‘Improved detection of airborne volcanic ash using multispectral infrared satellite data’, *Journal of Geophysical Research: Atmospheres* **108**(D12).
URL: <https://agupubs.onlinelibrary.wiley.com/doi/abs/10.1029/2002JD002802>
- EUMETSAT (2017), ‘IASI’, Website accessed in February 2017 .
URL: <http://www.eumetsat.int/website/home/Satellites/CurrentSatellites/Metop/MetopDesign/IASI/index.html>
- EUMETSAT (2019a), ‘Meteosat Third Generation’.
URL: <https://www.eumetsat.int/website/home/Satellites/FutureSatellites/MeteosatThirdGeneration/index.html>
- EUMETSAT (2019b), ‘IASI - next generation’.
URL: <https://www.eumetsat.int/website/home/Satellites/FutureSatellites/EUMETSATPolarSystemSecondGeneration/IASING/index.html>
- Filizzola, C., Lacava, T., Marchese, F., Pergola, N., Scaffidi, I. and Tramutoli, V. (2007), ‘Assessing RAT (Robust AVHRR Techniques) performances for volcanic ash cloud detection and monitoring in near real-time: The 2002 eruption of Mt. Etna (Italy)’, *Remote Sensing of Environment* **107**(3), 440 – 454.
URL: <http://www.sciencedirect.com/science/article/pii/S0034425706003543>
- Fioletov, V. E., McLinden, C. A., Krotkov, N., Yang, K., Loyola, D. G., Valks, P., Theys, N., Van Roozendaal, M., Nowlan, C. R., Chance, K., Liu, X., Lee, C. and Martin, R. V. (2013), ‘Application of OMI, SCIAMACHY, and GOME-2 satellite SO₂ retrievals for detection of large emission sources’, *Journal of Geophysical Research: Atmospheres* **118**(19), 11399–11418.
- Fioletov, V., McLinden, C., Krotkov, N. and Li, C. (2015), ‘Lifetimes and emissions of SO₂ from point sources estimated from OMI’, *Geophysical Research Letters*

- 42(6), 1969–1976.
- Fioletov, V., McLinden, C., Krotkov, N., Li, C., Joiner, J., Theys, N., Carn, S. and Moran, M. (2016), ‘A global catalogue of large SO₂ sources and emissions derived from the Ozone Monitoring Instrument’, *Atmospheric Chemistry and Physics* **16**, 11497–11519.
- Fischer, T. P., Morrissey, M. M., Calvache, V. M. L., Gomez, M. D., Torres, C. R., Stix, J. and Williams, S. N. (1994), ‘Correlations between SO₂ flux and long-period seismicity at Galeras volcano’, *Nature* **368**(6467), 135–137.
- Flemming, J. and Inness, A. (2013), ‘Volcanic sulfur dioxide plume forecasts based on UV satellite retrievals for the 2011 Grímsvötn and the 2010 Eyjafjallajökull eruption’, *Journal of Geophysical Research: Atmospheres* **118**(17), 10,172–10,189.
URL: <https://agupubs.onlinelibrary.wiley.com/doi/abs/10.1002/jgrd.50753>
- Flower, V. and Carn, S. (2015), ‘Characterising volcanic cycles at Soufriere Hills Volcano, Montserrat: Time series analysis of multi-parameter satellite data’, *Journal of Volcanology and Geothermal Research* **304**, 82 – 93.
URL: <http://www.sciencedirect.com/science/article/pii/S0377027315002504>
- Flower, V. J., Carn, S. A. and Wright, R. (2016), ‘The impact of satellite sensor viewing geometry on time-series analysis of volcanic emissions’, *Remote Sensing of Environment* **183**, 282–293.
- Flower, V. J., Carn, S. A. and Wright, R. (2016b), ‘The impact of satellite sensor viewing geometry on time-series analysis of volcanic emissions’, *Remote Sensing of Environment* **183**, 282–293.
- Francis, P. N., Cooke, M. C. and Saunders, R. W. (2012), ‘Retrieval of physical properties of volcanic ash using Meteosat: A case study from the 2010 Eyjafjallajökull eruption’, *Journal of Geophysical Research: Atmospheres* **117**(D20).
URL: <https://agupubs.onlinelibrary.wiley.com/doi/abs/10.1029/2011JD016788>
- Francis, P. and Rothery, D. (2000), ‘Remote sensing of active volcanoes’, *Annual Review of Earth and Planetary Sciences* **28**(1), 81–106.
URL: <https://doi.org/10.1146/annurev.earth.28.1.81>
- Francis, P. W., Wadge, G. and Mougini-Mark, P. J. (1996), *Satellite Monitoring of Volcanoes*, Springer Berlin Heidelberg, Berlin, Heidelberg, pp. 257–298.
URL: https://doi.org/10.1007/978-3-642-80087-0_8
- Frey, R. A., Baum, B. A., Menzel, W. P., Ackerman, S. A., Moeller, C. C. and Spinhirne, J. D. (1999), ‘A comparison of cloud top heights computed from airborne lidar and MAS radiance data using CO₂ slicing’, *Journal of Geophysical Research: Atmospheres* **104**(D20), 24547–24555.
URL: <https://agupubs.onlinelibrary.wiley.com/doi/abs/10.1029/1999JD900796>
- Furtney, M. A., Pritchard, M. E., Biggs, J., Carn, S. A., Ebmeier, S. K., Jay,

- J. A., Kilbride, B. T. M. and Reath, K. A. (2018), 'Synthesizing multi-sensor, multi-satellite, multi-decadal datasets for global volcano monitoring', *Journal of Volcanology and Geothermal Research* **365**, 38 – 56.
URL: <http://www.sciencedirect.com/science/article/pii/S0377027318302191>
- Galle, B., Johansson, M., Rivera, C., Zhang, Y., Kihlman, M., Kern, C., Lehmann, T., Platt, U., Arellano, S. and Hidalgo, S. (2010), 'Network for Observation of Volcanic and Atmospheric Change (NOVAC) - A global network for volcanic gas monitoring: Network layout and instrument description', *Journal of Geophysical Research: Atmospheres* (1984–2012) **115**(D5).
- Galle, B., Oppenheimer, C., Geyer, A., McGonigle, A. J., Edmonds, M. and Horrocks, L. (2003), 'A miniaturised ultraviolet spectrometer for remote sensing of SO₂ fluxes: a new tool for volcano surveillance', *Journal of Volcanology and Geothermal Research* **119**(1), 241–254.
URL: [https://doi.org/10.1016/S0377-0273\(02\)00356-6](https://doi.org/10.1016/S0377-0273(02)00356-6)
- Gangale, G., Prata, A. and Clarisse, L. (2010), 'The infrared spectral signature of volcanic ash determined from high-spectral resolution satellite measurements', *Remote Sensing of Environment* **114**(2), 414 – 425.
URL: <http://www.sciencedirect.com/science/article/pii/S003442570900279X>
- Gassó, S. (2008), 'Satellite observations of the impact of weak volcanic activity on marine clouds', *Journal of Geophysical Research: Atmospheres* **113**(D14), D14S19.
URL: <https://agupubs.onlinelibrary.wiley.com/doi/abs/10.1029/2007JD009106>
- Giglio, L., Descloitres, J., Justice, C. and Kaufman, Y. (2003), 'An Enhanced Contextual Fire Detection Algorithm for MODIS', *Remote Sensing of Environment* **87**(2), 273 – 282.
URL: <http://www.sciencedirect.com/science/article/pii/S0034425703001846>
- Glaze, L. S., Wilson, L. and Mougini, M. P. J. (1999), 'Volcanic eruption plume top topography and heights as determined from photoclinometric analysis of satellite data', *Journal of Geophysical Research: Solid Earth* **104**(B2), 2989–3001.
URL: <https://agupubs.onlinelibrary.wiley.com/doi/abs/10.1029/1998JB900047>
- Grainger, R. G., Peters, D. M., Thomas, G. E., Smith, A. J. A., Siddans, R., Carboni, E. and Dudhia, A. (2013), 'Measuring volcanic plume and ash properties from space', *Geological Society, London, Special Publications* **380**.
URL: <http://sp.lyellcollection.org/content/early/2013/07/04/SP380.7>
- Grainger, R. and Highwood, E. (2003), Atmospheric effects of volcanoes, in C. Oppenheimer, ed., 'Volcanic Degassing', Geological Society Special Publication.
- Grutter, M., Basaldud, R., Rivera, C., Harig, R., Junkermann, W., Caetano, E. and Delgado Granados, H. (2008), 'SO₂ emissions from Popocatepetl volcano: emission rates and plume imaging using optical remote sensing techniques', *Atmospheric*

Chemistry and Physics **8**, 6655–6663.

URL: <https://www.atmos-chem-phys.net/8/6655/2008/>

Gudmundsson, M. T., Pedersen, R., Vogfjörð, K., Thorbjarnardóttir, B., Jakobsdóttir, S. and Roberts, M. J. (2010), ‘Eruptions of Eyjafjallajökull Volcano, Iceland’, *EOS, Transactions American Geophysical Union* **91**(21), 190–191.

URL: <https://agupubs.onlinelibrary.wiley.com/doi/abs/10.1029/2010EO210002>

Guffanti, M. C. and Tupper, A. C. (2015), Volcanic ash hazards and aviation risk: Chapter 4, in P. Papale and J. Shroder, eds, ‘Volcanic hazards, risks and disasters’, Elsevier, Amsterdam, pp. 87–108.

URL: <http://pubs.er.usgs.gov/publication/70184999>

Guidard, V., Fourrié, N., Brousseau, P. and Rabier, F. (2011), ‘Impact of IASI assimilation at global and convective scales and challenges for the assimilation of cloudy scenes’, *Quarterly Journal of the Royal Meteorological Society* **137**(661), 1975–1987.

URL: <https://rmets.onlinelibrary.wiley.com/doi/abs/10.1002/qj.928>

GVP (1999), ‘Report on Guagua Pichincha (Ecuador)’, In: Wunderman, R. (ed.), *Bulletin of the Global Volcanism Network* **24**(2), Smithsonian Institution.

URL: <http://dx.doi.org/10.5479/si.GVP.BGVN199902-352020>

GVP (2008), ‘Report on Etna (Italy) — May 2008’, In: Wunderman, R. (ed.), *Bulletin of the Global Volcanism Network* **33**(5), Smithsonian Institution.

URL: <https://doi.org/10.5479/si.GVP.BGVN200805-211060>

GVP (2009a), ‘Report on Galeras (Colombia)’, In: Wunderman, R. (ed.), *Bulletin of the Global Volcanism Network* **34**(7), Smithsonian Institution.

URL: <http://dx.doi.org/10.5479/si.GVP.BGVN200907-351080>

GVP (2009b), ‘Report on Reventador (Ecuador)’, In: Wunderman, R. (ed.), *Bulletin of the Global Volcanism Network* **34**(3), Smithsonian Institution.

URL: <http://dx.doi.org/10.5479/si.GVP.BGVN200903-352010>

GVP (2009c), ‘Report on Reventador (Ecuador)’, In: Wunderman, R. (ed.), *Bulletin of the Global Volcanism Network* **34**(3), Smithsonian Institution.

URL: <http://dx.doi.org/10.5479/si.GVP.BGVN200903-352010>

GVP (2010a), ‘Report on Klyuchevskoy (Russia)’, In: Wunderman, R. (ed.), *Bulletin of the Global Volcanism Network* **35**(6), Smithsonian Institution.

GVP (2010b), ‘Report on Pacaya (Guatemala) — May 2014’, In: Wunderman, R. (ed.), *Bulletin of the Global Volcanism Network* **39**(5), Smithsonian Institution.

URL: <https://doi.org/10.5479/si.GVP.BGVN201405-342110>

GVP (2010c), ‘Report on Sheveluch (Russia)’, *Bulletin of the Global Volcanism Network* **35**(3).

GVP (2010d), ‘Report on Sheveluch (Russia)’, In: Sennert, S. K. (ed.), *Weekly Vol-*

- canic Activity Report, 3 November-9 November 2010* **Smithsonian Institution and US Geological Survey.**
- GVP (2012a), 'Report on Nevado del Huila (Colombia)', *In: Wunderman, R (ed.), Bulletin of the Global Volcanism Network* **37**(10), Smithsonian Institution.
URL: <http://dx.doi.org/10.5479/si.GVP.BGVN201210-351050>
- GVP (2012b), 'Report on Nevado del Ruiz (Colombia) — August 2012', *In: Wunderman, R. (ed.), Bulletin of the Global Volcanism Network* **37**(8), Smithsonian Institution.
URL: <https://doi.org/10.5479/si.GVP.BGVN201208-351020>
- GVP (2012c), 'Report on Popocatepetl (Mexico) — May 2012', *In: Wunderman, R. (ed.), Bulletin of the Global Volcanism Network* **37**(5), Smithsonian Institution.
URL: <https://doi.org/10.5479/si.GVP.BGVN201205-341090>
- GVP (2012d), 'Report on Tolbachik (Russia)', *In: Wunderman, R (ed.), Bulletin of the Global Volcanism Network* **37**(12), Smithsonian Institution.
<http://dx.doi.org/10.5479/si.GVP.BGVN201212-300240>.
- GVP (2013a), 'Report on Galeras (Colombia)', *In: Wunderman, R (ed.), Bulletin of the Global Volcanism Network* **38**(03), Smithsonian Institution.
URL: <http://dx.doi.org/10.5479/si.GVP.BGVN201303-351080>
- GVP (2013b), 'Report on Klyuchevskoy (Russia)', *Bulletin of the Global Volcanism Network* **38**(7), Smithsonian Institution.
URL: <http://dx.doi.org/10.5479/si.GVP.BGVN201307-300260>
- GVP (2013c), 'Report on Tungurahua (Ecuador)', *In: Sennert, S K (ed.), Weekly Volcanic Activity Report, 16 October-22 October 2013* **Smithsonian Institution and US Geological Survey.**
URL: <https://volcano.si.edu/showreport.cfm?doi=GVP.WVAR20131016-352080>
- GVP (2013d), 'Report on Tungurahua (Ecuador)', *n: Sennert, S K (ed.), Weekly Volcanic Activity Report, 30 October-5 November 2013* **Smithsonian Institution and US Geological Survey.**
URL: <https://volcano.si.edu/showreport.cfm?doi=GVP.WVAR20131030-352080>
- GVP (2013e), 'Report on Tungurahua (Ecuador)', *In: Sennert, S K (ed.), Weekly Volcanic Activity Report, 6 November-12 November 2013* **Smithsonian Institution and US Geological Survey.**
- GVP (2013f), *Volcanoes of the World*, v. 4.8.1, Venzke, E (ed.), Smithsonian Institution.
URL: <https://doi.org/10.5479/si.GVP.VOTW4-2013>
- GVP (2015a), 'Report on popocatepetl (mexico) — february 2015', *In: Wunderman, R. (ed.), Bulletin of the Global Volcanism Network* **40**(2), Smithsonian Institution.

- URL:** <https://doi.org/10.5479/si.GVP.BGVN201502-341090>
GVP (2015b), ‘Report on Wolf (Ecuador) — October 2016’, In: *Crafford, A.E., and Venzke, E. (eds.), Bulletin of the Global Volcanism Network* **41**(10), Smithsonian Institution.
- URL:** <https://doi.org/10.5479/si.GVP.BGVN201610-353020>
GVP (2017a), ‘Report on Erta Ale (Ethiopia) — July 2017’, *Bulletin of the Global Volcanism Network* **42**(7), Smithsonian Institution.
- URL:** <https://doi.org/10.5479/si.GVP.BGVN201707-221080>
GVP (2017b), ‘Report on Nevado del Ruiz (Colombia) — June 2017’, In: *Crafford, A.E., and Venzke, E. (eds.), Bulletin of the Global Volcanism Network* **42**(6), Smithsonian Institution.
- URL:** <https://doi.org/10.5479/si.GVP.BGVN201706-351020>
GVP (2018), ‘Report on Ambae (Vanuatu) — February 2018’, *Bulletin of the Global Volcanism Network* **43**(2), Smithsonian Institution.
- URL:** <https://doi.org/10.5479/si.GVP.BGVN201802-257030>
Halmer, M., Schmincke, H.-U. and Graf, H.-F. (2002), ‘The annual volcanic gas input into the atmosphere, in particular into the stratosphere: a global data set for the past 100 years’, *Journal of Volcanology and Geothermal Research* **115**(3), 511–528.
- URL:** [https://doi.org/10.1016/S0377-0273\(01\)00318-3](https://doi.org/10.1016/S0377-0273(01)00318-3)
Hansell, A. and Oppenheimer, C. (2004), ‘Health hazards from volcanic gases: A systematic literature review’, *Archives of Environmental Health: An International Journal* **59**(12), 628–639.
- URL:** <https://doi.org/10.1080/00039890409602947>
Harris, A. (2013), *Thermal Remote Sensing of Active Volcanoes: A User’s Manual*, Cambridge University Press.
- Haywood, J. M., Jones, A., Clarisse, L., Bourassa, A., Barnes, J., Telford, P., Bellouin, N., Boucher, O., Agnew, P., Clerboux, C. et al. (2010), ‘Observations of the eruption of the Sarychev volcano and simulations using the HadGEM2 climate model’, *Journal of Geophysical Research: Atmospheres (1984–2012)* **115**(D21).
- Heard, I. P., Manning, A. J., Haywood, J. M., Witham, C., Redington, A., Jones, A., Clarisse, L. and Bourassa, A. (2012), ‘A comparison of atmospheric dispersion model predictions with observations of SO₂ and sulphate aerosol from volcanic eruptions’, *Journal of Geophysical Research: Atmospheres (1984–2012)* **117**(D20), D00U22.
- URL:** <https://doi.org/10.1029/2011JD016791>
Hidalgo, S., Battaglia, J., Arellano, S., Steele, A., Bernard, B., Bourquin, J., Galle, B., Arrais, S. and Vásconez, F. (2015), ‘SO₂ degassing at Tungurahua volcano

- (Ecuador) between 2007 and 2013: transition from continuous to episodic activity', *Journal of Volcanology and Geothermal Research* **298**(0), 1 – 14.
- Hillger, D. W. and Clark, J. D. (2002), 'Principal Component Image Analysis of MODIS for Volcanic Ash. Part I: Most Important Bands and Implications for Future GOES Imagers', *Journal of Applied Meteorology* **41**(10), 985–1001.
- URL:** <https://journals.ametsoc.org/doi/abs/10.1175/1520-0450%282002%29041%3C0985%3APCIAOM%3E2.0.CO%3B2>
- Holasek, R. E., Self, S. and Woods, A. W. (1996), 'Satellite observations and interpretation of the 1991 Mount Pinatubo eruption plumes', *Journal of Geophysical Research: Solid Earth* **101**(B12), 27635–27655.
- URL:** <https://agupubs.onlinelibrary.wiley.com/doi/abs/10.1029/96JB01179>
- Holaske, R. E. and Rose, W. I. (1991), 'Anatomy of 1986 Augustine volcano eruptions as recorded by multispectral image processing of digital AVHRR weather satellite data', *Bulletin of Volcanology* **53**(6), 420–435.
- URL:** <https://doi.org/10.1007/BF00258183>
- Holz, R. E., Ackerman, S. A., Nagle, F. W., Frey, R., Dutcher, S., Kuehn, R. E., Vaughan, M. A. and Baum, B. (2008), 'Global Moderate Resolution Imaging Spectroradiometer (MODIS) cloud detection and height evaluation using CALIOP', *Journal of Geophysical Research: Atmospheres* **113**(D8).
- URL:** <https://agupubs.onlinelibrary.wiley.com/doi/abs/10.1029/2008JD009837>
- Holz, R. E., Ackerman, S., Antonelli, P., Nagle, F., Knuteson, R. O., McGill, M., Hlavka, D. L. and Hart, W. D. (2006), 'An Improvement to the High-Spectral-Resolution CO₂-Slicing Cloud-Top Altitude Retrieval', *Journal of Atmospheric and Oceanic Technology* **23**(5), 653–670.
- URL:** <https://doi.org/10.1175/JTECH1877.1>
- Horton, K. A., Williams-Jones, G., Garbeil, H., Elias, T., Sutton, A. J., Mougini-Mark, P., Porter, J. N. and Clegg, S. (2006), 'Real-time measurement of volcanic SO₂ emissions: validation of a new UV correlation spectrometer (FLYSPEC)', *Bulletin of Volcanology* **68**(4), 323–327.
- URL:** <http://link.springer.com/10.1007/s00445-005-0014-9>
- Horwell, C. J. (2007), 'Grain-size analysis of volcanic ash for the rapid assessment of respiratory health hazard', *Journal of Environmental Monitoring* **9**, 1107–1115.
- URL:** <http://dx.doi.org/10.1039/B710583P>
- Horwell, C. J. and Baxter, P. J. (2006), 'The respiratory health hazards of volcanic ash: a review for volcanic risk mitigation', *Bulletin of Volcanology* **69**(1), 1–24.
- URL:** <https://doi.org/10.1007/s00445-006-0052-y>
- Hunt, W. H., Winker, D. M., Vaughan, M. A., Powell, K. A., Lucker, P. L. and Weimer, C. (2009), 'CALIPSO Lidar Description and Performance Assessment',

- Journal of Atmospheric and Oceanic Technology* **26**(7), 1214–1228.
URL: <https://doi.org/10.1175/2009JTECHA1223.1>
- IATA Economic Briefing (2010), ‘The impact of Eyjafjallajökull volcanic ash plume’, International Air Transport Association.
URL: <https://www.iata.org/whatwedo/Documents/economics/Volcanic-Ash-Plume-May2010.pdf>
- Jay, J. A., Welch, M., Pritchard, M. E., Mares, P. J., Mnich, M. E., Melkonian, A. K., Aguilera, F., Naranjo, J. A., Sunagua, M. and Clavero, J. (2013), ‘Volcanic hotspots of the central and southern Andes as seen from space by ASTER and MODVOLC between the years 2000 and 2010’, *Geological Society, London, Special Publications* **380**(1), 161–185.
URL: <https://sp.lyellcollection.org/content/380/1/161>
- Jones, A. (2004), ‘Atmospheric dispersion modelling at the met office’, *Weather* **59**(11), 311–316.
URL: <https://rmets.onlinelibrary.wiley.com/doi/abs/10.1256/wea.106.04>
- Justice, C., Giglio, L., Korontzi, S., Owens, J., Morisette, J., Roy, D., Descloitres, J., Alleaume, S., Petitcolin, F. and Kaufman, Y. (2002), ‘The MODIS fire products’, *Remote Sensing of Environment* **83**(1), 244 – 262.
URL: <http://www.sciencedirect.com/science/article/pii/S0034425702000767>
- Kaneko, T. and Wooster, M. (1999), ‘Landsat infrared analysis of fumarole activity at Unzen Volcano: time-series comparison with gas and magma fluxes’, *Journal of Volcanology and Geothermal Research* **89**(1), 57 – 64.
URL: <http://www.sciencedirect.com/science/article/pii/S037702739800122X>
- Karagulian, F., Clarisse, L., Clerbaux, C., Prata, A. J., Hurtmans, D. and Coheur, P.-F. (2010), ‘Detection of volcanic SO₂, ash, and H₂SO₄ using the Infrared Atmospheric Sounding Interferometer (IASI)’, *Journal of Geophysical Research: Atmospheres* (1984–2012) **115**(D2).
- Kaufman, Y. J., Justice, C. O., Flynn, L. P., Kendall, J. D., Prins, E. M., Giglio, L., Ward, D. E., Menzel, W. P. and Setzer, A. W. (1998), ‘Potential global fire monitoring from EOS-MODIS’, *Journal of Geophysical Research: Atmospheres* **103**(D24), 32215–32238.
URL: <https://agupubs.onlinelibrary.wiley.com/doi/abs/10.1029/98JD01644>
- Kerminen, V.-M., Niemi, J. V., Timonen, H., Aurela, M., Frey, A., Carbone, S., Saarikoski, S., Teinilä, K., Hakkarainen, J., Tamminen, J., Vira, J., Prank, M., Sofiev, M. and Hillamo, R. (2011), ‘Characterization of a volcanic ash episode in southern Finland caused by the Grimsvötn eruption in Iceland in May 2011’, *Atmospheric Chemistry and Physics* **11**(23), 12227–12239.
URL: <https://www.atmos-chem-phys.net/11/12227/2011/>

- Klimont, Z., Smith, S. and Cofala, J. (2013), ‘The last decade of global anthropogenic sulfur dioxide: 2000-2011 emissions’, *Environmental Research Letters* **8**, 014003.
- Koukouli, M. E., Balis, D., van der A, R., Theys, N., Hedelt, R., Richter, A., Krotkov, N., Li, C. and Taylor, M. (2016), ‘Anthropogenic SO₂ load over China as observed from different satellite sensors’, *Atmospheric Environment* **145**, 45–59.
- Koukouli, M. E., Clarisse, L., Carboni, E., Van Gent, J., Spinetti, C., Balis, D., Dimopoulos, S., Grainger, R. and Theys, N. (2015), ‘Intercomparison of Metop-A SO₂ measurements during the 2010-2011 Icelandic eruptions’, *Annals of Geophysics* **57**.
URL: <https://doi.org/10.4401/ag-6613>
- Kristiansen, N. I., Stohl, A., Prata, A. J., Richter, A., Eckhardt, S., Seibert, P., Hoffmann, A., Ritter, C., Bitar, L., Duck, T. J. and Stebel, K. (2010), ‘Remote sensing and inverse transport modeling of the Kasatochi eruption sulfur dioxide cloud’, *Journal of Geophysical Research: Atmospheres* **115**(D2).
URL: <https://agupubs.onlinelibrary.wiley.com/doi/abs/10.1029/2009JD013286>
- Krotkov, N., McLinden, C., Li, C., Lamsal, L., Celarier, E., Marchenko, S., Swartz, W., Bucsela, E., Joiner, J., BN, D., Boersma, K., Veefkind, J., Levelt, P., Fioletov, V., Dickerson, R., He, H., Lu, Z. and Streets, D. (2016), ‘Aura OMI observations of regional SO₂ and NO₂ pollution changes from 2005 to 2015’, *Atmospheric Chemistry and Physics* **16**, 4605–4629.
URL: <http://www.atmos-chem-phys.net/16/4605/2016/>
- Krueger, A. (1983), ‘Sighting of El Chichón sulfur dioxide clouds with the Nimbus 7 Total Ozone Mapping Spectrometer’, *Science* **220**(4604), 1377–1379.
URL: <https://science.sciencemag.org/content/220/4604/1377>
- Krueger, A., Krotkov, N. and Carn, S. (2008), ‘El Chichón: The genesis of volcanic sulfur dioxide monitoring from space’, *Journal of Volcanology and Geothermal Research* **175**(4), 408–414.
URL: <https://doi.org/10.1016/j.jvolgeores.2008.02.026>
- Lacasse, C., Karlsdóttir, S., Larsen, G., Soosalu, H., Rose, I. and Ernst, G. (2004), ‘Weather radar observations of the Hekla 2000 eruption cloud, Iceland’, *Bulletin of Volcanology* **66**(5), 457–473.
URL: <https://link.springer.com/article/10.1007/s00445-003-0329-3>
- Laiolo, M., Massimetti, F., Cigolini, C., Ripepe, M. and Coppola, D. (2018), ‘Long-term eruptive trends from space-based thermal and SO₂ emissions: a comparative analysis of Stromboli, Batu Tara and Tinakula volcanoes’, *Bulletin of Volcanology* **80**(9), 68.
URL: <https://doi.org/10.1007/s00445-018-1242-0>
- Lavanant, L., Fourrié, N., Gambacorta, A., Giuseppe, G., Heilliette, S., I. Hilton,

- F., Kim, M.-J., P. McNally, A., Nishihata, H., G. Pavelin, E. and Rabier, F. (2011), ‘Comparison of cloud products within IASI footprints for the assimilation of cloudy radiances’, **137**, 1988 – 2003.
- Lechner, P., Tupper, A., Guffanti, M., Loughlin, S. and Casadevall, T. (2017), *Volcanic Ash and Aviation—The Challenges of Real-Time, Global Communication of a Natural Hazard*, Advances in Volcanology, Springer, Berlin, Heidelberg, pp. 1–14.
- URL:** <https://doi.org/10.1007/11157201649>
- Li, C., Joiner, J., Krotkov, N. A. and Bhartia, P. K. (2013), ‘A fast and sensitive new satellite SO₂ retrieval algorithm based on principal component analysis: Application to the Ozone Monitoring Instrument’, *Geophysical Research Letters* **40**(23), 6314–6318.
- URL:** <https://agupubs.onlinelibrary.wiley.com/doi/abs/10.1002/2013GL058134>
- Lopez, T., Fee, D., Prata, F. and Dehn, J. (2013), ‘Characterization and interpretation of volcanic activity at Karymsky Volcano, Kamchatka, Russia, using observations of infrasound, volcanic emissions, and thermal imagery’, *Geochemistry, Geophysics, Geosystems* **14**(12), 5106–5127.
- URL:** <https://doi.org/10.1002/2013GC004817>
- Lu, Z., Streets, D. G., de Foy, B., Lamsal, L. N., Duncan, B. N. and Xing, J. (2015), ‘Emissions of nitrogen oxides from US urban areas: estimation from Ozone Monitoring Instrument retrievals for 2005–2014’, *Atmospheric Chemistry and Physics* **15**(18), 10367–10383.
- URL:** <https://www.atmos-chem-phys.net/15/10367/2015/>
- Mackie, S., Millington, S. and Watson, I. M. (2014b), ‘How assumed composition affects the interpretation of satellite observations of volcanic ash’, *Meteorological Applications* **21**(1), 20–29.
- URL:** <https://rmets.onlinelibrary.wiley.com/doi/abs/10.1002/met.1445>
- Mackie, S. and Watson, M. (2014a), ‘Probabilistic detection of volcanic ash using a bayesian approach’, *Journal of Geophysical Research: Atmospheres* **119**(5), 2409–2428.
- URL:** <https://agupubs.onlinelibrary.wiley.com/doi/abs/10.1002/2013JD021077>
- Maes, K., Vandenbussche, S., Klüser, L., Kumps, N. and de Mazière, M. (2016), ‘Vertical Profiling of Volcanic Ash from the 2011 Puyehue Cordon Caulle Eruption Using IASI’, *Remote Sensing* **8**(2).
- URL:** <http://www.mdpi.com/2072-4292/8/2/103>
- Malinconico, L. (1979), ‘Fluctuations in SO₂ emission during recent eruptions of Etna’, *Nature* **278**, 43–45.
- URL:** <https://www.nature.com/articles/278043a0>

- Malinconico, L. (1987), 'On the variation of SO₂ emission from volcanoes', *Journal of Volcanology and Geothermal Research* **33**(1), 231 – 237.
URL: <http://www.sciencedirect.com/science/article/pii/0377027387900655>
- Marenco, F., Johnson, B., Turnbull, K., Newman, S., Haywood, J., Webster, H. and Ricketts, H. (2011), 'Airborne lidar observations of the 2010 Eyjafjallajökull volcanic ash plume', *Journal of Geophysical Research: Atmospheres* **116**(D20).
URL: <https://agupubs.onlinelibrary.wiley.com/doi/abs/10.1029/2011JD016396>
- Marzano, F., Corradini, S., Mereu, L., Kylling, A., Montopoli, M., Cimini, D., Merucci, L. and Stelitano, D. (2018), 'Multisatellite Multisensor Observations of a Sub-Plinian Volcanic Eruption: The 2015 Calbuco Explosive Event in Chile', *IEEE Transactions on Geoscience and Remote Sensing* **PP**, 1–16.
- Mastin, L., Guffanti, M., Servranckx, R., Webley, P., Barsotti, S., Dean, K., Durant, A., Ewert, J., Neri, A., Rose, W., Schneider, D., Siebert, L., Stunder, B., Swanson, G., Tupper, A., Volentik, A. and Waythomas, C. (2009), 'A multidisciplinary effort to assign realistic source parameters to models of volcanic ash-cloud transport and dispersion during eruptions', *Journal of Volcanology and Geothermal Research* **186**(1), 10 – 21.
URL: <http://www.sciencedirect.com/science/article/pii/S0377027309000146>
- Mather, T. A. (2015), 'Volcanoes and the environment: Lessons for understanding Earth's past and future from studies of present-day volcanic emissions', *Journal of Volcanology and Geothermal Research* **304**, 160–179.
URL: <http://creativecommons.org/licenses/by/4.0/>
- Matthias, V., Aulinger, A., Bieser, J., Cuesta, J., Geyer, B., Langmann, B., Serikov, I., Mattis, I., Minikin, A., Mona, L., Quante, M., Schumann, U. and Weinzierl, B. (2012), 'The ash dispersion over Europe during the Eyjafjallajökull eruption – Comparison of CMAQ simulations to remote sensing and air-borne in-situ observations', *Atmospheric Environment* **48**, 184 – 194.
URL: <http://www.sciencedirect.com/science/article/pii/S1352231011007011>
- McCormick, B. T., Edmonds, M., Mather, T. A., Champion, R., Hayer, C. S., Thomas, H. E. and Carn, S. A. (2013), 'Volcano monitoring applications of the Ozone Monitoring Instrument', *Geological Society, London, Special Publications* **380**(1), 259–291.
URL: <http://dx.doi.org/10.1144/SP380.11>
- McCormick, B. T., Herzog, M., Yang, J., Edmonds, M., Mather, T. A., Carn, S. A., Hidalgo, S. and Langmann, B. (2014), 'A comparison of satellite-and ground-based measurements of SO₂ emissions from Tungurahua volcano, Ecuador', *Journal of Geophysical Research: Atmospheres* **119**(7), 4264–4285.

- URL:** <http://onlinelibrary.wiley.com/doi/10.1002/2013JD019771/abstract>
- McCormick Kilbride, B., Edmonds, M. and Biggs, J. (2016), ‘Observing eruptions of gas-rich compressible magmas from space’, *Nature Communications* **7**, 13744.
- URL:** <https://doi.org/10.1038/ncomms13744>
- McCoy, D. T. and Hartmann, D. L. (2015), ‘Observations of a substantial cloud-aerosol indirect effect during the 2014–2015 Bárðarbunga-Veiðivötn fissure eruption in Iceland’, *Geophysical Research Letters* **42**(23), 10,409–10,414.
- URL:** <https://agupubs.onlinelibrary.wiley.com/doi/abs/10.1002/2015GL067070>
- McGonigle, A. J. (2005), ‘Volcano remote sensing with ground-based spectroscopy’, *Philosophical Transactions of the Royal Society A: Mathematical, Physical and Engineering Sciences* **363**(1837), 2915–2929.
- URL:** <https://royalsocietypublishing.org/doi/abs/10.1098/rsta.2005.1668>
- McGonigle, A. J. S., Oppenheimer, C., Galle, B., Mather, T. A. and Pyle, D. M. (2002), ‘Walking traverse and scanning DOAS measurements of volcanic gas emission rates’, *Geophysical Research Letters* **29**(20), 46–1–46–4.
- URL:** <http://doi.wiley.com/10.1029/2002GL015827>
- McGonigle, A. J. S., Oppenheimer, C., Tsanev, V. I., Saunders, S., Mulina, K., Tohui, S., Bosco, J., Nahou, J., Kuduon, J. and Taranu, F. (2004), ‘Sulphur dioxide fluxes from Papua New Guinea’s volcanoes’, *Geophysical Research Letters* **31**(8), L08606.
- URL:** <http://onlinelibrary.wiley.com/doi/10.1029/2004GL019568/full>
- McNally, A. and Watts, P. (2003), ‘A cloud detection algorithm for high-spectral-resolution infrared sounders’, *Quarterly Journal of the Royal Meteorological Society* **129**, 3411–3423.
- URL:** <https://doi.org/10.1256/qj.02.208>
- MEaSURES (2019), ‘Measures so2 source emission catalogue’.
- URL:** <https://so2.gsfc.nasa.gov/measures.html>
- Melnikov, D., Ushakov, S. and Galle, B. (2014), Estimation of the sulfur dioxide emission by Kamchatka volcanoes using differential optical absorption spectroscopy, in ‘Workshop on Japan-Kamchatka-Alaska Subduction Processes’, Vol. 8.
- Menard, G., S, M., Vlastélic, I., Aguilera, F., Valade, S., Bontemps, M. and González, R. (2014), ‘Gas and aerosol emissions from Lascar volcano (Northern Chile): Insights into the origin of gases and their links with the volcanic activity’, *Journal of Volcanology and Geothermal Research* **287**, 51–67.
- URL:** <http://dx.doi.org/10.1016/j.jvolgeores.2014.09.004>
- Menzel, W., Frey, R.A. and Zhang, H., Wylie, D., Moeller, C., Holz, R., Maddux, B., Baum, B., Strabala, K. and Gumley, L. (2008), ‘MODIS Global Cloud-Top Pressure and Amount Estimation: Algorithm Description and Results’, *Journal*

- of Applied Meteorology and Climatology* **47**, 1175–1198.
- URL:** <https://journals.ametsoc.org/doi/abs/10.1175/2007JAMC1705.1>
- Menzel, W. P., Smith, W. L. and Stewart, T. R. (1983), ‘Improved Cloud Motion Wind Vector and Altitude Assignment Using VAS’, *Journal of Climate and Applied Meteorology* **22**(3), 377–384.
- URL:** [https://doi.org/10.1175/1520-0450\(1983\)022<0377:ICMWVA>2.0.CO;2](https://doi.org/10.1175/1520-0450(1983)022<0377:ICMWVA>2.0.CO;2)
- Menzel, W. P., Wylie, D. P. and Strabala, K. I. (1992), ‘Seasonal and Diurnal Changes in Cirrus Clouds as Seen in Four Years of Observations with the VAS’, *Journal of Applied Meteorology* **31**(4), 370–385.
- URL:** [https://doi.org/10.1175/1520-0450\(1992\)031<0370:SADCIC>2.0.CO;2](https://doi.org/10.1175/1520-0450(1992)031<0370:SADCIC>2.0.CO;2)
- Miller, T. and Casadevall, T. (2000), Volcanic ash hazards to aviation, in H. Sigurdsson, ed., ‘Encyclopaedia of Volcanoes’, Academic Press, pp. 915–930.
- Millington, S. C., Saunders, R. W., Francis, P. N. and Webster, H. N. (2012), ‘Simulated volcanic ash imagery: A method to compare NAME ash concentration forecasts with SEVIRI imagery for the Eyjafjallajökull eruption in 2010’, *Journal of Geophysical Research: Atmospheres* **117**(D20).
- URL:** <https://agupubs.onlinelibrary.wiley.com/doi/abs/10.1029/2011JD016770>
- Moffat, A. and Millán, M. (1971), ‘The application of optical correlation techniques to the remote sensing of SO₂ plumes using skylight’, *Atmospheric Environment* **5**(8), 677–690.
- URL:** [https://doi.org/10.1016/0004-6981\(71\)90125-9](https://doi.org/10.1016/0004-6981(71)90125-9)
- Moussallam, Y., Tamburello, G., Peters, N., Apaza, F., Schipper, C., Curtis, A., Aiuppa, A., Masias, P., Boichu, M., Bauduin, S., Barnie, T., Bani, P., Giudice, G. and Moussallam, M. (2017), ‘Volcanic gas emissions and degassing dynamics at Ubinas and Sabancaya volcanoes; implications for the volatile budget of the central volcanic zone’, *Journal of Volcanology and Geothermal Research* **343**, 181 – 191.
- URL:** <http://www.sciencedirect.com/science/article/pii/S0377027317301944>
- Moxnes, E. D., Kristiansen, N. I., Stohl, A., Clarisse, L., Durant, A., Weber, K. and Vogel, A. (2014a), ‘Separation of ash and sulfur dioxide during the 2011 Grímsvötn eruption’, *Journal of Geophysical Research: Atmospheres* **119**(12), 7477–7501.
- URL:** <https://agupubs.onlinelibrary.wiley.com/doi/abs/10.1002/2013JD021129>
- Moxnes, E., Kristiansen, N., Stohl, A., Clarisse, L., Durant, A., Weber, K. and Vogel, A. (2014b), ‘Separation of ash and sulfur dioxide during the 2011 Grímsvötn eruption’, *Journal of Geophysical Research: Atmospheres* **119**(12), 7477 – 7501.
- URL:** <http://onlinelibrary.wiley.com/doi/10.1002/2013JD021129/abstract>
- Naismith, A. K., Watson, I. M., Escobar-Wolf, R., Chigna, G., Thomas, H., Coppola, D. and Chun, C. (2019), ‘Eruption frequency patterns through time for the

- current (1999–2018) activity cycle at Volcán de Fuego derived from remote sensing data: Evidence for an accelerating cycle of explosive paroxysms and potential implications of eruptive activity’, *Journal of Volcanology and Geothermal Research* **371**, 206 – 219.
- URL:** <http://www.sciencedirect.com/science/article/pii/S0377027318303378>
- Naranjo, M. F., Ebmeier, S., Vallejo, S., Ramón, P., Mothes, P., Biggs, J. and Herrera, F. (2016), ‘Mapping and measuring lava volumes from 2002 to 2009 at El Reventador Volcano, Ecuador, from field measurements and satellite remote sensing’, *Journal of Applied Volcanology* **5**(1), 8.
- URL:** <https://doi.org/10.1186/s13617-016-0048-z>
- Neal, C., Herrick, J., Girina, O., Chibisova, M., Rybin, A., McGimsey, R. and Dixon, J. (2014), *2010 Volcanic Activity in Alaska, Kamchatka, and the Kurile Islands: Summary of Events and Response of the Alaska Volcano Observatory, Scientific Investigations Report 2014–5034*, U.S. Department of the Interior U.S. Geological Survey.
- Newhall, C. (2007), 4.12 - Volcanology 101 for Seismologists, in G. Schubert, ed., ‘Treatise on Geophysics’, Elsevier, Amsterdam, pp. 351 – 388.
- URL:** <http://www.sciencedirect.com/science/article/pii/B9780444527486000729>
- Novak, M. A. M., Watson, I. M., Delgado-Granados, H., Rose, W. I., Cárdenas-González, L. and Realmuto, V. J. (2008), ‘Volcanic emissions from Popocatepetl volcano, Mexico, quantified using Moderate Resolution Imaging Spectroradiometer (MODIS) infrared data: A case study of the December 2000 - January 2001 emissions’, *Journal of Volcanology and Geothermal Research* **170**(1-2), 76–85.
- Oppenheimer, C. (1998), ‘Review article: Volcanological applications of meteorological satellites’, *International Journal of Remote Sensing* **19**(15), 2829–2864.
- URL:** <https://doi.org/10.1080/014311698214307>
- Oppenheimer, C. (2010), ‘Ultraviolet sensing of volcanic sulfur emissions’, *Elements* **6**(2), 87–92.
- URL:** <http://elements.geoscienceworld.org/content/6/2/87>
- Oppenheimer, C., Fischer, T. and Scaillet, B. (2014), Volcanic degassing: Process and impact, in ‘Treatise on Geochemistry’, Elsevier, pp. 111–179.
- Oppenheimer, C. and Francis, P. (1997), ‘Remote sensing of heat, lava and fumarole emissions from Erta Ale volcano, Ethiopia’, *International Journal of Remote Sensing* **18**(8), 1661–1692.
- URL:** <https://doi.org/10.1080/014311697218043>
- Oppenheimer, C., Francis, P. W., Rothery, D. A., Carlton, R. W. T. and Glaze, L. S. (1993), ‘Infrared image analysis of volcanic thermal features: Láscar Volcano, Chile, 1984–1992’, *Journal of Geophysical Research: Solid Earth* **98**(B3), 4269–

4286.

URL: <https://agupubs.onlinelibrary.wiley.com/doi/abs/10.1029/92JB02134>

Oppenheimer, C., Scaillet, B. and Martin, R. S. (2011), ‘Sulfur degassing from volcanoes: source conditions, surveillance, plume chemistry and earth system impacts’, *Reviews in Mineralogy and Geochemistry* **73**(1), 363–421.

URL: <http://rimg.geoscienceworld.org/content/73/1/363>

Pangaud, T., Fourrie, N., Guidard, V., Dahoui, M. and Rabier, F. (2009), ‘Assimilation of AIRS Radiances Affected by Mid- to Low-Level Clouds’, *Monthly Weather Review* **137**(12), 4276–4292.

URL: <https://doi.org/10.1175/2009MWR3020.1>

Pardini, F., Burton, M., Arzilli, F., Spina, G. L. and Polacci, M. (2018), ‘SO₂ emissions, plume heights and magmatic processes inferred from satellite data: The 2015 calbuco eruptions’, *Journal of Volcanology and Geothermal Research*.

URL: <http://www.sciencedirect.com/science/article/pii/S0377027318301896>

Pardini, F., Burton, M., de’ Michieli Vitturi, M., Corradini, S., Salerno, G., Merucci, L. and Di Grazia, G. (2017), ‘Retrieval and intercomparison of volcanic SO₂ injection height and eruption time from satellite maps and ground-based observations’, *Journal of Volcanology and Geothermal Research* **331**, 79 – 91.

URL: <http://www.sciencedirect.com/science/article/pii/S037702731630244X>

Patrick, M. R. (2007), ‘Dynamics of strombolian ash plumes from thermal video: Motion, morphology, and air entrainment’, *Journal of Geophysical Research: Solid Earth* **112**(B6).

URL: <https://agupubs.onlinelibrary.wiley.com/doi/abs/10.1029/2006JB004387>

Pavolonis, M. J., Heidinger, A. K. and Sieglaff, J. (2013), ‘Automated retrievals of volcanic ash and dust cloud properties from upwelling infrared measurements’, *Journal of Geophysical Research: Atmospheres* **118**(3), 1436–1458.

URL: <https://agupubs.onlinelibrary.wiley.com/doi/abs/10.1002/jgrd.50173>

Pergola, N., Tramutoli, V., Marchese, F., Scaffidi, I. and Lacava, T. (2004), ‘Improving volcanic ash cloud detection by a robust satellite technique’, *Remote Sensing of Environment* **90**(1), 1 – 22.

URL: <http://www.sciencedirect.com/science/article/pii/S003442570300347X>

Peters, D. (2010), ‘Aerosol Refractive Index Archive ARIA’.

URL: <http://eodg.atm.ox.ac.uk/ARIA/index.html>

Petersen, G. N. (2010), ‘A short meteorological overview of the Eyjafjallajökull eruption 14 April–23 May 2010’, *Weather* **65**(8), 203–207.

URL: <https://rmets.onlinelibrary.wiley.com/doi/abs/10.1002/wea.634>

Petersen, G. N., Bjornsson, H., Arason, P. and von Löwis, S. (2012), ‘Two weather radar time series of the altitude of the volcanic plume during the May 2011

- eruption of Grimsvötn, Iceland', *Earth System Science Data* **4**(1), 121–127.
URL: <https://www.earth-syst-sci-data.net/4/121/2012/>
- Pieri, D., Ma, C., Simpson, J. J., Hufford, G., Grindle, T. and Grove, C. (2002), 'Analyses of in-situ airborne volcanic ash from the February 2000 eruption of Hekla Volcano, Iceland', *Geophysical Research Letters* **29**(16), 19–1–19–4.
URL: <http://dx.doi.org/10.1029/2001GL013688>
- Pinel, V., Poland, M. and Hooper, A. (2014), 'Volcanology: Lessons learned from Synthetic Aperture Radar imagery', *Journal of Volcanology and Geothermal Research* **289**, 81 – 113.
URL: <http://www.sciencedirect.com/science/article/pii/S0377027314003084>
- Prata, A. (1989a), 'Observations of volcanic ash clouds in the 10–12 μ m window using AVHRR/2 data', *International Journal of Remote Sensing* **10**(4–5), 751–761.
URL: <https://doi.org/10.1080/01431168908903916>
- Prata, A. and Bernardo, C. (2007), 'Retrieval of volcanic SO₂ column abundance from Atmospheric Infrared Sounder data', *Journal of Geophysical Research: Atmospheres* (1984–2012) **112**(D20), D20204.
URL: <http://onlinelibrary.wiley.com/doi/10.1029/2006JD007955/full>
- Prata, A. J. (1989b), 'Infrared radiative transfer calculations for volcanic ash clouds', *Geophysical Research Letters* **16**(11), 1293–1296.
URL: <https://agupubs.onlinelibrary.wiley.com/doi/abs/10.1029/GL016i011p01293>
- Prata, A. J., Carn, S. A., Stohl, A. and Kerkmann, J. (2007), 'Long range transport and fate of a stratospheric volcanic cloud from Soufrière Hills volcano, Montserrat', *Atmospheric Chemistry and Physics* **7**(19), 5093–5103.
URL: <http://www.atmos-chem-phys.net/7/5093/2007/>
- Prata, A. J. and Grant, I. F. (2001a), 'Retrieval of microphysical and morphological properties of volcanic ash plumes from satellite data: Application to Mt. Ruapehu, New Zealand', *Quarterly Journal of the Royal Meteorological Society* **127**(576), 2153–2179.
URL: <https://rmets.onlinelibrary.wiley.com/doi/abs/10.1002/qj.49712757615>
- Prata, A. and Kerkmann, J. (2007), 'Simultaneous retrieval of volcanic ash and SO₂ using MSG-SEVIRI measurements', *Geophysical Research Letters* **34**(5), L05813.
- Prata, A., Rose, W., Slef, S. and O'Brien, D. (2003), Global, long-term sulphur dioxide measurements from TOVS data: A new tool for studying explosive volcanism and climate, in 'Volcanism and the Earth's Atmosphere', American Geophysical Union, pp. 75–92.
- Prata, A. and Tupper, A. (2009), 'Aviation hazards from volcanoes: the state of the science', *Natural Hazards* **51**(2), 239–244.
URL: <https://doi.org/10.1007/s11069-009-9415-y>

- Prata, A. and Turner, P. (1997), 'Cloud-top height determination using ATSR data', *Remote Sensing of Environment* **59**(1), 1 – 13.
URL: <http://www.sciencedirect.com/science/article/pii/S0034425796000715>
- Prata, F., Bluth, G., Werner, C., Realmuto, V., Carn, S. and Watson, M. (2015), Remote sensing of gas emissions from volcanoes, in K. Dean and J. Dehn, eds, 'Monitoring Volcanoes in the North Pacific', Springer, pp. 145–186.
- Prata, F. and Grant, I. (2001b), *Determination of mass loadings and plume heights of volcanic ash clouds from satellite data*, CSIRO Atmospheric Research, Aspendale.
- Prata, G., Ventress, L., Carboni, E., Mather, T., Grainger, R. and Pyle, D. (2019), 'A New Parameterization of Volcanic Ash Complex Refractive Index Based on NBO/T and SiO₂ Content', *Journal of Geophysical Research: Atmospheres* **124**, 1779–1797.
URL: <https://doi.org/10.1029/2018JD028679>
- Pugnaghi, S., Gangale, G., Corradini, S. and Buongiorno, M. (2006), 'Mt. etna sulfur dioxide flux monitoring using ASTER-TIR data and atmospheric observations', *Journal of Volcanology and Geothermal Research* **152**(1-2), 74–90.
URL: <http://www.sciencedirect.com/science/article/pii/S037702730500346X>
- Pyle, D. M., Mather, T. A. and Biggs, J. (2013), 'Remote sensing of volcanoes and volcanic processes: integrating observation and modelling – introduction', *Geological Society, London, Special Publications* **380**(1), 1–13.
URL: <http://sp.lyellcollection.org/content/early/2013/09/24/SP380.14>
- Quei er, M., Burton, M., Theys, N., Pardini, F., Salerno, G., Caltabiano, T., Varnam, M., Esse, B. and Kazahaya, R. (2019), 'TROPOMI enables high resolution SO₂ flux observations from Mt. Etna, Italy, and beyond', *Scientific Reports* **9**(1), 957.
URL: <https://doi.org/10.1038/s41598-018-37807-w>
- Realmuto, V. (2000), 'The potential use of Earth Observing System data to monitor the passive emission of sulfur dioxide from volcanoes', *Geophysical Monograph Series* **116**, 101 – 115.
URL: <http://onlinelibrary.wiley.com/doi/10.1029/GM116p0101/summary>
- Realmuto, V., Abrams, M., Buongiorno, M. and Pieri, D. (1994), 'The use of multispectral thermal infrared image data to estimate the sulfur dioxide flux from volcanoes: a case study from Mount Etna, Sicily, 29 July 1986', *Journal of Geophysical Research* **99**(B1), 481–488.
URL: <http://onlinelibrary.wiley.com/doi/10.1029/93JB02062/abstract>
- Realmuto, V., Sutton, A. and Elias, T. (1997), 'Multispectral imaging of sulfur dioxide plumes from the East Rift Zone of Kilauea Volcano, Hawaii', *Journal of Geophysical Research* **102**(B7), 15057–15072.

URL: <http://onlinelibrary.wiley.com/doi/10.1029/96JB03916/full>

Reath, K., Pritchard, M., Poland, M., Delgado, F., Carn, S., Coppola, D., Andrews, B., Ebmeier, S. K., Rumpf, E., Henderson, S., Baker, S., Lundgren, P., Wright, R., Biggs, J., Lopez, T., Wauthier, C., Moruzzi, S., Alcott, A., Wessels, R., Griswold, J., Ogburn, S., Loughlin, S., Meyer, F., Vaughan, G. and Bagnardi, M. (2019), 'Thermal, Deformation, and Degassing Remote Sensing Time Series (CE 2000–2017) at the 47 most Active Volcanoes in Latin America: Implications for Volcanic Systems', *Journal of Geophysical Research: Solid Earth* **124**(1), 195–218.

URL: <https://agupubs.onlinelibrary.wiley.com/doi/abs/10.1029/2018JB016199>

Reath, K., Ramsey, M., Dehn, J. and Webley, P. (2016), 'Predicting eruptions from precursory activity using remote sensing data hybridization', *Journal of Volcanology and Geothermal Research* **321**, 18 – 30.

URL: <http://www.sciencedirect.com/science/article/pii/S0377027316300695>

Remedios, J. J., Leigh, R. J., Waterfall, A. M., Moore, D. P., Sembhi, H., Parkes, I., Greenhough, J., Chipperfield, M. P. and Hauglustaine, D. (2007), 'MIPAS reference atmospheres and comparisons to V4.61/V4.62 MIPAS level 2 geophysical data sets', *Atmospheric Chemistry and Physics Discussions* **7**, 9973–10017.

URL: <https://www.atmos-chem-phys-discuss.net/7/9973/2007/>

Richards, M. (2006), Volcanic ash cloud heights using the MODIS CO₂-slicing algorithm, Master's thesis, University of Wisconsin- Madison.

URL: <http://www.aos.wisc.edu/uwaosjournal/Volume1/theses/Richards.pdf>

Richards, M., Ackerman, S., J. Pavolonis, M., F. Feltz, W. and Tupper, A. (2006), 'Volcanic ash cloud heights using the MODIS CO₂-slicing algorithm', *12th Conference on Aviation Range and Aerospace Meteorology*.

URL: https://www.academia.edu/8116777/Volcanic_Cloud_Heights_Using_the_MODIS_CO_2_Slicing_Algorithm

Rivera, M., J-C, T., Mariño, J., Berolatti, R. and Fuentes, J. (2010), 'Characteristics and management of the 2006 - 2008 volcanic crisis at the Ubinas volcano (Peru)', *Journal of Volcanology and Geothermal Research* **198**(1-2), 19–34.

URL: <http://dx.doi.org/10.1016/j.jvolgeores.2010.07.020>

Rivera, M., Thouret, J.-C., Samaniego, P. and Pennec, J.-L. L. (2014), 'The 2006–2009 activity of the Ubinas volcano (Peru): Petrology of the 2006 eruptive products and insights into genesis of andesite magmas, magma recharge and plumbing system', *Journal of Volcanology and Geothermal Research* **270**, 122 – 141.

URL: <http://www.sciencedirect.com/science/article/pii/S0377027313003466>

Rix, M., Valks, P., Hao, N., van Geffen, J., Clerbaux, C., Clarisse, L., Coheur, P.-F., Loyola, R., Erbetseder, T., Zimmer, W. et al. (2009), 'Satellite monitoring of

- volcanic sulfur dioxide emissions for early warning of volcanic hazards', *IEEE Journal of Selected Topics in Applied Earth Observations and Remote Sensing* **2**(3), 196 – 206.
- URL:** <http://ieeexplore.ieee.org/document/5286248/>
- Robock, A. (2000a), 'Volcanic eruptions and climate', *Reviews of Geophysics* **38**(2), 191–219.
- URL:** <http://onlinelibrary.wiley.com/doi/10.1029/1998RG000054/abstract>
- Robock, A. (2000b), 'Volcanic eruptions and climate', *Reviews of Geophysics* **38**(2), 191–219.
- URL:** <https://agupubs.onlinelibrary.wiley.com/doi/abs/10.1029/1998RG000054>
- Sahetapy-Engel, S. T. and Harris, A. J. L. (2009), 'Thermal-image-derived dynamics of vertical ash plumes at Santiaguito volcano, Guatemala', *Bulletin of Volcanology* **71**(7), 827–830.
- URL:** <https://doi.org/10.1007/s00445-009-0284-8>
- Saunders, R., Matricardi, M. and Brunel, P. (1998), 'An improved fast radiative transfer model for assimilation of satellite radiance observations', *Quarterly Journal of the Royal Meteorological Society* **125**, 1407–1425.
- URL:** <https://doi.org/10.1002/qj.1999.49712555615>
- Scaillet, B., Clemente, B., Evans, B. W. and Pichavant, M. (1998), 'Redox control of sulfur degassing in silicic magmas', *Journal of Geophysical Research: Solid Earth (1978–2012)* **103**(B10), 23937–23949.
- URL:** <http://onlinelibrary.wiley.com/doi/10.1029/98JB02301/abstract>
- Scollo, S., Prestifilippo, M., Pecora, E., Corradini, S., Merucci, L., Spata, G. and Coltelli, M. (2014), 'Eruption column height estimation of the 2011–2013 Etna lava fountains', *Annals of Geophysics* **57**(2), S0214.
- URL:** <https://doi.org/10.4401/ag-6396>
- Sears, T., Thomas, G., Carboni, E., Smith, A. and Grainger, R. (2013), 'SO₂ as a possible proxy for volcanic ash in aviation hazard avoidance', *Journal of Geophysical Research: Atmospheres* **118**, 5698–5709.
- URL:** <https://doi.org/10.1002/jgrd.50505>
- Seftor, C. J., Hsu, N. C., Herman, J. R., Bhartia, P. K., Torres, O., Rose, W. I., Schneider, D. J. and Krotkov, N. (1997), 'Detection of volcanic ash clouds from nimbus 7/total ozone mapping spectrometer', *Journal of Geophysical Research: Atmospheres* **102**(D14), 16749–16759.
- URL:** <https://agupubs.onlinelibrary.wiley.com/doi/abs/10.1029/97JD00925>
- Sigmundsson, F., Hooper, A., Hreinsdóttir, S., Vogfjörð, K. S., Ófeigsson, B. G., Heimisson, E. R., Dumont, S., Parks, M., Spaans, K., Gudmundsson, G. B., Drouin, V., Árnadóttir, T., Jónsdóttir, K., Gudmundsson, M. T., Högnadóttir,

- T., Fridriksdóttir, H. M., Hensch, M., Einarsson, P., Magnússon, E., Samsonov, S., Brandsdóttir, B., White, R. S., Ágústsdóttir, T., Greenfield, T., Green, R. G., Hjartardóttir, R., Pedersen, R., Bennett, R. A., Geirsson, H., La Femina, P. C., Björnsson, H., Pálsson, F., Sturkell, E., Bean, C. J., Möllhoff, M., Braiden, A. K. and Eibl, E. P. S. (2014), ‘Segmented lateral dyke growth in a rifting event at Bárðarbunga volcanic system, Iceland’, *Nature* **517**, 191.
URL: <https://doi.org/10.1038/nature14111>
- Smith, W. L. and Frey, R. (1990), ‘On Cloud Altitude Determinations from High Resolution Interferometer Sounder (HIS) Observations’, *Journal of Applied Meteorology* **29**(7), 658–662.
URL: [https://doi.org/10.1175/1520-0450\(1990\)029<0658:OCADFH>2.0.CO;2](https://doi.org/10.1175/1520-0450(1990)029<0658:OCADFH>2.0.CO;2)
- Smith, W. L. and Platt, C. M. R. (1978), ‘Comparison of satellite-deduced cloud heights with indications from radiosonde and ground-based laser measurements’, *Journal of Applied Meteorology* **17**(12), 1796–1802.
URL: [https://doi.org/10.1175/1520-0450\(1978\)017<1796:COSDCH>2.0.CO;2](https://doi.org/10.1175/1520-0450(1978)017<1796:COSDCH>2.0.CO;2)
- Someya, Y., Imasu, R., Saitoh, N., Ota, Y. and Shiomi, K. (2016), ‘A development of cloud top height retrieval using thermal infrared spectra observed with GOSAT and comparison with CALIPSO data’, *Atmospheric Measurement Techniques* **9**(5), 1981–1992.
URL: <https://www.atmos-meas-tech.net/9/1981/2016/>
- Sparks, R. (2003a), ‘Forecasting volcanic eruptions’, *Earth and Planetary Science Letters* **210**(1), 1 – 15.
URL: <http://www.sciencedirect.com/science/article/pii/S0012821X03001249>
- Sparks, R., Biggs, J. and Neuberg, J. (2012), ‘Monitoring volcanoes’, *Science* **335**(6074), 1310–1311.
URL: <http://science.sciencemag.org/content/335/6074/1310>
- Sparks, R., Burski, M., Carey, S., Gilbert, J., Glaze, L., Sigurdsson, H. and Woods, A. (1997), *Volcanic Plumes*, John Wiley & Sons.
- Sparks, R. S. J. (2003b), Dynamics of magma degassing, in ‘Volcanic Degassing’, Geological Society of London.
URL: <https://doi.org/10.1144/GSL.SP.2003.213.01.02>
- Stein, A. F., Draxler, R. R., Rolph, G. D., Stunder, B. J. B., Cohen, M. D. and Ngan, F. (2015), ‘NOAA’s HYSPLIT Atmospheric Transport and Dispersion Modeling System’, *Bulletin of the American Meteorological Society* **96**(12), 2059–2077.
URL: <https://doi.org/10.1175/BAMS-D-14-00110.1>
- Stix, J., Torres, R. C., M, L. N., J, G. P. C., Raigosa, J. A., M, D. G. and Castonguay, R. (1997), ‘A model of vulcanian eruptions at Galeras volcano, Colombia’, *Journal of Volcanology and Geothermal Research* **77**(1), 285 – 303.

Galeras Volcano, Colombia: Interdisciplinary Study of a Decade Volcano.

URL: <http://www.sciencedirect.com/science/article/pii/S037702739600100X>

Stohl, A., Prata, A. J., Eckhardt, S., Clarisse, L., Durant, A., Henne, S., Kristiansen, N. I., Minikin, A., Schumann, U., Seibert, P., Stebel, K., Thomas, H. E., Thorsteinsson, T., Tørseth, K. and Weinzierl, B. (2011), ‘Determination of time- and height-resolved volcanic ash emissions and their use for quantitative ash dispersion modeling: the 2010 Eyjafjallajökull eruption’, *Atmospheric Chemistry and Physics* **11**(9), 4333–4351.

URL: <https://www.atmos-chem-phys.net/11/4333/2011/>

Stohl, A., Seibert, P., Arduini, J., Eckhardt, S., Fraser, P., Grealley, B. R., Lunder, C., Maione, M., Mühle, J., O’Doherty, S., Prinn, R. G., Reimann, S., Saito, T., Schmidbauer, N., Simmonds, P. G., Vollmer, M. K., Weiss, R. F. and Yokouchi, Y. (2009), ‘An analytical inversion method for determining regional and global emissions of greenhouse gases: Sensitivity studies and application to halocarbons’, *Atmospheric Chemistry and Physics* **9**(5), 1597–1620.

URL: <https://www.atmos-chem-phys.net/9/1597/2009/>

Stoiber, R., Malinconico, L. and Williams, S. (1983), *Use of the correlation spectrometer at volcanoes*, Elsevier, Amsterdam, Netherlands, pp. 425–444.

Surono, Jousset, P., Pallister, J., Boichu, M., Buongiorno, M. F., Budisantoso, A., Costa, F., Andreastuti, S., Prata, F., Schneider, D., Clarisse, L. et al. (2012), ‘The 2010 explosive eruption of Java’s Merapi volcano - A 100-year event’, *Journal of Volcanology and Geothermal Research* **241**, 121–135.

URL: <http://doi.org/10.1016/j.jvolgeores.2012.06.018>

Symonds, R. B., Rose, W. I., Bluth, G. J. and Gerlach, T. M. (1994), ‘Volcanic-gas studies; methods, results, and applications’, *Reviews in Mineralogy and Geochemistry* **30**(1), 1–66.

Taquet, N., Stremme, W., Grutter, M., Baylón, J., Bezanilla, A., Schiavo, B., Rivera, C., Campion, R., Boulesteix, T., Nieto-Torres, A., Espinasa-Pereña, R., Blumenstock, T. and Hase, F. (2019), ‘Variability in the gas composition of the popocatepetl volcanic plume’, *Frontiers in Earth Science* **7**, 114.

URL: <https://www.frontiersin.org/article/10.3389/feart.2019.00114>

Taran, Y. A. (2009), ‘Geochemistry of volcanic and hydrothermal fluids and volatile budget of the Kamchatka-Kuril subduction zone’, *Geochimica et Cosmochimica Acta* **73**(4), 1067–1094.

URL: <https://doi.org/10.1016/j.gca.2008.11.020>

Taylor, I. A., Preston, J., Carboni, E., Mather, T. A., Grainger, R. G., Theys, N., Hidalgo, S. and Kilbride, B. M. (2018), ‘Exploring the Utility of IASI for Monitoring Volcanic SO₂ Emissions’, *Journal of Geophysical Research:*

Atmospheres **123**(10), 5588–5606.

URL: <https://agupubs.onlinelibrary.wiley.com/doi/abs/10.1002/2017JD027109>

Taylor, I., Mackie, S. and Watson, M. (2015), ‘Investigating the use of the Saharan dust index as a tool for the detection of volcanic ash in SEVIRI imagery’, *Journal of Volcanology and Geothermal Research* **304**, 126 – 141.

URL: <http://www.sciencedirect.com/science/article/pii/S037702731500270X>

Tesche, M., Glantz, P., Johansson, C., Norman, M., Hiebsch, A., Ansmann, A., Althausen, D., Engelmann, R. and Seifert, P. (2012), ‘Volcanic ash over Scandinavia originating from the Grímsvötn eruptions in May 2011’, *Journal of Geophysical Research: Atmospheres* **117**(D9), D09201.

URL: <https://agupubs.onlinelibrary.wiley.com/doi/abs/10.1029/2011JD017090>

Theys, N., Campion, R., Clarisse, L., Brenot, H., Van Gent, J., Dils, B., Corradini, S., Merucci, L., Coheur, P.-F., Van Roozendaal, M. et al. (2013), ‘Volcanic SO₂ fluxes derived from satellite data: a survey using OMI, GOME-2, IASI and MODIS’, *Atmos. Chem. Phys* **13**(12), 5945–5968.

URL: <https://doi.org/10.5194/acp-13-5945-2013>

Theys, N., De Smedt, I., Gent, J., Danckaert, T., Wang, T., Hendrick, F., Stavrakou, T., Bauduin, S., Clarisse, L., Li, C. et al. (2015), ‘Sulfur dioxide vertical column DOAS retrievals from the Ozone Monitoring Instrument: Global observations and comparison to ground-based and satellite data’, *Journal of Geophysical Research: Atmospheres* **120**(6), 2470–2491.

URL: <https://doi.org/10.1002/2014JD022657>

Theys, N., Hedelt, P., De Smedt, I., Lerot, C., Yu, H., Vlietinck, J., Pedernana, M., Arellano, S., Galle, B., Fernandez, D., Carlito, C. J. M., Barrington, C., Taisne, B., Delgado-Granados, H., Loyola, D. and Van Roozendaal, M. (2019), ‘Global monitoring of volcanic SO₂ degassing with unprecedented resolution from TROPOMI onboard Sentinel-5 Precursor’, *Scientific Reports* **9**(1), 2643.

URL: <https://doi.org/10.1038/s41598-019-39279-y>

Thomas, G. E. and Siddans, R. (2015), ‘Development of oca type processors to volcanic ash detection and retrieval’, *Final Report EUMETSAT RFQ 13/715490*.

Thomas, H. and Prata, A. (2011), ‘Sulphur dioxide as a volcanic ash proxy during the April–May 2010 eruption of Eyjafjallajökull Volcano, Iceland’, *Atmospheric Chemistry and Physics* **11**, 6871–6880.

URL: <https://doi.org/10.5194/acp-11-6871-2011>

Thomas, H. and Watson, I. (2010), ‘Observations of volcanic emissions from space: current and future perspectives’, *Natural Hazards* **54**(2), 323–354.

URL: <https://link.springer.com/article/10.1007/s11069-009-9471-3>

Tupper, A., Itikarai, I., Richards, M., Prata, F., Carn, S. and Rosenfeld, D. (2007),

- ‘Facing the challenges of the international airways volcano watch: The 2004/05 eruptions of manam, papua new guinea’, *Weather and Forecasting* **22**(1), 175–191.
URL: <https://doi.org/10.1175/WAF974.1>
- Urai, M. (2004), ‘Sulfur dioxide flux estimation from volcanoes using Advanced Spaceborne Thermal Emission and Reflection Radiometer—a case study of Miyakejima volcano, Japan’, *Journal of Volcanology and Geothermal Research* **134**(1-2), 1–13.
URL: <https://doi.org/10.1016/j.jvolgeores.2003.11.008>
- Ventress, L. J., McGarragh, G., Carboni, E., Smith, A. J. and Grainger, R. G. (2016), ‘Retrieval of ash properties from IASI measurements’, *Atmospheric Measurement Techniques* **9**(11), 5407–5422.
URL: <https://www.atmos-meas-tech.net/9/5407/2016/>
- Vernier, J.-P., Fairlie, T. D., Murray, J. J., Tupper, A., Trepte, C., Winker, D., Pelon, J., Garnier, A., Jumelet, J., Pavolonis, M., Omar, A. H. and Powell, K. A. (2013), ‘An Advanced System to Monitor the 3D Structure of Diffuse Volcanic Ash Clouds’, *Journal of Applied Meteorology and Climatology* **52**(9), 2125–2138.
URL: <https://doi.org/10.1175/JAMC-D-12-0279.1>
- Wadge, G., Saunders, S. and Itikarai, I. (2012), ‘Pulsatory andesite lava flow at Bagana Volcano’, *Geochemistry, Geophysics, Geosystems* **13**(11), Q11011.
URL: <https://agupubs.onlinelibrary.wiley.com/doi/abs/10.1029/2012GC004336>
- Walker, J., Carboni, E., Dudhia, A. and Grainger, R. (2012), ‘Improved detection of sulphur dioxide in volcanic plumes using satellite-based hyperspectral infrared measurements: Application to the Eyjafjallajökull 2010 eruption’, *Journal of Geophysical Research: Atmospheres* (1984–2012) **117**(D20).
- Walker, J., Dudhia, A. and Carboni, E. (2011), ‘An effective method for the detection of trace species demonstrated using the MetOp Infrared Atmospheric Sounding Interferometer’, *Atmospheric Measurement Techniques* **4**, 1567–1580.
- Watson, E. J., Swindles, G. T., Stevenson, J. A., Savov, I. and Lawson, I. T. (2016), ‘The transport of Icelandic volcanic ash: Insights from northern European cryptotephra records’, *Journal of Geophysical Research: Solid Earth* **121**(10), 7177–7192.
URL: <https://agupubs.onlinelibrary.wiley.com/doi/abs/10.1002/2016JB013350>
- Watson, I., Oppenheimer, C., Voight, B., Francis, P., Clarke, A., Stix, J., Miller, A., Pyle, D., Burton, M., Young, S., Norton, G., Loughlin, S. and Darroux, B. (2000), ‘The relationship between degassing and ground deformation at Soufriere Hills Volcano, Montserrat’, *Journal of Volcanology and Geothermal Research* **98**(1), 117–126.
URL: <http://www.sciencedirect.com/science/article/pii/S0377027399001870>

- Watson, I., Realmuto, V., Rose, W., Prata, A., Bluth, G., Gu, Y., Bader, C. and Yu, T. (2004), ‘Thermal infrared remote sensing of volcanic emissions using the moderate resolution imaging spectroradiometer’, *Journal of Volcanology and Geothermal Research* **135**(1-2), 75–89.
URL: <https://doi.org/10.1016/j.jvolgeores.2003.12.017>
- Webb, E. B., Varley, N. R., Pyle, D. M. and Mather, T. A. (2014), ‘Thermal imaging and analysis of short-lived Vulcanian explosions at Volcán de Colima, Mexico’, *Journal of Volcanology and Geothermal Research* **278-279**, 132 – 145.
URL: <http://www.sciencedirect.com/science/article/pii/S0377027314001139>
- Weber, K., Eliasson, J., Vogel, A., Fischer, C., Pohl, T., van Haren, G., Meier, M., Grobéty, B. and Dahmann, D. (2012), ‘Airborne in-situ investigations of the Eyjafjallajökull volcanic ash plume on Iceland and over north-western Germany with light aircrafts and optical particle counters’, *Atmospheric Environment* **48**, 9 – 21.
URL: <http://www.sciencedirect.com/science/article/pii/S1352231011010892>
- Webley, P. W., Wooster, M. J., Strauch, W., Saballos, J. A., Dill, K., Stephenson, P., Stephenson, J., Wolf, R. E. and Matias, O. (2008), ‘Experiences from near real time satellite based volcano monitoring in Central America: case studies at Fuego, Guatemala’, *International Journal of Remote Sensing* **29**(22), 6621–6646.
URL: <https://doi.org/10.1080/01431160802168301>
- Webster, H. N., Thomson, D. J., Johnson, B. T., Heard, I. P. C., Turnbull, K., Marengo, F., Kristiansen, N. I., Dorsey, J., Minikin, A., Weinzierl, B., Schumann, U., Sparks, R. S. J., Loughlin, S. C., Hort, M. C., Leadbetter, S. J., Devenish, B. J., Manning, A. J., Witham, C. S., Haywood, J. M. and Golding, B. W. (2012), ‘Operational prediction of ash concentrations in the distal volcanic cloud from the 2010 Eyjafjallajökull eruption’, *Journal of Geophysical Research: Atmospheres* **117**(D20).
URL: <https://agupubs.onlinelibrary.wiley.com/doi/abs/10.1029/2011JD016790>
- Wen, S. and Rose, W. (1994), ‘Retrieval of sizes and total masses of particles in volcanic clouds using AVHRR bands 4 and 5’, *Journal of Geophysical Research: Atmospheres* **99**(D3), 5421–5431.
URL: <https://agupubs.onlinelibrary.wiley.com/doi/abs/10.1029/93JD03340>
- Western, L. M., Rougier, J. and Watson, I. M. (2017), ‘Decision theory-based detection of atmospheric natural hazards from satellite imagery using the example of volcanic ash’, *Quarterly Journal of the Royal Meteorological Society* **144**(711), 581–587.
URL: <https://rmets.onlinelibrary.wiley.com/doi/abs/10.1002/qj.3230>

- Wilkins, K., Western, L. and Watson, I. (2016), ‘Simulating atmospheric transport of the 2011 Grímsvötn ash cloud using a data insertion update scheme’, *Atmospheric Environment* **141**, 48 – 59.
URL: <http://www.sciencedirect.com/science/article/pii/S1352231016304782>
- Wilson, T. M., Jenkins, S. and Stewart, C. (2015), Chapter 3 - impacts from volcanic ash fall, in J. F. Shroder and P. Papale, eds, ‘Volcanic Hazards, Risks and Disasters’, Elsevier, Boston, pp. 47 – 86.
URL: <http://www.sciencedirect.com/science/article/pii/B9780123964533000034>
- Wilson, T. M., Stewart, C., Sword-Daniels, V., Leonard, G. S., Johnston, D. M., Cole, J. W., Wardman, J., Wilson, G. and Barnard, S. T. (2012), ‘Volcanic ash impacts on critical infrastructure’, *Physics and Chemistry of the Earth, Parts A/B/C* **45-46**, 5 – 23.
URL: <http://www.sciencedirect.com/science/article/pii/S1474706511001112>
- Winker, D. M., Liu, Z., Omar, A., Tackett, J. and Fairlie, D. (2012), ‘CALIOP observations of the transport of ash from the Eyjafjallajökull volcano in April 2010’, *Journal of Geophysical Research: Atmospheres* **117**(D20).
URL: <https://agupubs.onlinelibrary.wiley.com/doi/abs/10.1029/2011JD016499>
- Winker, D. M., Vaughan, M. A., Omar, A., Hu, Y., Powell, K. A., Liu, Z., Hunt, W. H. and Young, S. A. (2009), ‘Overview of the CALIPSO Mission and CALIOP Data Processing Algorithms’, *Journal of Atmospheric and Oceanic Technology* **26**(11), 2310–2323.
URL: <https://doi.org/10.1175/2009JTECHA1281.1>
- Witham, C., Webster, H., Hort, M., Jones, A. and Thomson, D. (2012), ‘Modelling concentrations of volcanic ash encountered by aircraft in past eruptions’, *Atmospheric Environment* **48**, 219 – 229.
URL: <http://www.sciencedirect.com/science/article/pii/S1352231011006972>
- Wright, R. (2015), ‘MODVOLC: 14 years of autonomous observations of effusive volcanism from space’, *Geological Society, London, Special Publications* **426**(1), 23–53.
URL: <http://sp.lyellcollection.org/lookup/doi/10.1144/SP426.12>
- Wright, R., Flynn, L., Garbeil, H., Harris, A. and Pilger, E. (2002), ‘Automated volcanic eruption detection using modis’, *Remote Sensing of Environment* **82**(1), 135 – 155.
URL: [https://doi.org/10.1016/S0034-4257\(02\)00030-5](https://doi.org/10.1016/S0034-4257(02)00030-5)
- Wright, R. and Flynn, L. P. (2004), ‘Space-based estimate of the volcanic heat flux into the atmosphere during 2001 and 2002’, *Geology* **32**(3), 189–192.
URL: <https://doi.org/10.1130/G20239.1>
- Wright, R., Flynn, L. P., Garbeil, H., Harris, A. J. and Pilger, E. (2004),

- ‘MODVOLC: near-real-time thermal monitoring of global volcanism’, *Journal of Volcanology and Geothermal Research* **135**(1), 29–49.
URL: <https://doi.org/10.1016/j.jvolgeores.2003.12.008>
- Wylie, D. P. and Menzel, W. P. (1989), ‘Two Years of Cloud Cover Statistics Using VAS’, *Journal of Climate* **2**(4), 380–392.
URL: [https://doi.org/10.1175/1520-0442\(1989\)002<0380:TYOCCS>2.0.CO;2](https://doi.org/10.1175/1520-0442(1989)002<0380:TYOCCS>2.0.CO;2)
- Yu, T., Rose, W. I. and Prata, A. J. (2002), ‘Atmospheric correction for satellite-based volcanic ash mapping and retrievals using “split window” IR data from GOES and AVHRR’, *Journal of Geophysical Research: Atmospheres* **107**(D16).
URL: <https://agupubs.onlinelibrary.wiley.com/doi/abs/10.1029/2001JD000706>
- Zakšek, K., Hort, M., Zaletelj, J. and Langmann, B. (2013), ‘Monitoring volcanic ash cloud top height through simultaneous retrieval of optical data from polar orbiting and geostationary satellites’, *Atmospheric Chemistry and Physics* **13**(5), 2589–2606.
URL: <https://www.atmos-chem-phys.net/13/2589/2013/>
- Zhang, H. and Menzel, W. P. (2002), ‘Improvement in thin cirrus retrievals using an emissivity-adjusted CO₂ slicing algorithm’, *Journal of Geophysical Research: Atmospheres* **107**(D17), AAC 2–1–AAC 2–11.
URL: <https://agupubs.onlinelibrary.wiley.com/doi/abs/10.1029/2001JD001037>
- Zhu, L., Li, J., Zhao, Y., Gong, H. and Li, W. (2017), ‘Retrieval of volcanic ash height from satellite-based infrared measurements’, *Journal of Geophysical Research: Atmospheres* **122**(10), 5364–5379.
URL: <https://agupubs.onlinelibrary.wiley.com/doi/abs/10.1002/2016JD026263>



CO₂ Slicing - Appendix

This appendix includes additional figures from the CO₂ slicing study (chapter 2). Figures A.1 to A.6 show the maximum difference between the true (simulated) and retrieved pressures for the six investigated atmospheres for all the channel combinations between 660 and 800 cm⁻¹. The plots are divided into the different pressure levels. The figure also includes the percentage of successful retrievals (where there is an intersections between the two functions shown in Eq. 2.1 and 2.2 and all quality control conditions are met). This is out of a total of 8 simulations (for each pressure level) with ash optical depths ranging between 5 and 15, effective particle radius ranging between 5 and 10 μm . These could be used to select channels which are appropriate for specific climatologies. Figure A.7 shows the final simulation result for each atmosphere without the quality control applied.

Figure A.1-A.6: Simulation results for the RTTOV default, mid-latitude day, mid-latitude night, tropical, polar summer and polar winter atmospheres respectively. The top two line shows the maximum difference between the true (simulated) and retrieved pressures grouped into the different pressure levels. Each level consists of ash optical depths ranging between 5 and 15 and effective radius between 5 and 10 μm . The bottom two lines show the percentage of accepted retrievals (i.e. the percentage of cases where there is an intersection between equation 2.1 and 2.2, and where all quality control criteria are met)

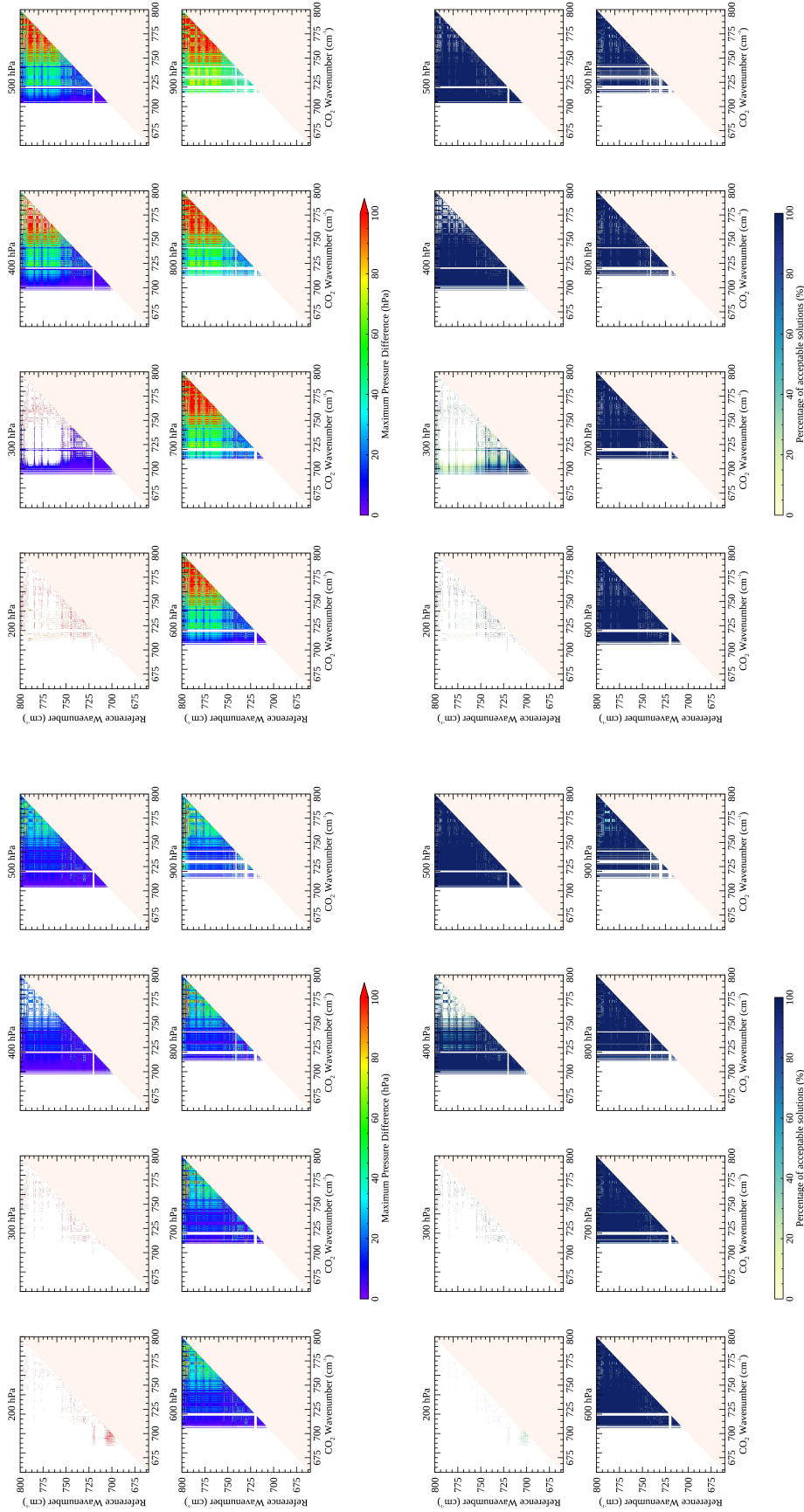


Figure A.1: Simulation results for RTTOV default atmosphere

Figure A.2: Simulation results for mid-latitude day atmosphere

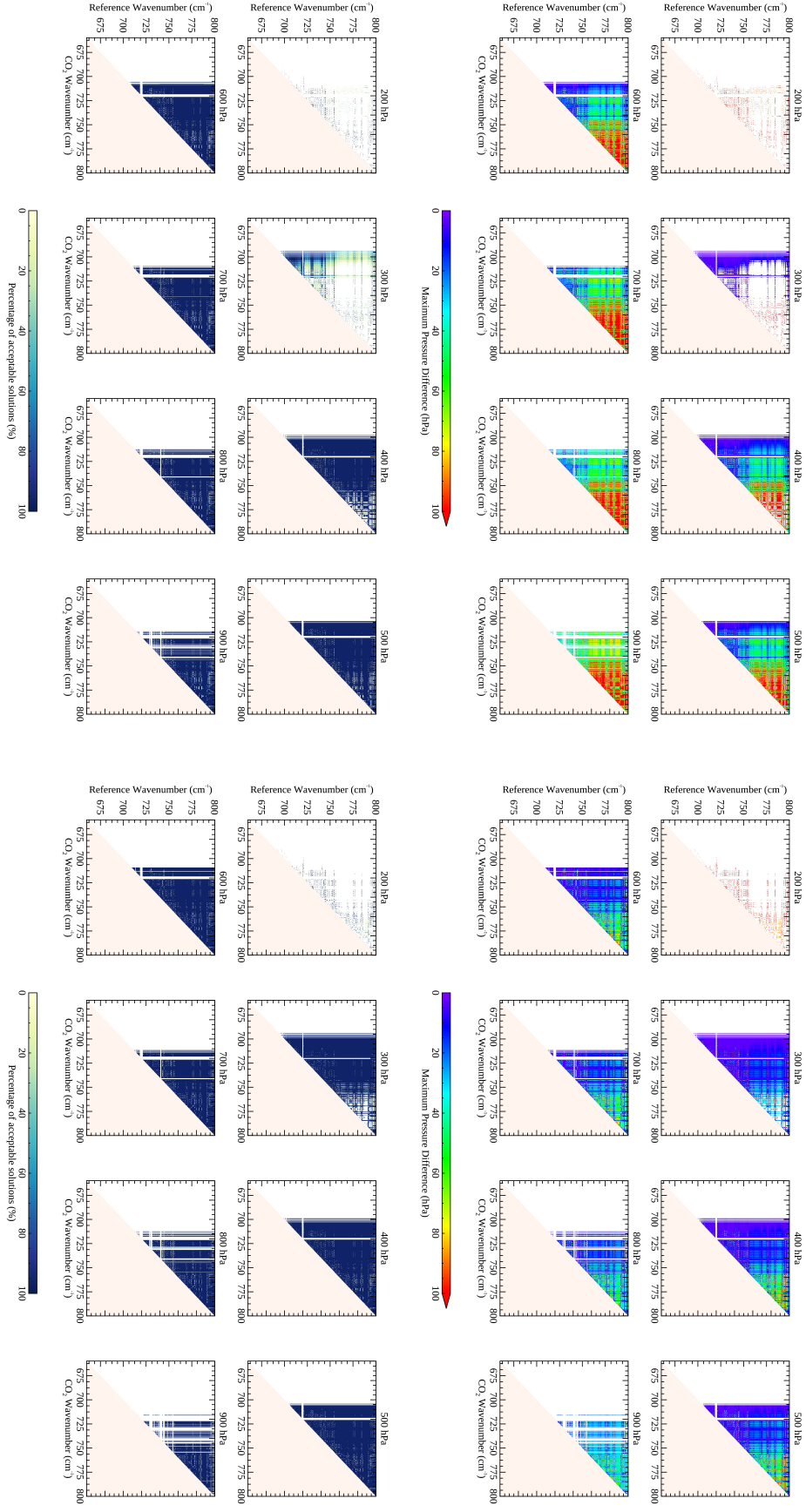


Figure A.3: Simulation results for a mid-latitude night atmosphere

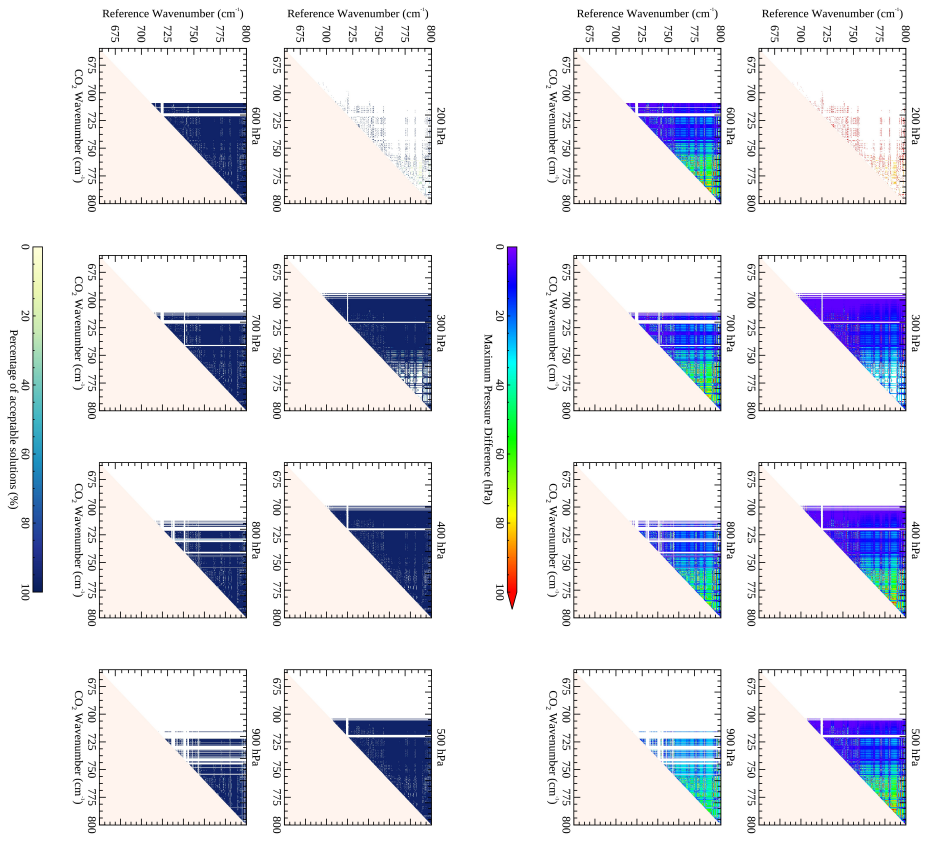


Figure A.4: Simulation results for a tropical atmosphere

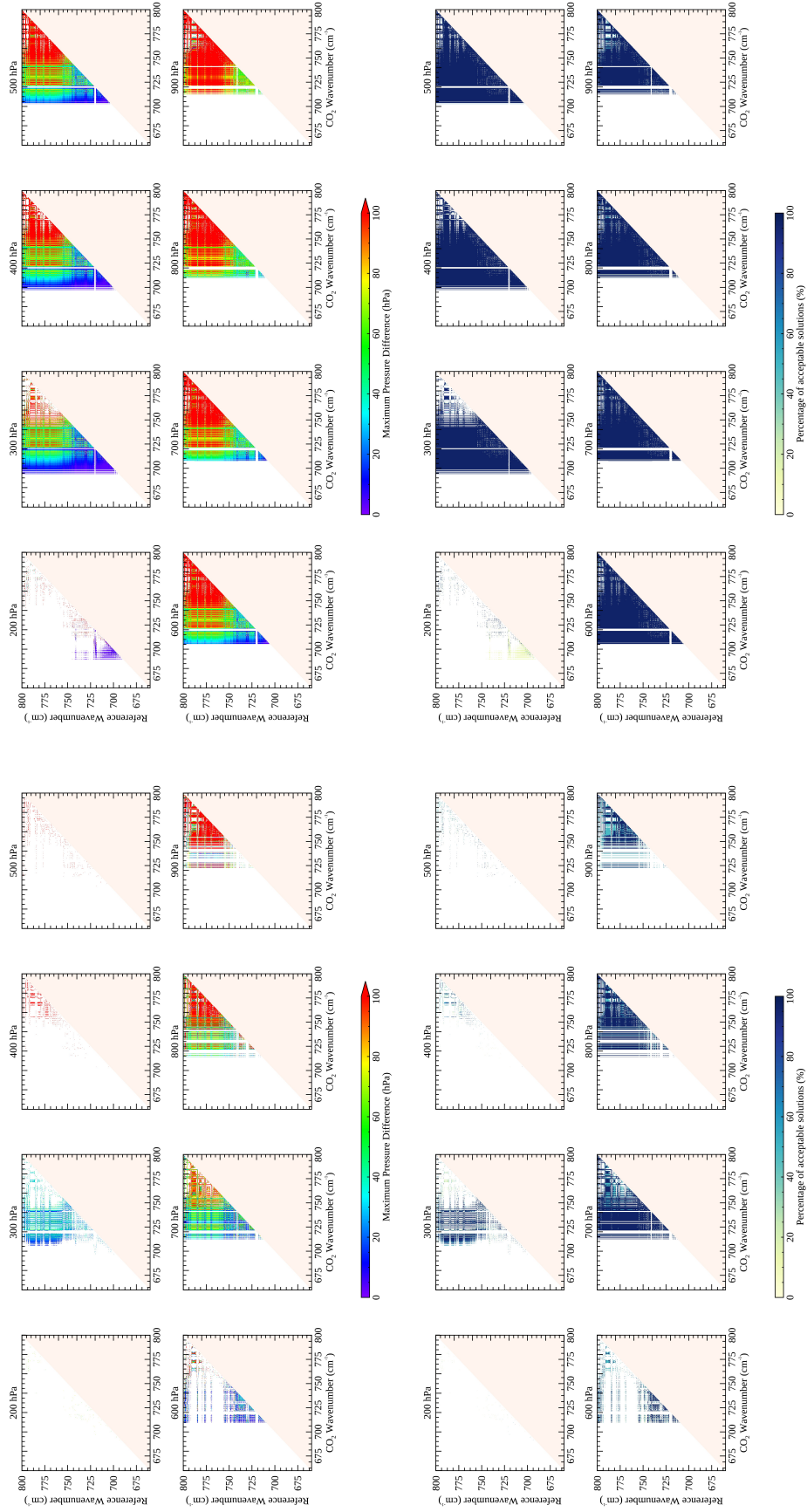


Figure A.5: Simulation results for a polar summer atmosphere

Figure A.6: Simulation results for a polar winter atmosphere

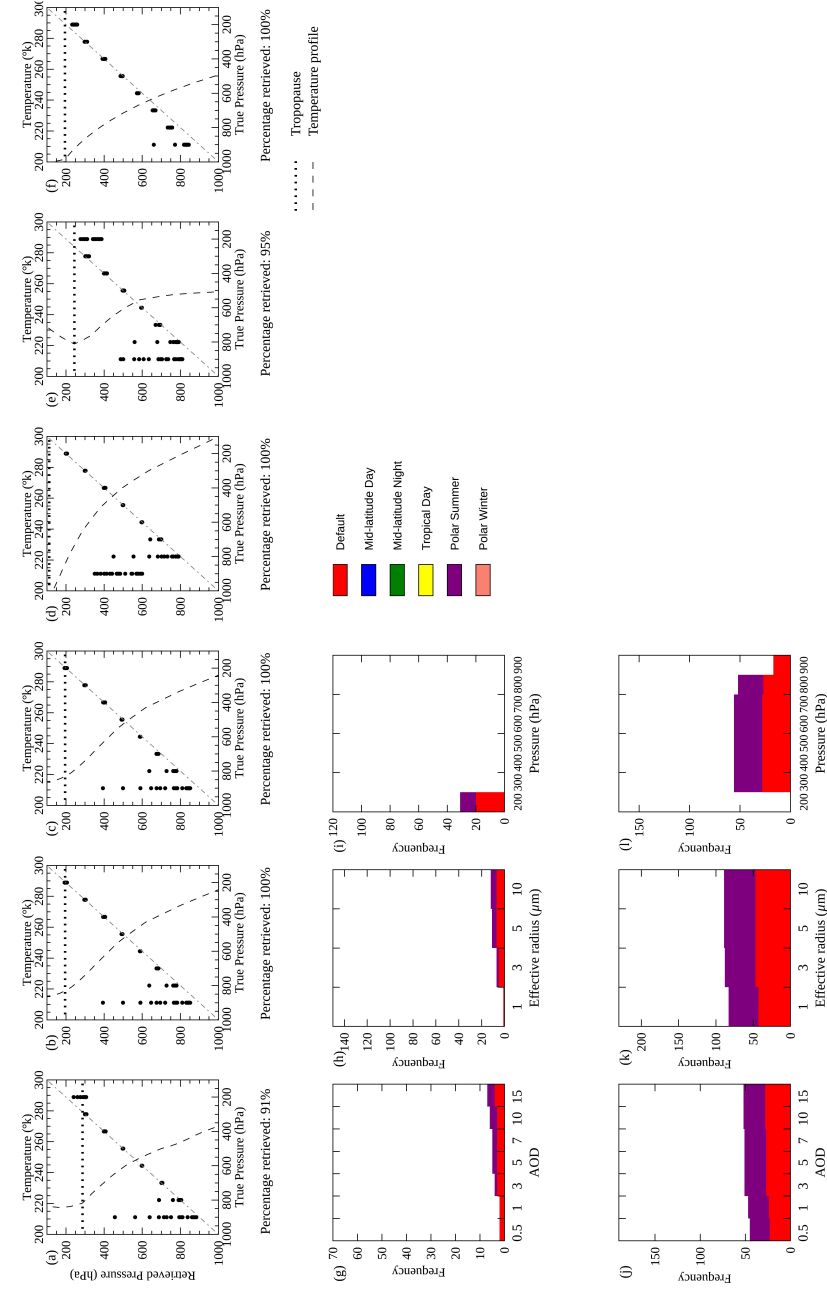


Figure A.7: Final CO₂ slicing pressure results for RTTOV simulated ash spectra (a total of 224 spectra per atmosphere). The plots show the true (simulated) pressure plotted against the CO₂ slicing retrieved value for the six different atmospheres. (a) RTTOV default atmosphere (high latitude), (b) Mid-latitude day, (c) Mid-latitude night, (d) Tropical day, (e) Polar summer (f) Polar winter. No quality control has been applied. In this case, the simulated spectra include the following ash properties: ash optical depth ranging between 0.5 and 15, ash effective radius ranging between 1 and 10 μm and pressure values between 200 and 900 mb. Below each plot is a value indicating the percentage of successful retrievals. (g) The frequency of ash optical depths for which the CO₂ slicing technique was unable to return a height value. (h) Same as (g) for the effective radius. (i) Same as (g) for the ash cloud pressure.

B

Monitoring SO₂ Emissions with IASI - Appendix

Included within the appendix is an animation (SM1) showing each of the global monthly averages of the linear retrieval output. This can be used to identify further eruptive activity and assess the persistency of signals. In the main text, each month is referred to by its frame number. Also included are monthly averages of the bias corrected iterative retrieval output over Ecuador and Kamchatka.

SM1: Animation of the global linear retrieval output averaged for each month between June 2007 and December 2014. This can be accessed at <https://doi.org/10.1002/2017JD027109> within the supplementary information (Taylor et al., 2018). A copy is also included on a memory stick attached to the back of this thesis.

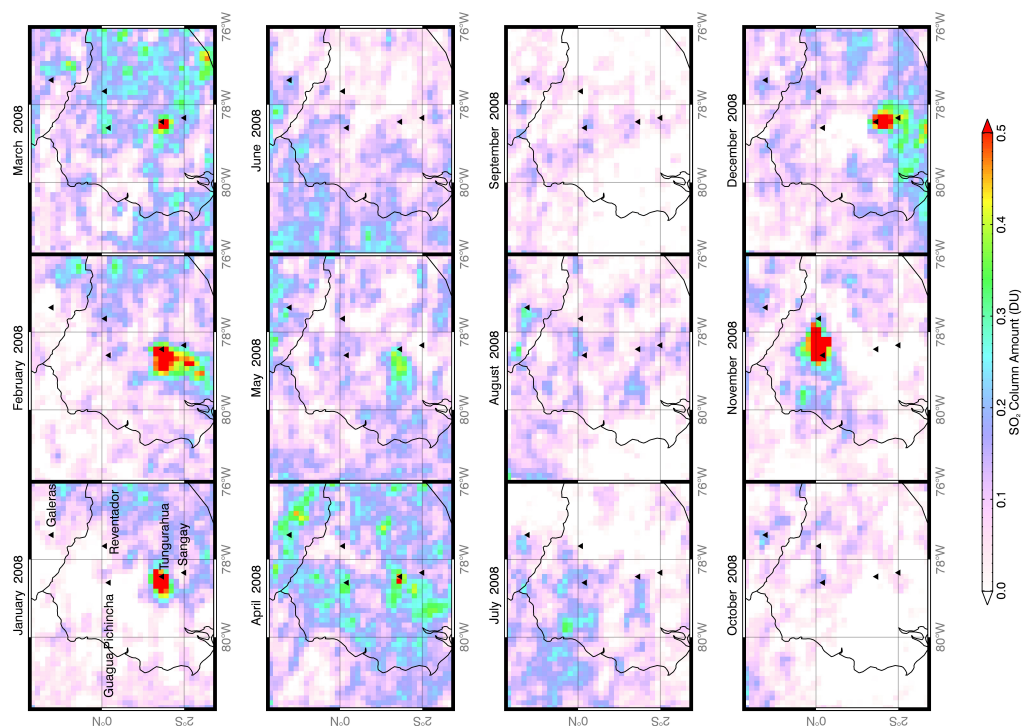


Figure B.2: Monthly average of the iterative retrieval output over Ecuador (2008)

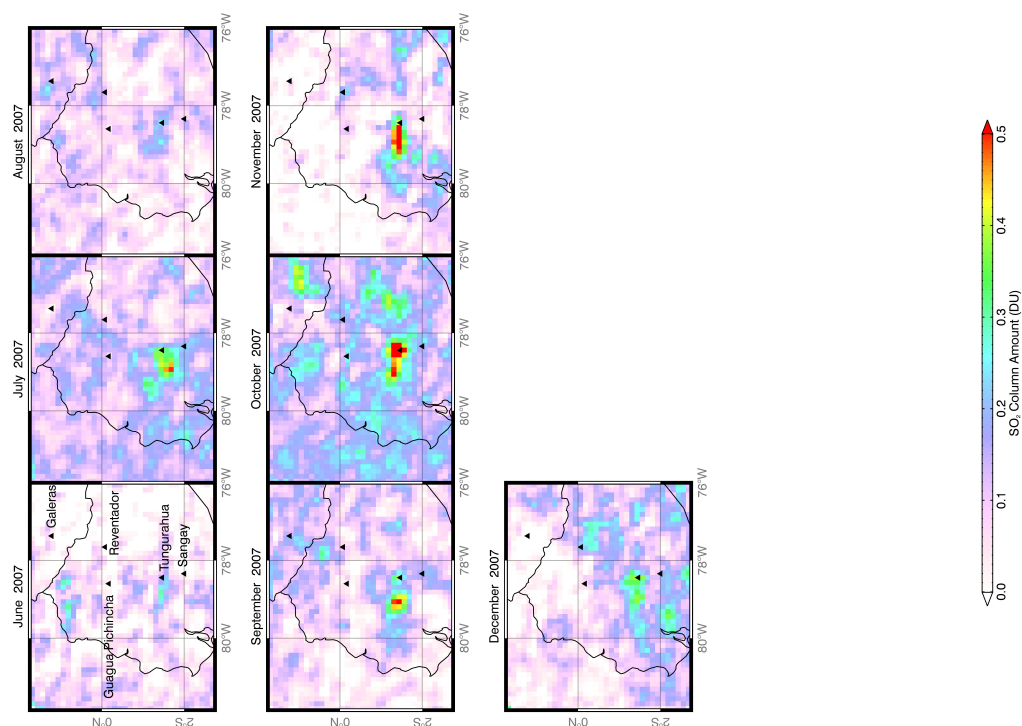


Figure B.1: Monthly average of the iterative retrieval output over Ecuador (2007)

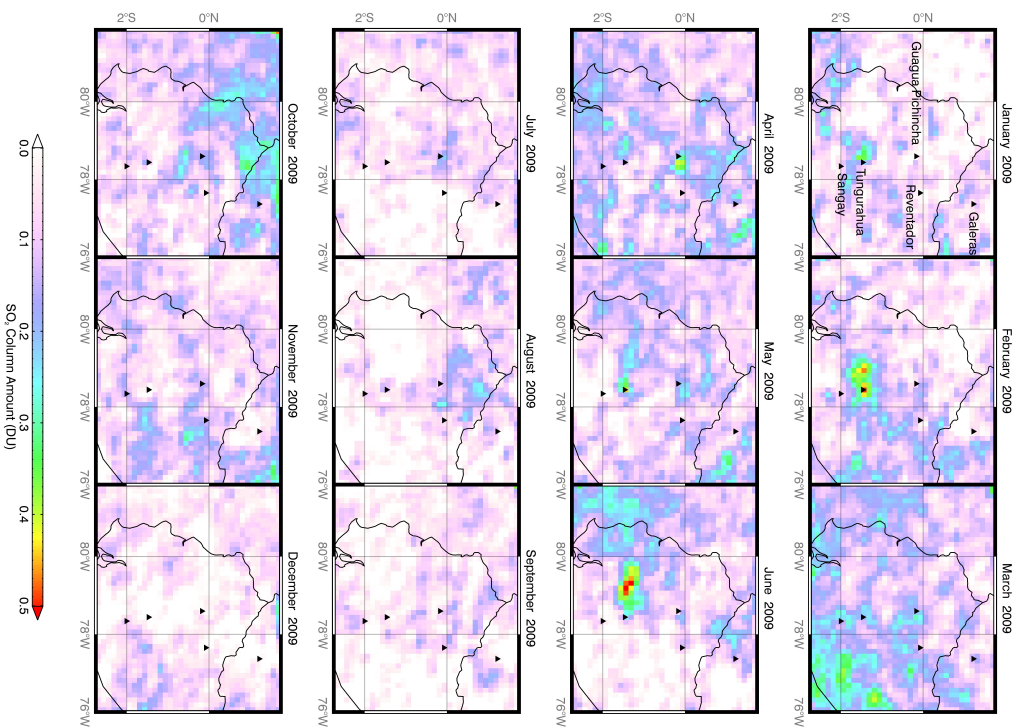


Figure B.3: Monthly average of the iterative retrieval output over Ecuador (2009)

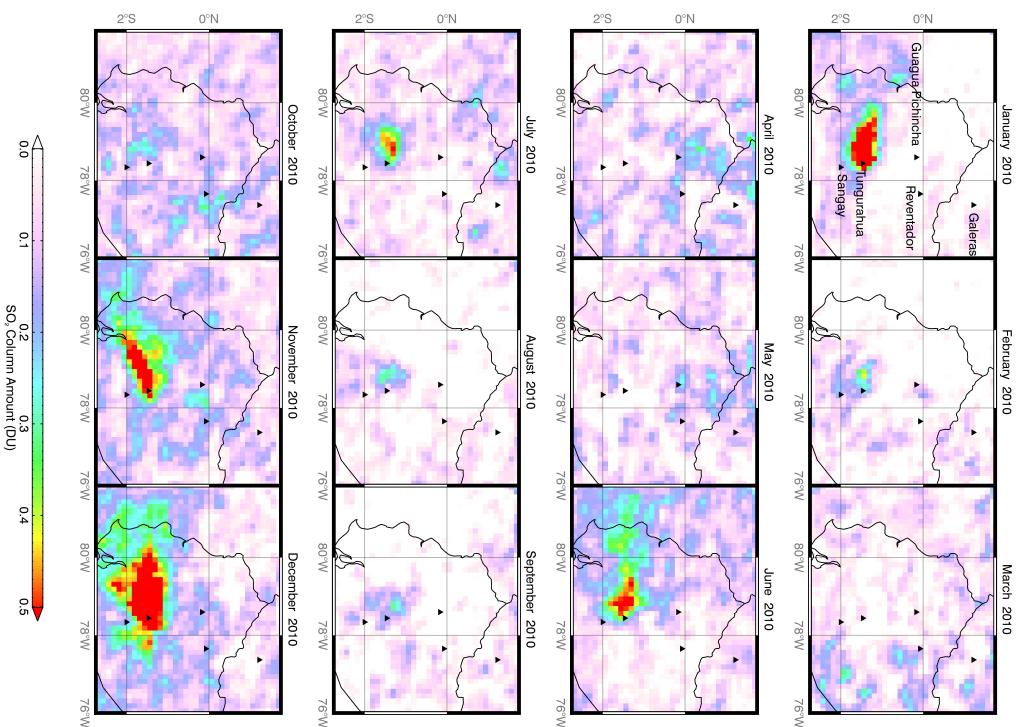


Figure B.4: Monthly average of the iterative retrieval output over Ecuador (2010)

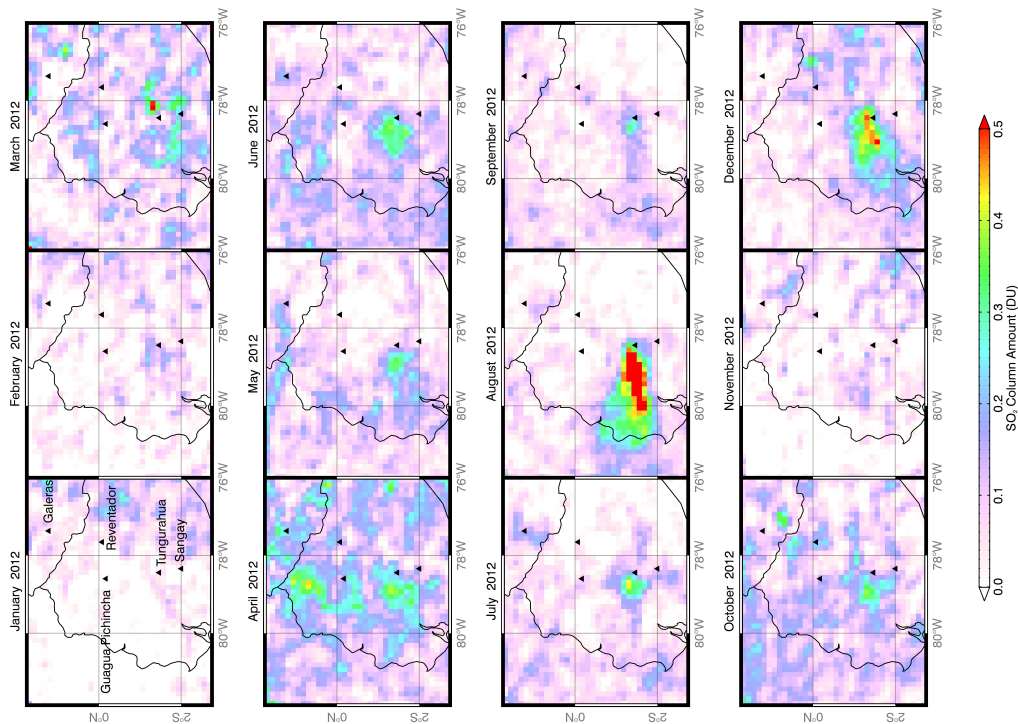


Figure B.6: Monthly average of the iterative retrieval output over Ecuador (2012)

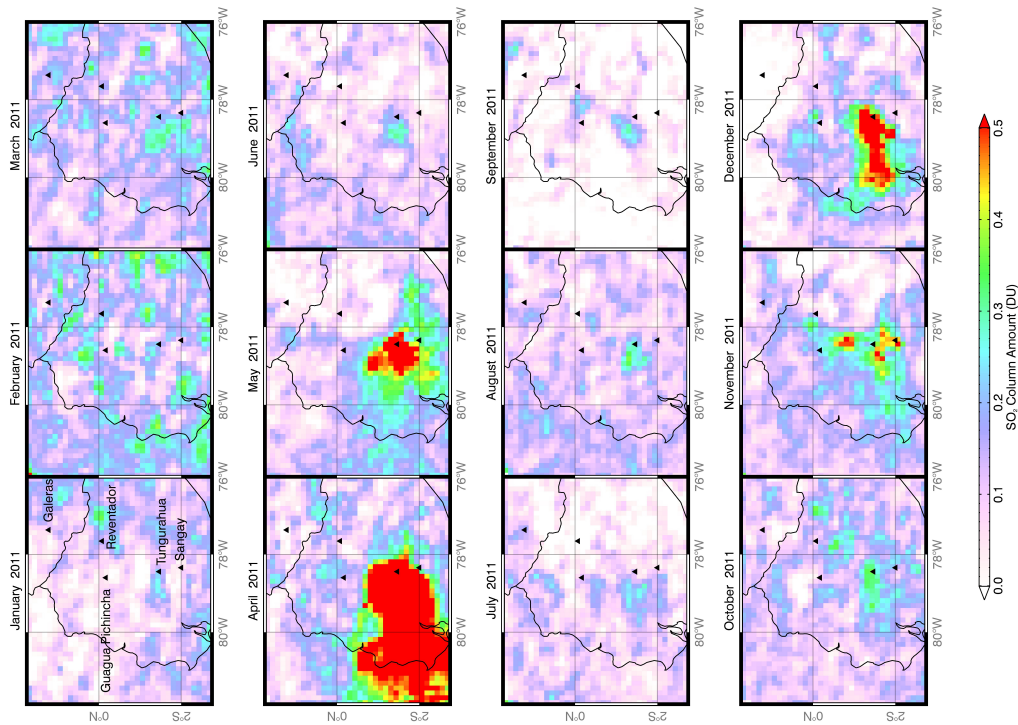


Figure B.5: Monthly average of the iterative retrieval output over Ecuador (2011)

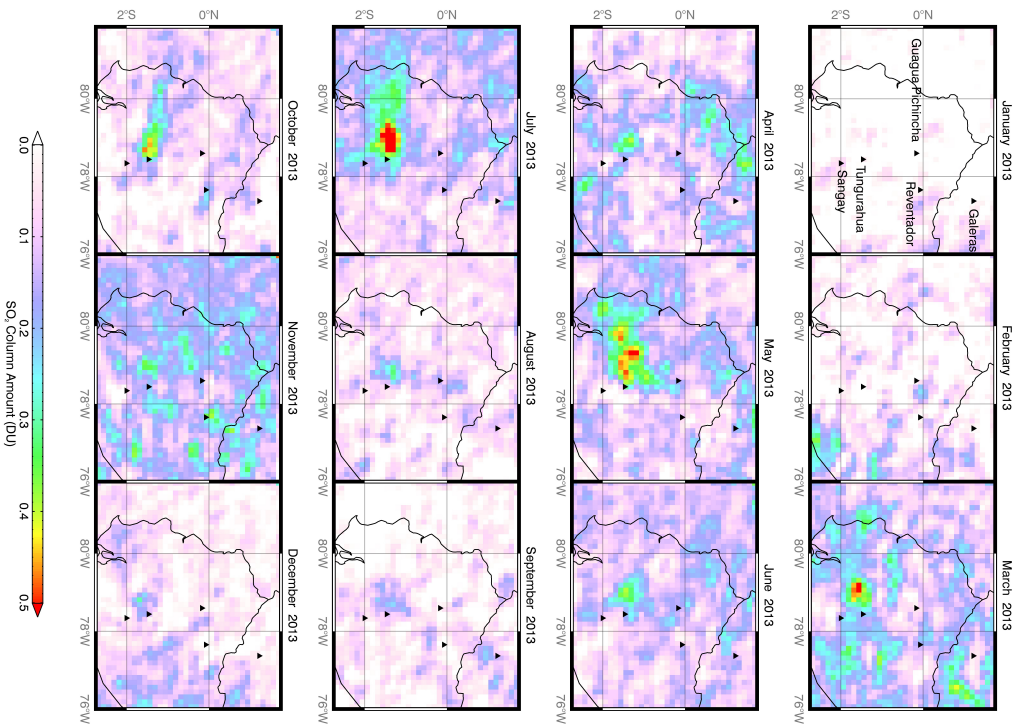


Figure B.7: Monthly average of the iterative retrieval output over Ecuador (2013)

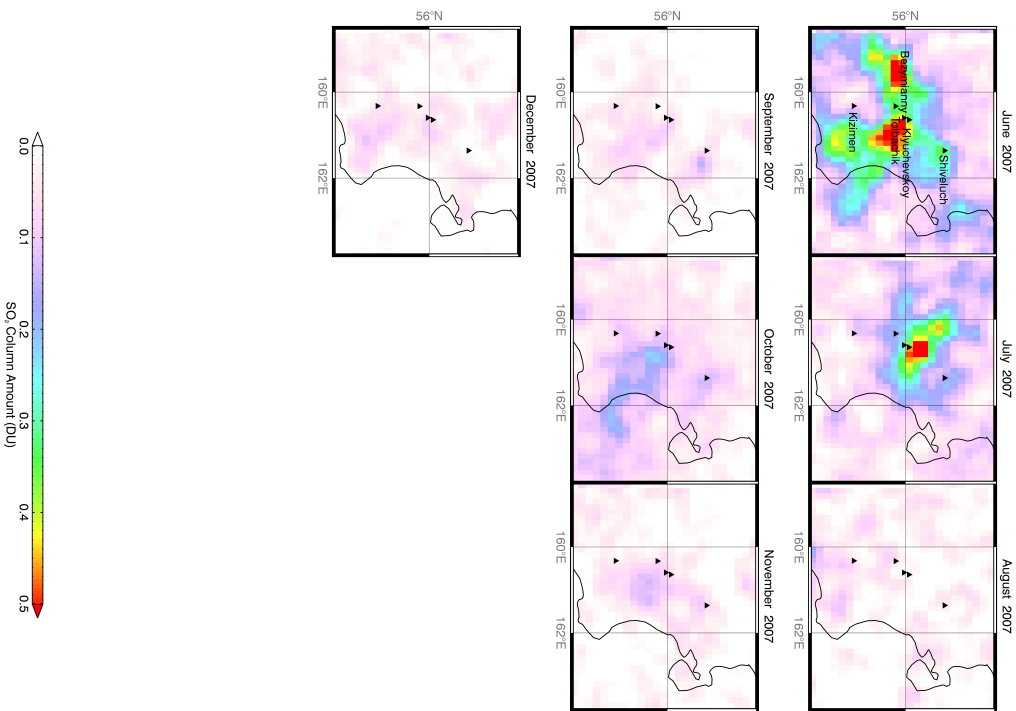


Figure B.8: Monthly average of the iterative retrieval output over Kamchatka (2007)

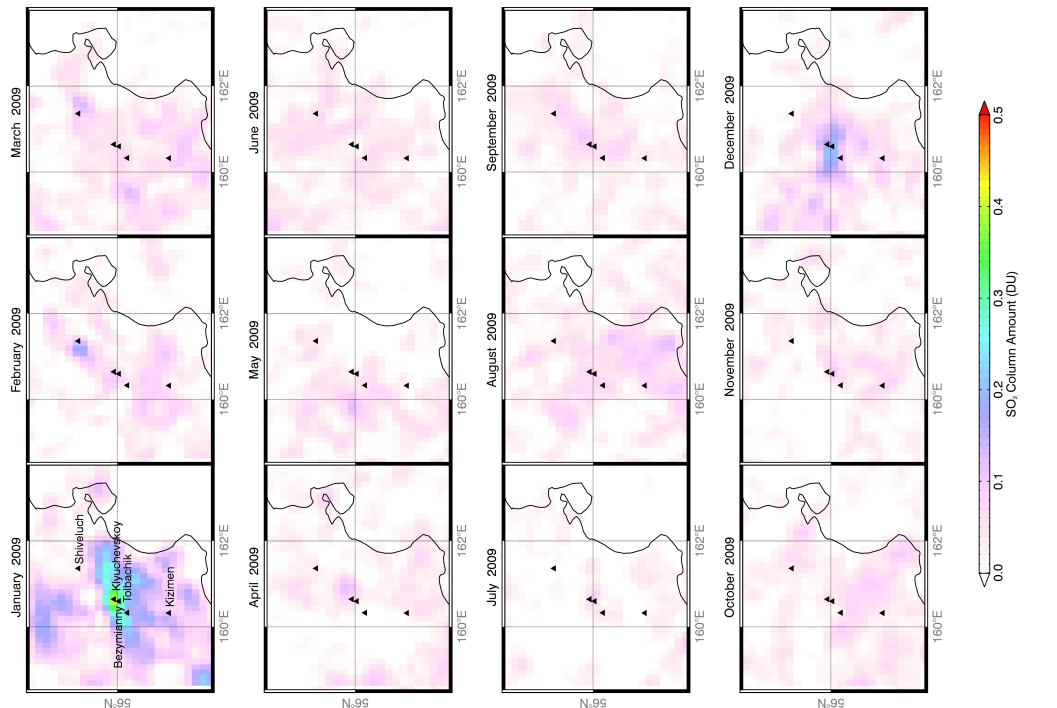


Figure B.10: Monthly average of the iterative retrieval output over Kamchatka (2009)

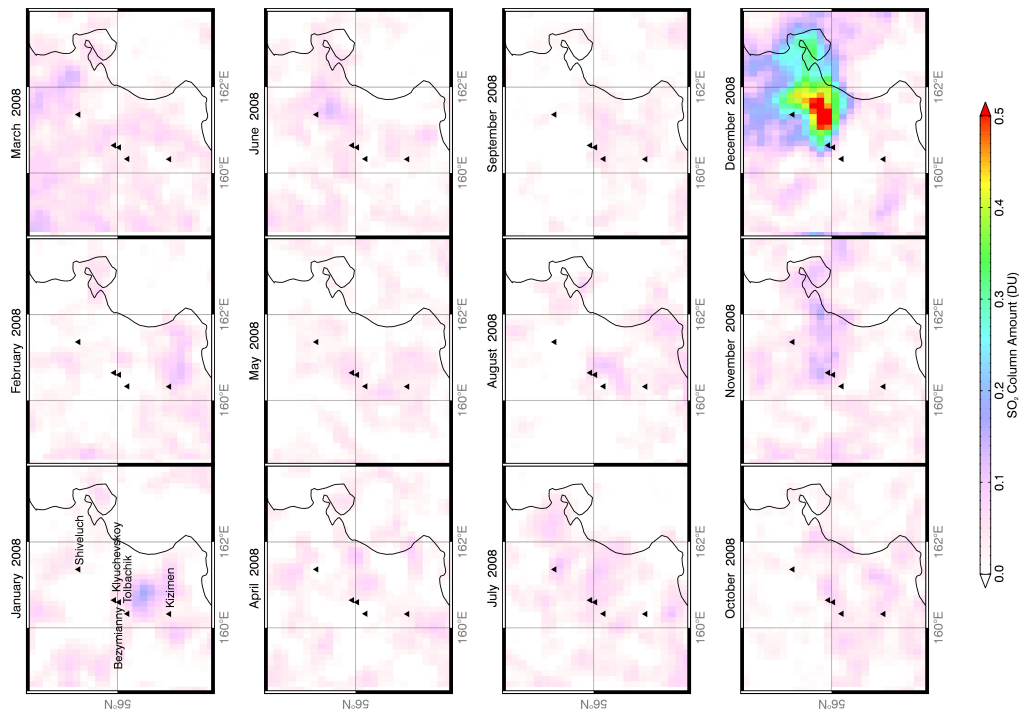


Figure B.9: Monthly average of the iterative retrieval output over Kamchatka (2008)

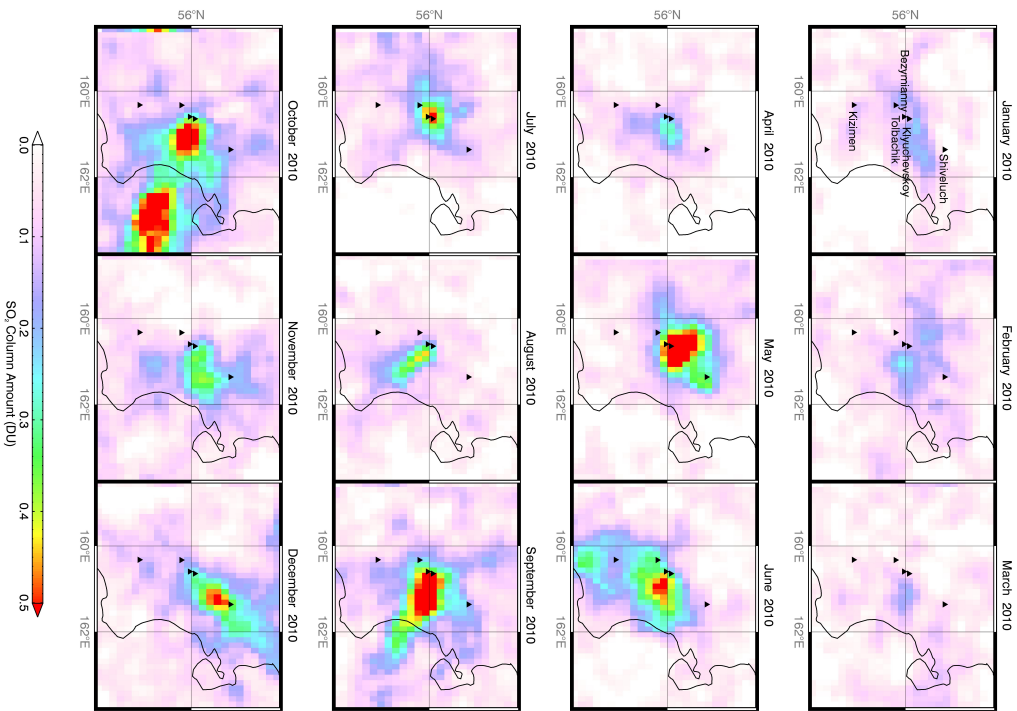


Figure B.11: Monthly average of the iterative retrieval output over Kamchatka (2010)

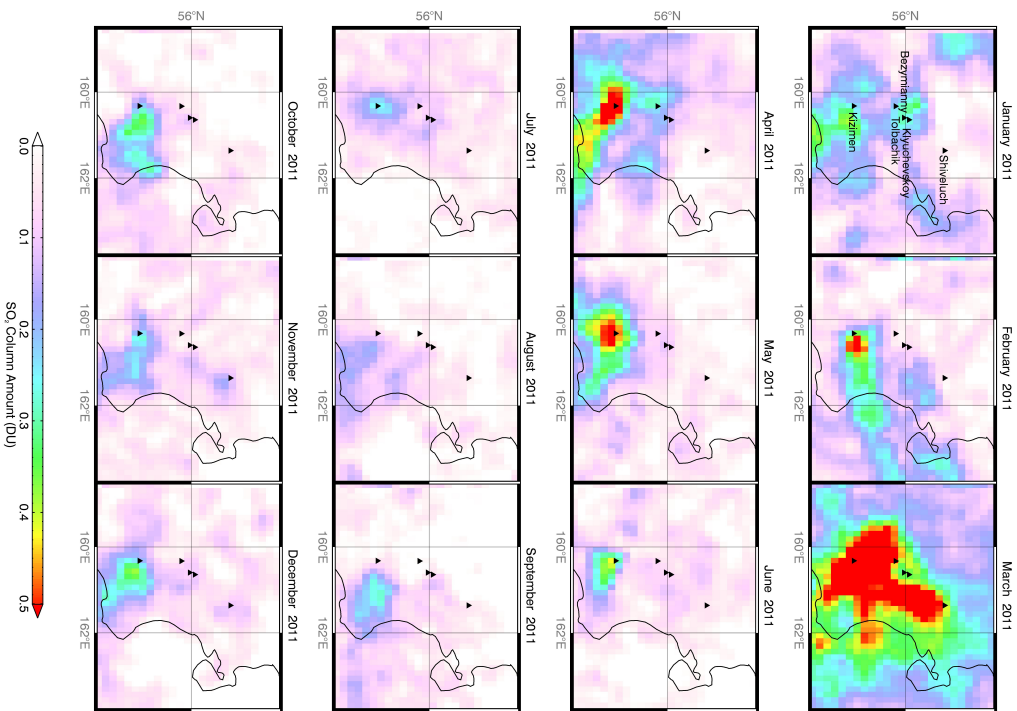


Figure B.12: Monthly average of the iterative retrieval output over Kamchatka (2011)

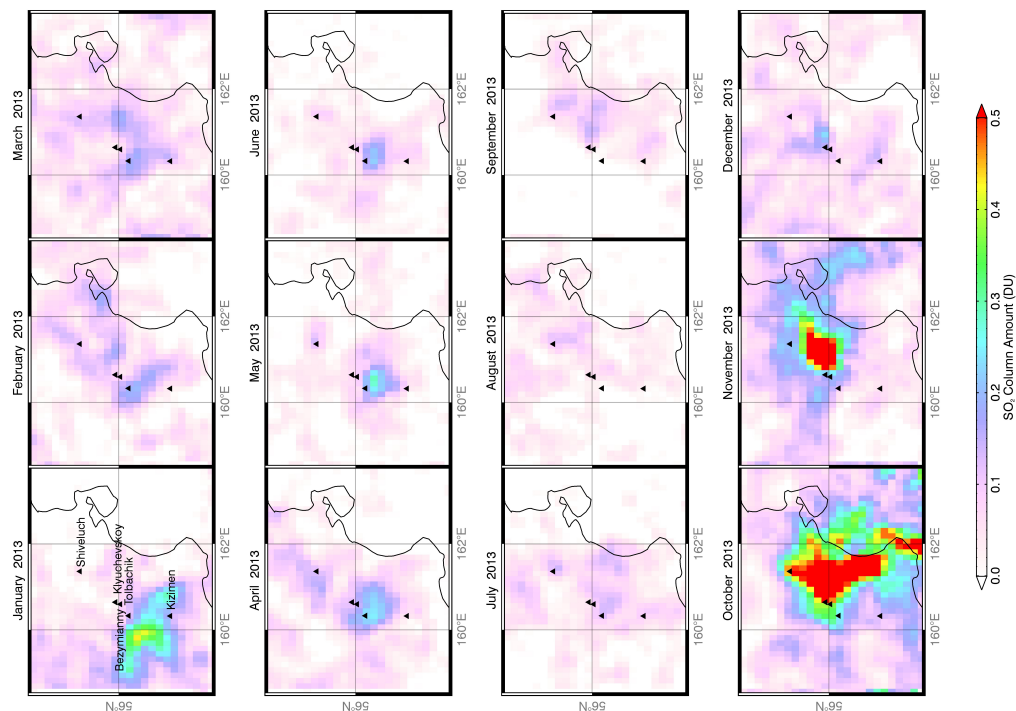


Figure B.14: Monthly average of the iterative retrieval output over Kamchatka (2013)

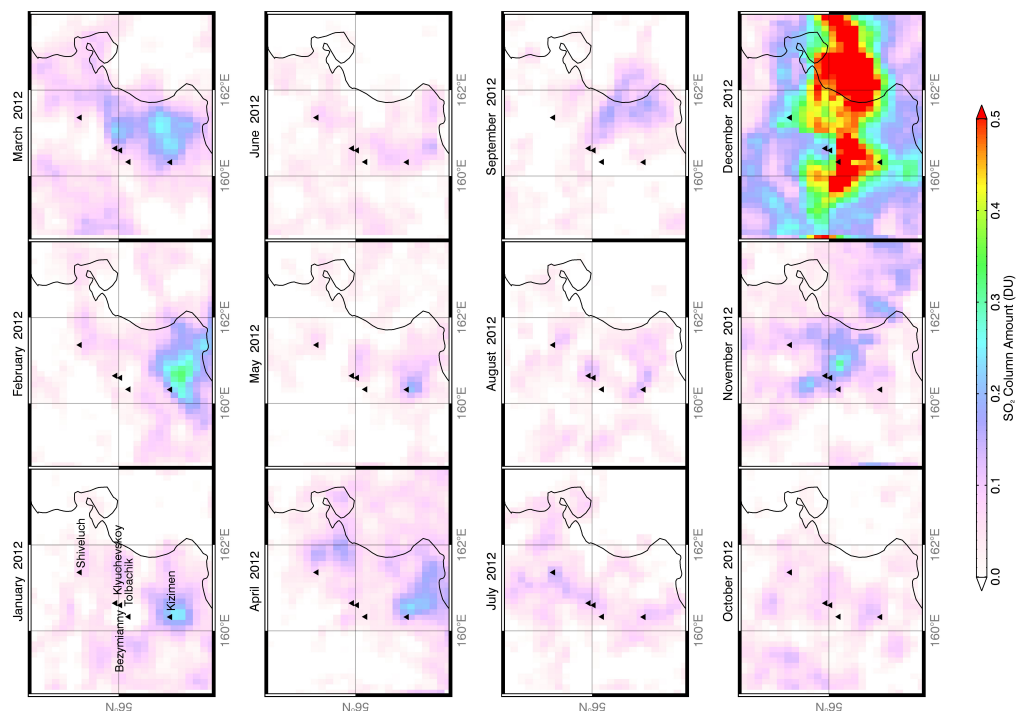


Figure B.13: Monthly average of the iterative retrieval output over Kamchatka (2012)

C

SO₂ rotation study - additional information

This appendix contains some further information related to the study of volcanic SO₂ emissions using the rotation scheme outlined in chapter 4, applied to the IASI SO₂ linear retrieval developed by Walker et al. (2011, 2012). Section C.1 discusses how the area used to compute the emission index was selected. Section C.2 contains tables showing the rankings of volcanoes based on the number of detections using the three rotation approaches applied in this study. Finally, section C.3 contains annual summery plots for 36 of the studied volcanoes.

C.1 Computing the emission index

An elevated emission at a volcano was defined by equation 4.1 and the emission index which shows the changing magnitudes of emissions at volcanoes was defined by equation 4.2. These require the mean and standard deviation of column amounts in the upwind and downwind of the volcano. These regions had to be defined and so a couple of tests were done at a few volcanoes to find the most appropriate

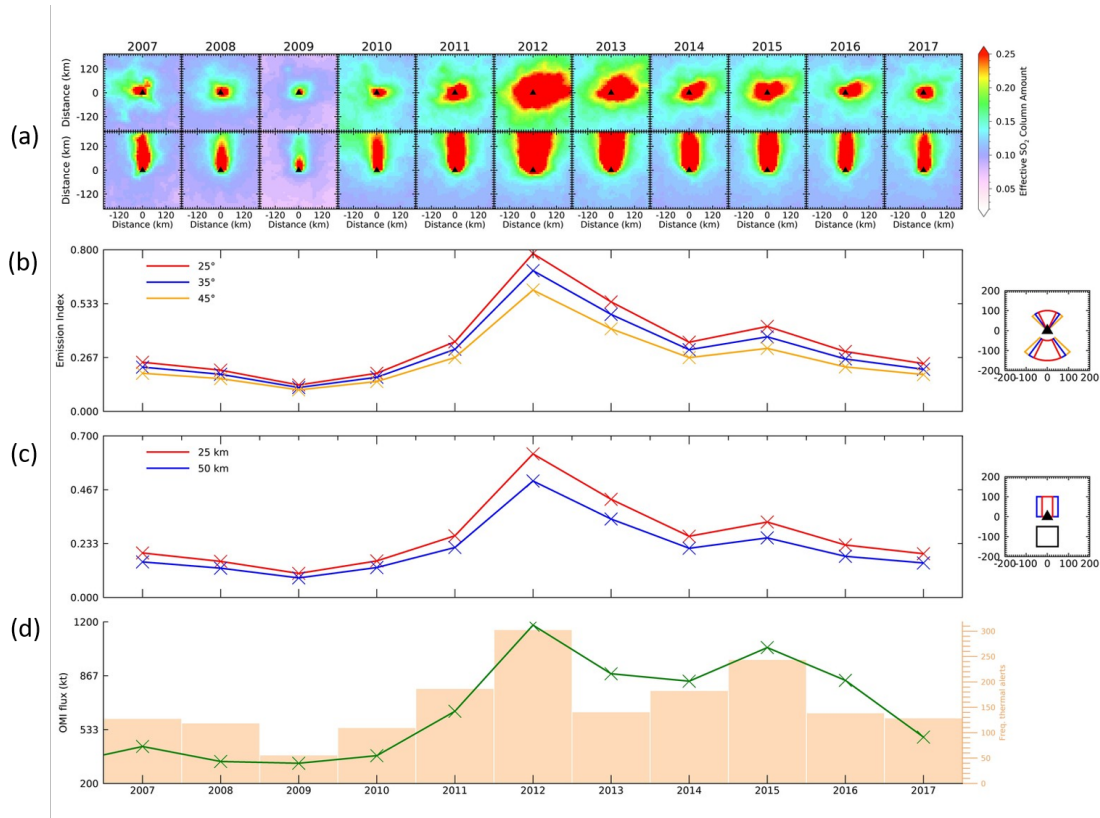


Figure C.1: Experiments with the regions used to calculate the upwind and downwind signal. (a) The unrotated and rotated annual averages for Popocatepetl. (b) the emission index ($\bar{x}_d - \bar{x}_u$) computed for sectors with angles 25, 35 and 45° from north. This has a set distance from the source of 100 km. (c) The emission index computed for each month for boxes with widths of 100 and 200 km. (d) the number of thermal anomalies detected with MODVOLC in each year and the OMI flux.

areas to use. A variety of distances from the volcano in the upwind and downwind were explored. In addition to this, the use of a box or a sector to compute the emission index was also investigated.

An example is shown in figure C.1. In this it is possible to see the unrotated and plume rotated annual averages at Popocatepetl and the emission index computed using different areas: (b) using sectors with different angles and (c) using different box sizes. Little difference in the computed trends can be seen. Based on the plume rotated annual averages seen in figure C.1a, it was decided it was more appropriate

to use a box instead of a segment as the plumes are fairly elongated.

A downwind box length of 100 km was selected. This is fairly small compared to the length of the plumes seen in figure C.1a. This is so that a smaller plume would still affect the computed emission index: the mean in the downwind might be diluted by calculating this over a larger area. The width of the box was also shown in figure C.1c to not significantly affect the trend observed. 100 km was selected partially based on the width of the plumes seen in C.1a and again taking into consideration the effect on the signal if a larger area was chosen.

An upwind box of the same size was chosen. However, it was offset by 50 km. This is to avoid any elevated SO₂ signal that might be seen just upwind of the volcano.

Future studies might want to consider a different approach. One possible alternative would be to calculate the total mass within the downwind box and varying the size of the downwind box based on the size of the plume.

C.2 Plume rotation rankings

Each volcano was ranked based on the number of detections for the three rotation methods described in table 4.1. These rankings are included in the tables below.

Table C.1: The tables on the next two pages show the ranking of each volcano based on the frequency with which a signal is detected. R1 = ranking based on plume rotation; R2 = ranking based on vent rotation; R3 = ranking based on passive emission rotation.

Volcano	Code	R1	R2	R3
Popocatepetl	Popo	1	1	1
Etna	Etn	2	2	2
Tolbachik	Tol	3	7	7
Klyuchevskoy	kly	4	4	4
Bezymianny	Bez	5	5	7
Sheveluch	She	6	11	9
Nyiragongo	Nyi	7	3	3
Zhupanovsky	Zh	8	12	12
Koryaksky	Kor	9	15	14
Nyamuragira	Nya	10	6	5
Kizimen	Kiz	11	25	28
Karymsky	Kary	12	20	20
Sabancaya	Sab	13	10	10
Nevado del Ruiz	NR	14	8	6
Ubinas	Ub	15	15	11
Lascar	Las	16	9	15
Gorely	Gor	17	26	18
Chikurachki	Chi	18	28	28
Ebeko	Eb	19	30	28
Tungurahua	Tun	20	13	13
Alaid	Ala	21	42	49
Etorofu-Yakeyama	EY	22	51	46
Kilauea	Kil	23	14	19
Chirinkotan	Ch	24	51	43
Akan	Aka	25	70	62
Asamayama	Asa	26	23	23
Sarychev Peak	SP	27	59	62
Kambalny	Kamb	28	54	62
Cotopaxi	Cot	29	21	21
Copahue	Cop	30	17	34
Shishaldin	Shi	31	23	24
Chirpoi	Chir	32	79	119
Ekarma	Ek	33	59	50
Turrialba	Tur	34	18	17
Sangay	San	35	21	21
Nevado del Huila	NH	36	18	16
Ambrym	Ambr	37	32	39
Lopevi	Lop	38	36	43
Semisopochnoi	Sem	39	54	50
Kusatsu-Shiranesan	KS	40	30	33
Aira	Ai	41	27	34
Semeru	Se	42	36	28
Hakoneyama	Ha	43	44	39
Bagana	Bag	44	39	32
Miyakejima	Mi	45	44	39
Asosan	Aso	46	53	43
Veniaminof	Ve	47	48	50
Tengger Caldera	TC	48	44	38
Poas	Poa	49	28	24

Volcano	Code	R1	R2	R3
Pavlof	Pav	50	48	54
Kirishimayama	Kir	51	39	54
Galeras	Gal	52	32	26
Villarrica	Vi	53	32	46
Stromboli	Str	54	79	86
Raung	Rau	55	32	34
Kikai	Kik	56	70	54
Fuego	Fue	57	42	73
Okmok	Ok	58	54	99
Cleveland	Cl	59	79	73
Ulawun	Ul	60	44	39
Reventador	Rev	61	39	34
Colima	Col	62	54	62
Bardarbunga	Bar	63	70	86
Korovin	Ko	64	79	119
Eyjaflajallajokull	Eyj	65	65	54
Ambae	Amba	66	70	62
Erebus	Ere	67	36	27
Redoubt	Red	68	59	73
Llaima	ll	69	48	54
Kasatochi	Kasa	70	103	119
Kanaga	Kana	71	103	99
Grimsvotn	Gri	72	65	99
Great Sitkin	GS	73	103	119
Bogoslof	Bog	74	103	119
Ontakesan	On	75	139	145
Pacaya	Pa	76	59	99
Yasur	Ya	77	90	73
Santa Maria	SMa	78	90	119
Soputan	So	79	70	73
Kelut	Kel	80	90	119
Gaua	Gau	81	103	73
Rinjani	Ri	82	70	62
Rabaul	Rab	83	54	46
Kuchinoerabujima	Kuc	84	103	86
Arenal	Are	85	65	50
Witori	Wi	86	59	54
Sinabung	Sin	87	65	62
Lokon-Empung	LE	88	70	62
Agung	Agu	89	119	99
Puyehue-Cordon Caulle	PCC	90	59	62
Dieng Volcanic Complex	DVC	91	90	73
Zubair Group	Zu	92	90	86
Jebel at Tair	JT	93	119	119
Suwanosejima	Su	94	119	99
St. Helens	MSH	95	103	99
Merapi	Me	96	119	99
Krakatau	Kra	97	90	73
Kadovar	Kad	98	79	86

Volcano	Code	R1	R2	R3
Calbuco	Cal	99	79	73
Batu Tara	BT	100	79	119
Sangeang Api	SA	101	139	119
Nishinoshima	Ni	102	103	86
Manam	Man	103	90	86
Heard	He	104	70	54
Piton de la Fournaise	PF	105	90	73
Erta Ale	EA	106	79	119
Egon	Eg	107	119	119
Bristol Island	BrI	108	65	62
Saunders	Sa	109	90	73
Ritter Island	RI	110	79	62
Paluweh	Pal	111	119	145
Montagu Island	MI	112	90	73
Manda Hararo	MH	113	90	99
Karangetang	Kar	114	70	54
Iliwerung	Ili	115	119	145
Hierro	Hi	116	139	119
Fogo	Fo	117	90	73
Dukono	Duk	118	90	86
Wolf	Wo	119	119	99
Slamet	Sl	120	103	99
Sirung	Sir	121	139	145
Planchon-Peteroa	PP	122	79	86
Lewotolo	Le	123	119	145
Krummel-Garbuna-Welcker	KGW	124	119	99
Hunga Tonga-Hunga Haapai	HTHH	125	119	99
Nevados de Chillan	NC	126	119	99
Chaiten	Cha	127	119	99
Anatahan	Ana	128	103	99
Alu-Dalafilla	AD	129	79	145
Zavodovski	Za	130	103	86
White Island	WI	131	119	99
Tofua	Tof	132	103	86
Tangkubanparahu	Tan	133	157	145
Soufriere Hills	SH	134	119	119
Ruapehu	Ru	135	103	99
Nabro	Nab	136	103	119
Mayon	May	137	103	86
Ol Doinyo Lengai	ODL	138	139	119

Volcano	Code	R1	R2	R3
Ioto	Ioto	139	139	119
Dempo	Dem	140	139	119
Concepcion	Con	141	119	86
Tongariro	Ton	142	119	119
Rincon de la Vieja	RV	143	157	145
Momotombo	Mo	144	119	119
Marapi	Mar	145	119	99
Kerinci	Ker	146	139	119
Karthala	Kart	147	139	119
Ibu	Ibu	148	139	145
Hudson Cerro	CH	149	103	145
Gamalama	Ga	150	139	119
Fernandina	Fer	151	139	119
Tinakula	Tin	152	157	145
Talang	Tal	153	119	99
San Miguel	SMi	154	139	145
Pagan	Pag	155	157	145
Negra Sierra	SN	156	157	145
Masaya	Mas	157	139	119
Langila	Lan	158	157	145
Gamkonora	Gam	159	139	145
Barren Island	BaI	160	157	119
Cerro Azul	CA	161	157	145
Telica	Tel	162	157	145
San Cristobal	SC	163	139	145
Karkar	Kar	164	139	145
Bulusan	Bul	165	139	145
Kanlaon	Kanl	166	157	145

C.3 Volcano Annual Summaries

The rotation algorithm, outline in section 4.2.3, was applied to 166 volcanoes worldwide. Summary plots for 36 of these volcanoes are included here. These were selected either because they are discussed in the main text or because they fall within the top 20 volcanoes as ranked with the plume rotation technique. These plots for any of the other volcanoes can be made available on request.

Figure C.2: Annual summary plot for Aira, Japan. The first row shows a map of the region used for the initial processing (a 12° box around the volcano). The number of volcanoes, which have been active since 2007, within specified distances are listed to the right of the map (these are also plotted on the map in the corresponding colours). To the right of this are plots showing the multi-annual average (2007-2017) for the unrotated (UR; included as these help identify other SO_2 sources in the region), unrotated without SO_2 flagged pixels (UR - PE), passive emission rotation (PER), vent rotated (VR) and plume rotated grids (PR). Note that these have been reduced to 200 km from the volcano to better show the plumes. Beneath this are the equivalent plots for each year (years going across, and the different grids going down). The third plot shows the vent (blue) and plume (red) rotated emission index (equation 4.2) for each year along with the flux obtained with OMI (right axis) and the number of thermal anomalies identified by MODVOLC in each year (2nd axis on the right). The chart beneath this shows the emission index computed using passive emission, vent and plume rotated methods respectively. An increase in colour intensity implies an increase in SO_2 emission. The final line shows the number of MODVOLC thermal anomalies for each month studied.

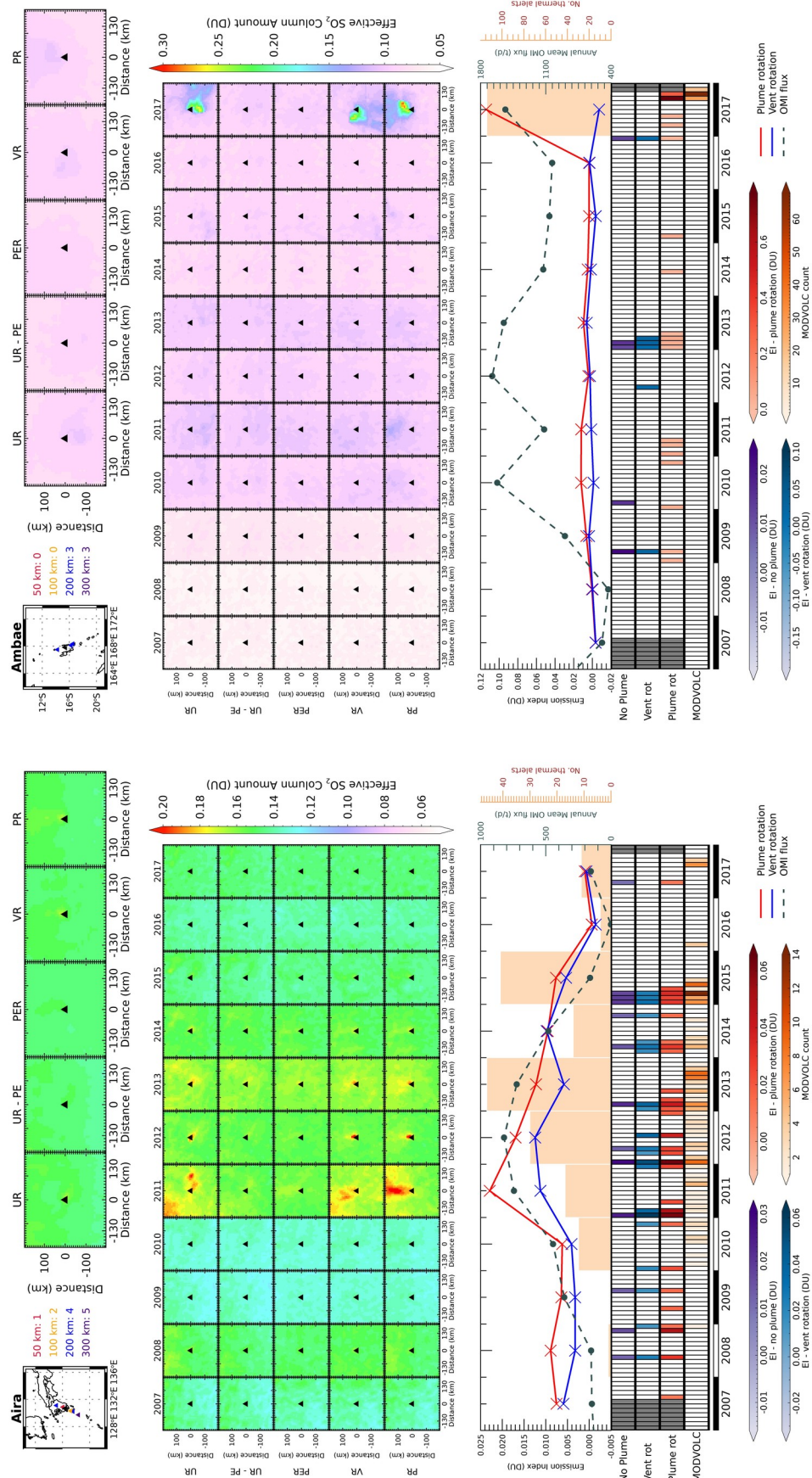


Figure C.3: As for figure C.2 for Ambae, Vanuatu

Figure C.2: Caption on previous page

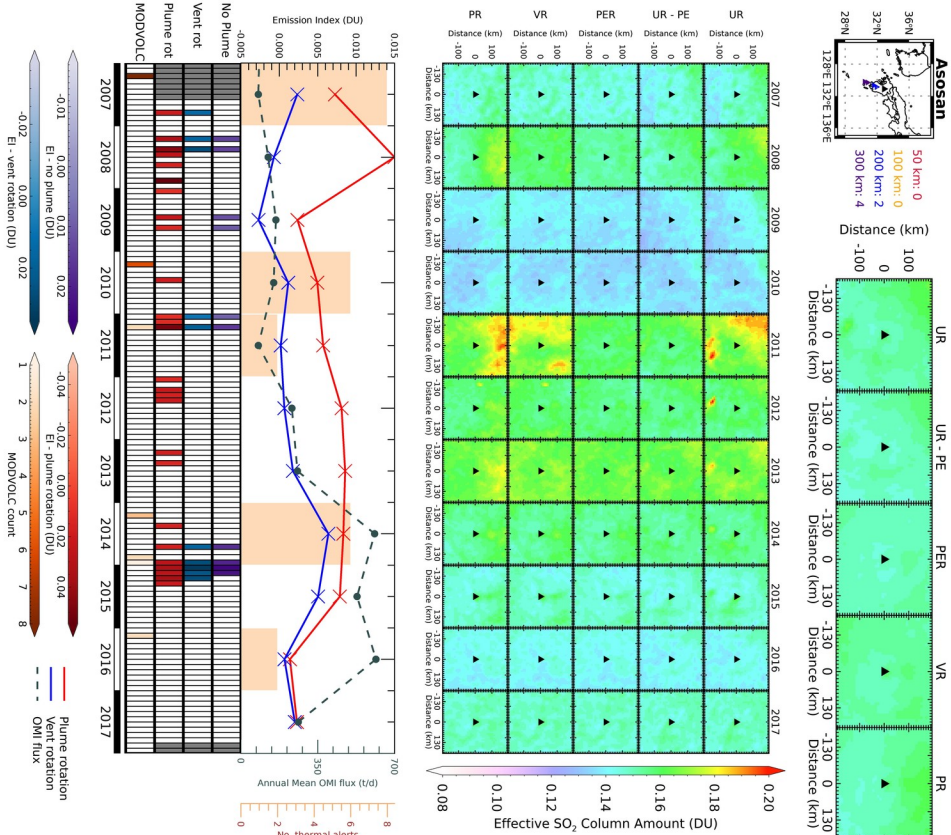


Figure C.4: As for figure C.2 for Asosan, Japan.

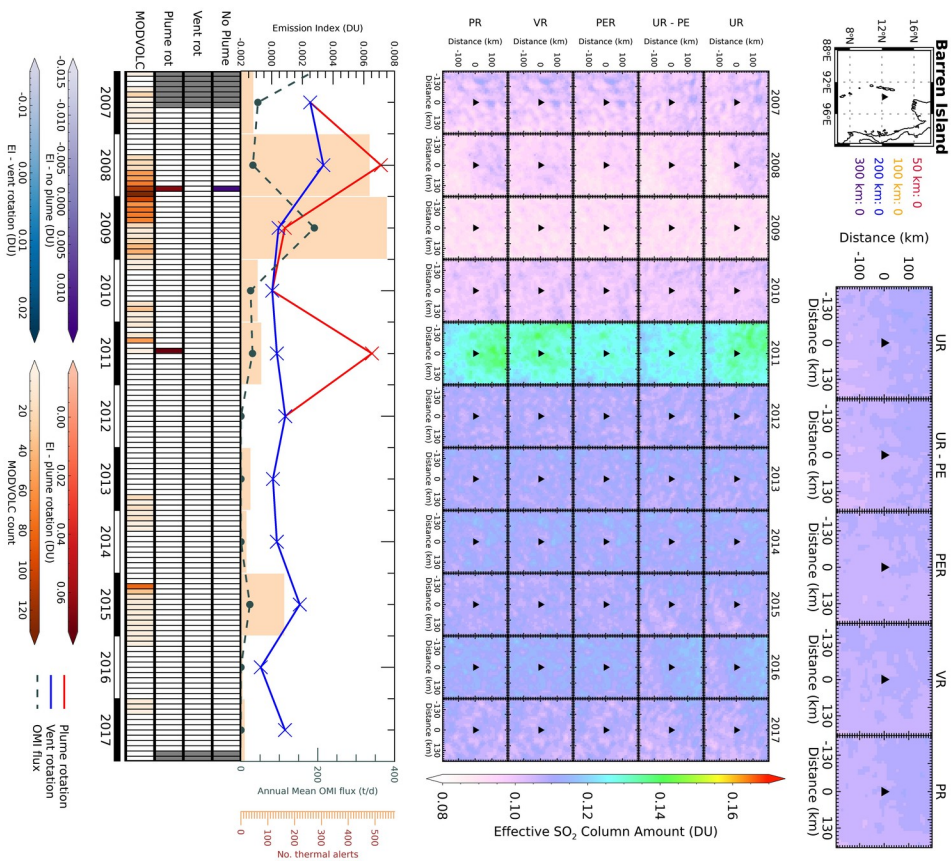


Figure C.5: As for figure C.2 for Barren Island, Indian Ocean.

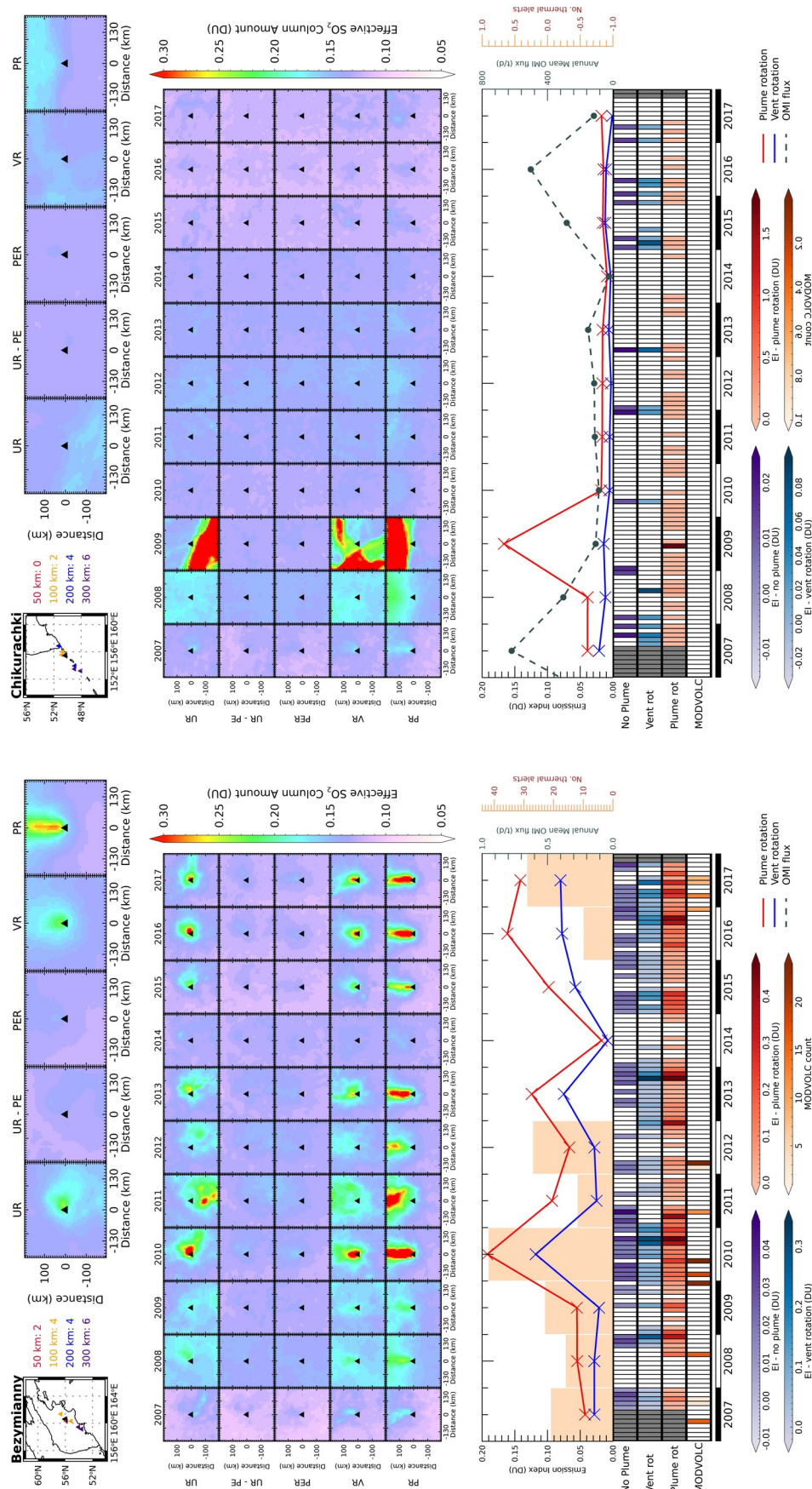


Figure C.6: As for figure C.2 for Bezymianny, Kamchatka.

Figure C.7: As for figure C.2 for Chikurachki, Kuril Islands.

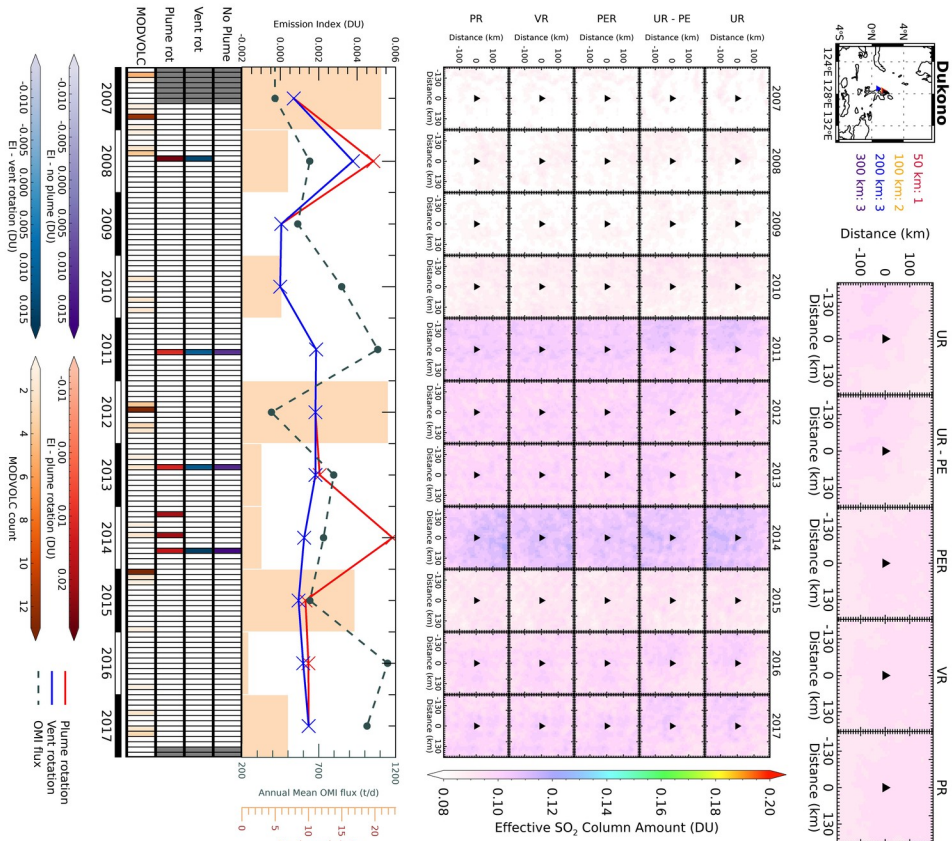


Figure C.8: As for figure C.2 for Dukono, Indonesia.

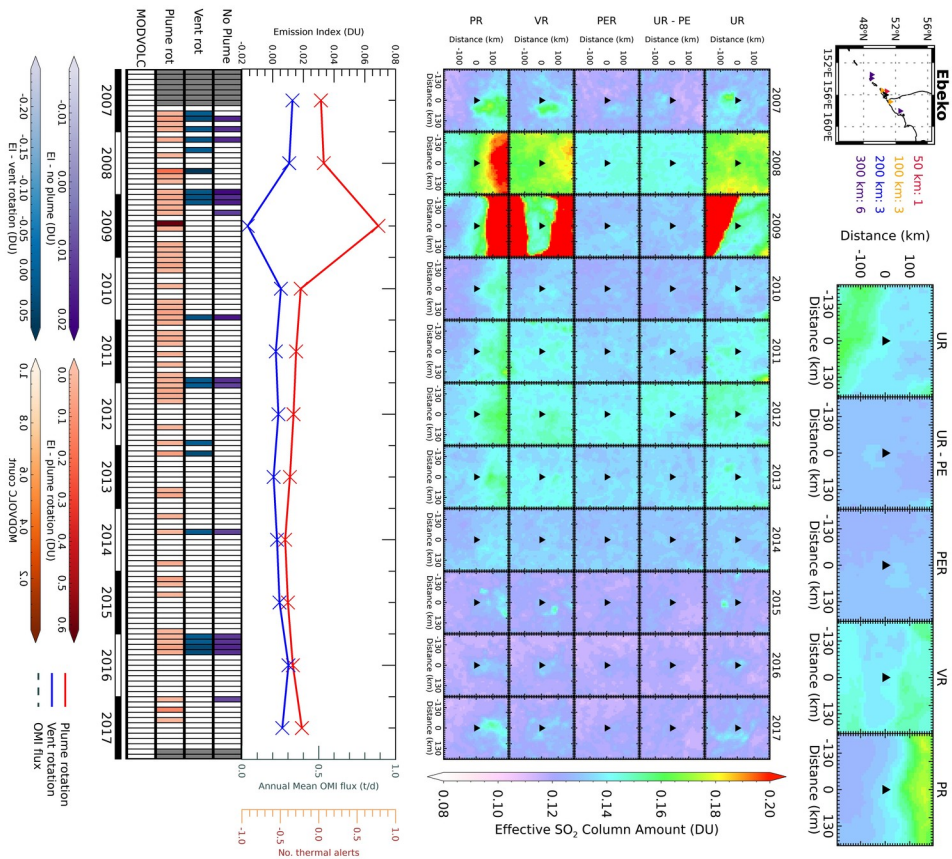


Figure C.9: As for figure C.2 for Ebeko, Kuril Islands.

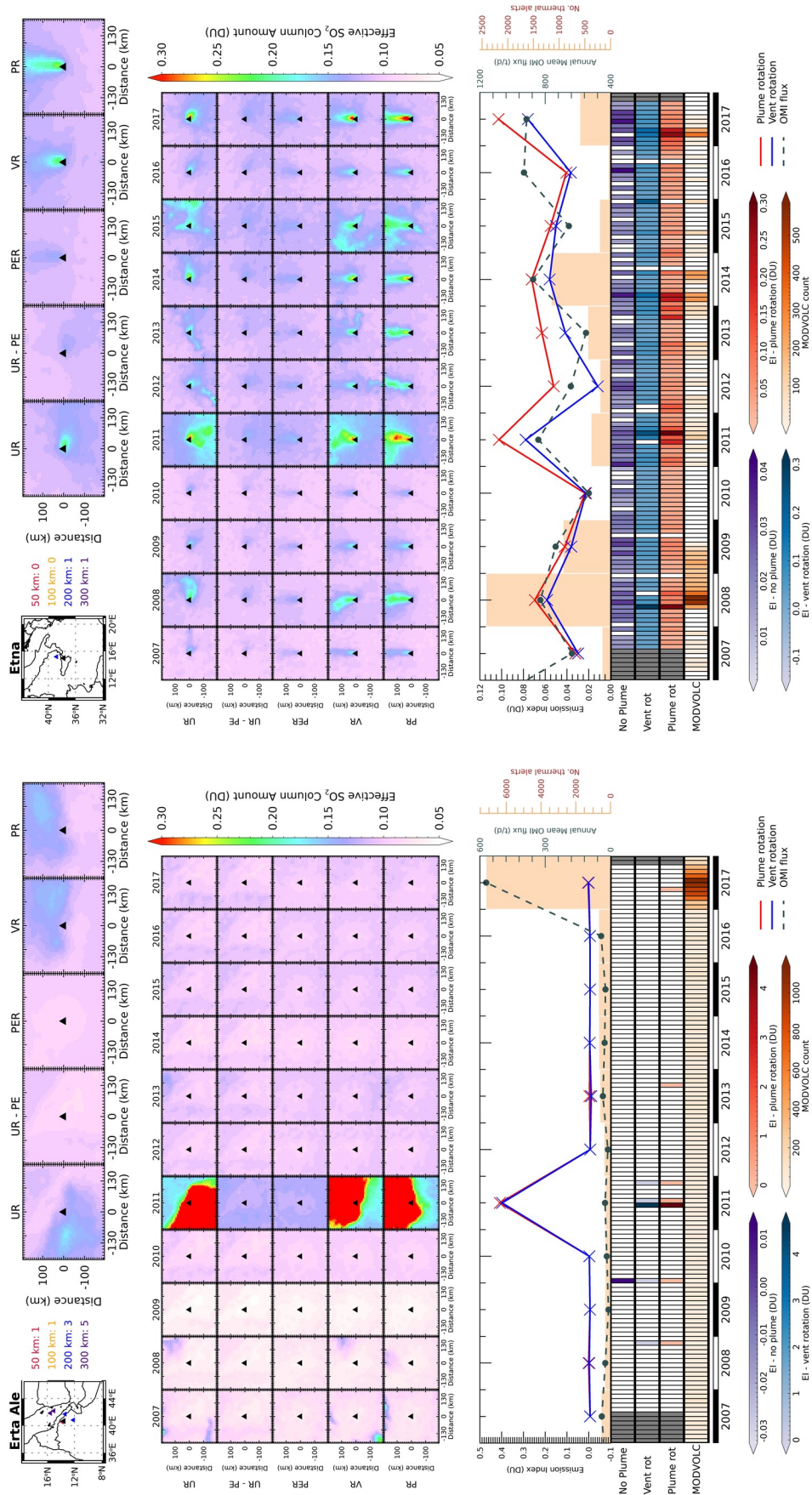


Figure C.10: As for figure C.2 for Erta Ale, Ethiopia.

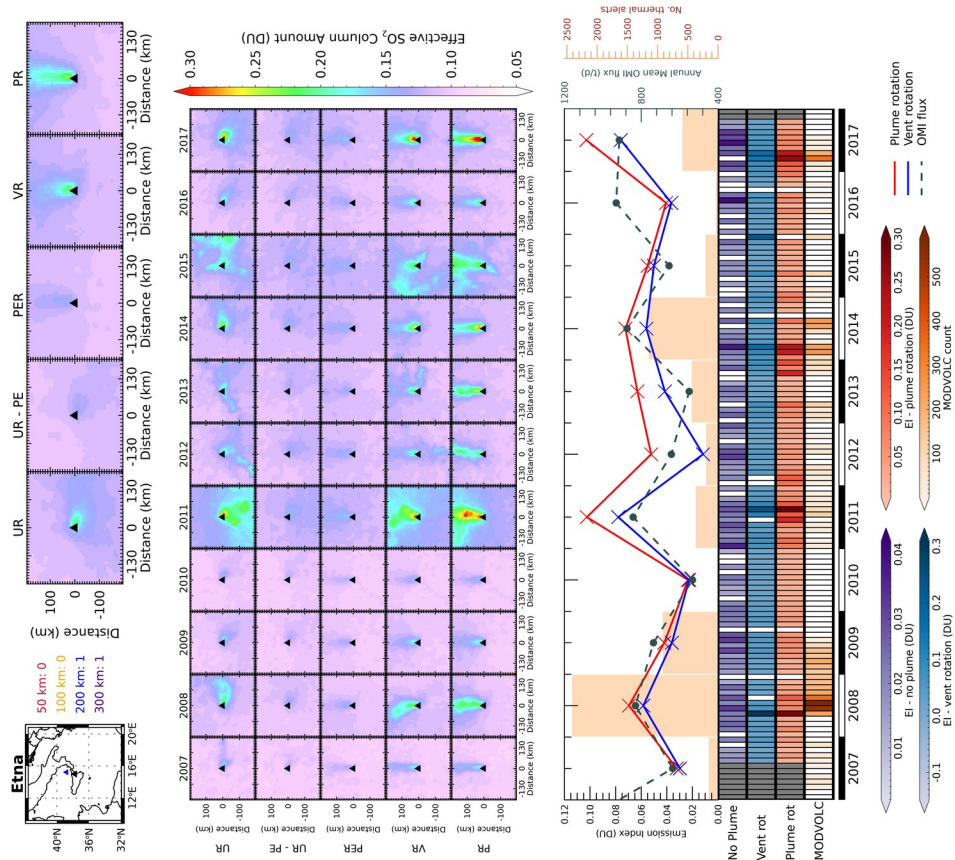


Figure C.11: As for figure C.2 for Etna, Italy.

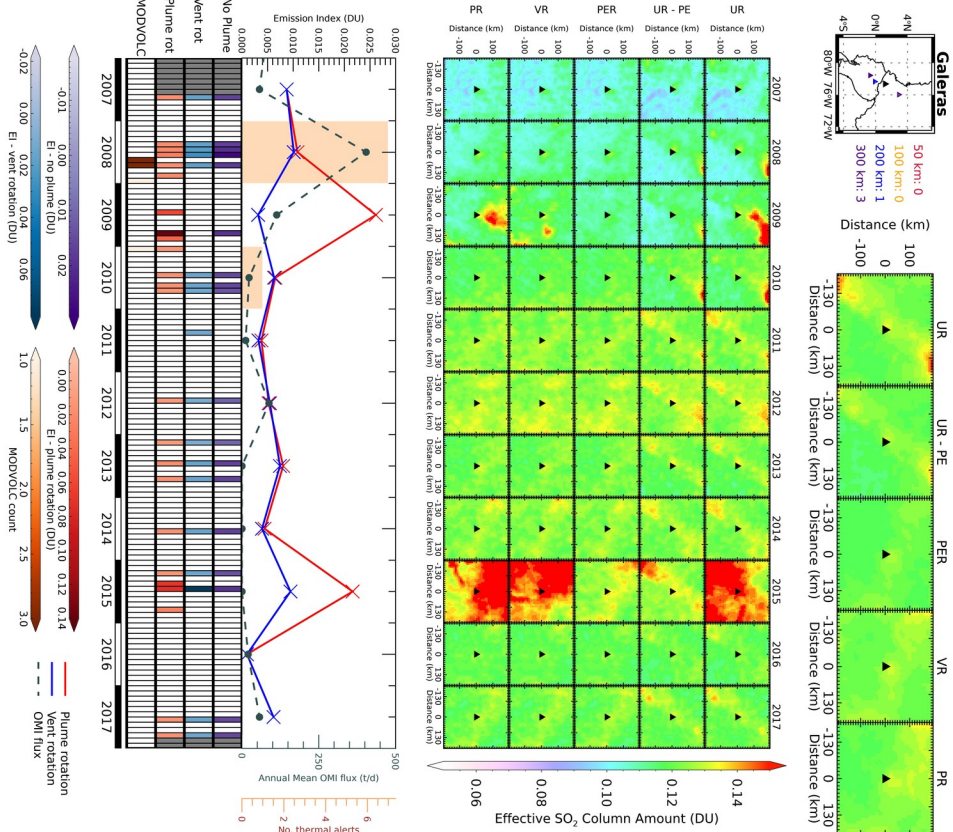


Figure C.12: As for figure C.2 for Galeras, Colombia.

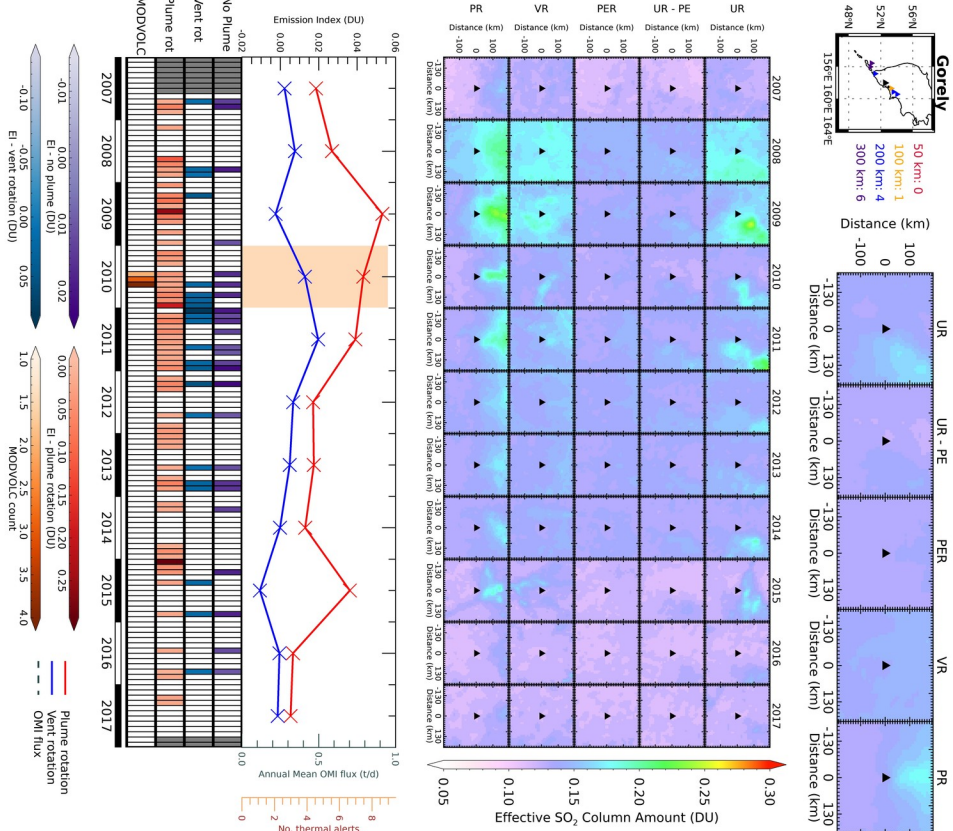


Figure C.13: As for figure C.2 for Gorely, Kamchatka.

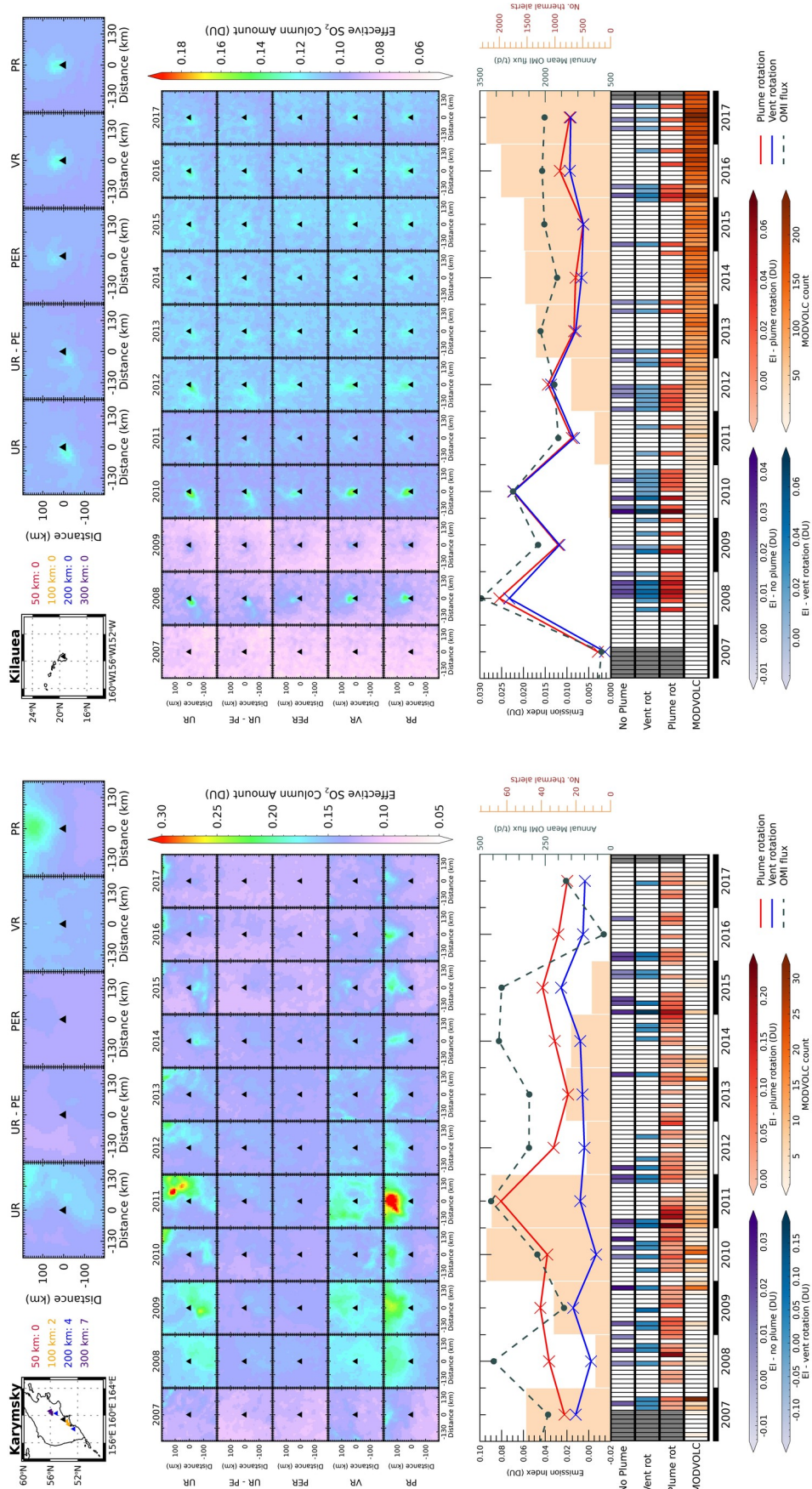


Figure C.14: As for figure C.2 for Karynsky, Kamchatka.

Figure C.15: As for figure C.2 for Kilauea, Hawaii.

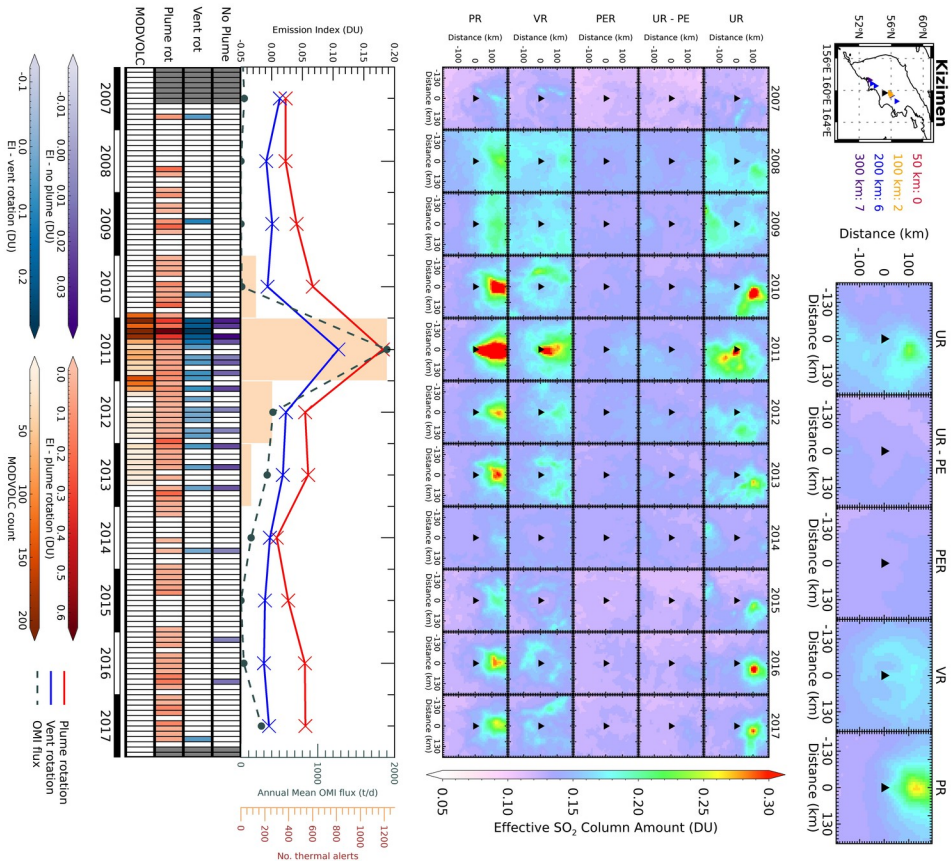


Figure C.16: As for figure C.2 for Kizimen, Kamchatka.

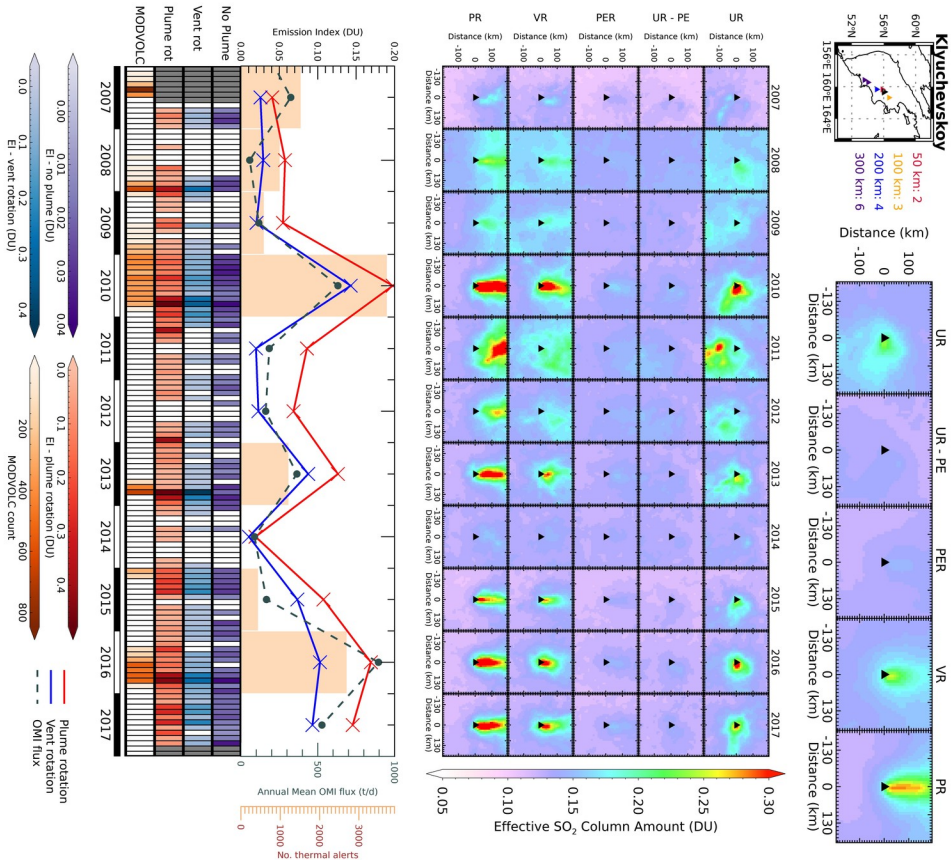


Figure C.17: As for figure C.2 for Klyuchevskoy, Kamchatka.

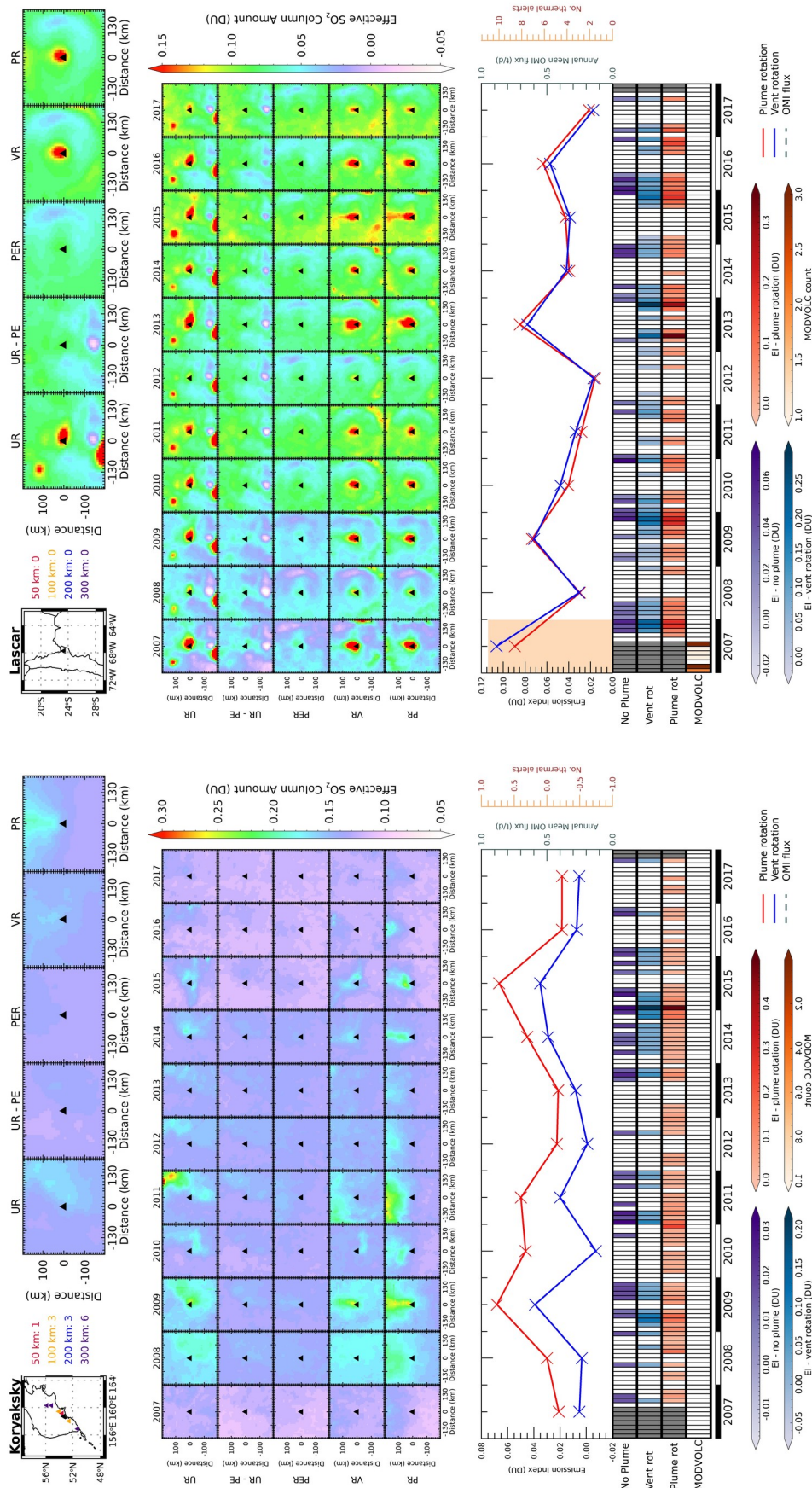


Figure C.18: As for figure C.2 for Koryaksky, Kamchatka.

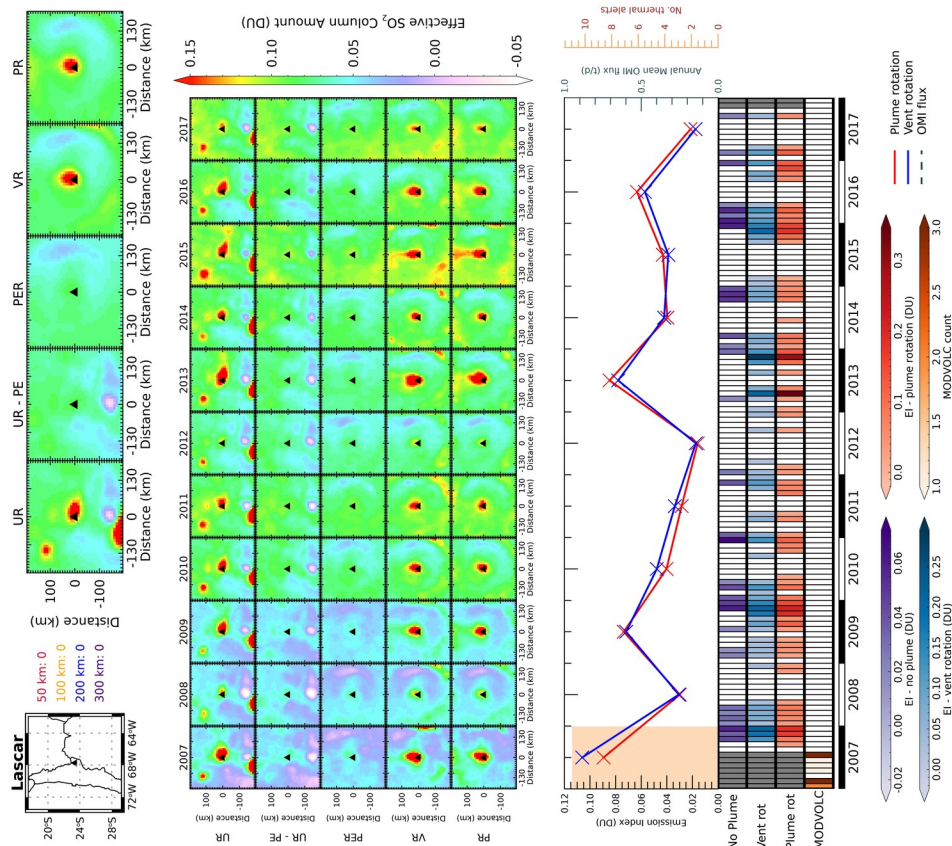


Figure C.19: As for figure C.2 for Lascar, Chile.

Figure C.20: As for figure C.2 for Lokor-Empung, Indonesia.

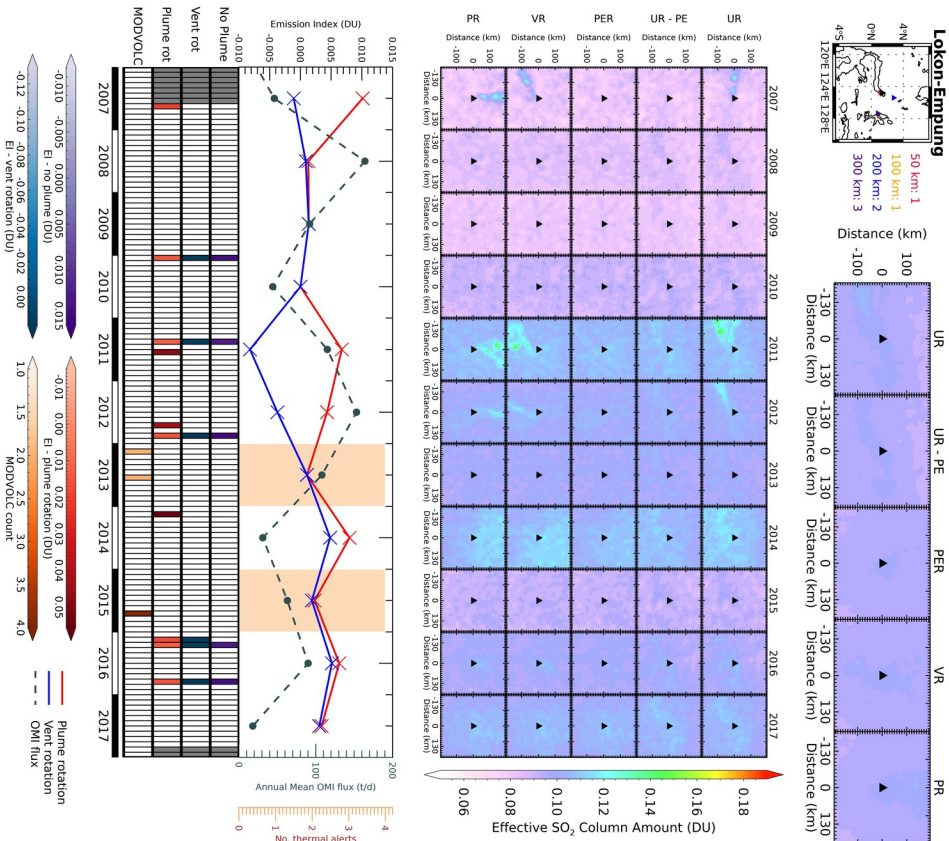
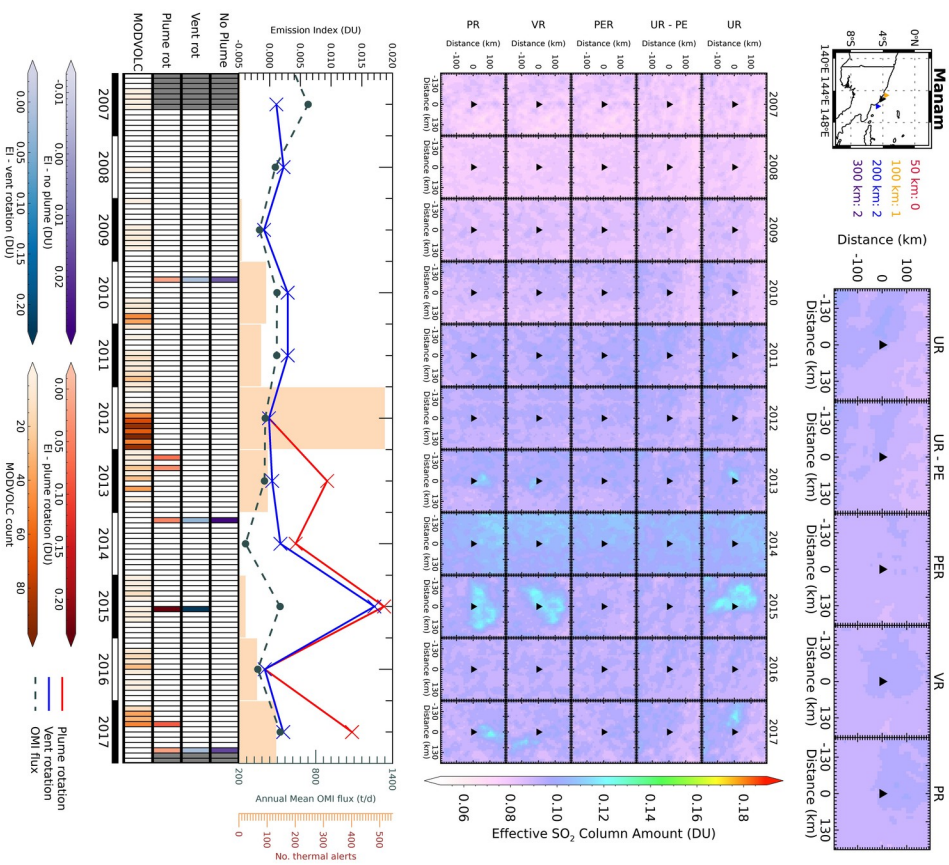


Figure C.21: As for figure C.2 for Manam, Papua New Guinea.



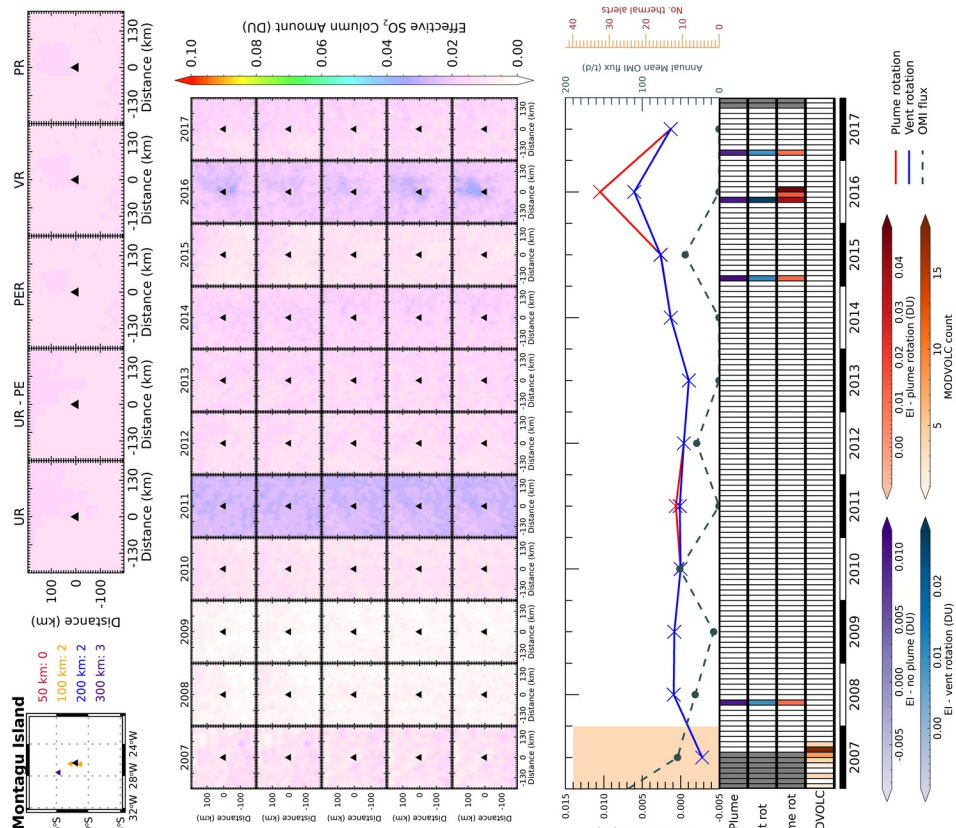


Figure C.23: As for figure C.2 for Montagu Island, South Sandwich Islands.

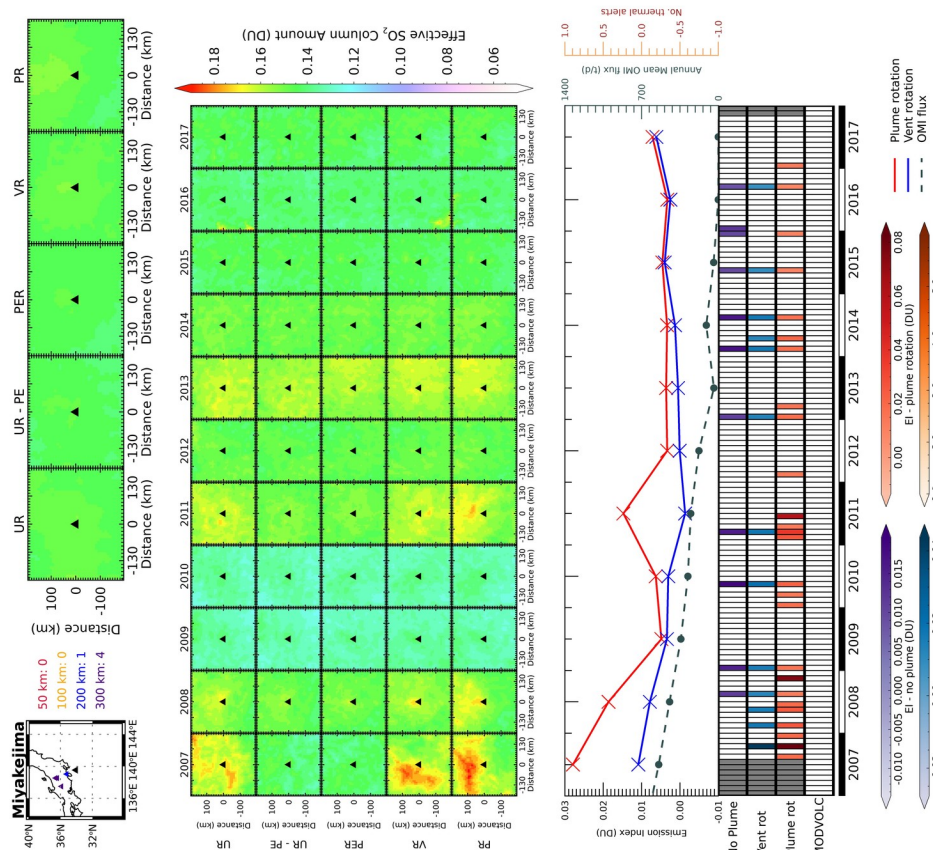


Figure C.22: As for figure C.2 for Miyakejima, Japan.

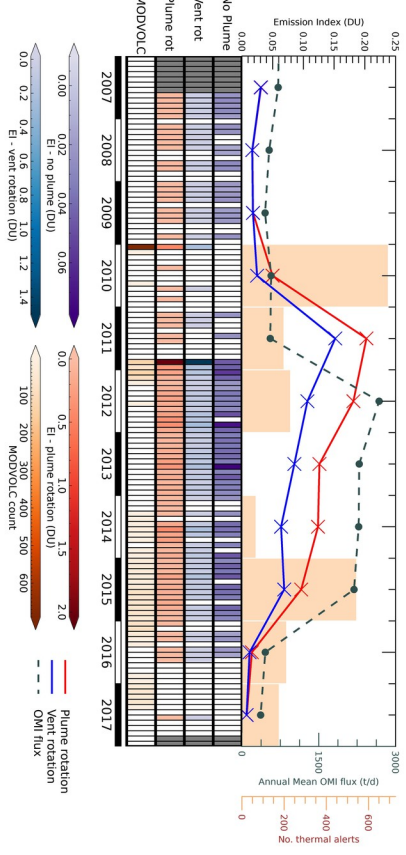
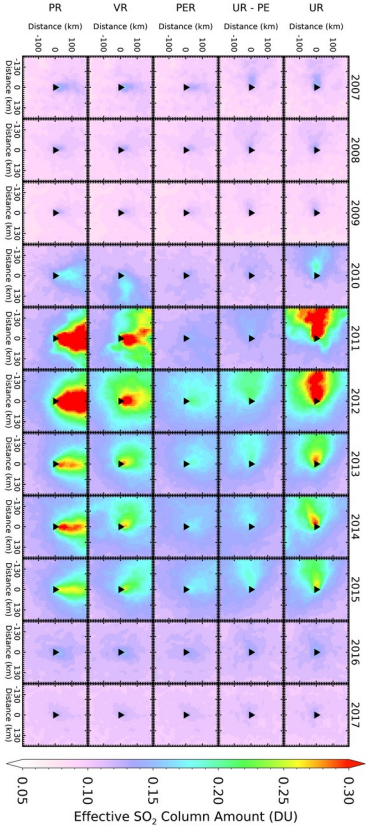
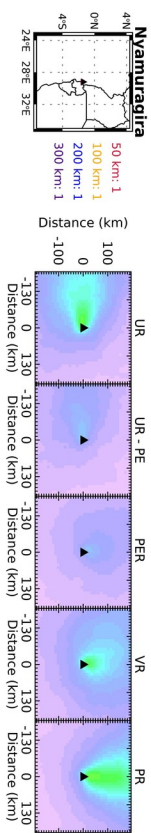


Figure C.24: As for figure C.2 for Nyanunagira, Democratic Republic of the Congo.

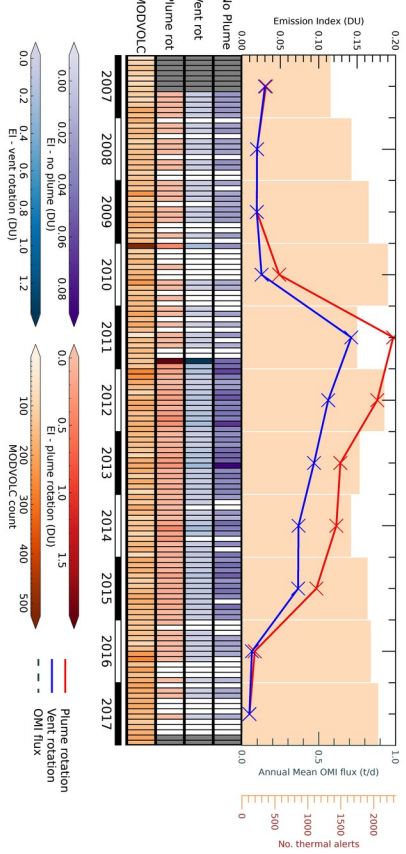
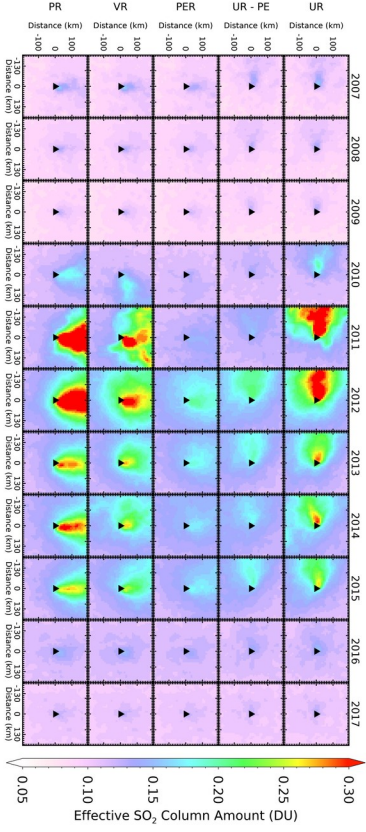
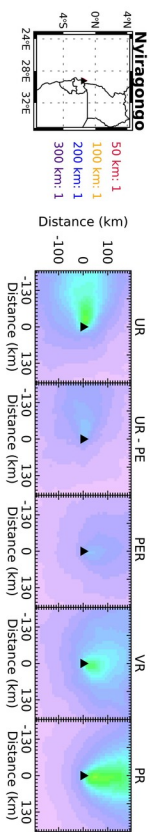


Figure C.25: As for figure C.2 for Niyiragongo, Democratic Republic of the Congo

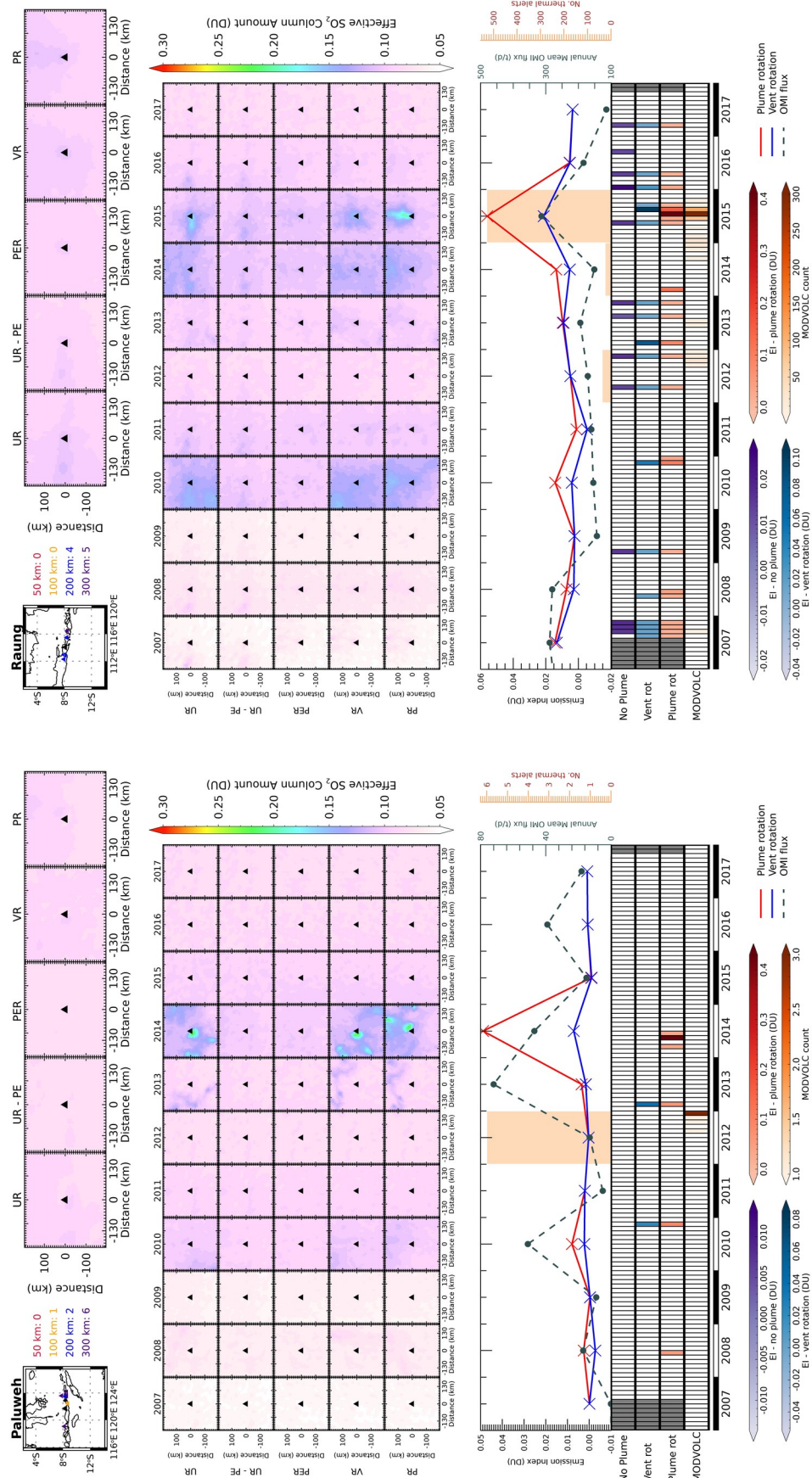


Figure C.26: As for figure C.2 for Paluweh, Indonesia.

Figure C.27: As for figure C.2 for Raung, Indonesia.

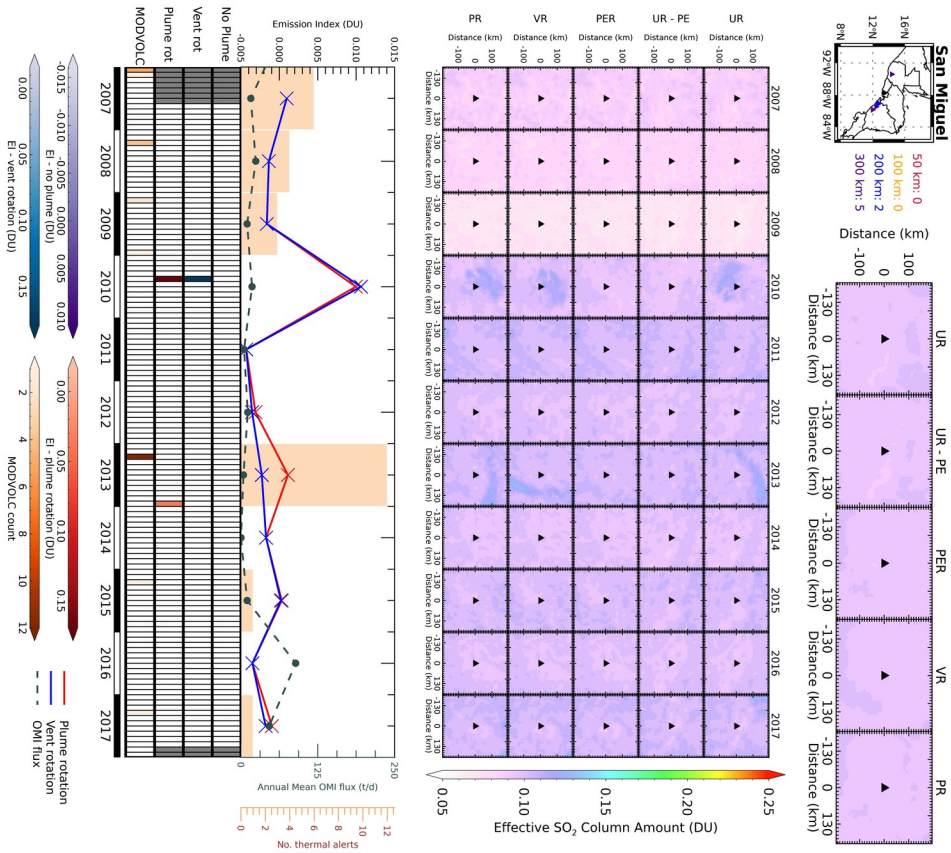


Figure C.28: As for figure C.2 for San Miguel, El Salvador.

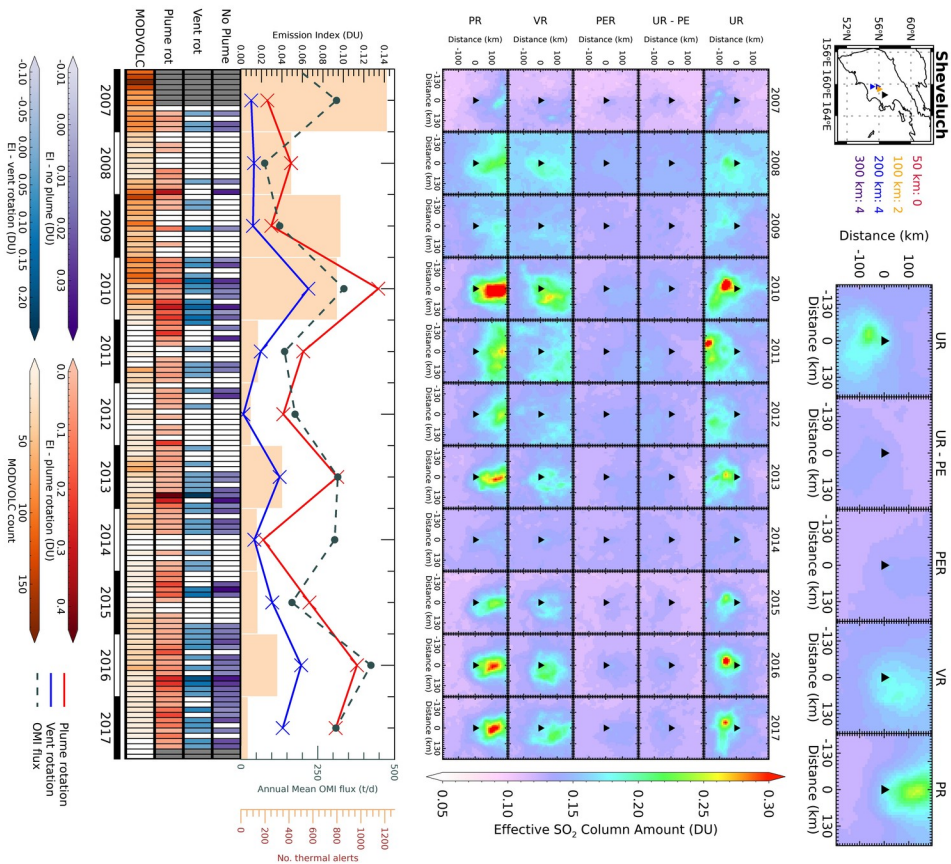
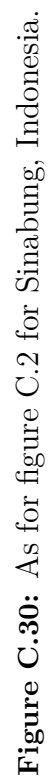


Figure C.29: As for figure C.2 for Sheveluch, Kamchatka.



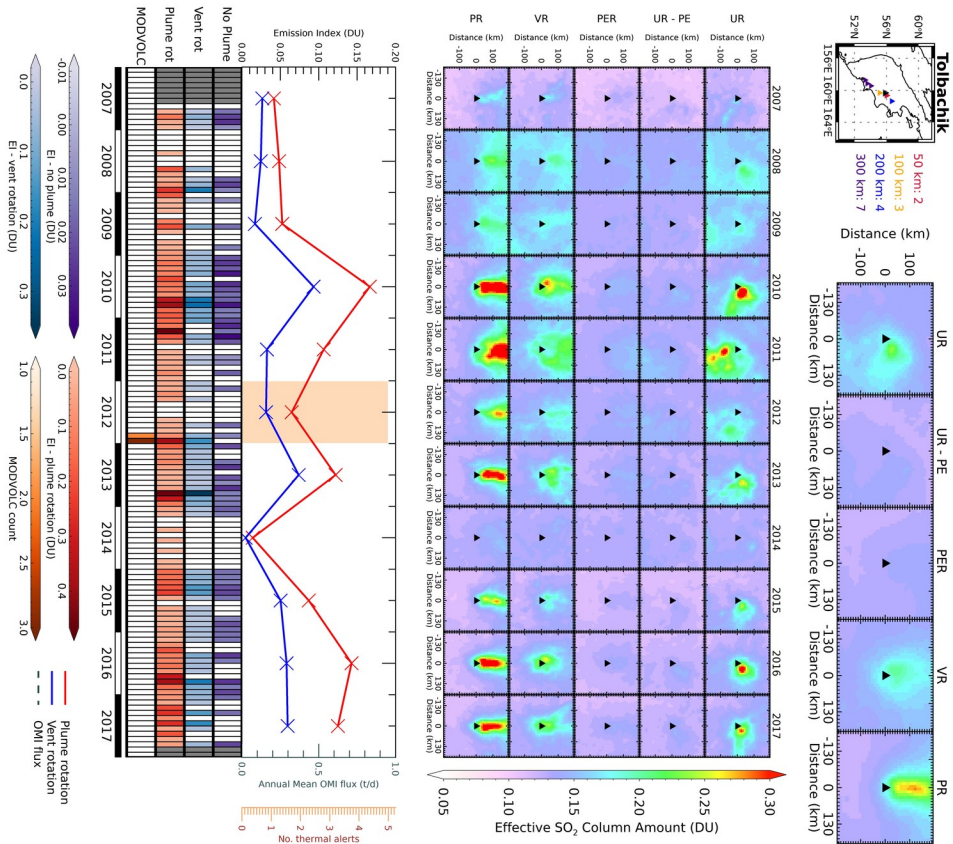


Figure C.32: As for figure C.2 for Tolbachik, Kamchatka.

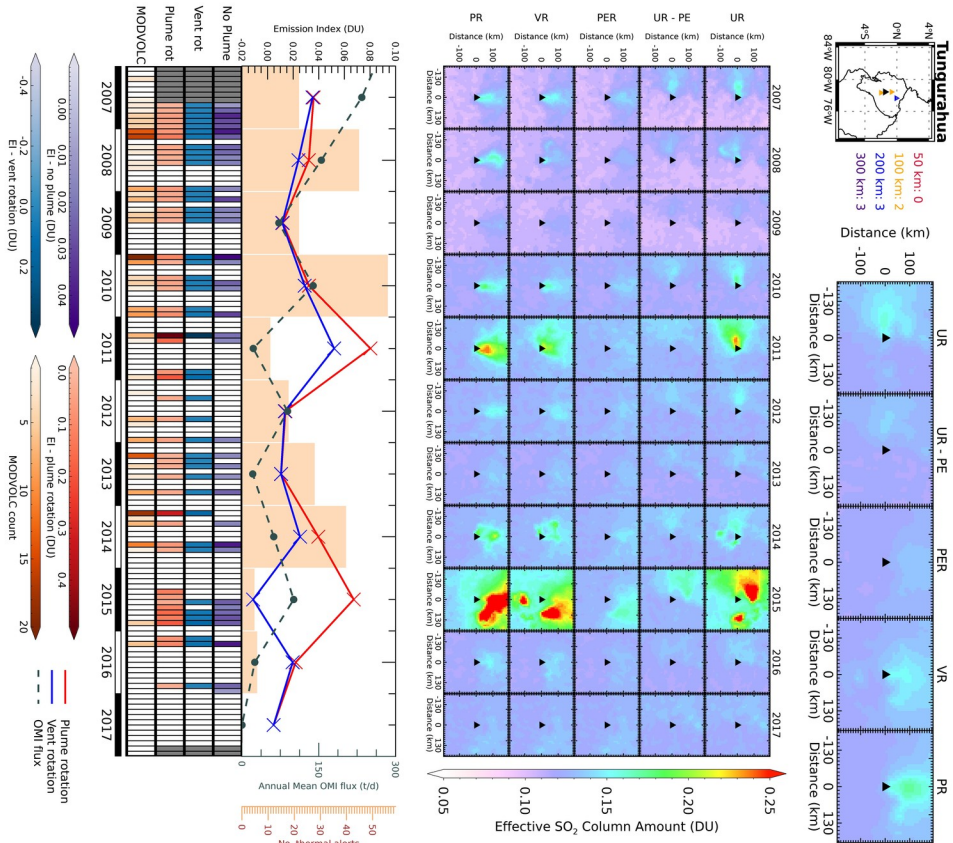


Figure C.33: As for figure C.2 for Tungurahua, Ecuador.

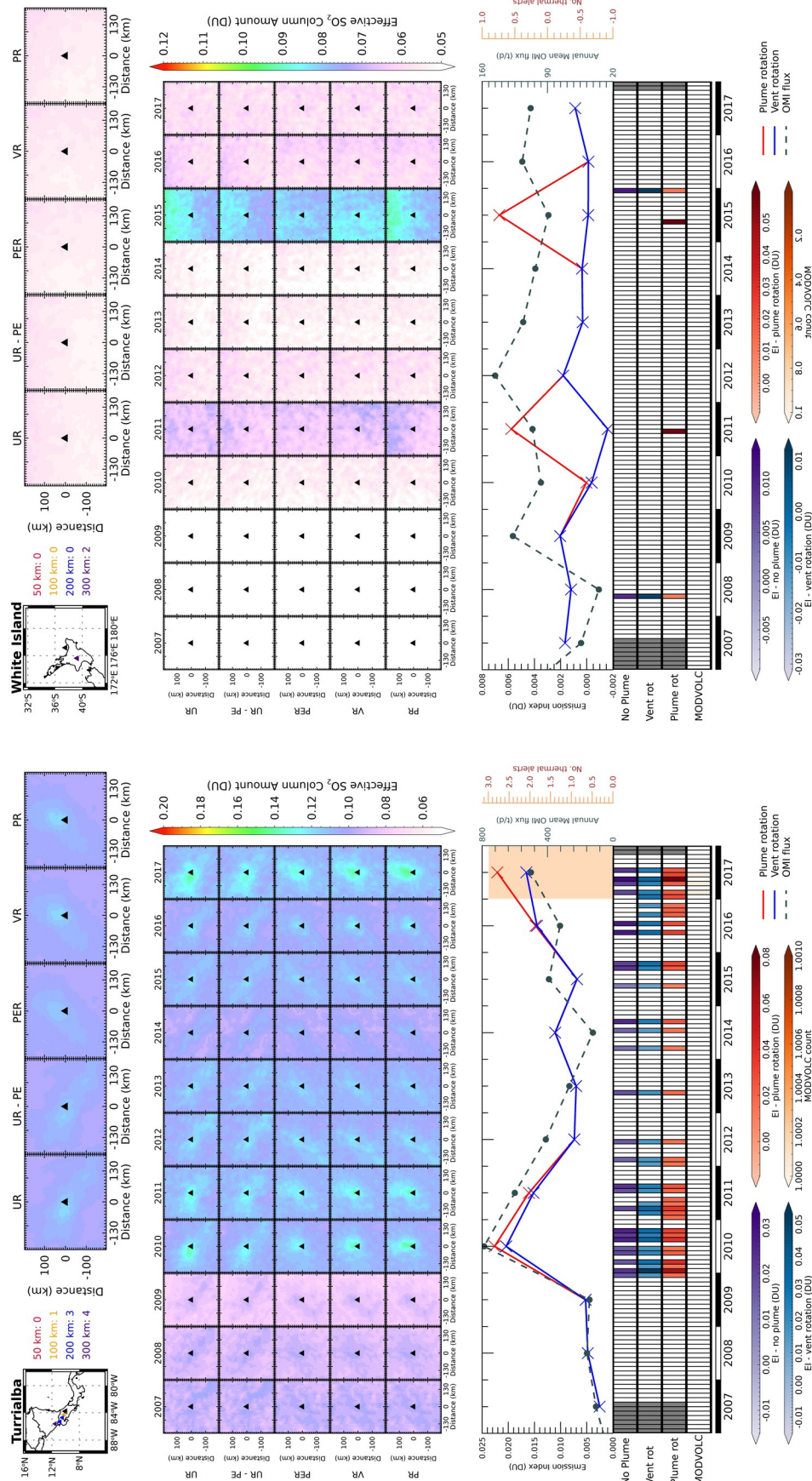


Figure C.34: As for figure C.2 for Turrialba, Costa Rica.

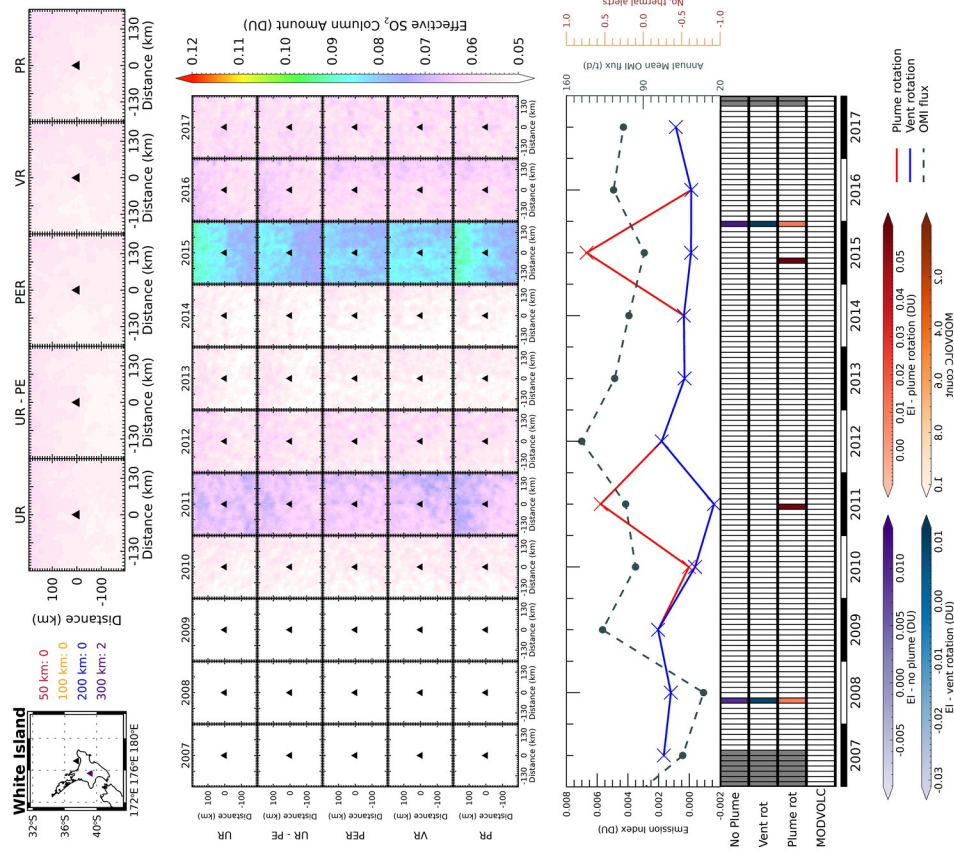


Figure C.35: As for figure C.2 for White Island, New Zealand.

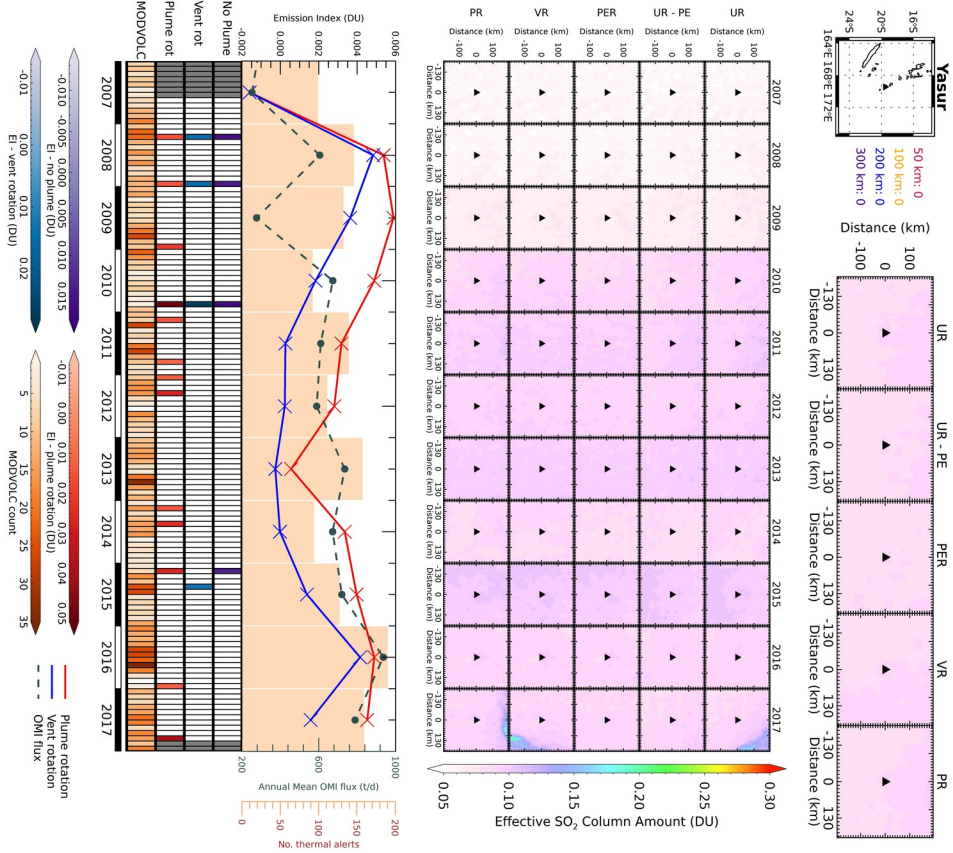


Figure C.36: As for figure C.2 for Yasur, Vanuatu.

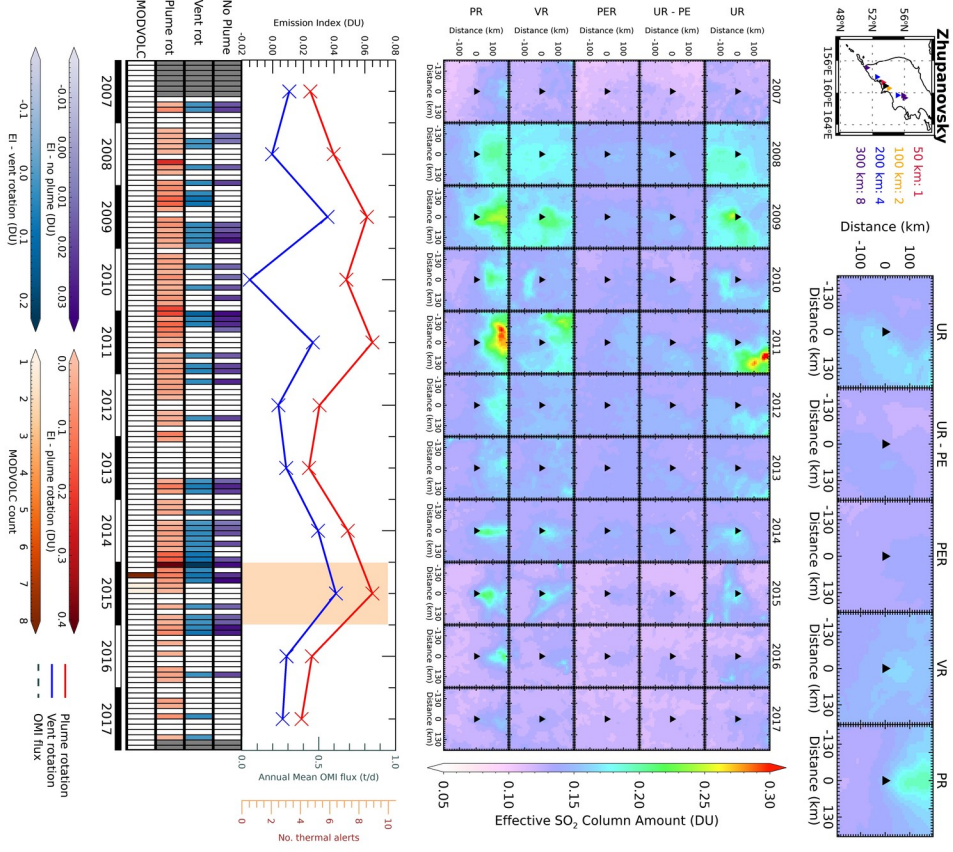


Figure C.37: As for figure C.2 for Zhupanovsky, Kamchatka.